

 **DTU Physics**
Department of Physics

Creating model systems for catalysis with mass-selected nanoparticles

Characterization and properties

Bela Sebok

Supervisor: Professor Ib Chorkendorff

Co-supervisor: Professor Jane Hvolbæk Nielsen

Kgs. Lyngby 2017



Cover image: Illustration of the mass-selected nanoparticle source. Image created by Jakob Kibsgaard and used with his kind permission.

DTU Physics
Department of Physics
Technical University of Denmark

Fysikvej
Building 307
2800 Kongens Lyngby, Denmark
Phone +45 4525 3344
info@fysik.dtu.dk
www.fysik.dtu.dk

Summary

This PhD thesis reports research on the fundamental properties of nanoscale catalysts related to energy conversion processes. These processes and the connected materials will hopefully become more and more important in our future as humanity is shifting to renewable energy sources, but already today plenty of industrial heterogeneous catalysts are based on nanoparticles and their properties. The chapters in this thesis contain research on different processes and give examples of the possibilities of nanoscale catalyst materials. Because of the wide range of processes and materials involved, a brief summary of the included projects is given individually.

If we were to switch to renewable energy sources, utilizing sunlight would be an obvious choice. With the use of a suitable photoabsorber and catalysts, sunlight can be directly used to drive the water splitting process generating O_2 in the oxygen evolution reaction (OER) and H_2 in the hydrogen evolution reaction (HER). It is well known that platinum is the best catalyst for the HER, but its scarcity and cost hinders its large scale use. However, in case of a photoelectrocatalytic water splitting process the rate of HER is limited by the amount of sunlight reaching the photoabsorber, therefore the question arises: how much platinum is actually needed to utilize sunlight? In order to investigate this, we produced silicon photocathodes with different mass loadings of 5 nm mass-selected platinum nanoparticles between $1000 \frac{ng}{cm^2}$ down to $10 \frac{ng}{cm^2}$ and investigated their behaviour. The results showed that even the cathodes with the lowest loadings ($10 \frac{ng}{cm^2}$) have significant catalytic activity, while this loading cannot be detected with X-ray photoelectron spectroscopy (XPS). This means that in non-noble HER catalyst research more sensitive methods than XPS have to be used to ensure truly platinum free electrodes. Based on our results by accepting an overpotential of approx. 50 mV to achieve a current density of $10 \frac{mA}{cm^2}$, which is comparable to the best non-noble HER catalysts, platinum seems feasible and scalable on the TW scale as an HER catalyst in a photoelectrochemical water splitting device despite its scarcity and yearly production of just approx. 180 t.

The other half cell reaction of watersplitting is the OER, for which cheap and abundant catalysts with high activity are still missing. However, in alkaline media mixed Ni and Fe oxides have been used for decades as electrocatalysts for the OER. The exact mechanism and active sites in case of these catalysts are still under debate, and by investigating well-defined model systems further insights can be gained. We studied the OER activity of mass-selected NiFe nanoparticles as a function of their size in 1 M KOH electrolyte. Particles with a diameter of 5.4 nm proved to be the

most active in the investigated size range (3.9-8.4 nm). The data shows that the 5.4 nm nanoparticles are among the most active non-noble alkaline OER electrocatalysts on a turnover frequency basis. We also explored the effect of particle proximity on the OER activity of the particles. It seems that as the particles are getting closer to each other their activity decreases. This could be the result of mass transport limitations and it is under further investigation. Creating well-defined and clean model systems also allowed us to investigate the stability of the NiFe particles during OER. With samples having only a 100 ng of NiFe nanoparticles on their surface, no significant decline of activity was found throughout a 1000 h chronoamperometry at 1.6 V vs. the reversible hydrogen electrode (RHE) in 1M KOH electrolyte showing the stability of the catalyst.

Apart from (photo)electrochemical reactions, nanoparticles play a very important role in different heterogeneous catalytic reactions where the reactants are in the gas phase. In order to investigate some of these reactions we created model systems utilizing the silicon μ -reactors developed earlier at DTU Physics. Unfortunately, because of practical issues with the temperature measurement and control in case of the μ -reactors, the catalytic activity data for both projects included here are compromised, but there are still conclusions which can be drawn. We investigated the size dependent activity of NiFe nanoparticles in the methanation reaction, where methane is created from CO and H₂. The particles proved to be active and produce methane at low pressures and relatively low temperatures. Another reaction investigated was CO oxidation with AuTi bimetallic mass-selected nanoparticles. This is to explore the possibility of utilizing gold as a nanocatalyst. Nanometer sized gold is active for multiple reactions, but gold particles tend to sinter rapidly. It seems possible to stabilize gold particles by alloying them with a different metal, for example titanium. Our results showed that titanium does not cover all gold atom completely even when the alloy particles are heated in and oxidizing environment and TEM results show that the alloying is indeed stabilizing the particles.

Resumé

Denne Ph. D.-afhandling formidler forskning i de fundamentelle egenskaber af nanoskala-katalysatorer som er relaterede til energikonverteringsprocesser. Disse processer og de dertil hørende materialer vil forhåbentlig blive vigtigere og vigtigere i fremtiden, eftersom menneskeheden overgår til vedvarende energikilder, men allerede i dag findes der adskillige industrielle heterogene katalysatorer som er baseret på nanopartikler og deres egenskaber. Kapitlerne i denne afhandling indeholder forskning i forskellige processer og viser eksempler på mulighederne i katalytiske materialer i nanoskala. Eftersom rapporten omhandler en bred vifte af processer og materialer, gives der et kort, individuelt resumé for hvert af de inkluderede projekter.

Hvis vi skulle overgå til vedvarende energikilder, ville brugen af sollys være et oplagt valg. Ved at bruge passende fotoabsorptionsmateriale og katalysator, så kan sollys bruges til direkte at drive vandspaltningsprocessen, som laver O_2 i oxygen-udviklingsreaktionen (OER), og H_2 i hydrogen-udviklingsreaktionen (HER). Det er alment kendt at platin er den bedste katalysator til HER, men dets sjældenhed og pris forhindrer dets brug i stor skala. I en fotoelektrokatalytisk vandspaltningsproces begrænses raten af HER imidlertid af den mængde sollys som når fotoabsorptionsmaterialet, hvilket frembringer spørgsmålet: hvor meget platin er rent faktisk nødvendigt for at udnytte sollys? For at undersøge dette fremstillede vi fotokatoder i silicium med 5 nm masse-selektede platin-nanopartikler i forskellige mængder fra $1000 \frac{ng}{cm^2}$ ned til $10 \frac{ng}{cm^2}$ og undersøgte deres opførsel. Resultatet viste at selv katoderne med de mindste Pt-mængder ($10 \frac{ng}{cm^2}$) har signifikant katalytisk aktivitet, selvom disse mængder ikke kan detekteres med røntgen-fotoelektron-spektroskopi (XPS). Det betyder, at man i HER-forskning på ikke-ædle katalytiske materialer er nødt til at bruge mere følsomme metoder end XPS for at sikre fuldkommen platin-fri elektroder. Baseret på vores resultater, og ved at acceptere et overpotentiale på ca. 50 mV for at opnå en strømtæthed på $10 \frac{mA}{cm^2}$, hvilket er sammenligneligt med de bedste ikke-ædle HER-katalysatorer, så virker platin realistisk og skalerbart på TW-skala som HER-katalysator i fotoelektrokemiske vandspaltnings-anlæg, på trods af dets pris og en årlig produktion på blot ca. 180 t.

Den anden halvcellereaktion i vandspaltning er OER, for hvilken billige og hyppigt forekommende katalysatorer stadig mangler. I basiske medier har blandede Ni og Fe-oxider imidlertid været brugt i årtier som elektrokatalysatorer til OER. Den præcise mekanisme og aktive sites for disse katalysatorer er stadig under debat, og ved at undersøge veldefinerede modelsystemer kan der opnås videre indsigter. Vi stud-

erede OER-aktivitet af masseselektrede NiFe-nanopartikler som funktion af deres størrelse i en elektrolyt af 1 M KOH. Partikler med en diameter på 5.4 nm viste sig at være de mest aktive i det undersøgte størrelses-område (3.9-8.4nm). Resultaterne viser at nanopartiklerne på 5.4 nm er blandt de mest aktive ikke-ædle OER-elektrokatalysatorer i base, hvis man måler i forhold til deres katalytiske omsætningsfrekvens. Vi undersøgte også effekten af partikel-tæthed på OER-aktiviteten af partiklerne. Det ser ud til at aktiviteten falder når partiklerne kommer tættere på hinanden. Det kunne være et resultat af massetransport-begrænsninger og er under videre undersøgelse. De veldefinerede og rene modelsystemer tillod os desuden at undersøge stabiliteten af NiFe-partiklerne under OER. Med prøver som kun havde 100 ng NiFe-nanopartikler på overfladen så vi intet signifikant fald i aktivitet gennem 1000 timers kronoamperometri ved 1.6 V vs. den reversible hydrogen-elektrode (RHE) i 1 M KOH-elektrolyt, hvilket viser stabiliteten af katalysatoren.

Ud over (foto)elektrokemiske reaktioner så spiller nanopartikler en meget vigtig rolle i forskellige heterogene katalysereaktioner hvor reaktanterne er i gasfase. For at undersøge nogle af disse reaktioner lavede vi modelsystemer, hvor vi brugte de silicium-mikroreaktorer som tidligere er udviklet på DTU Fysik. Uheldigvis, så er de katalytiske aktivitetsresultater for begge projekter påhæftet med fejl, pga. praktiske problemer med temperaturmålingerne- og kontrollen på mikroreaktorerne, men der kan stadig drages konklusioner af arbejdet. Vi undersøgte størrelsesafhængig aktivitet af NiFe-nanopartikler til methaniseringsreaktionen, hvor methan produceres af CO og H₂. Partiklerne viste sig at være aktive og danne methan ved lave tryk og relativt lave temperaturer. En anden undersøgt reaktion var CO-oxidation med bimetalliske, masseselektrede AuTi-nanopartikler. Det blev gjort for at undersøge muligheden for at bruge guld som nanokatalysator. Guld i nanometerstørrelse er aktivt til adskillige reaktioner, men guldparkler har en tendens til at sintre hurtigt. Det ser ud til at være muligt at stabilisere guld-partikler ved at leger dem med et andet metal, fx titanium. Vores resultater viste at titanium ikke dækker alle guldatomer fuldstændigt, selv når legeringspartiklerne varmes op i et oxiderende miljø, og TEM-resultater påviser at legeringen vitterligt stabiliserer partiklerne.

Preface

This PhD thesis was written under the supervision of Prof. Ib Chorkendorff and Prof. Jane Hvolbæk Nielsen at the Department of Physics of the Technical University of Denmark (DTU) in fulfilment of the requirements for acquiring a PhD degree in physics. The project was funded by the European Union's Seventh Framework Programme (FP7/2007-2013) grant 607417 (CATSENSE ITN). Most of the work was carried out at the Surface Physics & Catalysis (SurfCat) group at DTU, but some results were acquired during external stays at the Nanoscale Physics Research Laboratory at the University of Birmingham. I had a major role in the production and physical characterization of the samples for the projects included in the thesis, but I could not have done all the work without collaborating with others mentioned in the acknowledgement section. I have done my best to indicate what was my contribution to the projects throughout the thesis and to give credit to others for their work.

Kgs. Lyngby, April 2, 2017



Bela Sebok

Acknowledgements

First and foremost I would like to say thank you for the support and help to the professors who made it possible for me to go through with the experiments. To Ib Chorkendorff for believing in me, helping along the way and for the countless ideas. To Jane Hvolbæk Nielsen for her kind words and guidance in need and for the fact that she always had a smile for all of us. To Ifan Stephens for the interesting discussions, the huge amount of help and for the nice experience of my first visit to the USA, which I will never forget.

For funding, I would like to thank the European Union's Seventh Framework Programme (FP7/2007-2013) for the support of the CATSENSE ITN (grant no. 607417) program I was funded from. I would also like to thank the Villum Foundation's V-SUSTAIN grant 9455 to the Villum Center for the Science of Sustainable Fuels and Chemicals for funding the laboratory.

I would like to extend my gratitude to the staff, students and guests of DTU SurfCat who were around during the three years. I have had a great time and made new friendships and experiences I will never forget. First and foremost I would like to mention Anders Bodin. We spent a lot of time together sharing an office and room in the laboratory and I think it was a great three years! He also made it possible for me to meet my girlfriend and to adapt to the Danish lifestyle. Bastian Mei for countless nights out doing stupid things and having a lot of scientific discussions as well (not at the same time of course) and occasionally also doing sports. Daniel Trimarco for the ever interesting discussions and all the fun he brings to everyone's life (although maybe unintentionally). Jakob Riedel for many many friendly discussions about the big things of life (and science) and for putting out the small fire I started in the laboratory. Claudie Roy for not just the common work and her help, but tolerating me as a close co-worker and for expertly pointing out my flaws. Sine Olesen, Ann-Louise Christoffersen, Martin Bækbo, Søren Scott and Erlend Bertheussen for all the discussions. Anders-Filsøe Pedersen for the nice time in the USA. Jakob Kibsgaard for all the discussions about career choices and science. And of course Kenneth Nielsen and Robert Jensen without whom the laboratory would not function.

From a wider circle, I would like to thank first and foremost Elisabetta Fiordaliso for all the help with microscopy, her patience and generally "just" making some days happier. Zoltan Balogh for all the discussions in Hungarian and for reminding me that there are some really weird Hungarians (including myself). Dan Shacham and Peder Heise for all the help from the workshop and by making me realise that

my obsession with classic vehicles is not unique. Thomas Pedersen for helping with cleanroom-related work.

From the CATSENSE project, I would like to thank everyone for the opportunity to learn and experience new things while having great time and fun together. I would especially like to say thank you to Philomena Schlexer and Yubiao Niu for our joint work. I would also like to mention Jinlong Yin, who made it possible for me to spend my external stay at Teer Coatings, which provided me with a lot of interesting experiences.

A big-big thank you to Josefine for being next to me all the time, every day no matter what. Her family for welcoming me, accepting me and for all the interesting experiences. I hope everything is going to continue like this in the future and then I will be happy!

And finally thank you for my family for years and years of support, during my education, years in Hungary and now years in Denmark. I do not know how to formulate how immensely grateful I am for all they have done for me and given me. I hope that in the end I prove to be worthy of their support.

List of Papers

Papers appended to the thesis

Scalability and feasibility of photoelectrochemical H₂ evolution: the ultimate limit of Pt nanoparticle as an HER catalyst

Erno Kemppainen, Anders Bodin, Béla Sebok, Thomas Pedersen, Brian Seger, Bastian Mei, Dowon Bae, Peter CK Vesborg, Janne Halme, Ole Hansen, Peter D Lund, Ib Chorkendorff

Energy & Environmental Science, 2015, **8**, 2991-2999 DOI: 10.1039/C5EE02188J

Oxygen evolution on well characterized mass-selected NiFe nanoparticles: mechanism and size-effect

Claudie Roy*, Béla Sebok*, Elisabetta M. Fiordaliso, Anders Bodin, Søren B Scott, Daniel B Trimarco, Christian D. Damsgaard, Jakob Kibsgaard, Ifan E L Stephens, Ib Chorkendorff

In preparation

*: These authors contributed equally.

Sintering of mass-selected Au and AuTi clusters on SiO₂: A STEM and computational study

Yubiao Niu, Philomena Schlexer, Béla Sebok, Ib Chorkendorff, Gianfranco Pacchioni, Richard E Palmer

In preparation

Papers not appended

H₂/D₂ exchange reaction on mono-disperse Pt clusters: enhanced activity from minute O₂ concentrations

Jakob Nordheim Riedel, Marian David Rötzer, Mikkel Jørgensen, Ulrik Grønbjerg Vej-Hansen, Thomas Pedersen, Béla Sebok, Florian Frank Schweinberger, Peter Christian Kjærgaard Vesborg, Ole Hansen, Jakob Schiøtz, Ulrich Heiz and Ib Chorkendorff

Catalysis Science & Technology, 2016, **6**, 6893-6900 DOI: 10.1039/C6CY00756B

In-situ XAS study of the oxygen evolution reaction on Ir and Ru in acidic media

Anders F. Pedersen, Maria Escudero-Escribano, Bela Sebok, Anders Bodin, Elisa Paoli, Rasmus Frydendal, Daniel Friebe, Ifan E. L. Stephens, Jan Rossmeisl, Anders Nilsson, Ib Chorkendorff

In preparation

Melting point on the nanometer scale: an HRTEM and computational study of mass-selected Au and Pt nanoparticles

Philomena Schlexer, Anton B Andersen, Bela Sebok, Ib Chorkendorff, Thomas W Hansen, Gianfranco Pacchioni

In preparation

List of Abbreviations and Symbols

Abbreviations

ALD	Atomic Layer Deposition
BV	Buffer Volume
CEN	Center for Electron Nanoscopy, DTU
CV	Containment Volume (μ -reactor setup)
CV	Cyclic Voltammetry (electrochemistry)
FWHM	Full Width at Half Maximum
HAADF STEM	High Angle Annular Dark Field Scanning Transmission Electron Microscopy
HDI	Human Development Index
HER	Hydrogen Evolution Reaction
HSA	HemiSpherical energy analyser
ICP-MS	Inductively Coupled Plasma Mass Spectrometry
ISS	Ion Scattering Spectroscopy
IV	current-voltage
MFC	Mass Flow Controller
NND	Nearest Neighbour Distance
NPRL	Nanoscale Physics Research Laboratory, University of Birmingham
OCV	Open Circuit potential

OER	Oxygen Evolution Reaction
PC	Pressure Controller
pcAu	polycrystalline Au
PEC	PhotoElectroCatalytic
PV	PhotoVoltaic
QCM	Quartz Crystal Microbalance
QMS	Quadrupole Mass Spectrometer
RDE	Rotating Disk Electrode
RDF	Radial Distribution Function
RHE	Reversible Hydrogen Electrode
RTD	Resistance Temperature Detector
SEM	Scanning Electron Microscope
TEM	Transmission Electron Microscopy
TOF	Turn Over Frequency
ToF	Time-of-Flight
TOF _{max}	TOF assuming only the surface metal (Ni and Fe) atoms of the particles are active
TOF _{min}	TOF assuming all metal atoms in the (NiFe) particles are active
TP	Turbomolecular Pump
TPD	Temperature Programmed Desorption
TPR	Temperature Programmed Reduction
UNIMIB	University of Milano-Bicocca
UoB	University of Birmingham
XPS	X-ray Photoelectron Spectroscopy

Symbols

η Viscosity

$\eta_{10 \frac{\text{mA}}{\text{cm}^2}}$ Overpotential to achieve $10 \frac{\text{mA}}{\text{cm}^2}$ of current

$\eta_{Kinetic}$	The overpotential due to reaction kinetics
η_{MT}	The overpotential due to mass transport losses
η_{total}	The total overpotential, which is constituted of the overpotentials due to mass transport losses and due to reaction kinetics
λ	Mean free path of a gas molecule
ν	Frequency of photons
ϕ	Work function of the energy analyser
ρ_{bulk}	Density of the bulk material
$\rho_{ND}(r)$	Average number density of particles
$\rho_{ND}^{rand}(r)$	Average number density of randomly distributed particles
Θ	Scattering angle (ISS)
A_i	Integrated XPS peak area after background subtraction
A_{Fe}	Area of the Fe 2p _{3/2} XPS peak after background subtraction
A_{Ni}	Area of the Ni 2p _{3/2} XPS peak after background subtraction
A_{NP}^{TEM}	The area of the projection of a nanoparticle determined from bright field TEM imaging
c_i	Concentration of element i in at%
c_{int}	Conductance of a capillary in the intermediate flow regime
c_{mol}	Conductance of a capillary in the molecular flow regime
d_p	Diameter of a particle
d_{calc}	Calculated diameter of a nanoparticle
E_P	Kinetic energy of the primary ion (ISS)
E_{bin}	Binding energy of an electron (XPS)
E_{BS}	Kinetic energy of the backscattered ion (ISS)
E_{gap}	Band gap
E_{kin}	Kinetic energy of electrons (XPS)
$g(r)$	Radial Distribution Function (RDF)

h	Planck constant, $6.626 \times 10^{-34} \frac{\text{m}^2\text{kg}}{\text{s}}$
I_{depo}	Deposition current
i_{Ph}	Photocurrent density
i_{rec}	Current density corresponding to the recombination rate
k_B	Boltzmann constant, $k_B = 1.381 \times 10^{-23} \frac{\text{J}}{\text{K}}$
K_n	Knudsen number
M_P	Mass of the primary ion (ISS)
m_p	Mass of a single particle
M_S	Mass of the scattering atom (ISS)
m_{depo}	Mass of the deposited nanoparticles
n_{SC}	Ideality factor
p_1	Pressure in the high pressure volume (capillary flow)
p_2	Pressure where the flow changes from an intermediate flow to a molecular flow (capillary flow)
p_3	Pressure in the vacuum chamber (capillary flow)
P_{avg}	Average power of a PEC device
r	Radius
R_{max}	The maximum of the radius investigated in the calculation of the RDF
RSF_i	Relative Sensitivity Factor of a given XPS peak of element i
RSF_{Fe}	Relative sensitivity factor of the Fe 2p _{3/2} XPS peak
RSF_{Ni}	Relative sensitivity factor of the Ni 2p _{3/2} XPS peak
t_{depo}	Deposition time
V_{OC}^{PV}	open circuit photovoltage

List of Figures

1.1	Illustration for how a catalyst works	2
1.2	Total primary energy supply of the world from 1990 to 2015	4
1.3	Human development index and the energy consumption	5
1.4	Atmospheric CO ₂ concentration at Manua Loa (Hawaii) from March 1958 until today	6
1.5	Historical atmospheric CO ₂ concentration reconstructed from ice cores . .	6
1.6	Electricity production by wind turbines in Denmark along with the electricity consumption	7
1.7	Total surface area of 1 m ³ of material formed into smaller and smaller cubes	8
1.8	Simulated shape of Au nanoparticles containing different numbers of Au atoms	10
2.1	The Omicron Multiscan Lab XP and the NanoBeam 2011 system	14
2.2	Mean free path of electrons as a function of their energy in different materials ("universal curve")	16
2.3	Illustration of an ISS measurement and spectrum	18
2.4	Energy loss of different incident primary ions after backscattering as a function of the mass of the target atom	19
2.5	Illustration of the depth information carried by ISS spectra	20
2.6	Schematic of the magnetron sputtering gas aggregation mass-selected nanoparticle source	21
2.7	Picture of a heavily used Ru sputter target showing the "racetrack" pattern of the plasma sputtering	23
2.8	Schematic of the lateral ToF mass filter	25
2.9	Picture of the mask used to define the deposition area and to measure the current of the mass-selected nanoparticle beam	27
2.10	Example mass spectra to illustrate the capabilities of the nanoparticle source and the lateral ToF mass filter	28
2.11	Images of the front and back side of a μ -reactor	29
2.12	Illustration of a small capillary connecting high pressure to vacuum	30
2.13	Illustration of the cold bonding of the μ -reactors	33
2.14	Temperature distribution during the cold bonding of μ -reactors from finite element analysis	33

2.15	Opening of a bonded μ -reactor	34
2.16	Schematic layout of the μ -reactor setup	34
2.17	Schematic layout of an alkaline electrolyser	36
2.18	Picture of an RDE setup along with a polycrystalline Au working electrode	38
2.19	Illustration of the interaction of an electron beam with a material	39
2.20	Schematic illustration of a transmission electron microscope (TEM) and a scanning electron microscope (SEM)	39
2.21	Schematic illustration of a quadrupole mass filter (QMS)	42
3.1	Illustration to the simulation of the TiO_2 protected Si photocathode and Pt nanoparticle catalyst	45
3.2	Size distribution of the mass selected Pt nanoparticles having 850k amu mass along with an example image from bright field TEM imaging	47
3.3	XPS survey spectra and detailed spectra of the Pt 4f region of photocathodes with different Pt nanoparticle loadings	47
3.4	ISS spectrum of a TiO_2 proteted Si photocathode with $10 \frac{\text{ng}}{\text{cm}^2}$ mass-selected Pt nanoparticle loading	48
3.5	SEM images taken of photocathodes having different Pt nanoparticle loadings	49
3.6	Measured and simulated IV-curves of the TiO_2 proteted Si photocathodes having different Pt nanoparticle loadings	50
3.7	Comparison of the effect of mass transport and reaction kinetics on the overpotential of photocathodic HER as a function of Pt nanoparticle loading	52
3.8	Overpotential as a function of current density and Pt nanoparticle loading along with the amount of Pt required for a TW of energy produced	53
4.1	ISS spectrum of an empty, cleaned and annealed pcAu stub before deposition	59
4.2	Identical location SEM images of a pcAu stub with 350k amu NiFe nanoparticles before and after OER measurements	60
4.3	Size-distributions and example images of the NiFe nanoparticles	62
4.4	Reproducibility of NiFe nanoparticle depositions on pcAu stubs shown by ISS spectra	63
4.5	Reproducibility of NiFe nanoparticle depositions on pcAu stubs shown by peak areas in the XPS spectra	64
4.6	ISS spectra of 5.4 nm (350k amu) NiFe nanoparticles on pcAu after deposition and after OER activity testing	65
4.7	XPS survey spectra of 5.4 nm (350k amu) NiFe nanoparticles on pcAu after deposition and after OER activity testing	66
4.8	Average Fe content of the NiFe nanoparticles having different sizes as determined by XPS	67
4.9	Example XPS detailed spectra of the Ni $2p_{3/2}$ region after deposition and after OER activity testing in case of all 4 sizes of NiFe nanoparticles	68
4.10	Example XPS detailed spectra of the Fe $2p_{3/2}$ region after deposition and after OER activity testing in case of all 4 sizes of NiFe nanoparticles	69

4.11	Comparison of the Ni 2p _{3/2} and Fe 2p _{3/2} XPS detailed spectra of 6.7 nm (950k amu) NiFe nanoparticles after activity testing, after 14h of air exposure and after 2.5 h in 1M KOH at OCV (different samples)	70
4.12	Cyclic voltammetry measurements of three samples with 5.4 nm (350k amu) NiFe nanoparticles before and after 2 h chronoamperometry	71
4.13	OER activity of the NiFe nanoparticles at 300 mV overpotential vs their size	72
4.14	OER TOF of 5.4 nm (350k amu) NiFe nanoparticles compared to the literature	73
4.15	Long term chronoamperometric measurement of a sample with 6.7 nm (950k amu) NiFe nanoparticles at 1.6 V vs. RHE	74
4.16	Bright field TEM images of lacey C covered Cu TEM grids having different loadings of 6.7 nm (950k amu) NiFe nanoparticles	76
4.17	SEM images of pcAu stubs having different coverages of 6.7 nm (950k amu) NiFe nanoparticles	77
4.18	Calculated Radial Distribution Functions based on TEM and SEM images recorded of samples with different loadings of NiFe particles	78
4.19	Average NND of 6.7 nm (950k amu) NiFe nanoparticles as a function of loading	79
4.20	Mass activity of 6.7 nm (950k amu) NiFe nanoparticles as a function of the average NND	80
5.1	CO oxidation activity of Au nanoparticles on different substrates as a function of their size	85
5.2	Representative HAADF-STEM images of Au ₂₀₅₇ and 400k amu AuTi nanoparticles along with their size distributions. Figure courtesy of Yubiao Niu (UoB, NPRL)	87
5.3	Sequential HAADF-STEM images of Au and AuTi dimers sintering under electron irradiation on unsputtered SiO _x	88
5.4	Sequential HAADF-STEM images of AuTi dimers further apart under electron irradiation on unsputtered SiO _x	88
5.5	The very first μ-reactor tested with 400k amu AuTi nanoparticles showing CO oxidation activity and deactivation below 100°C	90
5.6	Examples of CO oxidation activity measurements with μ-reactors containing Au ₂₀₅₇ and 400k amu AuTi nanoparticles as well as the result of running the same test with empty μ-reactors	91
5.7	SEM images of Au ₂₀₅₇ nanoparticles in a μ-reactor before testing and after testing at 100°C	91
5.8	Representative SEM images of 400k amu AuTi nanoparticles in μ-reactors before testing and after testing with temperature ramps to 100°C and 150°C. Images courtesy of Elisabetta Fiordaliso (DTU CEN)	92
5.9	Size-distributions of 400k amu AuTi nanoparticles deposited on μ-reactors before and after CO oxidation activity testing with temperature ramps to 100°C and 150°C	93

5.10	Identical location SEM images of Au and AuTi nanoparticles in μ -reactors after heating them to 100°C for an hour under CO oxidation conditions	94
5.11	XPS spectra of μ -reactors with Au ₂₀₅₇ and 400k amu AuTi nanoparticles before and after 1 h at 100°C under CO oxidation conditions (1 bar, O ₂ :CO=4:1)	95
5.12	ISS spectra of μ -reactors with Au ₂₀₅₇ and 400k amu AuTi nanoparticles before and after 1 h at 100°C under CO oxidation conditions (1 bar, O ₂ :CO=4:1)	96
5.13	ISS spectrum recorded after activity test with temperature ramps to 100°C in case of the only μ -reactor with 400k amu AuTi nanoparticles which showed CO oxidation activity	96
5.14	Volcano curve depicting the methanation activity of selected metals at 550 K in a flow reactor with 1% CO in H ₂ as a function of the dissociative adsorption energy of CO calculated by DFT	99
5.15	Gas flow and temperature profile used for testing the activity of NiFe mass-selected nanoparticles as model catalyst for the methanation reaction in μ -reactors	100
5.16	Methanation activity of NiFe mass-selected nanoparticles as measured with μ -reactors	101
5.17	Effect of the reduction between methanation runs on the activity of the NiFe mass-selected nanoparticles	103
5.18	Identical location SEM images of NiFe mass-selected nanoparticles having different mass deposited into μ -reactors before and after methanation activity test	104
5.19	XPS survey and Ni 2p _{3/2} detailed spectra of the same μ -reactor containing NiFe mass-selected nanoparticles after deposition and after methanation activity testing	105
5.20	ISS spectra recorded after deposition in case of μ -reactors with NiFe mass-selected nanoparticles having different mass	106
5.21	XPS detailed spectra of the Ni 2p _{3/2} region recorded in case of as deposited μ -reactors with NiFe mass-selected nanoparticles having different mass	107
5.22	XPS detailed spectra of the Ni 2p _{3/2} region recorded in case of nine μ -reactors after deposition of 980k amu (approx. 7 nm) mass-selected Ni nanoparticles	108
5.23	ISS spectra recorded in case of the nine μ -reactors after deposition of 980k amu (approx. 7 nm) Ni mass-selected nanoparticles	109
5.24	Illustration of the instability of the Pt RTDs on the backside of the μ -reactors	110
5.25	SEM image of a filament blocking the shadowmask used for the deposition of the Pt RTDs on the backside of the μ -reactors	111
5.26	SEM image of a constriction in the shadowmask used for the deposition of the Pt RTDs on the backside of the μ -reactors	111
A.1	Reduction of Ni by bombardment with He ⁺ ions as shown by the detailed XPS spectra of the Ni 2p _{3/2} region	116

B.1	Mass spectrum of particles leaving the aggregation zone with single and double mass shown	117
B.2	TEM image showing overlapping NiFe nanoparticles, nanoparticles having double mass and doublet of half mass nanoparticles too	119
B.3	Illustration for the determination of the deposition current (I_{depo})	121
C.1	Rendered image of the original Omicron sample plate used to transfer samples in the chamber and on which all the sample holder designs are based	126
C.2	Rendered image of the general use sample holder with the mask for TEM grids	127
C.3	Rendered image of the μ -reactor sample holder	128
C.4	Image of the μ -reactor sample holder with a μ -reactor attached	128
C.5	Rendered image of the sample holder for RDE stubs	129
D.1	Steps of determining the size-distribution of nanoparticles from TEM images	132
D.2	Bright field TEM image to illustrate particles landed on top of each other and particles having double mass	133
E.1	Illustration for the calculation of the RDF in 2D	136
E.2	Validation of the self written script calculating RDFs in 2D: RDF of random ensembles	137
E.3	Validation of the self written script calculating RDFs in 2D: 2D square lattice	137
E.4	Illustration for particle position determination from TEM images	138
E.5	Illustration for particle position determination from SEM images	139
F.1	XPS and ISS spectra of an uncleaned, undeposited μ -reactor showing signs of Ba and Ga/Ge contaminations	141
F.2	Determination of the sputter time needed to remove the adventitious carbon contamination from the surface of the μ -reactors by ion sputtering (1 keV Ar^+) based on XPS spectra	142
F.3	XPS and ISS spectra recorded of undeposited but previously cleaned μ -reactors	143

List of Tables

3.1	Measured overpotentials to achieve $10 \frac{\text{mA}}{\text{cm}^2}$ current density ($\eta_{10 \frac{\text{mA}}{\text{cm}^2}}$) as a function of Pt nanoparticle loading on the photocathodes	51
4.1	Summary of the start and endpoints of the Shirley backgrounds fitted to the Ni 2p _{3/2} and Fe 2p _{3/2} XPS peaks recorded of the NiFe nanoparticles on pcAu stubs	66
B.1	Comparison between the number of 6.7 nm (950k amu) NiFe nanoparticles in a given area (TEM image) calculated based on the deposition current and determined based on TEM images	123

Contents

Summary	i
Resumé	iii
Preface	v
Acknowledgements	vii
List of Papers	ix
List of Abbreviations and Symbols	xi
List of Figures	xi
List of Tables	xvii
Contents	xix
1 Introduction	1
1.1 Catalysis is around/in us	1
1.2 Why going nano?	8
1.3 Thesis outline	10
2 Experimental techniques and procedures	13
2.1 UHV techniques and the mass-selected nanoparticle source	13
2.2 μ -reactors and the μ -reactor setup	29
2.3 Water splitting and investigating its half cell reactions	35
2.4 Electron microscopy techniques	38
2.5 Other techniques referred to in the thesis	41
3 The limit of Pt as a catalyst for hydrogen evolution	43
3.1 Introduction	43
3.2 Physical characterization of the deposited nanoparticles	46
3.3 Activity of ultra-low loadings of Pt nanoparticles for PEC hydrogen evolution	50
3.4 Pt as a TW scale HER catalyst	52

3.5	Summary	54
4	Mass-selected NiFe nanoparticles as a catalyst modelsystem for the oxygen evolution reaction in alkaline media	55
4.1	Introduction	56
4.2	Electrochemical measurements and the protocol used	57
4.3	Deposition of mass-selected NiFe nanoparticles	58
4.4	Physical characterization of the NiFe nanoparticles and substrates	61
4.5	Electrochemical measurements	71
4.6	Summary	80
5	Investigation of gas phase heterogeneous catalytic reactions in μ-reactors using mass-selected nanoparticles	83
5.1	AuTi bimetallic mass-selected nanoparticles for CO oxidation	84
5.2	NiFe bimetallic mass-selected nanoparticles for the methanation reaction	97
5.3	Problems with the μ -reactors and the depositions discovered	107
6	Conclusion and outlook	113
A	Reduction of oxidized NiFe nanoparticles by sputtering with He⁺ (ISS)	115
B	Additional details of the depositions	117
C	New sample holder designs	125
D	Determination of the size-distribution of nanoparticiles with bright field TEM imaging	131
E	Calculation of the radial distribution function and the centre to centre nearest neighbour distance: method and validation	135
F	Cleaning of the μ-reactors	141
	Bibliography	145
	Appended papers	157

CHAPTER 1

Introduction

What is catalysis and what is a catalyst? Most probably a random person on the street would answer either nothing or something about the catalytic converter under cars (busses, on ships and locomotives etc.). But catalysis is a lot more than that and a broad field involving several industries and life itself.

1.1 Catalysis is around/in us

Almost all of our everyday products are somehow connected to a catalytic process. The vast majority (85-90%) of the products from the chemical industry are from catalytic processes [1]. Think of polymers, medicine, transportation and the list of areas where catalysis is crucial goes on. Fertilizers made out of ammonia from a catalytic reaction (Haber-Bosch process) are making possible to feed the population of Earth [2]. Actually, life itself is based on catalysis: the enzymatic processes in our body are also catalytic reactions.

1.1.1 What is a catalyst? What is catalysis?

In general a catalyst is accelerating chemical processes [1]. It is doing so by forming bonds with the reactants, facilitating the process and then releasing the products. The catalyst is not consumed in the process, therefore it is able to promote the reaction of new reactants. In this description the catalyst can be anything (enzymes, metal surfaces etc.). For ease of explanation and because this thesis deals with these specific systems, from this point on catalyst is meant as a metal (or oxide) surface and catalysis as heterogeneous catalysis (catalyst and reactants are in different phase). Figure 1.1 illustrates how catalysis works. The catalyst surface (blue) binds molecules and facilitates breaking of some of the bonds. As a result the species on the surface can form new bonds and compounds (products) and the formed product molecules can leave the surface after the reaction. The right hand side of Figure 1.1 shows the schematic Gibbs free energy diagram of the hypothetical catalytic reaction (blue line) and the reaction catalysed by the surface (red line). A few conclusions are straightforward: naturally, the Gibbs free energy change is the same with or without the catalyst and the process should run spontaneously (the Gibbs free energy is decreasing). However, without the catalyst the reaction has a large energy barrier,

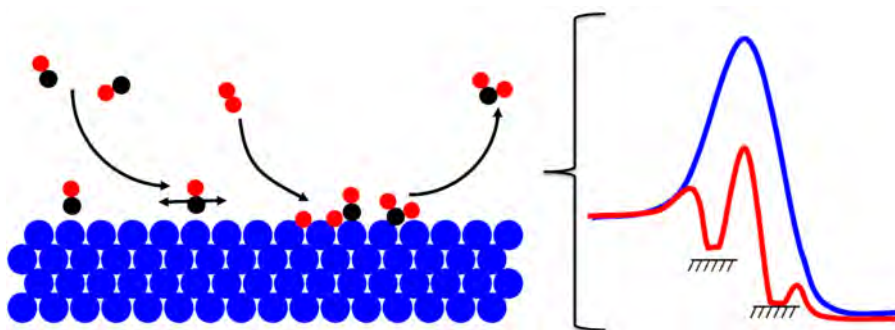


Figure 1.1: Illustration for how a catalyst works. The catalyst surface (blue) binds reactants facilitating the breaking of some of the bonds and the formation of new compounds. The formed products can leave the surface and the process is repeated afterwards. The free energy diagram on the right hand side illustrates the energetics of the reaction: even though the process is favourable by thermodynamics (overall decrease of Gibbs free energy) it has a large energy barrier without the catalyst (blue line). Using the catalyst opens a new, more complex reaction pathway with lower energy barriers (red line). Image reproduced from [3].

meaning that the process is slow (or practically not running at all). The reactants can be heated up to facilitate the reaction without the catalyst, but that is not always technically possible (safety, required temperatures are too high etc.) and usually not economical. On the other hand, with the catalyst the reaction is running a slightly more complex pathway with smaller energy barriers, meaning a higher reaction rate. This is how a catalyst works: by creating a new reaction pathway with lower energy barriers. It is very important to keep in mind that the catalyst is only changing the kinetics and not thermodynamics.

The binding energies of reactants, reaction intermediates and products are important properties of a catalyst. It is fairly straightforward to see that the best catalyst is not the material which binds the surface species the strongest or the weakest. In the first case (strong binding), the products cannot leave the surface or the surface adsorbs so much of the reactants that there is no space for new species to form. In the latter case (weak binding), there are no species on the surface which could form the product as no reactant is bound to the surface. This line of thought describes Sabatier's principle from 1911 [4]: the ideal catalyst has an interaction with the reactants which is not too weak and not too strong. This is a vague statement and it was much later with the advancement of DFT calculations and material simulations, when this principle could be put to use in designing catalysts [5].

1.1.2 Energy and catalysis

The total energy consumption of the world is continuously increasing (Figure 1.2), which can be directly linked to the development of humanity and the lifestyle of people. Unfortunately the increase of total energy production is not based on renewable sources. The vast majority of the increase in the last 30-40 years was covered by the more intense use of coal, oil and gas. Figure 1.3 shows the Human Development Index (HDI) of different countries along with their average per capita energy consumption and population (circle size). HDI is a composite index made by the United Nations, which measures the well-being of a population in general. Naturally, developed countries have a high HDI and high energy consumption as well. Countries with big populations are still developing on the HDI scale (Figure 1.3), therefore the total energy consumption of humanity is expected to grow even further. Because most of the energy comes from fossil sources this also means an increasing emission of greenhouse gases. By far the biggest pollutant is CO_2 and its concentration is steadily increasing in the atmosphere. Figure 1.4 shows the continuously measured concentration of atmospheric CO_2 at the Manua Loa (Hawaii) volcano since March 1958. These are direct measurements showing the seasonal variations of the CO_2 levels as well as the clear increasing trend of the concentration. One could easily say that this is surely not great, but it does not seem that bad. However, in the life and natural cycles of the Earth, 60 years is a short period of time. Looking at reconstructions from ice core data, a completely different picture emerges (Figure 1.5). It seems that there was no point in time in the last 400000 years, when the CO_2 concentration in the atmosphere was as high as today and the rate of increase is exorbitant.

The solution could be the use of renewable energy and generating electricity using wind turbines or solar cells. Unfortunately these technologies pose new problems. An example can be showed with data from the wind turbines in Denmark. Denmark is especially well suited for the building of (off-shore) wind farms and their electricity production data are readily available on the internet [10]. Figure 1.6 shows the electricity consumption in Denmark during the course of a randomly chosen week in the beginning of 2017, along with the amount of electricity produced by wind turbines. As a thought experiment the figure also shows what would happen if we would double the amount of electricity produced by wind turbines (e.g. by building new wind farms). The figure shows the periodic nature of electricity consumption: there are peaks in the consumption every evening, due to people getting home, cooking, watching TV and switching on lights and there is a lot less electricity consumed during the nights when people are sleeping. The general consumption during the weekends is also less than what is consumed during the week, most probably because some industrial consumers drain less power. Looking at the electricity production by wind turbines (which are already supplying approx. 40% of the total electricity consumption) it is prevalent that there are times when their electricity production is higher than the consumption and there are times, when it is a lot lower. In this sense the situation would get even worse if we would double the electricity production of wind turbines. Right now, the electricity grid can handle these inequalities as electricity can be exported

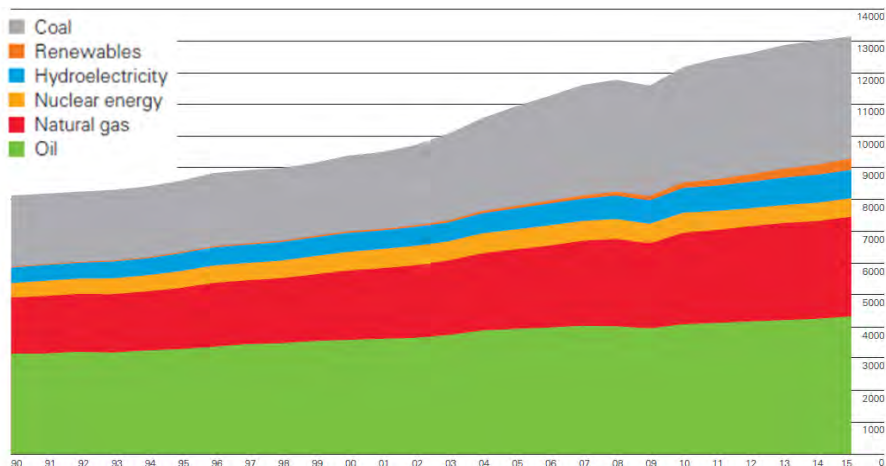


Figure 1.2: Total primary energy supply of the world from 1990 to 2015 in Mtoe (million tons oil equivalent). Around 80% of the energy supply is covered by coal, gas and oil and their importance is not decreasing. Notice how small portion (approx. 2.8%) of the total energy renewables provide. Figure reprinted from [6].

or imported as needed, but if every country would change to renewable electricity sources the intermittent nature of them would be a serious problem. In order to solve this problem the storage of energy is needed. This could be done for example by using electrocatalysis to produce chemicals like H_2 when there is an excess of electricity and convert them back when there is a need for electricity. The excess electricity could also be used to produce fuels and other chemicals in a sustainable way too. A possibility is for example to produce H_2 using renewable electricity and CO from biomass and turn them into different hydrocarbons using gas phase heterogeneous catalysis. These hydrocarbons (e.g. methane or methanol) could be used as fuels or energy carrier with the already existing infrastructure. There are countless possibilities of what to create and how to convert it into useful chemicals, fuels or energy, but there is one common aspect of all of these processes: they would involve catalysis.

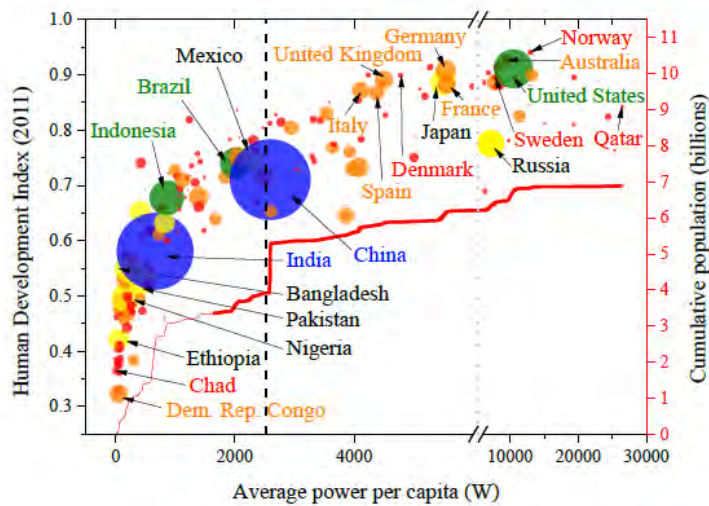


Figure 1.3: Human Development Index (HDI) and the average per capita energy consumption of different countries along with their population (size of circles) and the cumulative population. The HDI describes the welfare of a population (including housing, health and schooling) and it is created by the United Nations. Developed countries have high HDI and high energy consumption, while developing countries with large populations are still climbing both the HDI and energy consumption scales. Figure by Anders Filsøe Pedersen, reproduced from [7].

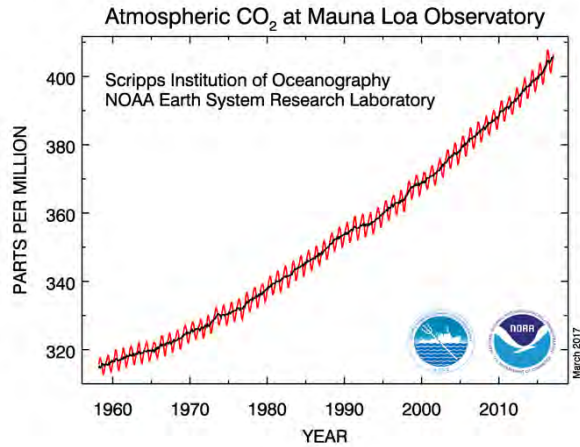


Figure 1.4: Atmospheric CO₂ concentration at Manua Loa (Hawaii) from March 1958 until today. Notice that the increase is much larger than the seasonal variations. Figure from [8].

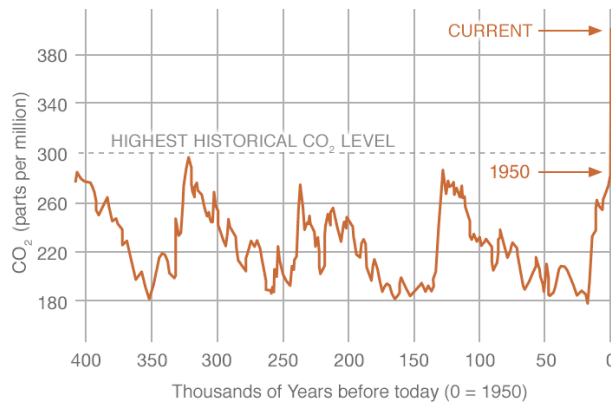


Figure 1.5: Historical atmospheric CO₂ concentration reconstructed from ice cores. Even though these are indirect measurements, the trend is fairly striking: there was no earlier point in time in the last 400000 years when the atmospheric CO₂ concentration was as high as today and the rate of increase is immense. Figure from [9].

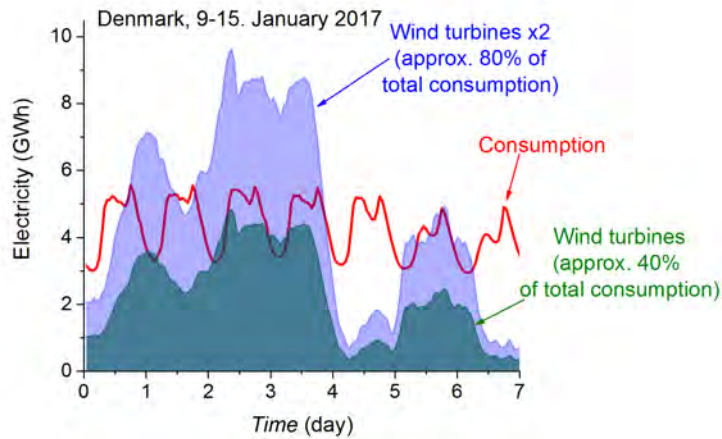


Figure 1.6: Electricity production by wind turbines in Denmark along with the electricity consumption. Notice that already now there are times when more electricity is generated by the wind turbines than the consumption. Figure idea from Rasmus Frydendal [3], data updated from [10].

1.2 Why going nano?

Catalysts consisting of particles dispersed on some kind of support (e.g. alumina or carbon) are common in industry. The size of these particles is usually in the sub μm range. Getting into the nanometer size regime gives a multitude of advantages, e.g. high surface area to volume ratio or special properties. So far catalysis was introduced as something which requires the surface of a metal or an oxide. As a consequence, the catalyst material should provide a high surface area without the use of too much material to keep the costs down. If we take 1 m^3 of material and form a cube with an edge length of 1 m , it will have a surface area of 6 m^2 . If we form the 1 m^3 material into smaller and smaller cubes (the number of these cubes will increase), the total surface area of these smaller cubes will get bigger and bigger as the edge length is decreasing (Figure 1.7). Therefore, in general minimising the size of the catalyst particles helps in increasing the surface area of them using the same amount of material, which ideally means the same cost. As smaller and smaller cubes are made, it is not only the surface area which is increasing. The total amount of undercoordinated sites on the surface, practically the edges of the small cubes, are also increasing and as it turns out these can play a crucial role in some of the catalytic processes (e.g. [11]). Nevertheless, real nanoparticles are not small cubes and exhibit a lot of unique and size dependent properties regarding their catalytic activity (shown earlier for example for the oxygen reduction reaction in our group [12]), optical (e.g. size-dependent non linear optical behaviour of Ag nanoclusters and nanoparticles [13, 14]) or magnetic properties (e.g. the magnetic relaxation method in small goethite particles is different than in bigger forms of the same material [15]) etc.

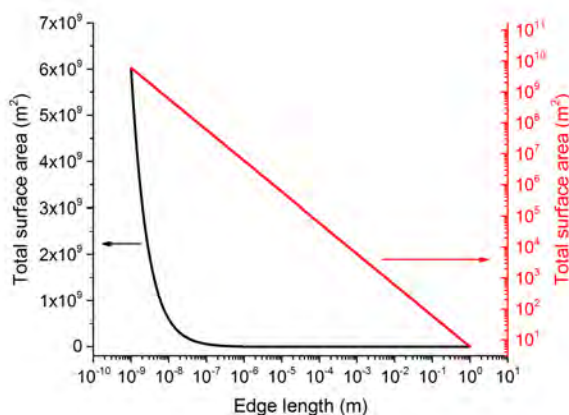


Figure 1.7: Total surface area of 1 m^3 of material formed into smaller and smaller cubes. The two lines show the same data set, but the red line is a log-log plot.

The shape of nanoparticles is determined by energetics and the equilibrium shape of an unsupported nanoparticle can be determined using Wulff's theorem [16]. It states that the distance of a specific plane from the centre point of the particle is proportional to the surface energy of that plane. Therefore, a surface plane which has a small surface energy is closer to the centre point and cuts out all other plane and dominates the surface of the partricle [1]. Naturally, the particles are usually on some kind of support. The strength of the particle - support interaction (the interface energy) influences their shape: as the interface energy increases, the particles become more and more truncated. Nowadays the shape of particles can be calculated with computers and the results visualized highlighting the atoms with different coordination numbers on the surface. An example is given in Figure 1.8 for Au particles constituted of different number of Au atoms [17]. The shape of the biggest particle (having 8000 atoms) looks as expected from the Wulff construction, with the (111) facet dominating the particle (atoms having a coordination number of 9). However, as the particles are getting smaller, shapes different compared to the Wulff construction can be found as having the lowest energy, in order to accommodate the arbitrary number of atoms contained in the particles. This also shows one of the limitations of the Wulff construction. As the size of the particles are getting so small that the addition or removal of a single atom is changing their properties significantly, the Wulff construction, which is a continuum model, is not valid anymore. Figure 1.8 also shows the general trend increasing ratio of undercoordinated sites with decreasing particle size.

1.2.1 Model systems

As mentioned before, nanoparticles exhibit size-dependent properties. In catalysis it could be beneficial to take advantage of these unique properties to create more active and efficient catalysts. As the methods used to characterize surfaces usually require well-defined samples which fulfil a multitude of requirements (cleanliness, size, weight, conductivity etc.) model systems are needed. Creating mass-selected nanoparticles under ultra high vacuum conditions and investigating their properties provide a way to produce well controlled and clean samples which can provide an insight into size dependent properties and ultimately can lead to designing new catalysts. The field of catalyst research has reached a point where atomically accurate clusters of materials can be created and investigated to gain knowledge about their catalytic properties as shown in recent reviews from Tyo and Vajda [18] and Vajda and White in [19].

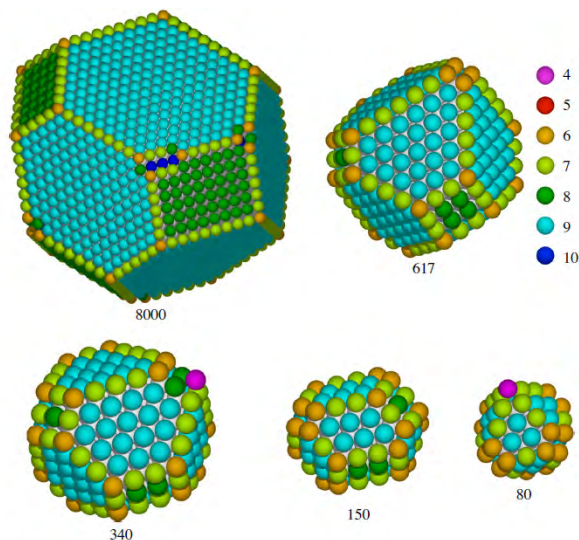


Figure 1.8: Simulated shapes of Au nanoparticles containing different numbers of Au atoms. These shapes represent the lowest energy found in simulations. The biggest particle (8000 atoms) is dominated by (111) facets with an atomic coordination number of 9 and resembles closely to a Wulff constructed particle. As the size is decreasing, the shape departs from the Wulff construction to accommodate the arbitrary number of atoms. As the size of the particles is getting smaller, the ratio of undercoordinated atoms on the surface is increasing. Image taken from [17].

1.3 Thesis outline

This thesis revolves mainly around the production and characterization of mass-selected nanoparticles used as model catalysts. The projects included in the thesis are not the only ones I have been involved in, but these were the most important projects of my three years at DTU. Here I would like to give a short summary of the chapters in the thesis.

Chapter 2 gives a short summary of the experimental methods used or mentioned throughout the thesis. Emphasis is on the production and physical characterization of the particles. I cannot hope to give a comprehensive review of all the methods in the space available, but I intend to give enough information to make the following chapters understandable.

Chapter 3 explores just how good a catalyst Pt is for the hydrogen evolution reaction and shows that it is indeed feasible to use Pt on the TW scale in a solar

water splitting device as a hydrogen evolution catalyst regardless of its scarcity and price. This project ended up as a publication in *Energy & Environmental Science* [20] which is appended to this thesis.

Chapter 4 is the main project of my three years at DTU. It has been going on for almost two years now and when I am writing this, there are still a few experiments planned. We gathered experimental data on NiFe mass-selected nanoparticles as electrocatalysts for the oxygen evolution reaction in alkaline media. We investigated their activity as a function of their size, their stability and the effect of particle proximity on the activity of the nanoparticles. There is a manuscript in preparation containing the results of our research, whose abstract is appended to the thesis.

Chapter 5 contains investigation of gas phase heterogeneous reactions in μ -reactors developed at DTU Physics. We studied the possibility to stabilize Au particles on SiO_2 by alloying them with Ti in order to create an active and sintering resistant CO oxidation catalyst. Furthermore, we studied the activity of NiFe nanoparticles in the methanation reaction as a function of their size. Unfortunately our activity data turned out to be compromised as there were technical issues with the Si chips used as μ -reactors. However, there is a manuscript in preparation about the sintering behaviour of Au and AuTi nanoparticles based on STEM and computational study, which will include some of my XPS and ISS measurements. The abstract of this paper is appended to the thesis.

Appendices The appendices contain information which is not strictly part of the projects described in the main chapters, but which are necessary for supporting the data in them. Some of the work shown in the appendices (like the new sample holder designs) are things which I really enjoyed doing and wanted to share with everyone.

CHAPTER 2

Experimental techniques and procedures

In this chapter I would like to give a short overview of the techniques used to attain the results contained in this thesis. Each of these techniques would require a full PhD thesis to describe in depth, therefore my intentions are to give the basics, so the following chapters can be understood.

As I was mainly participating in the production and physical characterization of samples, those sections will have priority. Especially in case of electrochemistry and photoelectrochemistry, I am only trying to convey a short introduction to watersplitting and describe the measurements briefly so the results can be understood.

2.1 UHV techniques and the mass-selected nanoparticle source

The system that this entire thesis relies most on is a Scienta-Omicron GmbH (Germany) made complex surface analytical system (Multiscan Lab XP), modified extensively by our group for various projects and needs, which is equipped for the use of a multitude of surface analytical techniques. Coupled to this system is a magnetron sputtering gas aggregation nanoparticle source, capable of producing mass-selected nanoparticles (Nano-Beam 2011, Birmingham Instruments Ltd., UK) and described in details in Section 2.1.2. Both these systems are UHV compatible and routinely reach base pressures in the low 10^{-10} - 10^{-11} mbar region. The sample transfer system allows the investigation of samples after mass-selected nanoparticle deposition by surface analytical methods without breaking the UHV conditions. The entire system is situated in a vibration-damped and temperature-controlled annex and it is shown in Figure 2.1.

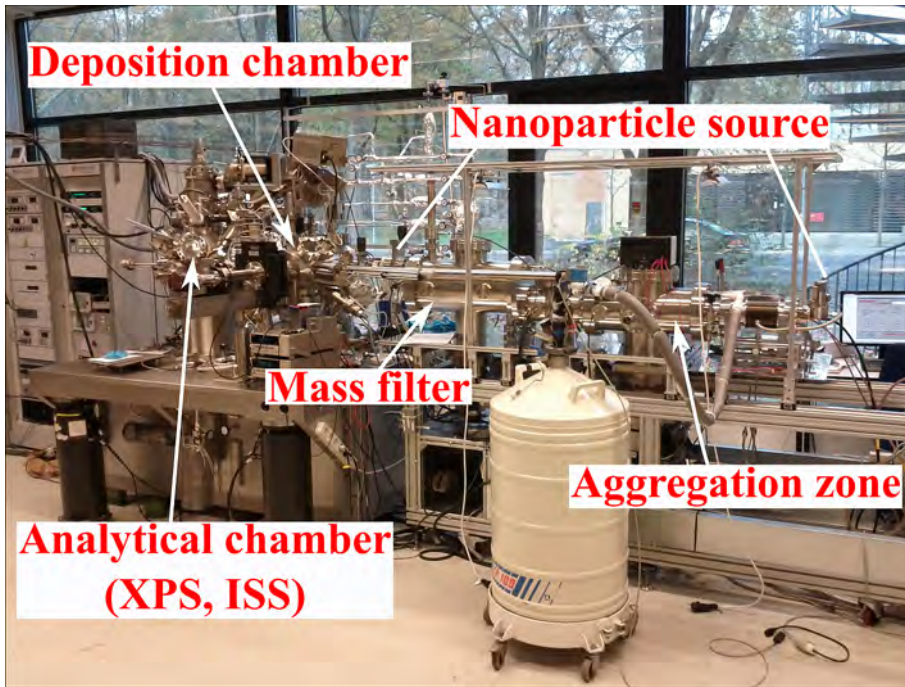


Figure 2.1: The Omicron Multiscan Lab XP and the NanoBeam 2011 system in the laboratory.

2.1.1 Omicron UHV system and the integrated techniques

For the projects described in this thesis three techniques were used out of the analytical capabilities of the Omicron system, namely X-ray photoelectron spectroscopy (XPS), ion scattering spectroscopy (ISS) and the UHV scanning electron microscope (SEM). The latter is described in Section 2.4.2. For XPS and ISS a short description is given in the following. The energy analyser used for both techniques is the same Omicron NanoSAM 7-channel hemispherical energy analyser (HSA). The X-ray gun attached to the chamber is a non-monochromatised, twin anode (Mg and Al) SPECS XR50 gun. The ion gun used for the ISS measurements is a differentially pumped Omicron ISE100 focused ion gun equipped with a rastering ion optics.

2.1.1.1 X-ray photoelectron spectroscopy

XPS is a method for quantitatively determining the composition of a surface and the binding state of the elements on the surface [21]. The technique is based on the measurement of the kinetic energy of electrons leaving the surface as a result of the photoelectric effect [22] induced by X-ray radiation. If the incoming X-ray photon

has an energy of $h\nu$, the maximum kinetic energy of an electron (E_{kin}) leaving the surface can be described by [23]:

$$E_{kin} = h\nu - E_{bin} - \phi \quad (2.1)$$

Here E_{bin} is the binding energy of the electron and ϕ is the work function of the energy analyser (characteristic to the system used, usually given in the manual or can be determined with standards). Therefore, by bombarding the surface with monochromatic X-rays and measuring the kinetic energy of the photoelectrons leaving the surface, the binding energy of these electrons can be calculated. The set of binding energies are fully element specific and carry information about the binding state of the corresponding element [1].

X-rays with a narrow energy distribution can be generated using the characteristic X-ray emission of metals as a result of bombardment with high energy electrons. Usually electrons from a heated filament are accelerated towards a water cooled anode (10-15 kV, 20 mA). The incident high energy electrons might remove electrons from the 1s level of the atoms in the anode and the hole might be filled from electrons from the 2p_{1/2} or 2p_{3/2} levels. The decrease in electron energy is released in the form of X-ray photons, denoted by K_{α1,2}. The anode of an X-ray gun is usually coated with magnesium or aluminium giving rise to characteristic energies of 1253.6 eV (Mg) and 1486.3 eV (Al) with full width at half maximum (FWHM) of 0.7 eV (Mg) and approx. 1 eV (Al) [1]. However other transitions are possible and the emission spectra of elements are fairly complex [24]. Without monochromation the photoelectrons induced by these additional lines create "X-ray satellites" in the spectra with given energy and distance from the main line. For example an Mg anode has a line at 8.5 eV higher energy than the main K_α X-ray line with 9.1% of its intensity [24]. For the spectra shown in this thesis the Mg K_α radiation was used without monochromation if not otherwise stated.

The kinetic energy of the electrons leaving the surface is usually measured by a hemispherical electron energy analyser. It is constituted of two concentric hemispheres having a potential difference, such that electrons entering the analyser are forced onto a circular path. Electrons with different energies are moving on trajectories with different radii. With the aid of a slit at the exit a given energy can be selected and an electron multiplier after the slit detects the electrons with the right energy. The energy of the electrons passing the slit can be changed by tuning the potentials on the two hemispheres. In a multichannel analyser, there are more than one electron multiplier (and correspondingly more than one slit or a bigger slit) and the electrons for more than one energy can be measured at the same time increasing the signal-to-noise ratio (with the same measurement time) or lowering the measurement time (with the same signal-to-noise ratio). During XPS measurement the HSA is usually used in a constant pass energy mode, meaning that electrons are decelerated to a given energy before entering the analyser by electron optical lenses and the potentials in the analyser are not changed. This gives the same energy resolution throughout the entire spectrum.

The X-ray photons are penetrating deep into the target material and generate photoelectrons. However, these electrons have a finite mean free path depicted in the "universal curve" (Figure 2.2). The curve contains the mean free path of electrons vs. their kinetic energy in different materials compiled from experimental results [25]. In the kinetic energy range of photoelectrons, the mean free path is between 5-100 Å (the information depth of XPS), with a minimum at around 50-100 eV kinetic energy. This is the reason for the surface sensitivity of XPS: electrons from deeper regions might reach the surface (with exponentially decaying chance) but they lose energy by doing so and only contribute to the background. However, electrons from the topmost layer(s) can leave the surface without losing energy and create the peaks in the XPS spectrum.

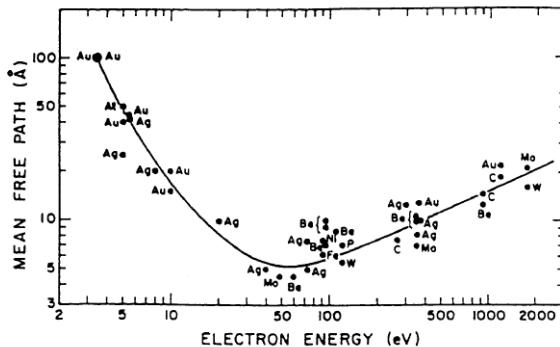


Figure 2.2: Mean free path of electrons as a function of their energy in different materials ("universal curve"). In the usual range of photoelectron kinetic energies, the mean free path of electrons is in the range of 5-100 Å with a minimum at around 50-100 eV. Reprinted from [25], data from [26].

The positions of the measured photoelectron peaks are not only carrying information about the elements on the surface, but also their oxidation states because the binding energy of core electrons depend slightly on the chemical state of the atom. Tables and databases are compiled with measured binding energies of different elements in different binding states (e.g. [23, 27]). The chemical shifts in binding energies are usually on the order of 0-4 eV. As a general rule, the more oxidized an element gets, the higher the measured binding energy is.

The detection limit of XPS is around 0.1-1 atomic percent (at%). XPS is also quantifiable (although with limited accuracy) based on the peak areas [26]. First a background is fitted to the peaks. The most commonly used background type is the Shirley-background, which is calculated in an iterative process based on the assumption that at a given binding energy the background is proportional to the background subtracted peak area below that binding energy [28]. After fitting a background, the peak area is calculated by numerical integration. The concentration

of element i in at% (c_i) is given by (2.2), where A_i is the integrated XPS peak area after background subtraction and RSF_i is the relative sensitivity factor of element i . The relative sensitivity factors are usually given normalized to the C 1s or F 1s peak area and can be found in the manual of the instrument or in software libraries for the processing of XPS data, such as CasaXPS RSF library [29].

$$c_i = \frac{A_i/RSF_i}{\sum_j \text{all elements } A_j/RSF_j} \quad (2.2)$$

During a measurement electrons are continuously removed from the material, therefore the sample might charge-up to a positive bias, especially in case of semiconductor or insulator samples, causing an apparent increase in the binding energies. This shift is the same for the entire spectrum. The usual way to deal with this problem is to make use of a peak with a known position such as Au 4f_{7/2} at 84 eV, SiO₂ 2p at 103.4 eV or C 1s at 284.6 eV (adventitious carbon) and shift the entire spectrum to attain the corresponding energy of one of these peaks. For further details about XPS I refer to [23] containing the basics of the technique along with best practices about experiments and a compiled table of the spectra of elements. There are countless more recent textbooks about electron spectroscopy and its use in catalysis research, such as [21].

2.1.1.2 Ion Scattering Spectroscopy

Ion Scattering Spectroscopy (ISS) or Low Energy Ion Scattering (LEIS) is based on the binary collision and scattering of noble ions on surface atoms. The principles were described already in the '60s [30] and the technique was used to study adsorbates on surfaces already in the beginning of the '70s [31]. ISS is extremely surface sensitive, quantifiable and also carries some depth information from the first few nm of the sample, although the latter two are not straightforward to subtract from the data. As it is based on the measurement of the reflected ion energies, the HSA of an XPS instrument can be used to make ISS measurements if the polarity of the hemispheres can be reversed in the machine, although with limited resolution and effectivity [32]. The Omicron energy analyser provides this possibility. Typical ion energies in ISS investigation are between 1-8 keV with He⁺, Ne⁺, Ar⁺ or Kr⁺ ions used. In the thesis all measurements were done with 1 keV He⁺ ions, with a scattering angle of 146.7°. The process of an ISS measurement is illustrated in Figure 2.3. A material consisting of three different atoms is bombarded with monoenergetic noble ions. After measuring the kinetic energy spectrum of the reflected ions, two peaks appear. These peaks uniquely identify the two different atoms on the surface of the material. Because of the extreme surface sensitivity, the atoms only present in the "bulk" (2nd monolayer) do not contribute to the spectrum.

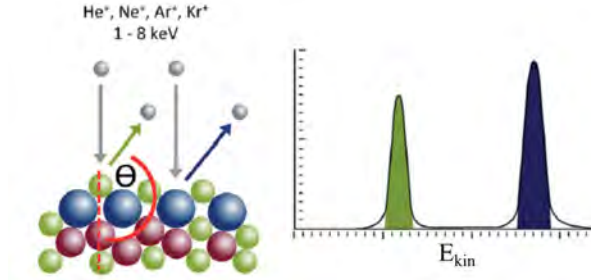


Figure 2.3: Illustration of an ISS measurement and spectrum. The surface of a substrate containing three different atoms is bombarded by monoenergetic noble ions. The number of reflected ions as a function of their kinetic energy is measured. The peaks appearing uniquely identify the mass of the surface atoms. Notice that the red ("bulk") atoms do not contribute to this idealized spectrum. Figure reprinted from [33].

ISS is based on the binary, elastic collision of the noble ion and the surface atom and its governing equation can be derived from classical mechanics. The energy of the reflected ions (E_{BS}) can be derived from the following equation [30]:

$$E_{BS} = \left(\frac{\cos \Theta + \sqrt{\left(\frac{M_S}{M_P}\right)^2 - \sin^2 \Theta}}{1 + \frac{M_S}{M_P}} \right)^2 \times E_P \quad \text{if } \frac{M_S}{M_P} \geq 1 \quad (2.3)$$

Here E_P is the energy of the incident ion, M_P the mass of the incident ion, M_S is the mass of the scattering atom and Θ is the scattering angle. In most cases Θ is set by the instrument and we control E_P and M_P , thus M_S can be determined. (2.3) is only valid if $M_S/M_P \geq 1$ meaning that the atom on the surface is heavier than the incident noble ion. In the other case, there is no backscattering, only forward scattering. In case of a real measurement, inelastic processes influence the energy of the reflected ions too. As a result of these inelastic processes the energy of ISS peaks are usually lower than calculated from (2.3). For 1 keV He^+ Mikhailov and co-workers found that the peak energies are 19-35 eV lower, than the ones calculated from (2.3) [34].

One of the problems of ISS is also highlighted by (2.3). Figure 2.4 shows the kinetic energy of different noble primary ions (in % of their original kinetic energy) after a binary collision with a surface atom as a function of the mass of the surface atom. As the scattering surface atoms are getting heavier, the difference in the energy loss is getting smaller and smaller, therefore distinguishing between two heavy elements (like Pt and Au) is difficult using He^+ . Using heavier ions, the relative energy difference is bigger. The different colours show the different regions where the corresponding

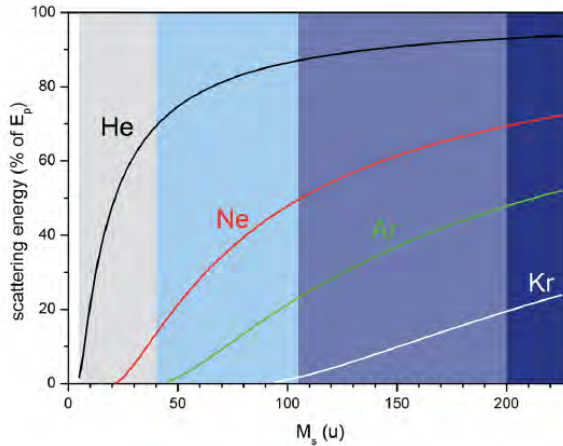


Figure 2.4: Energy loss of different incident primary ions after backscattering as a function of the mass of the target atom. Data is given as the kinetic energy of the backscattered ion in a percentage of the primary kinetic energy. The relative difference of the energy lost for two different surface atoms is lower and lower the heavier they get, therefore it is more and more difficult to distinguish between them. The different colors depict the surface atom mass regions where the use of different noble primary ions is ideal. He^+ is suited for investigating surface atoms with low mass. Figure reprinted from [33].

noble ion is ideal to use. Keep in mind that by increasing the mass of the incident ion, the chance of damaging the surface by sputtering is increasing. Even using He, the effect of ion sputtering can change the surface of the sample (removal of material, reduction of surface etc.) which always has to be considered when choosing methods and parameters. This is illustrated by the reduction of oxidized NiFe nanoparticles during our ISS measurements as shown in Appendix A.

The extreme surface sensitivity of ISS is due to the interaction of the surface and the ion beam. This interaction depends on the scattering cross section and the neutralization probability. The vast majority of ions penetrating the first atomic layer of the surface is neutralized, therefore even if they reach the surface again, they are not measured by the analyser. These interactions are very complex [35, 36] and so far there is no good model to describe them [33]. Nevertheless, ISS spectra carry some information of the deeper regions. This is due to processes illustrated by Figure 2.5. There is a chance, that neutralized ions penetrating the first monolayers return to the surface after multiple scattering and get ionized again. This process cannot be described with classical physics and the elements on the surface can influence the reionization probability. For example the presence of O was found to greatly enhance

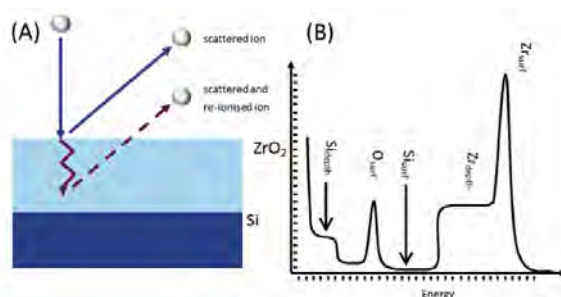


Figure 2.5: Illustration of the depth information carried by ISS spectra. A: Ions penetrating the first layer and being neutralized have a chance to return to the surface after multiple scattering and being ionized again. These ions are also detected. B: Schematic ISS spectrum of the ZrO_2/Si layer structure in (A). There are no Si atoms on the surface, so there is no Si peak in the spectrum as expected. However, a tail at the low energy side of the Zr peak is detected, corresponding to "bulk" Zr. Furthermore, a plateau corresponding to Si can be seen at lower energies. Figure reprinted from [33].

the chance of reionization [32]. In Figure 2.5 the structure and hypothetical ISS spectrum of a ZrO_2/Si layered structure can be seen. The ISS spectrum (Figure 2.5/B) does not contain a Si peak, as there are no Si atoms on the surface. However, due to the presence of O, reionized ions corresponding to Zr and Si in the "bulk" are recorded in the spectrum as flat plateaus.

ISS is inherently quantitative [32] as there is virtually no matrix effect, meaning that the different components of the surface do not influence the signals coming from each other. However, the determination of sensitivity factors is complicated and because of the absence of a good model describing the neutralization probabilities of materials it is mainly done by experimental observations. With the use of standards, quantitative measurements can be done. Nevertheless, ISS is very good at detecting surface contaminations, coverages and dispersion.

For further reading on ISS, [33] is an easy-to-follow and nicely illustrated introduction to the method, while [32] is a comprehensive review which together with the references contained in it covers all aspects of ISS.

2.1.2 Mass-selected nanoparticle source

The nanoparticle source is fully UHV compatible, pumped with turbomolecular pumps and rotary vane pumps. It is bakeable to 150°C and the base pressure in the mass-filter is in the low 10^{-10} mbar region. The schematic of the source is shown in Figure 2.6 and the actual equipment can be seen in Figure 2.1. The nanoparticle source can

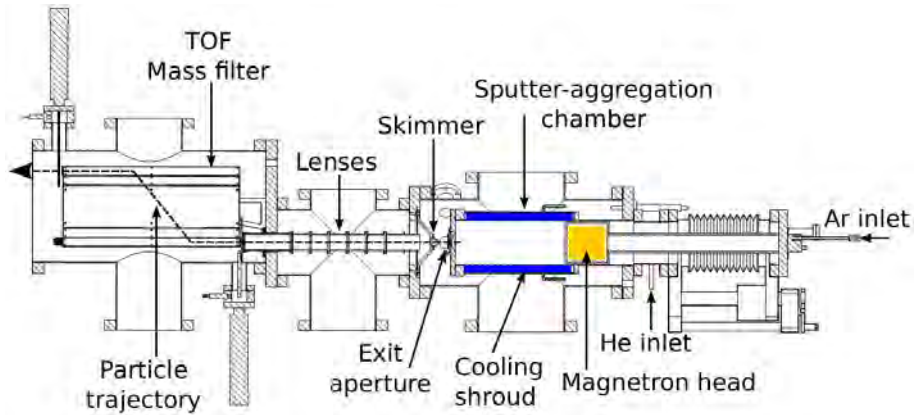


Figure 2.6: Schematic of the magnetron sputtering gas aggregation mass-selected nanoparticle source. Figure reprinted from [37].

be divided into 3 different regions: liquid nitrogen cooled sputter-aggregation zone, where cluster formation happens; the transfer region, where ion optical lenses guide and focus the beam and finally the lateral Time-of-Flight (ToF) mass filter. After the mass-filter, the particles are led into the deposition chamber for deposition and characterization. A similar nanoparticle source is described in details and its behaviour is explored in [38], the only difference being the usage of DC sputtering in our case instead of RF sputtering. There are other kinds of mass-selected nanoparticle source based on e.g. laser ablation or spark ablation. The method for mass filtering can be different as well e.g. using a quadrupole mass filter instead of the lateral time-of-flight mass filter. Here I will concentrate on describing the source used throughout the thesis. I will give a short description of the steps of mass-selected nanoparticle formation and production following the way of the metal species through the system starting with the formation of particles, mass-filtering and finally measuring their mass-distribution and how all the practical experience was gathered with the behaviour of the nanoparticle source.

2.1.2.1 Cluster formation by gas-aggregation and magnetron sputtering

The production of "ultrafine" metal species in gas-flow of inert gases were described already in the '70s [39, 40] and beginning of '80s [41, 42]. In these sources, metals were usually evaporated from heated crucibles which limited the cleanliness and rate of the particle generation. Using evaporation, the gas-aggregation technique was described to form species first from 2 to 500 atoms in 1980 [43], then from single atoms up to 10^5 atoms in 1985 [44]. It is worth mentioning that the metal species produced by evaporation are neutral, therefore in order to get the mass-spectrum of the species created these systems all had a separate ionization source (usually an electron gun or

a heated filament). In the meantime, experiments with sputtering processes showed that nanometer sized particles could be formed by sputtering too [45].

Magnetron sputtering was patented in 1975 [46] and described in details shortly afterwards [47]. In case of magnetron sputtering a plasma is created in front of a target (cathode). Various geometries and magnetron sputtering sources were described [48], but it is common in case of them that the plasma is localized in front of the target (cathode) by a magnetic field created by permanent magnets. Magnetron sputtering is done under relatively low pressures (< 1 mbar) and temperatures, therefore providing a way to integrate the technique into vacuum chambers with differential pumping. Magnetron sputtering was used to produce metal clusters in macroscopic quantities in a gas flow in the early '90s [49]. In this system a target was sputtered with around 1200 W and a liquid nitrogen cooled finger collected the created metal species. An inbuilt scraper mechanically removed the sputter products into a funnel, where these "microcrystals" were compacted into disks for further investigations. Combining the gas-aggregation technique and magnetron sputtering, provided a way to create relatively intense, continuous beams of nanoparticles [50, 51]. It also provided a way to change the size of these particles by changing different parameters of the system. As around 60% of the particles created are charged [50], their manipulation and mass filtering is readily possible without the use of a separate ionization source. The magnetron sputtering of ferromagnetic (like Ni and Fe or their alloys) targets poses a difficulty [52]. The target disrupts the magnetic field and field lines are kept inside the target material. As long as the material is not saturated and magnetised fully, no magnetic confinement of electrons and thereby plasma is happening in front of the target, meaning that the sputtering process is not running. There are a couple of "tricks" to help: the use of extra strong permanent magnets, thinner targets and placement of the target as close to the magnets as possible. Different geometries can also be devised, which help with the issues with ferromagnetic targets [52]. In our magnetron head, extra strong permanent magnets are situated right behind the target and it is possible to sputter Ni targets up to 6 mm and Fe targets up to 3 mm thickness. To be on the safe side, all of the ferromagnetic targets we used for the NiFe projects (Chapter 4 and Section 5.2) were 3 mm thick.

In our system a 2 inch circular target is used, with Ar entering concentrically around the target as the sputtering gas. Multiple permanent magnets create a magnetic field, which forces electrons in the plasma on a spiral path, increasing the chance of ionization by orders of magnitude and confining the plasma. The target is bombarded by energetic Ar ions from the plasma (in our case the target has a negative bias of approx. -240 V), which sputter the atoms of the target away creating a trench ("racetrack") in the target (Figure 2.7). Magnetron sputtering provides a way to create high density vapours of not only metals, but also semiconductors or insulators (RF sputtering). In our system usual working pressures are between 0.1-1 mbar and sputtering power between 15-60 W (the magnet assembly and the backing plate of the target is water cooled).

In front of the plasma He is added into the liquid nitrogen cooled aggregation zone. Together with Ar, He atoms provide heat transfer from the energetic metal (in



Figure 2.7: Picture of a heavily used Ru sputter target (2 inch in diameter and 6 mm thick) showing the "racetrack" pattern of the plasma sputtering.

our case) species and the cold walls. The exact process of particle formation is very complicated to study. The first step of the process is embryo formation due to three-body collisions between metal species and the gas atoms in the aggregation zone [51]. These embryos are so small, that they can either evaporate or grow further due to thermodynamic fluctuations [53]. The growth of these embryos can proceed with 2 ways: cluster-cluster collision or atomic condensation. Hihara and co-workers investigated and modelled these pathways in case of Ni nanoparticles and concluded that their experimental results can only be explained by atomic condensation [51]. However, their size distributions on which they based their conclusion were not particularly accurate. Some results in our lab on the other hand, suggest a cluster-cluster collision mechanism. When producing Ru mass-selected nanoparticles in our laboratory Paoli and co-workers found that particles above 500k amu mass showed peculiar "raspberry" like shapes even after thermally annealing them to 400°C [54]. These particles are most probably agglomerates of smaller nanoparticles, directly indicating a dominant cluster-cluster collision growth method. Most probably the two growth mechanisms (cluster-cluster collision and atomic condensation) coexist and which method becomes the dominant depends on the conditions in the system and material in question. In general, if the production of particles is purely through sputtering, small clusters and an exponential decay of the number of particles towards heavier species is expected [55]. If the particles are produced by aggregation, a log-normal size distribution describes their size-distribution [40].

In our system, the particles carried by the flow of gases leave the aggregation zone through an exit aperture (variable diameter) as a result of the pressure difference between the aggregation zone (pressure approx. 0.1-1 mbar) and the next stage (pressure approx. 10^{-4} mbar). The following parameters of the nanoparticle source can be controlled: flow of Ar and He by means of mass flow controllers (typical flows are around 60 sccm Ar and 15 sccm He), sputtering power (typical values between 15-60 W), the length of the aggregation zone (it can be varied continuously between 150-250

mm) and the diameter of the exit aperture. On top of these, in principle also the temperature of the aggregation zone could be changed and controlled by controlling the flow of the LN₂ coolant, but we did not investigate this so far. These parameters define a complex parameter space, where different parameters are not completely independent of each other: closing the exit aperture increases the pressure in the aggregation zone and also increases the velocity of the gas molecules exiting. Increasing the flow of the gases also increases the pressure and the flow through the exit aperture. A somewhat systematic investigation of the effects of the different parameters on the size-distribution of the resulting particles can be found in [38]. Based on experience a few rules of thumb can be established: addition of more He in general shifts the size-distribution of the particles towards lower masses. Shortening the length of the aggregation zone has the same effect. In practice, finding the right conditions is usually fairly straightforward, based on earlier parameter sets for similar masses. Another interesting effect has to be noted here: the parameters for producing particles having the same mass from the same target are changing slightly over time (on the scale of days) or if a target is removed and remounted after some time. This might be an effect of the target geometry changing (racetrack forming), drift in the powersupplies or some other effect. Unfortunately the conditions in the aggregation zone seem to influence the crystal structure of particles having the same mass as demonstrated by Plant and co-workers in a systematic study of Au₉₂₃ [56]. This underlines a very important fact: we are controlling the mass of the particles in our model systems, not the diameter, shape or even the crystal structure.

When the particles exit the aggregation zone, the beam consists of approximately 1/3 neutral, 1/3 negatively charged and 1/3 positively charged particles [50]. Most of the charged particles carry a single charge (an electron in excess, or missing), but some of the particles exiting carry double charge, which has implications for the size-distribution and mass filtering explored in Appendix B. The central part of the flow passes through a conical aperture, due to a pressure difference compared to the next stage. At this stage the beam passes through ion optical lenses and accelerated to 500 eV. The task of these lenses is to focus and align the beam to the entrance of the mass filter. Our system is capable of handling and filtering either positively or negatively charged particles and changing between the two modes can be done automatically at the controlling computer. As only charged (either negative or positive) particles are capable of passing the mass-filter, 2/3 of the particles produced before mass-filtering are lost due to the wrong charge or no charge at all. We usually use negatively charged particles for our depositions, thus all the explanation and description from now on is for negatively charged particles if it is not otherwise stated. Experience showed, that for small particles (1-100 atoms), positively charged particles have a much higher current, therefore for depositing small clusters we use the positively charged particles.

2.1.2.2 Mass filter

After passing through the ion lenses the cluster beam enters a lateral ToF mass filter shown schematically in Figure 2.8 and described in details in [57]. The preaccelerated

and convergent beam enters the mass-filter through an entrance aperture. A high voltage pulse on plate 1 displaces part of the beam in the lateral direction. With some time delay the same voltage pulse is applied to plate 4. As a result particles continue to fly towards the exit slit displaced in the lateral direction, and also ordered by mass in the lateral direction. With the first pulse the particles gain the same amount of momentum, therefore lighter particles fly faster in the lateral direction and heavier particles fly slower. After the second pulse the particles lose their momentum in the lateral direction but lighter particles flew further than heavy particles. After the second pulse, the exit aperture only lets through the chosen mass. By changing the frequency of the pulses while keeping the pulse width and the delay between the pulses on the two plates the same, the transmitted mass can be tuned while keeping the transmission constant [57]. The mass resolution of the mass filter depends on the total displacement (x) and the size of the exit slit (Δx). Calculations show that the mass-resolution is simply given by $m/\Delta m = x/\Delta x$ [57]. The mass resolution is independent of the mass and by changing the size of the exit slit it can be changed easily. Note that we are controlling the m/z ratio of the species passing the mass filter. This has implications for the depositions as there is a chance for particles having double charge exiting the aggregation zone as described in Appendix B.

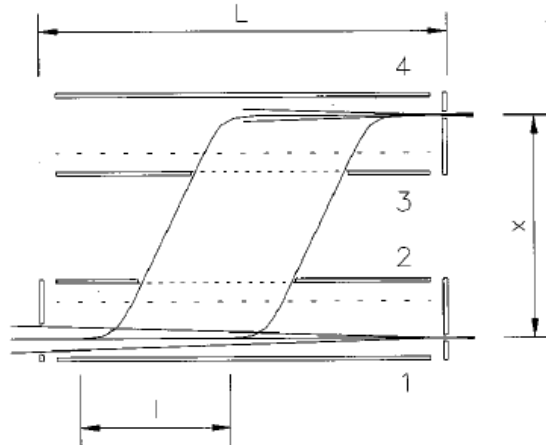


Figure 2.8: Schematic of the lateral ToF mass filter. A convergent and preaccelerated beam enters the mass-filter. High voltage pulses on plate 1 and 4 displace part of the beam labelled by 1. The total displacement (x) and length (L) are also labelled in the figure. Notice the entry and exit slits for the particle beam. Figure adapted from [57].

In our system, the total displacement of the mass filter is 160 mm and the exit aperture can be varied between 0.5-8 mm. All the results shown in the thesis were produced by using the biggest exit slit (giving a theoretical mass resolution

of $m/\Delta m = 20$), in order to maximise the current leaving the nanoparticle source. The electronics are capable of producing pulses to filter masses between 30 amu - 20 million amu. The mass filter can be continuously cycled through a mass range, thus effectively scanning the entire mass-distribution of the beam and the particles leaving the aggregation zone.

2.1.2.3 Measuring the mass spectra of particles - capabilities of the nanoparticle source and practical considerations

The particles exiting the mass filter are led into the deposition chamber. Ion optical lenses defocus the beam and create a relatively large, diffuse spot, which we assume to be homogeneous in the middle. In front of the beam there is a movable plate (mask) with multiple holes and a quartz crystal microbalance (QCM). Figure 2.9 shows the exit aperture of the cluster source and the mask with multiple holes. The beam current of mass-selected nanoparticles exiting the mass filter can be measured by positioning a part of the mask in front of the exit aperture where there is no hole (as shown in Figure 2.9). The holes with different diameters are used to define the deposition area. The 9 mm is used to deposit μ -reactors and the 4.5 mm is used to deposit 5 mm cylinders ("stubs") for electrochemical measurements (Section 2.3.2). The mask is biased to approx. +45 V (-45 V if positive particles are used) to provide a mild attractive force, and the current is measured with a Keithley 6514 system electrometer. In order to illustrate the capabilities of the nanoparticle source, two mass spectra are shown here, an example for small positively charged species (Figure 2.10/A) and an example of heavy negatively charged nanoparticles (Figure 2.10/B). Figure 2.10/A shows a mass spectrum of ions and clusters leaving the aggregation zone while sputtering a 90 at% Ta / 10 at% Ir target. Peaks for Ar^+ , Ar_2^+ , Ar_3^+ , Ta^+ , TaAr^+ and TaAr_2^+ are easily identifiable. As the atomic mass of Ta (approx. 181 amu) and Ir (approx. 191 amu) are close together and the Ir content of the target (thus the amount of sputtered Ir) is low, there is no Ir^+ peak visible. However, the higher mass side of the Ta^+ peak includes the Ir^+ peak shown by the small shoulder around 191 amu. Figure 2.10/B shows the mass spectrum of Pt particles above 10^7 amu up until 20×10^7 amu (the upper limit of our mass filter). The mass of these particles corresponds to a diameter above 10 nm showing that the nanoparticle source can produce species from single atoms to relatively large nanoparticles. However, experiments showed that samples for catalytic testing, where a given loading is needed, can usually only be made with sizes ranging between 3-9 nm in reasonable time (less than 2 hours of deposition/sample). For TEM investigations, where even a few particles are enough, samples in the entire mass range can easily be produced.

2.1.2.4 Deposition of mass-selected nanoparticles

The usual way of depositing samples for TEM investigation or catalytic testing is the following. First the sample is loaded into the vacuum chamber through a loadlock in self designed sample holders (Appendix C) and moved away from the mask and

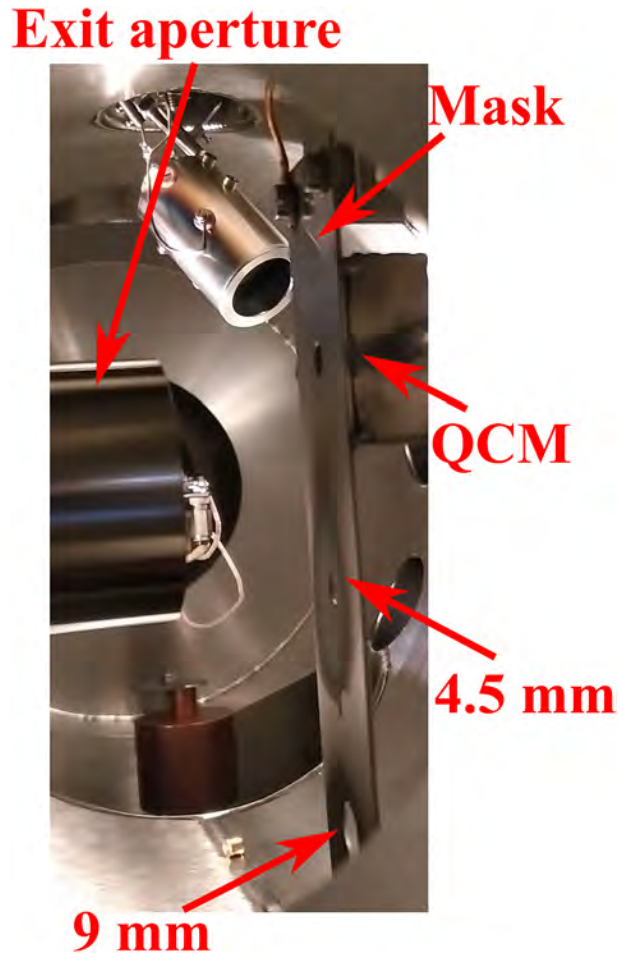


Figure 2.9: Picture of the mask used to define the deposition area and to measure the current of the mass-selected nanoparticle beam. The mask is movable, therefore it is possible to position either the quartz crystal microbalance (QCM), one of the holes (4.5 or 9 mm in diameter) or a part which is a complete plate (shown on picture) in front of the exit aperture where the nanoparticle beam exits the nanoparticle source. Notice the dark areas around the 9 mm and 4.5 mm hole. Those are caused by the diffuse nanoparticle beam (the beam is larger than the holes).

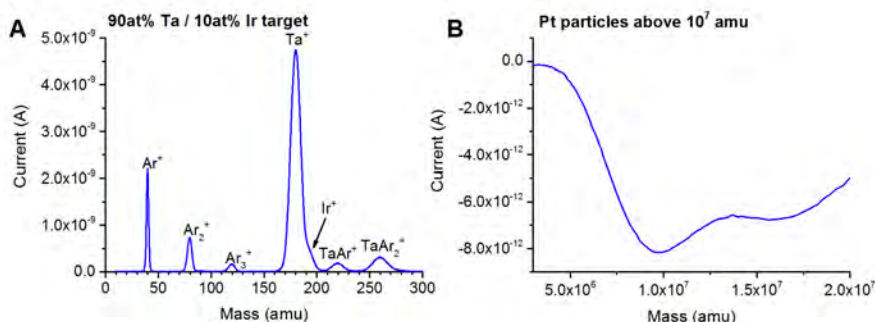


Figure 2.10: Example mass spectra to illustrate the capabilities of the nanoparticle source and the lateral ToF mass filter. A: Positively charged clusters attained by sputtering a 90 at% Ta/ 10 at% Ir target. Notice the clusters of Ar and the shoulder on the high energy side of the Ta^+ peak, which is caused by Ir^+ ions. B: Negatively charged Pt nanoparticles with higher than 10^7 amu mass. The mass of these particles corresponds to diameters well above 10 nm.

the nanoparticle beam to avoid any unwanted particle deposition. The mask is kept lowered and conditions for the deposition are optimized on the mask. Care has to be taken to avoid double mass-double charge particles forming in the aggregation zone as these pass through the mass filter just as single mass-single charge particles (Appendix B). Once appropriate conditions are found, the mass-filter is set to only let a single mass/charge ratio through (the one we want to deposit) and the nanoparticle beam is diverted away from entering the mass filter with the help of the ion optical lenses, while the sputtering, gas flows and all the electronics are still switched on. Now the mask is raised, to position one of the holes in front of the exit of the nanoparticle source. The sample is moved and positioned behind the hole. The electrometer is switched over to measure the current through the sample, which is also biased to +45 V (or -45 V for positive particles) just as the mask. When the nanoparticle beam is switched back to enter the mass filter, the deposition starts. The deposition current on the sample can be measured and the loading can be directly calculated from the elapsed time assuming single charge particles (Appendix B). The +45 V bias means that the particles land with approx. 45 eV energy. This energy is in the soft landing regime (<0.1 eV/atom) for most of the particle sizes we routinely deposit, where no fragmentation or implantation of the particles is expected [58]. During deposition the conditions in the clustersource are kept as constant as possible, but the mass spectrum of the nanoparticles cannot be measured without depositing a minute amount of all the sizes on the sample, therefore it is never done. When the calculated deposition time is elapsed, the beam is diverted away from the mass filter again, the sample is moved away from the mask and the line of deposition, and the mask is lowered

again to the position where it serves as a plate. The electrometer is attached to the mask again and the mass spectrum of the particles is measured again after letting the beam back into the mass filter. Sometimes during deposition the mass spectrum of the particles change and for example develop a higher amount of double mass particles. In these cases the sample has to be discarded. Details about how the mass of a given sized particle is calculated, the determination and accuracy of the loadings and the issues with double mass and half mass particles are described in Appendix B.

2.2 μ -reactors and the μ -reactor setup

The μ -reactors are silicon chips, with microfabricated gas channels and reactor volume produced by DTU Danchip. Heating and temperature measurement is achieved by Pt conductors evaporated to the backside. These reactors were designed to test minute amounts (in the range of nanograms) of catalysts in heterogeneous reactions and were first described in 2009 [59]. Compared to the published design, they were further developed in the recent years. Here I will show them in their present form.

2.2.1 μ -reactor design and its implications

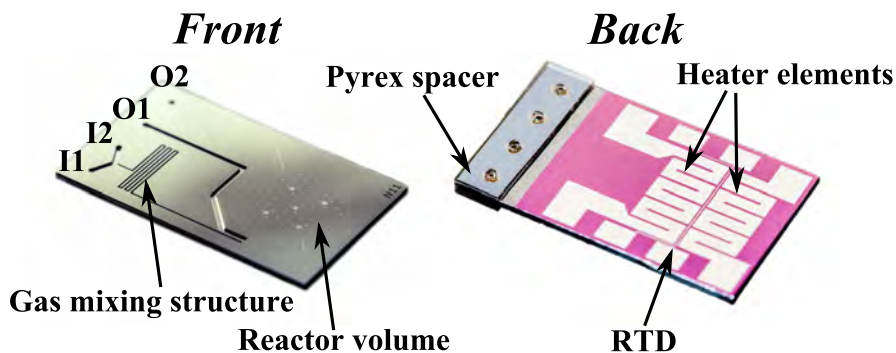


Figure 2.11: Images of the front and back side of a μ -reactor showing the reactor volume, the gas inlets (I1 and I2) and outlets (O1 and O2) along with the heater structures and the RTD. Images courtesy of Thomas Pedersen (DTU Danchip).

The μ -reactors are 16 mm x 27 mm Si chips, fabricated from 350 μ m thick n-type (10^{-16}cm^{-3} P dopant) Si wafers (Figure 2.11). During the fabrication process a thermally grown, 50 nm SiO_2 layer is formed on the reactors. Gases enter the chip from a gas handling system (see Section 2.2.3) through one (or two) of the inlets I1 and

12. The gas mixing structure after the inlet ensure a thorough mixing of the gasses. After the gas mixing structure, most of the gas continues to the first outlet (O1). This outlet is used to control the pressure in the reactor and the lines. Some of the gas enters the reaction chamber through a shallow channel ($3\ \mu\text{m}$) to limit back diffusion of reaction products. The reaction chamber has a diameter of 10 mm and a depth of $3\ \mu\text{m}$, giving a volume of approx. 240 nl and an extraordinarily high surface to volume ratio. The reactants and products from the reactor chamber leave through a $1500\ \mu\text{m}$ long, $3\ \mu\text{m}$ deep and $5\ \mu\text{m}$ wide flow restricting capillary through O2. The capillary is designed to restrict the flow to a level (approx. 3×10^{-14} molecules/s under typical conditions) which is safe to let directly into a quadrupole mass spectrometer (QMS, Section 2.5.1) which operates in high vacuum. This means that almost all of the molecules entering the reactor (except the ones reacted) or produced in the reactor chamber are passing through the mass spectrometer. Pt structures with around a 100 nm thickness serving two different purposes are evaporated on the backside of the μ -reactors and subsequently thermally annealed. The two heater structures are to ensure the near homogeneous heating of the reaction chamber. As the thermal mass of the system is low, rapid heating and cooling can be achieved. The other Pt feature is a resistance temperature detector (RTD) with four contact pads for 4-point measurement of the resistance of the platinum wire. The small dots, which can be seen in the reactor are Si pillars, $200\ \mu\text{m}$ in diameter and placed 1 mm apart. The role of these pillars are to hold the pyrex lid away from the bottom of the reactor during bonding (Section 2.2.2). Another feature is the five larger dots in the reactor chamber. These are finder grids etched in the bottom, to help in making identical location SEM studies.

Catalysts can be loaded in several ways in the μ -reactors. Mass-selected nanoparticles are deposited on the Si chips in a vacuum chamber (Section 2.1.2). In case of the experiments described in this thesis, they were deposited in our Omicron chamber in a 9 mm circular spot (see details in Section 2.1.2). The typical total mass of the deposited particles is approx. 100 ng.

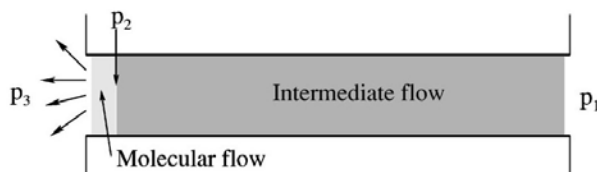


Figure 2.12: Illustration of a small capillary connecting high (atmospheric) pressure (p_1) to vacuum (p_3). Reprinted from [60].

A feature which influences a handful of properties of the μ -reactors and also sets some constraints on the measurements is the flow-limiting capillary between the reactor chamber and O2. A flow through a small circular capillary can be calculated and described analytically [59–62]. This is not strictly valid for the capillary in the

μ -reactors as it is not circular, but the consequences and general results are nevertheless true. Here I will show some of the background and the result of the calculation of the flow through the capillary and its implications for the μ -reactors. The transport behaviour of gases is influenced by the ratio of the mean free path of the molecules (λ) and the typical size of the containing volume, for example the diameter of a pipe (d). This ratio is called the Knudsen number (K_n) [61, 62]. $K_n < 0.001$ means the gas behaves as a continuum (continuum flow) and $K_n > 1$ indicates a molecular flow. Between these two regimes, the gas is in the intermediate flow region. Under the typical experimental conditions in the μ -reactor, gases are in the intermediate region in the capillary (Figure 2.12). The gas enters from a high pressure region (p_1) and flows to the QMS, which has a low pressure of p_3 in the molecular flow regime. Somewhere along the capillary, the flow changes from an intermediate flow to a molecular flow (at pressure p_2). The flow in a circular capillary with a diameter of d under these circumstances can be written:

$$\dot{N} = \frac{1}{k_B T} \frac{1}{l} (c_{int}(p_1 - p_2) + c_{mol}(p_2 - p_3)) \quad (2.4)$$

where k_B is the Boltzmann constant, T is the temperature and l is the total length of the capillary. c_{int} is the conductance of the capillary in the intermediate flow regime and c_{mol} is the conductance of the capillary in the molecular flow regime. c_{int} is given by:

$$c_{int} = \frac{\pi}{128} \frac{\bar{p} d^4}{\eta} + \frac{1}{3} \sqrt{\frac{\pi}{2}} \frac{d^3}{v(T)} \frac{1 + dv(T)\bar{p}/\eta}{1 + 1.24dv(T)\bar{p}/\eta} \quad (2.5)$$

where $\bar{p} = (p_1 + p_2)/2$, η is the viscosity, $v(T) = \sqrt{m/K_B T}$ and m is the mass of a single molecule. Using the same notation c_{mol} is given by:

$$c_{mol} = \frac{1}{3} \sqrt{\frac{\pi}{2}} \frac{d^3}{v(T)} \quad (2.6)$$

In practice, (2.4) has some consequences not usually seen in conventional reactors. The flow is dependent on the temperature and as the temperature is rising, the flow is decreasing. The flow is also dependent on the gas composition. These have to be kept in mind when making experiments with the μ -reactors. Assuming 1 bar of air in the reactor and room temperature, the flow through the capillary is around 2.6×10^{14} molecules/s and the residence times of the molecules in the reactor is approx. 12 s.

2.2.2 Bonding and opening the μ -reactors

After catalyst deposition to the reactor chamber the μ -reactors have to be sealed. In order to create an airtight and mechanically strong seal (it has to withstand pressure differences) a 500 μm thick planar pyrex slab with the same dimensions as the μ -reactor is bonded anodically (also called Mallory bonding) [63] to the Si chip. This widely used technique requires high temperatures dependent on the materials used (in

the range of 300-700°C) and relatively high voltages (up to approx. 2 kV) set across the materials to be bonded. In our case, the temperature required for bonding is around 450°C, which is usually too high and it would induce sintering of the deposited nanoparticles. In order to avoid sintering, the anodic bonding is done with cooling of the sensitive area (reactor volume) [64]. A cross-sectional view of the cold bonding setup can be seen in Figure 2.13. The μ -reactor along with the pyrex lid is placed on a water cooled (and grounded) Cu finger contacted with thermal paste to ensure a good thermal contact. The Cu finger has a diameter of around 11 mm to ensure cooling of the entire reactor area. An Al block equipped with two halogen lightbulbs is placed on top of the pyrex lid. The Al block has a hole drilled in it right on top of the reactor area in order to limit heat transfer. During bonding, the Al block is heated by the lightbulbs and around -1 kV is applied to it. As a result of the high temperature and the electrical field ions are formed in the glass (primarily Na^+ ions) which migrate away from the pyrex-Si interface setting up an intrinsic electrostatic attraction between the two [64]. The bonding process takes about 1 h to complete and provides a gas tight, mechanically stable sealing. Finite element analysis shows (Figure 2.14), that in this arrangement the reactor area stays close to room temperature.

There are a couple of drawbacks of this process. In order to succeed, the surfaces to be bonded have to be smooth and clean. Even the tiniest speck of dust can create unbonded areas. Depending on the position of these unbonded areas, this can render a μ -reactor completely unusable for testing. As a practical rule of thumb when the pyrex lid is placed on top of the Si, intact interference fringes must be seen in order to create a proper bonding. Another problem is the irreversible nature of the bonding. In order to investigate the catalyst after reaction the reactor has to be damaged to be opened and cannot be used anymore.

In order to be able to make XPS, ISS and/or SEM after testing, the μ -reactors have to be opened. A method to achieve this without contaminating the catalyst was developed by Thomas Pedersen (DTU Danchip) and Jakob Riedel. The 500 μm thick pyrex lids of the bonded (and tested) μ -reactors can be cut almost all the way through with a water cooled precision diamond saw in an approx. 5 mm x 5 mm square pattern above the reactor area, leaving only about 35-50 μm of pyrex (Figure 2.15/A). The remaining layer of pyrex ensures, that the cooling water of the saw does not contaminate the μ -reactor. After weakening the pyrex lid in this way, the small square piece of pyrex can be broken off by superglueing something to it and twisting the weakened piece (Figure 2.15/B). The only contaminant getting in the reactor volume is glass shards due to the breaking of the remaining pyrex. These shards can be removed by turning the reactor upside down or a gentle flow of a clean and dry gas (e.g. Ar or N_2).

2.2.3 Setup for activity tests

The bonded μ -reactor is mounted to a stainless steel interface block and fixed in place by a stainless steel bar pushing it down. Gas connections are sealed with vi-

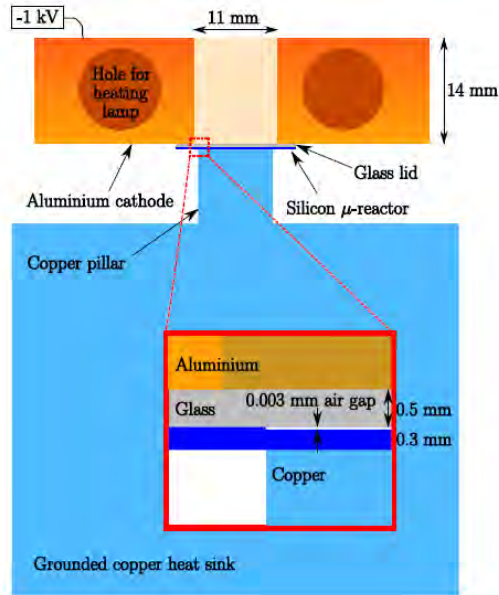


Figure 2.13: Illustration of the cold bonding of the μ -reactors (cross-sectional view). The reactor is placed on a water cooled (and grounded) Cu block with a pillar in order to cool the area of the reactor volume. An Al cathode is set on top of the reactor, heated by two halogen lightbulbs. Right on top of the reactor area a hole is drilled in the aluminium block to lower the heat transfer to the reactor volume. Reprinted from [64].

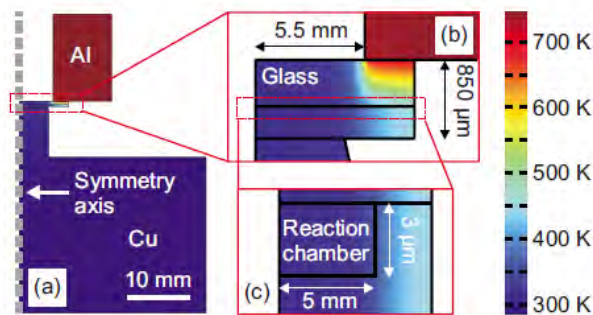


Figure 2.14: Temperature distribution during the cold bonding of μ -reactors from finite element analysis. For the simulation a model with axial symmetry was used. A: The entire setup with the cathode and the μ -reactor, B: zoom-in on the pyrex-Si interface and C: zoom-in on the edge of the reactor volume etched in the Si chip. Reprinted from [64].

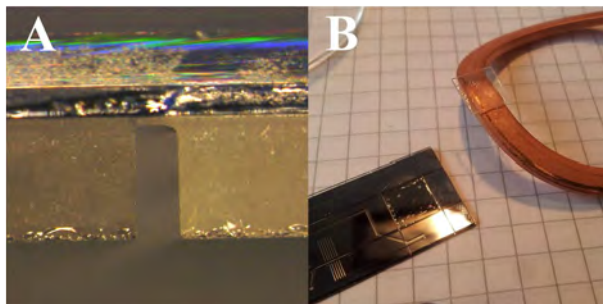


Figure 2.15: A bonded μ -reactors can only be opened by breaking its lid open and rendering it unusable for activity measurements afterwards. A: Pyrex lid cut partially through (photo by Thomas Pedersen); B: The lid of a μ -reactor broken open (photo by Jakob Riedel).

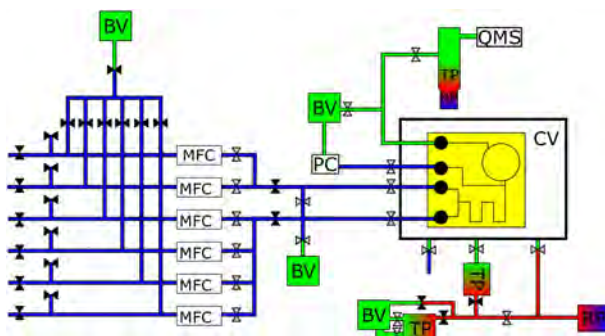
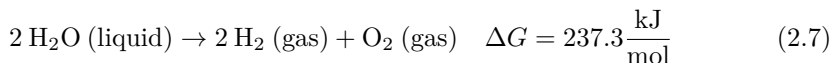


Figure 2.16: Schematic layout of the μ -reactor setup used for the measurements in this thesis. MFC: mass flow controller, PC: pressure controller, BV: buffer volume, CV: containment volume, TP: turbomolecular pump and RP: roughing pump. Blue lines are gaslines with high pressure (1 bar or higher), red lines represent roughing lines and green lines are pumped by the buffer volume. Valves denoted by gray are pneumatic and the black valves are manual. Figure adapted from [65].

ton O-rings. Spring loaded Au coated poker pins create electrical connection to the contact pads of the heater elements and the RTD on the backside of the μ -reactor (Figure 2.11). As the O-rings are not completely leaktight, the entire assembly is placed in a containment volume (CV) pumped by a turbomolecular pump (TP). As a result, no contaminants can enter the gaslines and give false signal in the mass spectrometer. Gases are introduced to the system through 6 gas lines equipped with mass flow controllers (MFC). The pressure in the μ -reactor is controlled by the pressure controller (PC) connected to O1 (Figure 2.11). The gas lines and the μ -reactor are pumped through a relatively big chamber. This chamber acts as a buffer volume (BV) and expanding the gases into this volume ensures the gradual pump down of the system and the safety of the pumps. The gases exiting the reactor volume are ionized by electrons from a heated filament, passing through a Pfeiffer QMG 422 quadrupole mass filter (QMS, Section 2.5.1) and detected by an electron multiplier. The system is pumped by turbomolecular pumps backed by rotary vane pumps. Gas handling and temperature control are automatized with LabView and Python programs created by Robert Jensen (DTU SurfCat).

2.3 Water splitting and investigating its half cell reactions

As mentioned earlier (Section 1.1.2) one of the problems of an energy system based on renewables is the intermittent nature of renewable energy. In order to solve this, energy has to be stored. One possibility is splitting water (2.7) using electricity from renewable sources when there is an excess of electricity and convert the H_2 back to electricity with a fuel cell, when there is a need for it. The basic schematics of an electrolyser utilizing alkaline electrolyte is shown in Figure 2.17. Compared to Figure 2.17 an electrolyser working in acidic media would have a membrane conducting H^+ instead of OH^- . In any case, by supplying electricity (energy) O_2 gas is generated at the anode side (oxygen evolution reaction, OER) and H_2 gas at the cathode (hydrogen evolution reaction, HER). The energy is needed to overcome the Gibbs free energy difference of $237.3 \frac{\text{kJ}}{\text{mol}}$ (1.23 eV/electron) between liquid water and gas phase O_2 and H_2 (2.7). The energy source for water splitting can come in the form of electricity generated from e.g. wind or sunlight. Furthermore, sunlight can also be directly converted into energetic electron - hole pairs with a semiconductor photoabsorber to drive watersplitting in a photoelectrochemical (PEC) device. There is an intense research by the scientific community on both half cell reactions (HER at the cathode and OER at the anode). For the purpose of this thesis a short summary of these reactions and the techniques we used to study them (a Si photocathode for HER and rotating disk electrode (RDE) for OER) are given here.



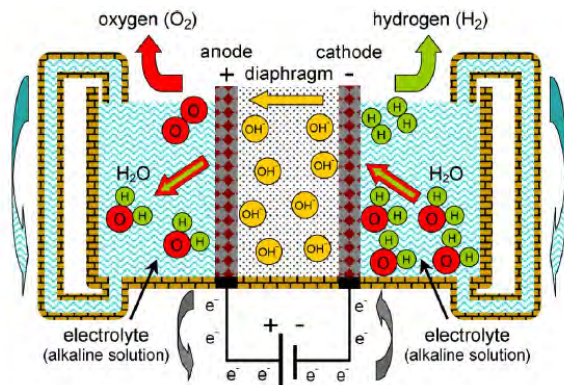


Figure 2.17: Schematic layout of an electrolyser utilizing an alkaline electrolyte. H_2 is generated at the cathode and O_2 is generated at the anode. A semi-permeable membrane is separating the two compartments of the electrolyser to separate the produced gases. In an electrolyser using acidic electrolyte, the membrane is conducting H^+ instead of OH^- ions. Figure reprinted from [66].

2.3.1 Testing of the hydrogen evolution reaction in a photoelectrochemical device

Hydrogen evolution reaction (HER) is one of (if not) the most studied electrocatalytic process. The most active catalyst for HER is Pt. The process is running virtually without overpotential and in acidic media a current density of 1 A/cm^2 can be achieved with as little as 50 mV overpotential with $50 \mu\text{gPt/cm}^2$ loading [67]. In alkaline media the reaction runs slower (with a higher overpotential) on Pt, which was shown by Shen and co-workers [68]. Chapter 3 deals with elucidating just how good Pt is as an HER catalyst in acidic media using ultralow loadings of mass-selected Pt nanoparticles with a model photoelectrochemical (PEC) half-cell.

2.3.1.1 Bottom cell of a tandem PEC device for HER

In a PEC watersplitting device energetic electrons driving the OER and HER are created by photon absorption in a semiconductor. The absorbed photons excite valence band electrons to the conduction band. The amount of energy that can theoretically be harvested is determined by the bandgap of the semiconductor: only photons which have high enough energy to excite electrons from the valence band to the conduction band are absorbed ($h\nu \geq E_{\text{gap}}$, where E_{gap} is the band gap, h is the Planck constant and ν is the frequency of the photons). If the energy of the incoming photons are higher than the bandgap, that energy is "wasted": electrons excited above the bottom of the conduction band relax to the lowest unoccupied energy of the band by creating

phonons thus heating the material. For solar watersplitting a photovoltage of at least 1.23 V (plus overpotential) is needed to overcome the energy barrier. This can either be supplied by a large bandgap material or two (or more) lower bandgap materials. As the solar spectrum is not monochromatic [69], using a single absorber with a large bandgap only a small photocurrent can be achieved. More effective capture of the energy radiated by the sun can be achieved by combining two (or more) absorbers. In this case the required voltage is split between the two photoabsorbers and because more photons are absorbed, the photocurrent is higher too. In case of a tandem device a higher bandgap material is used to absorb the photons with higher energy (blue part of the spectrum) and a low bandgap material is used to absorb the lower energy photons (red part of the spectrum). Simulations show that the bandgap of Si (1.1 eV) is ideal for the bottom cell (low bandgap) capturing the photons with lower energy in a solar to hydrogen tandem device [70, 71]. In order to simulate sunlight a 1000 W Xe lamp (Oriel) was used in Chapter 3. In the setup the light from the xenon lamp is guided to a photoelectrochemical quartz cell through an AM1.5 filter and a high pass wavelength filter. By placing the electrochemical cell and the sample closer or further away from the end of the lightguide, the amount of light reaching the sample surface can be changed. This way, the total photon intensity reaching the sample can be calibrated to the intensity what the Sun (AM1.5, high pass filter with 635 nm threshold) would provide. Apart from this, the cell is a 3 electrode electrochemical cell similar to the one described in Section 2.3.2, except the working electrode being stationary.

2.3.2 Testing the oxygen evolution activity of a catalyst - rotating disk electrode (RDE) setup

The oxygen evolution reaction ($4 e^-$ process) is significantly more complex than HER ($2 e^-$ process). It has attracted a lot of research interest. As opposed to HER, where almost negligible overpotentials are needed for relatively high currents, in case of OER, even with the best catalysts significant overpotentials are required for achieving meaningful reaction rates. This, together with the already oxidizing 1.23 V (vs. the reversible hydrogen electrode, RHE) equilibrium potential impose much stricter requirements on the stability of catalyst materials as the Pourbaix diagrams of different materials depict [72]. Nevertheless, in alkaline media multiple oxide/hydroxide materials are stable and the oxides of Ni, Fe and Co have been used for decades as catalyst materials. A systematic study of different catalyst materials for OER in both acidic and alkaline solution is contained in [73].

We used a rotating disk electrode (RDE) setup for the investigation of the OER (Figure 2.18). It consists of three electrodes: reference electrode, counter electrode and a working electrode which is continuously rotated to facilitate mass transport of reactants and products to and from the surface of the electrode. The catalyst is deposited on a cylinder 5 mm in diameter and approx. 4 mm in height which acts as the working electrode. The potential of the working electrode is measured with

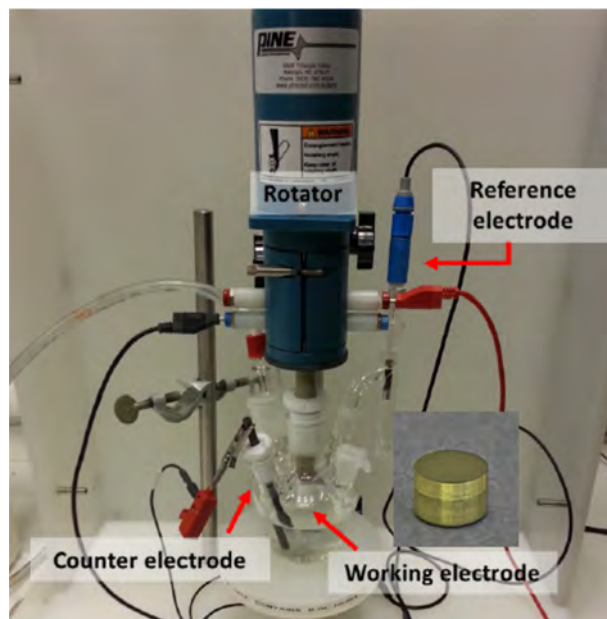


Figure 2.18: Picture of a rotating disk electrode (RDE) setup along with a polycrystalline Au working electrode. In Chapter 4 we report data collected in a 1 M KOH electrolyte. Glass is etched by KOH, thus we used a PTFE cell instead of the glass cell depicted in the picture. Adapted from [3].

respect to the reference electrode (in our case it was a Hg/HgO reference electrode). The current is measured between the working electrode and counter electrode. The counter electrode is running the cathodic reaction (in our case HER) and must provide high enough reaction rates not to limit the current, therefore we used a high surface area graphite rod as a counter electrode.

2.4 Electron microscopy techniques

Electron microscopy is based on the interaction of electrons (0.3-300 keV) with the sample. These energetic electrons have sub Å wavelength, however the resolution is not determined by this, but rather the interaction of the electron beam with the material. When an electron hits the surface of the sample, it can interact with the material in a multitude of ways illustrated by Figure 2.19. Practically all of these signals can be used to investigate different properties of the materials. Here I will summarize bright field TEM (direct transmitted beam) and SEM (secondary and

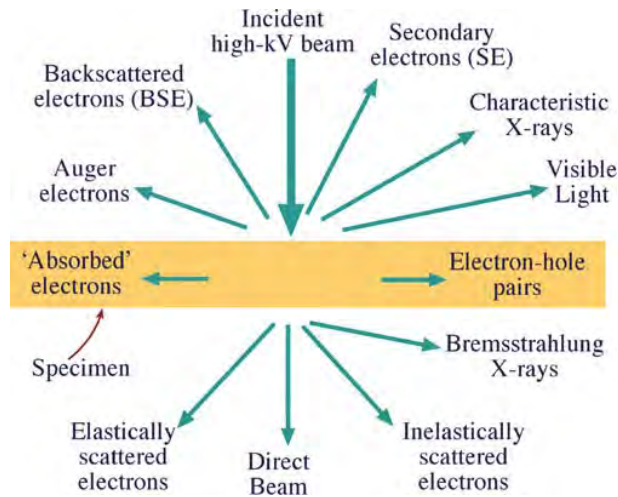


Figure 2.19: Illustration of the interaction of an electron beam with a material. Image reprinted from [74].

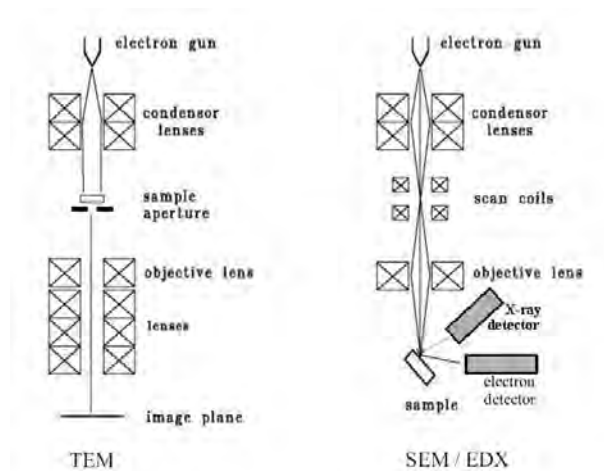


Figure 2.20: Schematic illustration of a transmission electron microscope (TEM) and a scanning electron microscope (SEM). The SEM has an X-ray detector for energy dispersive spectroscopy (EDX) measurements for compositional analysis, which can also be performed in a TEM. Figure reprinted from [1].

backscattered electron) imaging. Figure 2.20 shows the schematics of a transmission electron microscope (TEM) and a scanning electron microscope (SEM). The main difference between the two being the signals detected and the method of image creation. As electron microscopy is a very broad field, I would like to give a short summary of the techniques we used for the projects included in this thesis. For further reading on SEM I refer to the work of Goldstein et al. [75], on TEM to Williams et al. [74] and the multitude of other textbooks available on the topic.

2.4.1 Transmission electron microscopy

In a TEM a thin (on the order of nanometers) sample is placed in the way of a diffuse and parallel high energy (80-300 keV) electron beam. The electrons pass through the sample and can be detected at the bottom of the microscope column (Figure 2.20). Depending on the method used, either the direct transmitted beam or the scattered electrons are used for imaging. For the results in this thesis (mainly size distributions) bright field TEM imaging was used. In this case, the direct transmitted beam is detected. Thicker areas of the specimen (or where particles are present on a thin substrate) scatter or absorb more electrons than thinner areas creating contrast. The brightness difference depends on the atomic number of the material present and its thickness, and the recorded images show a 2D projection of a 3D shape. All the size distributions were determined using a FEI Tecnai T20 G² microscope equipped with a thermionic LaB₆ electron source having a line resolution of 0.14 nm. The main drawback of TEM is the need for thin samples. This means that the actual samples going through activity measurements usually cannot be investigated. In our case the size distribution or the position of the particles could be investigated with TEM by depositing on lacey carbon covered TEM grids, but the actual samples (μ -reactors or polycrystalline Au stubs) could not be investigated. For the latter SEM was used with a compromise on resolution.

Chapter 5 contains high angle annular dark field scanning transmission electron microscopy (HAADF STEM) images recorded at the University of Birmingham. In this imaging mode a focused electron beam is rastered on the surface of the sample just like in an SEM and the transmitted, but scattered electrons are detected. This means that areas with higher atomic number show up brighter on the images. Using modern aberration corrected equipment atomic resolution can be routinely achieved with HAADF-STEM imaging.

2.4.2 Scanning electron microscopy

In an SEM, a focused electron beam (typical energy 0.3-20 kV) is rastered on the surface of the sample and secondary electrons (low energy electrons escaping the surface) or backscattered electrons (electrons colliding with atoms and scattered back) are detected. The intensity of these signals is correlated with the position of the beam and an image is formed. Secondary electrons carry information about the

morphology of the surface, backscattered electrons show contrast based mainly on the atomic number of the surface atoms. In a usual SEM these signals are detected by detectors placed close to the surface. However, newer SEMs utilize in-lens/through the lens/immersion lens detectors. This type of detector is placed into the column concentric around the primary beam and magnetic and electric fields around the pole piece guide the secondary electrons towards this detector. In general, an in-lens detector provides more effective collection of secondary electrons and a higher contrast, especially with low primary beam energies. All of the SEM images shown in the thesis were recorded using an in-lens detector. Images shown in Chapter 3 were acquired with a Zeiss Gemini UHV SEM column mounted on the Omicron vacuum chamber, having a lateral resolution of 3 nm. All of the other SEM images were taken by an FEI Helios EBS3 dual-beam instrument, having a resolution better than 1.5 nm.

2.5 Other techniques referred to in the thesis

2.5.1 Quadrupole Mass Spectrometer (Filter)

A quadrupole mass spectrometer or filter (QMS), is a vacuum instrument to filter ions by their m/z ratio. In this thesis it is used to quantitatively detect different gases in the μ -reactor setup (Section 2.2.3). It was first described in the '50s [76, 77], where [77] also contains the detailed mathematical description of its working principle. Here I would like to give a phenomenological summary. The schematics of a quadrupole mass filter can be seen in Figure 2.21/A.

In order for a QMS to be able to detect gases, the atoms/molecules have to be ionized first. This is usually done by electron bombardment from a heated filament. After the species are ionized they enter the mass filter. In a QMS there are four rods pairwise connected to a DC and RF potential ($U + V \cos \Theta$, where $|U| < |V|$) creating an electrical field. One pair of the rods have a negative DC component another pair a positive (Figure 2.21/B). If we assume positive ions, the filtering works in the following way: The two positive rods create a field, where positive ions are stable in the middle. However, with the RF components these rods frequently turn negative. Heavy ions have too much inertia to be affected by this, but light ions are moved out of the stable region and neutralized on one of the rods. This creates a high-pass mass filter. In case of the negative rods, positive ions are attracted towards them and when the RF components turns the rods positive, the ions are pushed back towards the middle. Heavier ions have high inertia and they are not affected by the temporary repelling force that much. They are attracted to one of the rods and neutralized. This creates a low-pass mass filter. The two effects working together ensures, that only a single mass is let through. The mass getting through can be tuned by the potentials (frequency). After the rods, the filtered ions are detected by a detector, usually a secondary electron multiplier.

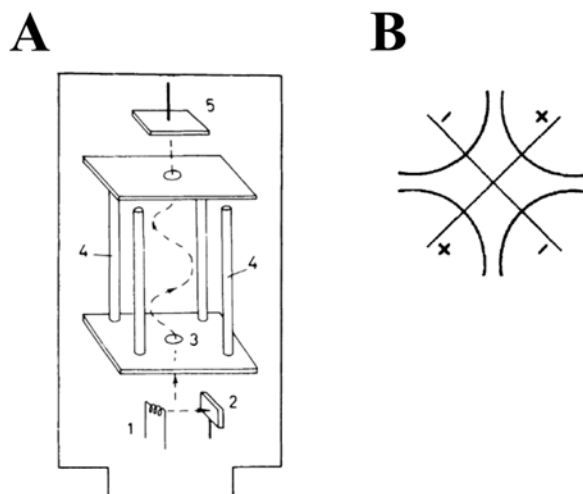


Figure 2.21: Schematic illustration of a quadrupole mass filter (QMS). A: quadrupole mass filter. 1: e^- source, 2: collector for ionization; 3: entrance aperture, 4: rods and 5: ion detector. Reprinted from [61]. B: Ideal cross section of the rods. Reprinted from [62].

2.5.2 Inductively coupled plasma mass spectrometry

Inductively coupled plasma-mass spectrometry (ICP-MS) is a quantitative analytical method capable of measuring concentrations down to ppt-ppb level of almost all the elements in the periodic table [78]. During measurement, a liquid sample is injected through a nebulizer as aerosol droplets into an RF argon plasma. The droplets are dried and the molecules are fragmented and ionized in the plasma. Through an interface and ion optical lenses, the ions created are led to a mass spectrometer (most often a quadrupole mass spectrometer) where the elemental composition can be analysed. With the aid of 3 standards (known concentrations) the concentration of the element in the investigated sample can be determined. As this method is very sensitive, the dissolution of catalysts during electrochemical stability measurements or the nanoparticle loadings can be investigated. The ICP-MS system used for the project described in Chapter 3 is a Thermo Fischer Scientific iCAP-QC ICP-MS.

CHAPTER 3

The limit of Pt as a catalyst for hydrogen evolution

This project started out with the idea that using the unique capabilities of our cluster source we could study how good is Pt as a catalyst for the hydrogen evolution reaction (HER), supported by simulations made by Erno Kemppainen (Aalto University). Photoelectrocatalytic (PEC) hydrogen evolution process was chosen, as in this process the achievable current is limited by the illumination, thus we are not dealing with current densities on the order of $\frac{\text{A}}{\text{cm}^2}$ rather on the order of $\frac{\text{mA}}{\text{cm}^2}$. My contribution to the project was mainly the deposition and physical characterization of the samples together with Anders Bodin. As the main focus of my thesis is not PEC process or simulation of focus, focus will be on characterization of the nanoparticles and the implications of our results. Further information about the PEC measurements and the simulations can be found in the paper and the supporting information published in Energy & Environmental Science [20]. I also have to mention that a similar study has been done earlier with Pt by Dasgupta and co-workers [79]. They used atomic layer deposition (ALD) to deposit islands (particles) of Pt on Si nanowires. However, as they used a nanowire structure the determination of their exact loadings (per geometric area) seems to be rather difficult. Nevertheless, the loadings were ranging from a few hundred $\frac{\text{ng}}{\text{cm}^2}$ to the range of several $\frac{\mu\text{g}}{\text{cm}^2}$. Furthermore, due to the ALD process the size of the particles were also loading dependent in the study.

3.1 Introduction

If we would like to shift to a hydrogen based society and we are planning to produce hydrogen using a (photo)electrocatalytic device, it is necessary to find an HER catalyst which can be scaled-up to the TW level. Pt is widely used and considered to be the best catalyst for the HER, thanks to its high activity and stability [71]. However, Pt is fairly expensive and as an even bigger issue, the yearly production is "only" about 180 t [80]. Because of these issues, there was a huge urge to find a more

abundant and scalable HER catalyst to substitute Pt. The best of these non-precious materials are usually phosphides or sulfides of transition metals (Mo, Co, Fe, Ni). The progress in the synthesis of these materials and their activity is summarized by [81] and the recent review of Montoya and co-workers [71]. In general there are two issues with these materials: they are not as stable as Pt in acidic environment and the amount of material required to achieve the same current density at a given overpotential as with Pt is significantly higher. The latter in turn has two consequences: with a higher amount of material deposited on a light absorber (if we are considering a direct PEC cell) the higher parasitic light absorbance of the catalyst material decreases the efficiency of the absorber material [82]. The other issue is the price and abundance: even though the non-platinum catalysts comprise of elements of much higher abundance than Pt, if the required amount is thousands of times higher than in case of Pt, they still might have a disadvantage in terms of scale-up (as it turns out, they do [20]). In order to determine just how good a HER catalyst Pt is, we deposited ultralow loadings of Pt mass-selected nanoparticles on the photocathodes described in detail earlier [83, 84] and tested the activity of these for photocatalytic HER. The photocathodes comprise of a Si n+p junction and a thin TiO₂ layer to protect the Si from the electrolyte. Simulations were also made to further investigate PEC HER with ultralow loadings of Pt as a catalyst. The system reported here for Pt is a highly optimized one close to the actual limit what is achievable with Pt, while the search for new non-precious HER catalysts and the optimization of these catalysts are an ongoing effort which could suddenly result in the discovery of a new, highly active, cheap and abundant catalyst. More importantly the extreme low loadings of Pt we used were very sensitive to contamination, thus no stability data is reported (see in Section 3.1.2.1).

3.1.1 Nanoparticle deposition and activity measurements

We deposited mass-selected Pt nanoparticles with our nanoparticle source (Section 2.1.2) by sputtering a Pt target (99.99%, Kurt J Lesker). As a substrate we used a Si light absorber with a sputtered thin protection layer of TiO₂ (see details in [83, 84]). We deposited particles with a mass of 850k amu, which corresponds to approx. 5 nm in diameter. The loadings investigated were: 1000 $\frac{\text{ng}}{\text{cm}^2}$, 200 $\frac{\text{ng}}{\text{cm}^2}$, 50 $\frac{\text{ng}}{\text{cm}^2}$ and 10 $\frac{\text{ng}}{\text{cm}^2}$ corresponding to approx. 14%, 2.8%, 0.7% and 0.14% projected surface area coverage. The loadings were chosen to span orders of magnitudes, thus even if the mass loadings were not completely accurate, the conclusions and trends should be valid. The exact Pt loadings were verified with dissolving the Pt in aqua regia (nitric acid (HNO₃) and hydrochloric acid (HCl) in a molar ratio of 1:3) and using ICP-MS (Section 2.5.2). After deposition the samples were characterized with XPS. The samples having a loading of 10 $\frac{\text{ng}}{\text{cm}^2}$ were also characterized with ISS in order to prove that Pt was successfully deposited on the surface as XPS did not show a Pt signal. One example of each loading was imaged using the in-lens detector of the UHV SEM in the Omicron chamber with an electron acceleration voltage of 7 kV and a current of

400 pA. The photocathodes were tested in 1M HClO₄ (99.99%, Sigma Aldrich) under illumination with a 1000W (Oriel) xenon lamp. The lamp was equipped with a 635 nm cut-off and an AM1.5 filter to simulate the red part of the solar spectrum reaching the bottom cell of a PEC tandem device. The intensity of illumination was calibrated to the intensity of the red part of the solar spectrum ($38.6 \frac{\text{mW}}{\text{cm}^2}$). The measurements were made with a sweep rate of $50 \frac{\text{mV}}{\text{s}}$ and the graphs contain the third CVs. The maximum photocurrent (between -22 and $-22.4 \frac{\text{mA}}{\text{cm}^2}$) and the average open circuit voltage (0.495 V vs RHE) of the substrates were comparable to the value reported for similar Si-based photocathodes earlier [83].

3.1.2 Simulating the behaviour of the photocathode

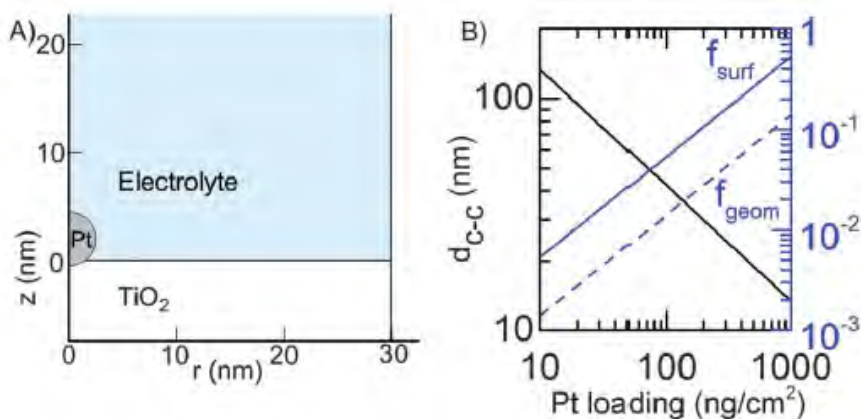


Figure 3.1: Illustration to the simulation of the TiO₂ protected Si photocathode and Pt nanoparticle catalyst. A: schematic of the simulated unit cell in case of a loading of $50 \frac{\text{ng}}{\text{cm}^2}$. Note that the TiO₂ substrate continues till -100 nm; B: Average particle-particle distance (black line), ratio of Pt surface area to the geometric electrode area (f_{surf} , continuous blue line) and the ratio of the Pt covered electrode area to the entire electrode area (f_{geom} , dashed blue line) as the function of mass loading. Figure reproduced from [20].

For the sake of the simulation a few assumptions had to be made. The Pt particles were assumed perfectly spherical with a diameter of 5 nm (this was supported by the determined size distribution, see Section 3.2.1) which are sunk in by 0.25 nm into a 100 nm TiO₂ layer (Figure 3.1/A). For simulating mass transport and PEC behaviour a cylindrical unit cell was defined around the spherical Pt particle with the diameter of the average particle-particle distance (Figure 3.1/B) and the mass transport across the sides of this cell was set to 0. The effect of the Si photovoltaic

(PV) cell was simulated by assuming it is ideal and its current-voltage (IV) curve can be described with (3.1), where i_{Ph} is the photocurrent density, i_{rec} is the current density corresponding to the recombination rate in the device, V is the photovoltage, n_{SC} is the ideality factor (for PV cells made from Si $n = 1$) and k_B is the Boltzmann constant [85]. For further details and the values used for all the material properties see [20].

$$i = i_{Ph} - i_{rec} \left(e^{\frac{q_e V}{n_{SC} k_B T}} - 1 \right) \quad (3.1)$$

3.1.2.1 Note on the stability of the Pt particles

During the measurements, the performance of the photocathodes degraded fairly rapidly especially the ones with very low particle loadings, even though the cell was extensively cleaned. This has most probably happened because of the epoxy resin the electrodes were enclosed in during sample mounting [86]. The resin was also immersed into the electrolyte together with the sample. Nevertheless, all of the electrodes were stable for at least 5 scans. Because of the instability, we did not make any stability tests and this should be taken into consideration if ultra low loadings of Pt (and possibly other metals as well) should be used in industrial long-term applications.

3.2 Physical characterization of the deposited nanoparticles

3.2.1 Size-distribution of the deposited nanoparticles

We deposited 850k amu Pt particles on the prepared TiO₂ protected Si photocathodes. The size distribution of the particles was determined with the method outlined in Appendix D and can be found in Figure 3.2, along with a representative image of the particles. The diameter of the particles is around 5 nm and they look round, supporting the assumptions made during the simulations (Section 3.1.2). At this point in time we did not have a sample holder capable of holding TEM grids at the same distance from the mask and aperture as the other samples. Therefore, we could not make particle-particle distance statistics or representative images of the different loadings with TEM, as we did in case of the NiFe particles (see Section 4.5.4). This was one of the reasons why we needed new and improved sample holders and I started designing them (Appendix C).

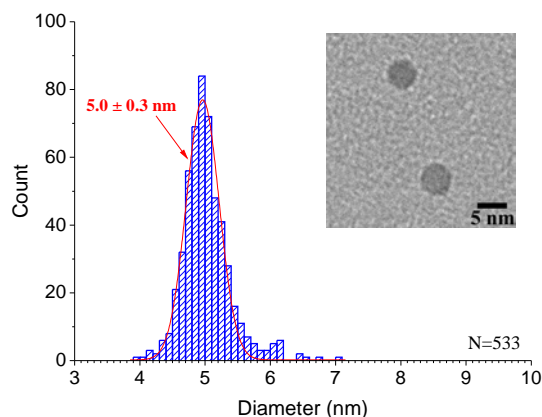


Figure 3.2: Size distribution of the mass selected Pt nanoparticles having 850k amu mass along with an example image from bright field TEM imaging. The particles were deposited on lacey C covered Cu TEM grids under similar nanoparticle source conditions as the photocathodes. Figure adapted from [20].

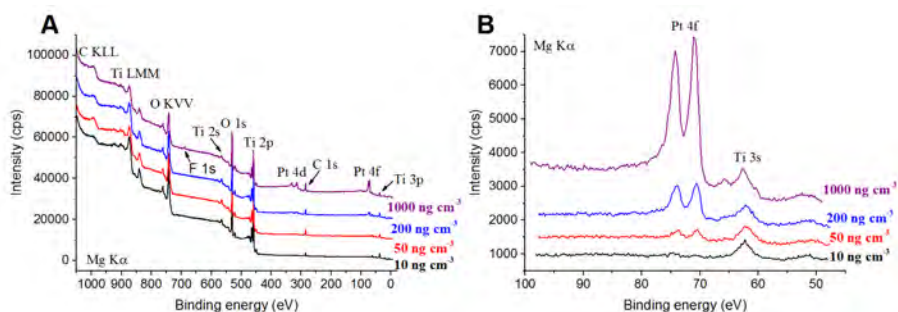


Figure 3.3: XPS survey spectra and detailed spectra of the Pt 4f region of photocathodes with different Pt nanoparticle loadings. The spectra were offset in the y direction for ease of view. A: Survey spectra taken of photocathodes having the 4 different loadings; B: Detailed spectra of the Pt 4f region in case of the 4 different loadings. Figure adapted from [20].

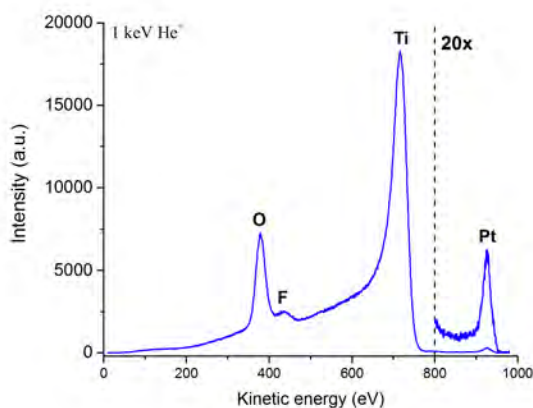


Figure 3.4: ISS spectrum of a TiO_2 protected Si photocathode with $10 \frac{\text{ng}}{\text{cm}^2}$ mass-selected Pt nanoparticle loading. The spectrum clearly shows a Pt peak. Figure adapted from [20].

3.2.2 XPS and ISS characterization of the photocathodes with the deposited Pt nanoparticles

Each sample made was characterized with XPS after deposition to ensure that there are no contaminants on their surface. Figure 3.3 shows example survey spectra taken of photocathodes having different loadings along with detailed spectra of the Pt 4f region. Each spectrum was shifted to attain a C 1s binding energy of 284.6 eV, which gave a binding energy of 70.7-70.9 eV for the Pt 4f_{7/2} in case of all the samples. A small amount of F could be found on the surface of some of the samples. This is most probably due to the handling of the samples and should not influence the PEC activity. As expected, the Pt 4f peak is getting smaller and smaller as the loading of the samples decreases and in case of the samples with a loading of $10 \frac{\text{ng}}{\text{cm}^2}$ the Pt particles cannot be detected any more with XPS (Figure 3.3/B). In order to confirm that Pt was indeed deposited to the surface, we recorded ISS spectra on the samples with the lowest loading (an example is shown in Figure 3.4). Even the lowest loading of Pt nanoparticles ($10 \frac{\text{ng}}{\text{cm}^2}$) can easily be detected, thus confirming the existence of Pt particles on the surface. Furthermore, samples with $10 \frac{\text{ng}}{\text{cm}^2}$ loading still had significant HER activity (see Section 3.3), which has serious implications for research aimed at finding non-precious HER catalysts. Even the tiniest amount of Pt can influence the activity of samples thought to be Pt free and the detection limit of XPS is not enough to detect these contaminations. Therefore, methods with higher sensitivity (like ISS) have to be employed to ensure Pt free electrodes for non-precious HER catalyst research.

3.2.3 SEM images of the different nanoparticle loadings on the photocathodes

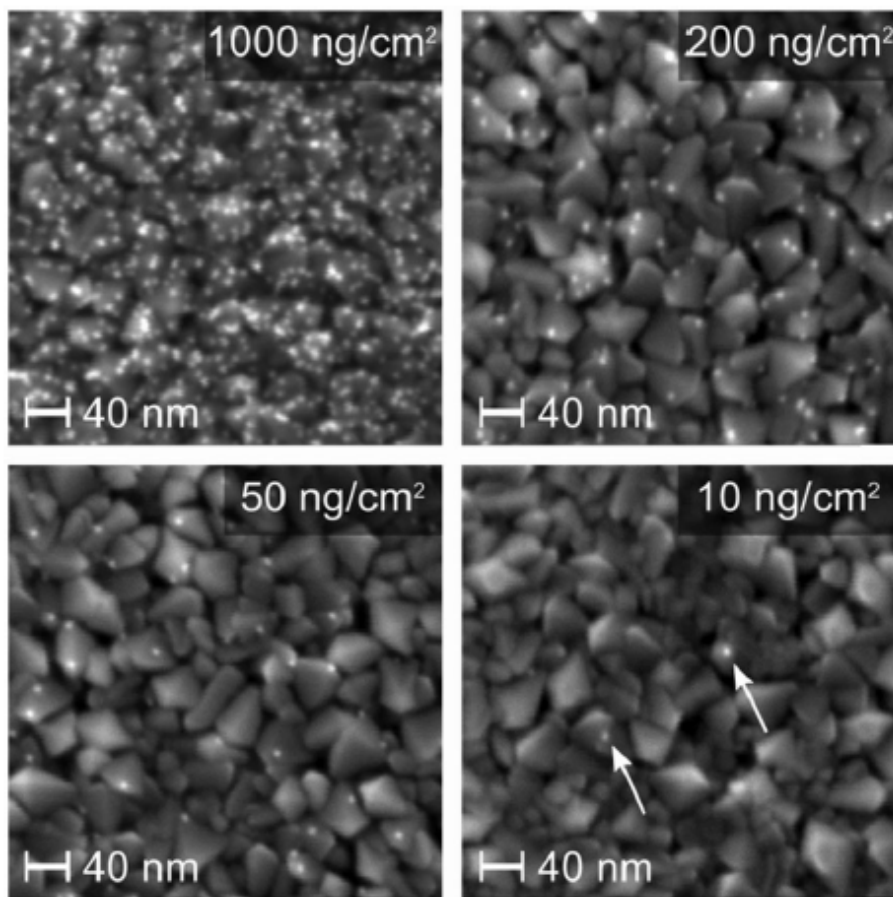


Figure 3.5: SEM images taken of photocathodes having different Pt nanoparticle loadings. The arrows in the image corresponding to the lowest loading ($10 \frac{\text{ng}}{\text{cm}^2}$) mark the Pt particles on the surface. Figure reprinted from [20].

To further characterize the samples and give an to provide a way to visualise the low loadings of Pt investigated, a photocathode of each loading was imaged with SEM (Figure 3.5). The images were taken after deposition without breaking the vacuum using the SEM column attached to the Omicron chamber (Section 2.1.1). Pt particles are showing up as bright dots on the rough sputtered TiO_2 background. In case of

the lowest loading only a handful of Pt particles can be found on the surface which are still providing easily measurable HER activity.

3.3 Activity of ultra-low loadings of Pt nanoparticles for PEC hydrogen evolution

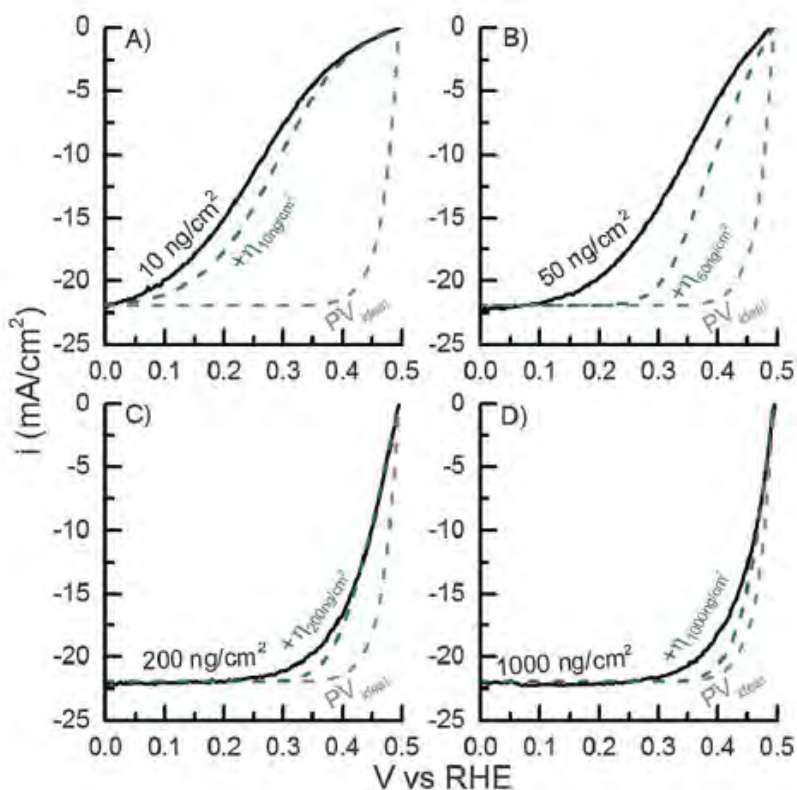


Figure 3.6: Measured (continuous black line) and simulated (dashed green line) IV-curves of the TiO_2 protected Si photocathodes having different Pt nanoparticle loadings. The continuous grey line depicts the behaviour of an ideal PV cell. Figure reprinted from [20].

Figure 3.6 shows the measured and simulated IV-curves in case of the photocathodes having different Pt nanoparticle loadings along with the behaviour of an ideal PV cell. In case of all the investigated samples an open circuit photovoltage (V_{OC}^{PV})

of approx. 500 mV and a light limited photocurrent of approx. $22 \frac{\text{mA}}{\text{cm}^2}$ was measured regardless of Pt the loading. This shows the advantage of nanoparticles as photocatalyst: regardless of the loading (at least as long as it is sufficiently low), they do not block significant portion of the light reaching the photoabsorber. The measured values for the photovoltage and photocurrent are close to the ones reported earlier for similar photocathodes produced by our group [83]. They also act as a confirmation that the photocathodes can be manufactured in a reproducible manner. In order to compare the different loadings, the overpotential ($\eta_{10 \frac{\text{mA}}{\text{cm}^2}} = V_{OC}^{PV} - V_{10 \frac{\text{mA}}{\text{cm}^2}}$) required to drive a current of $10 \frac{\text{mA}}{\text{cm}^2}$ can be used. The overpotentials ($\eta_{10 \frac{\text{mA}}{\text{cm}^2}}$) determined in case of the different loadings are summarized in Table 3.1. Even the lowest loading provides significant catalytic activity.

Loading (ng)	Measured overpotential ($\eta_{10 \frac{\text{mA}}{\text{cm}^2}}$, mV)
1000 ng/cm ²	32
200 ng/cm ²	46
50 ng/cm ²	142
10 ng/cm ²	231

Table 3.1: Measured overpotentials to achieve $10 \frac{\text{mA}}{\text{cm}^2}$ current density ($\eta_{10 \frac{\text{mA}}{\text{cm}^2}}$ as a function of Pt nanoparticle loading on the photocathodes.

Based on Figure 3.6 the simulated IV-curves can be compared to the measured ones and to the IV-curves of an ideal PV-cell. The simulated IV-curves in general underestimate the overpotentials, or in other words overestimate the activity of the samples. This effect is especially prevalent at the $50 \frac{\text{mA}}{\text{cm}^2}$ loading and at higher current densities. This might be due to differences in mass transport between the experiments and the simulations. Nevertheless, the simulated curves at least at low current densities describe the trend of the experimentally measured IV-curves. It is also worth noting, that as the loading decreases the measured and simulated curves are getting further away from the ideal behaviour.

In order to further investigate the behaviour of the system, the effect of mass transport and reaction kinetics can be investigated separately based on the simulations. For ease of comparison, the total overpotential at small overpotentials can be written as $\eta_{total} = \eta_{MT} + \eta_{Kinetic}$, where η_{total} is the determined overpotential, η_{MT} is the overpotential due to mass transport losses and $\eta_{Kinetic}$ is the overpotential due to reaction kinetics. Figure 3.7/A shows the simulated IV-curves corresponding to the different loadings along with the mass transport overpotential and the simulated curves of a compact (flat) Pt thin film. Based on Figure 3.7 the behaviour of the highest nanoparticle loading (1000 ng/cm^2) is similar to a compact Pt thin film. Therefore, further increasing the loading is not expected to increase the performance of the system significantly. It is interesting that the curves representing the mass

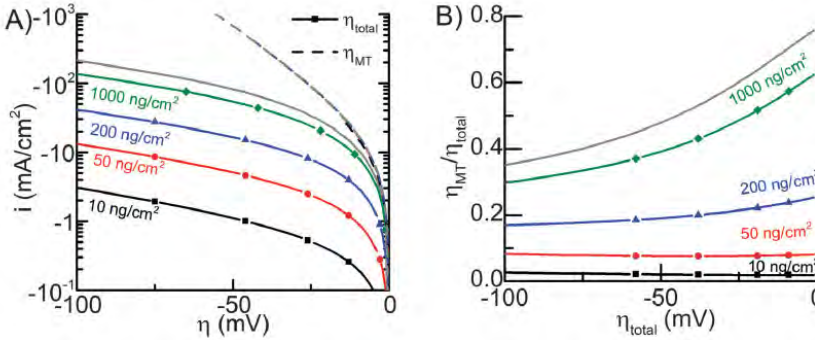


Figure 3.7: Comparison of the effect of mass transport and reaction kinetics on the overpotential of photocathodic HER as a function of Pt nanoparticle loading. A: IV-curves depicting η_{MT} , the overpotential due to mass transport (perfect catalyst) as a function of loading (dashed lines) and the total overpotential (solid lines); B: Significance of mass transport in the total overpotential as a function of Pt nanoparticle loading and total overpotential (η_{total}). The gray line in A&B shows the corresponding simulated data for a flat Pt surface. Figure reprinted from [20].

transport losses overlap. This might be due to the fact that, even in case of the lowest loading, H₂ molecules have to travel significantly longer in axial directions away from the electrode, than the distance between Pt particles. Figure 3.7/B shows that in case of the highest loading more than 50% of the losses are due to mass transport limitations and not the catalyst. This means that further increasing the loading would only increase the performance slightly.

3.4 Pt as a TW scale HER catalyst

Based on the calculated values backed with the experimental results some projections can be made about the usage of Pt as a TW scale HER catalyst in a PEC device. As the simulated values were used to create the following graphs and tables the exact numbers might be not perfectly accurate, but the order of magnitudes should be correct. Investigating the behaviour of Pt as an HER catalyst on the TW scale is important, as our energy consumption is already in the TW range (around 17.5 TW) [6]) and it is likely to increase in the future (Section 1.1.2). In order to estimate the amount of Pt needed to generate a TW of energy, the following procedure can be used. The average power of the PEC device (P_{avg}) can be calculated using (3.2), where 0.15 is the capacity factor and i is the current density. The capacity factor is a unitless value which depicts how much of the built-in power can be actually utilized in average. In case of a solar device it takes into account e.g. nights or cloudy days. A

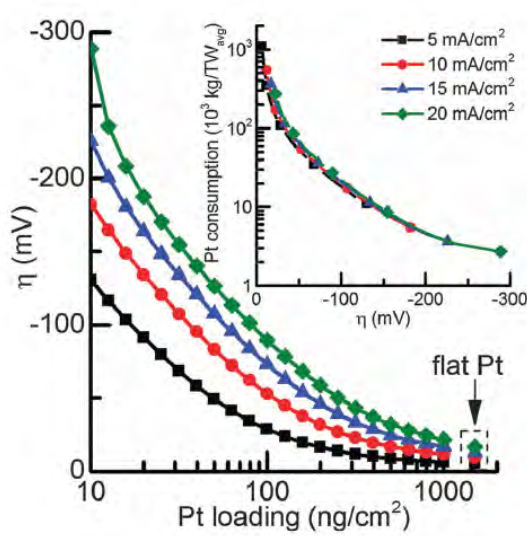


Figure 3.8: Overpotential as a function of current density and the Pt nanoparticle loading along with the amount of Pt required for a TW of power produced. Figure reprinted from [20].

capacity factor of 0.15 is a conservative estimate for a PV [87]. Using the calculated value in (3.2), the electrode area required for 1 TW of power can be calculated as a function of current density (3.3). From these, the total consumption of Pt to a TW generated can be calculated with the choice of an acceptable overpotential (losses) as depicted in Figure 3.8.

$$P_{avg} = 0.15 \times i \times 1.23V = 0.1854V \times i \quad (3.2)$$

$$A_{TW} = 1 \frac{TW}{P_{avg}} = \frac{542000km^2}{i[mA/cm^2]} \quad (3.3)$$

The yearly production of Pt was approx. 180 t in 2010 [80] and most probably it is on the same order of magnitude today too. Keeping this in mind and looking at the amount of Pt required for a TW of power as a function of the overpotential it is not unimaginable, that Pt is a feasible HER catalyst on the TW scale. The best non noble NiMo and MoP/S catalysts require an overpotential of approx. 50 mV to reach 10 mA/cm² [71]. If we accept the same overpotential approx. 70-80 t of Pt would be required for a TW of power. This is well inside the yearly production of Pt and as the transition to a H₂ based society would not be instantaneous, the required Pt amount would not be needed immediately. For further details and implications see [20].

3.5 Summary

The study of ultra-low loadings of mass-selected Pt nanoparticles as a TW scale HER catalyst gave a couple of interesting results. On the long term it seems feasible to use Pt even on the TW scale as an HER catalyst in a PEC device, despite the limited quantity available. This statement is valid for a highly specialized and developed system and new non-noble catalyst might yet to surface in research which surpass Pt as a HER catalyst. Nevertheless, for our present knowledge Pt seems to be a viable option. A more immediate and practical result of investigating these low loadings of Pt nanoparticles is that even 10 ng/cm^2 of Pt provides a significant catalytic activity in HER, while it is not detectable by XPS. This means that for research in non-noble HER catalysis more sensitive methods than XPS have to be used to ensure that the electrodes are really Pt free, otherwise minor Pt impurities might alter the results. A few questions we did not investigate were the stability of the electrodes with these low loadings and the effect of the Pt particle size, which are actually connected. With the lower loadings contaminants in the electrolyte become a problem and the electrodes with the lowest loading lost their activity rapidly. This might become a problem if practical application of such low loadings of catalysts is considered. Lowering the particle size lowers the amount of Pt required for a TW of power as more surface area per mass is available (see the Supporting Information of [20]). On the other hand with lowering the size the surface energy is going up and the particles become more prone to sintering or corrosion further decreasing the stability [88].

CHAPTER 4

Mass-selected NiFe nanoparticles as a catalyst modelsystem for the oxygen evolution reaction in alkaline media

As mentioned earlier (Section 2.3) an important half-cell reaction in an electrochemical water splitting device is the oxygen evolution reaction (OER). For this reaction in alkaline media mixed oxides of Ni and Fe are widely used catalysts owing to their high activity, abundance and low price [89, 90]. However, even after years of research efforts there are still a open questions about the active sites and the exact mechanism of the OER on mixed Ni and Fe oxides. Furthermore, there is no size study available on the size effects with bimetallic NiFe particles of different sizes. I will try to give an overview of the entire project focusing on the work coordinated and done mainly by me (the production and physical characterization of the particles). Claudie Roy (DTU SurfCat) conducted all the electrochemical measurements and Elisabetta Fiordaliso (DTU CEN) did all the SEM imaging, for which I am immensely grateful to both of them.

4.1 Introduction

There is a huge amount of research data available on the topic of NiFe mixed oxides as electrocatalysts for the OER in alkaline media. I cannot hope to give a comprehensive review in the space available of all the different research going on in the field right now, for that I refer to a recent review from Dionigi and Strasser [91]. Here I will summarize some of the results interesting for the research shown in this chapter.

4.1.1 Activity and active sites

It is widely known that Ni(Fe)OOH is highly active electrocatalyst for the OER in alkaline media. In fact, industrial alkaline electrolyzers use a mixture of Ni, Fe, Al or Co as their catalyst although details of these materials are usually secret [89]. For a long time it was believed that NiOOH in itself is a good catalyst. As it turns out, Fe from the electrolyte is readily intercalated into the Ni lattice replacing Ni atoms and this is needed to reach high activity [92, 93]. Nevertheless, Ni can be investigated in completely Fe-free electrolyte [92] and NiOOH turns out to be a poor catalyst for OER. It seems that for high OER activity isolated Fe sites are needed in the NiOOH lattice [94] and to maintain these sites phase separation and formation of Fe hydroxides has to be avoided [91]. This gives an upper limit of what the ideal Fe content of a NiFe mixed oxide OER electrocatalyst could be, as above approx. 33 at% Fe content phase separation of FeOOH can occur, which decreases the activity [91]. The ideal Fe content of a NiFe mixed oxide electrocatalyst was explored by various studies. It has been found to be around 11 at% [93] or around approx. 25 at% [94]. The difference between the two reports might be the result of different catalyst preparation techniques or different aging of the samples in the electrolyte [93]. An interesting aspect of the research on NiFeOOH electrocatalysts is that even though we know the structure [94] and the composition, the active sites are still somewhat elusive. Intercalated Fe sites were identified as having high activity [94] and this is supported by the fact that meticulously Fe-free NiOOH is a poor catalyst [92]. Nevertheless, the question still arises: where does the reaction take place? Trotochaud and co-workers [95] wrote, that almost all Ni atoms are active, thus all the bulk of the catalyst. This is also implied in turn over frequency (TOF) data given as a function of different catalyst thin film thicknesses in [92]. On the other hand, Friebel and co-workers [94] imply that Fe atoms on the surface are the active sites, but they are not clear on the matter. There are a lot of other works dealing with identifying different mechanisms to facilitate the OER on Ni(Fe)OOH (for example a recent paper from Diaz-Morales [96] dealing specifically with the role of the surface species), but the question still remains somewhat elusive.

We thought that investigating mass-selected nanoparticles could give some further insight into how OER works in case of a NiFe mixed oxide catalyst and what are the active sites, whether it is the surface which is active or the bulk of the material. The particle size dependence of the rate of a reaction carries information about the active sites (for example [11]), which is ideally straightforward to determine. If we assume

that the particles are perfect homogeneous spheres and it is the bulk which is active, the mass-activity (current/unit mass) of the samples should be the same regardless of size, if there are no mass transport limitations. If it is only the surface (which is assumed homogeneous) what is active, the surface area normalized current density should be constant regardless of the size, again assuming no mass transport limitations. We used turnover frequencies (TOFs) calculated with different assumptions as a unit of comparison, but the logic behind the investigation is the same as described. We chose TOF as a unit of measurement to be able to compare the activity of our particles to literature values. Activities are reported in the literature in different ways, normalized with geometric surface area, electrochemical surface area or mass. All of these units make sense for some applications, but we chose TOF as it is maybe the most fundamental one and one which is straightforward to determine from the details of the depositions.

4.1.2 Effect of particle proximity

The effect of particle proximity on the activity of Pt for the oxygen reduction reaction was reported by Nesselberger and co-workers [97]. They found that as Pt particles are getting closer, their surface area normalized activity is increasing. A similar study was made with Cu nanoparticles which showed that the selectivity of Cu nanoparticles changes in electrochemical CO₂ reduction depending on the interparticle distance [98]. For OER and NiFe no similar study exists. Different groups explored the effect of depositing ultrathin films and very low metal loadings and how the loading influences the activity [92, 99, 100]. These studies are similar to a possible particle proximity effect in the sense that films <1 ML most probably form islands. However, the results reported in these studies are fairly inconclusive and explore layers >1 ML more than low loadings. We deposited different loadings of mass-selected NiFe nanoparticles having the same size and evaluated their activity. With increasing the nanoparticles loading the average interparticle distance between the particles decreases and the effect of this on the OER activity can be investigated in a well controlled manner.

4.2 Electrochemical measurements and the protocol used

The samples were tested in N₂ saturated 1 M KOH (Sigma-Aldrich, 99.99%) in a PTFE cell. Before each measurement the reference electrode potential was measured vs. the reversible hydrogen electrode (RHE) using a clean Pt mesh and by saturating the same electrolyte with H₂. After mounting a sample, activity measurements were taken following a strict protocol at a rotation speed of 1600 rpm: first the ohmic loss was estimated by impedance spectroscopy. Afterwards, 5 cyclic voltammeteries (CVs) were recorded with a scan rate of 10 mV/s between 0.9 V and 1.6 V vs. RHE. After the CVs a 2 h chronoamperometry measurement at 1.6 V vs. RHE was conducted

to assess the stability of the samples. And finally all the reported activity data were recorded using CVs after the 2 h chronoamperometry. As Au is slightly active for OER, three Au stubs were cleaned with the same method as all the substrates used for deposition (Section 4.3), checked with ISS (thus receiving the same ion dose as all other samples) and measured for OER. The results were averaged to establish a background for the measurements, corresponding to the empty substrates. All activity data reported are corrected for ohmic losses, the background based on the empty Au stubs is subtracted and based on the average of at least 3 samples. All the potentials are reported vs. RHE.

For the long term stability tests polycrystalline Au foils were used as a substrate, cleaned and characterized the same way as the stubs. During these measurements the samples were not rotated. The data reported for the long term measurements are 85% ohmic drop corrected.

4.3 Deposition of mass-selected NiFe nanoparticles

We tested 4 different sizes of NiFe nanoparticles, deposited using the nanoparticle source (Section 2.1.2) sputtering a 75 at% Ni and 25 at% Fe target (Kurt J. Lesker). For the different sizes we chose 120k amu, 350k amu, 950k amu and 2 mil amu mass corresponding to approx. 3.5 nm, 5 nm, 7 nm and 9 nm diameters assuming bulk density and spherical shape. The usual loading of the samples was 15% projected surface area if not stated otherwise (details of how we calculate our loadings and sizes can be found in Appendix B).

Two different substrates were used: polycrystalline Au (pcAu) stubs (cylinders with a diameter of 5 mm and height of approx. 4 mm which serve as the working electrode in the RDE setup) from Pine Research and lacey carbon covered Cu TEM grids. Each Au stub was cleaned thoroughly before testing according to the following procedure: First the stubs were polished with 0.25 μm diamond paste. Then the disks were sonicated in isopropanol and mili-Q water (18.1 $M\Omega\text{cm}$ resistivity) for 3 minutes each. The sonication process was repeated 4 times. Finally, the disks were annealed for 1 min at 500°C under a flow of oxygen using an induction heater in order to decrease surface roughness, get rid of carbonaceous contaminants and make contaminating elements migrate to the surface of the stub. After cleaning, the substrates were loaded into the UHV chamber and checked for contaminating metals with ISS. An example ISS spectrum of a cleaned and annealed pcAu stub can be seen in Figure 4.1, showing the cleanliness of the substrates used. However, the Au peak is relatively broad, thus it might hide some contaminants. All samples were checked with XPS after deposition and apart from the deposited Ni and Fe (and Au) no metals were found on them. Some substrates had minute amounts of Ca or K as contaminants (around 40 amu) in the ISS spectra. These substrates were used for activity testing anyway, as we do not expect these elements to influence the results. Furthermore, owing to the extreme surface sensitivity of ISS (Section 2.1.1.2) it is very difficult to get rid of these contaminants in the ISS spectra. If any element

heavier than 40 amu (except Au) was found on a cleaned substrate, it was discarded and went through another round of cleaning and annealing before checking it again with ISS.

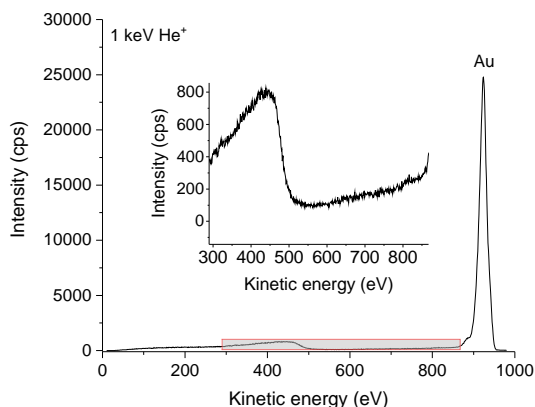


Figure 4.1: ISS spectrum of an empty, cleaned and annealed pcAu stub before deposition. No contaminants apart from some carbon were detected.

After deposition, the samples went through the same cycle of measurements and treatments (if not otherwise noted) consisting of XPS and ISS measurements without exposing them to air, electrochemical characterization (as described in Section 4.2) and after the electrochemical measurements XPS and ISS characterization again. After the electrochemical measurements the electrolyte drying on the surface of the samples formed a "thick" K layer, which made XPS and ISS measurements impossible. To avoid this, the samples were thoroughly rinsed with mili-Q water before loading them into the UHV chamber for further characterization. In order to investigate that this treatment is not removing particles from the surface and in general submerging samples into an electrolyte, rotating them and handling them does not mechanically remove the particles, identical location SEM images were taken of a sample having 350k amu (approx. 5 nm) NiFe particles after deposition and after the measurement procedure was completed (Figure 4.2). No loss or migration of particles can be seen, all the particles in the image taken before electrochemical measurements can be found in the image taken afterwards.

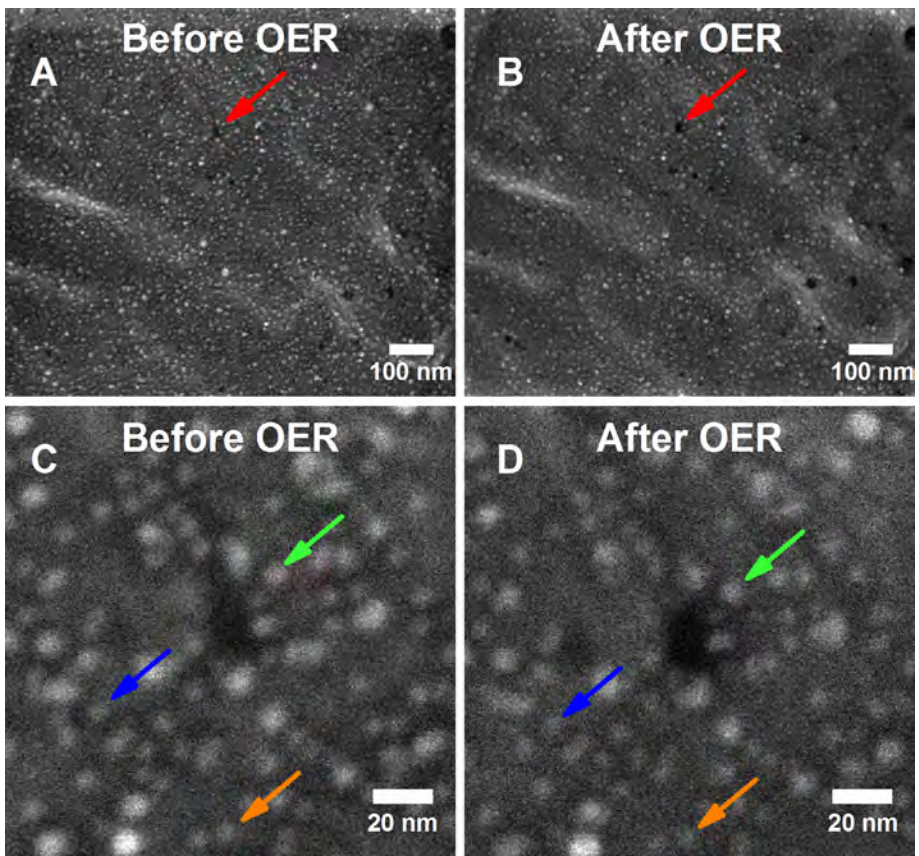


Figure 4.2: Identical location SEM images of a pcAu stub with 350k amu NiFe nanoparticles before and after OER measurements. No loss or migration of the particles can be seen. A&B: Overview of the surface before and after measurements, respectively (red arrow is pointing at the surface defect zoomed in in C&D); C&D: Close-up on the same feature before and after measurement. The arrows point at the same particles before and after electrochemical measurement. Images courtesy of Elisabetta Fiordaliso.

4.4 Physical characterization of the NiFe nanoparticles and substrates

4.4.1 Size-distributions of the nanoparticles

I used bright field TEM imaging in order to evaluate the size-distribution of the NiFe nanoparticles having different mass. The particles were deposited on lacey C covered Cu TEM grids (approx. 3 % projected surface are coverage). Figure 4.3 shows the size-distributions determined following the procedure described in Appendix D with normal distributions fitted to the peaks and an example image of the particles for each deposited size.

The 4 different sizes are well separated. Even with the simple assumption of spherical particles and taking into account the bulk density, the determined sizes are fairly close to the calculated ones. The counts around 10.5-11 nm in case of the 2 mil amu particles and the counts around 7.5-8.5 nm in case of the 950k amu particles are most probably due to double mass-double charge particles passing through the mass filter (Appendix B). For ease of discussion I will use the size of the different particles to reference them, but keep in mind that we control the mass of the particles.

4.4.2 Reproducibility of the depositions

With the chosen rastering parameters, the ion beam from the iongun used for ISS covers most of the surface of the pcAu stubs. As multiple samples of the same loading and size were made, the reproducibility of our depositions can be investigated based on the ISS spectra. Figure 4.4 shows the 3 samples of each size which are included in the activity data. The ISS signals were normalized to the Au peak to make the comparison easier. As a first approximation the Fe&Ni peak in the ISS spectrum should be proportional to the number of Fe and Ni atoms on the surface, thus the Fe&Ni peaks of the different samples should be similar (as the projected surface area coverage of the different samples is the same). For samples having the same size nanoparticles (theoretically identical samples) the Fe&Ni peaks are fairly similar in the ISS spectra. However, for the samples having different sizes of NiFe particles the differences are slightly bigger. Nevertheless, the spectra show the control and reproducibility of our sample preparation.

Similar comparison can be made based on the XPS spectra. Figure 4.5 shows the average of the Ni + Fe peak areas normalized with the peak areas of Ni + Fe + Au, thus all the metals detected on the surface, before and after activity measurements. In case of the XPS spectra, the reproducibility of the samples after deposition seems to be worse than with ISS. On the other hand, after activity testing the values get closer to each other.

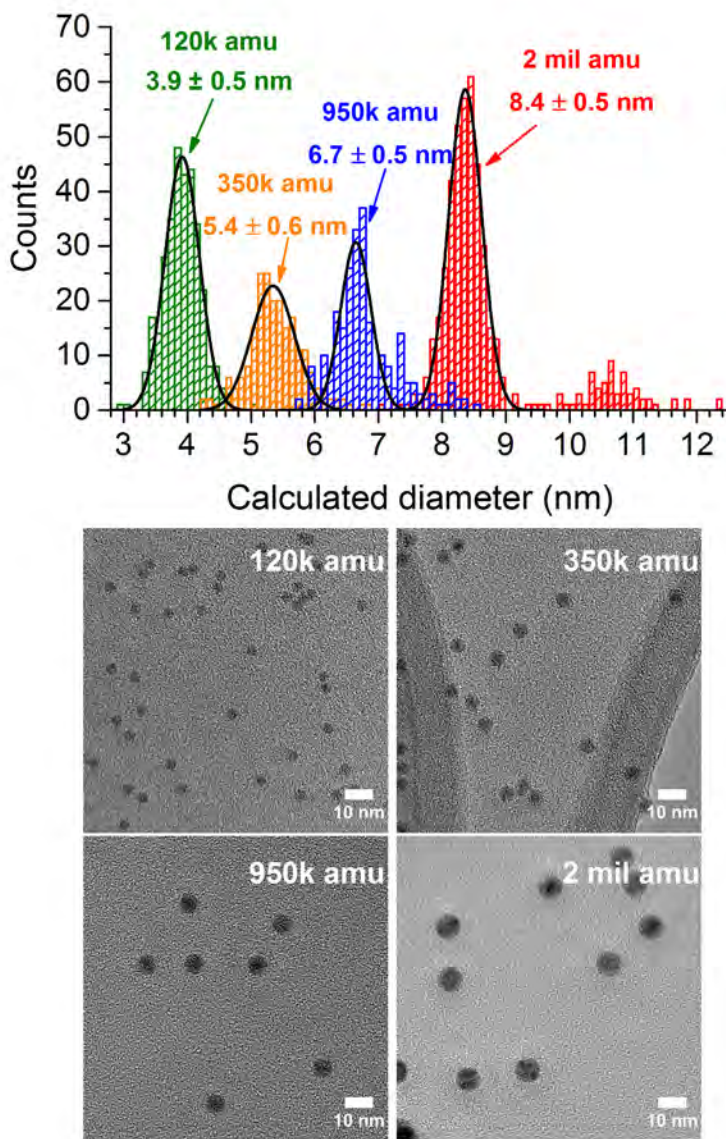


Figure 4.3: Top: size-distributions of the NiFe nanoparticles having different masses. Black lines are normal distributions fitted to the peaks. Uncertainties correspond to 2σ of the fitted distributions. Bottom: A, B, C and D show example TEM images of the nanoparticles having 120k amu (A), 350k amu (B), 950k amu (C) and 2 mil amu (D) mass, respectively.

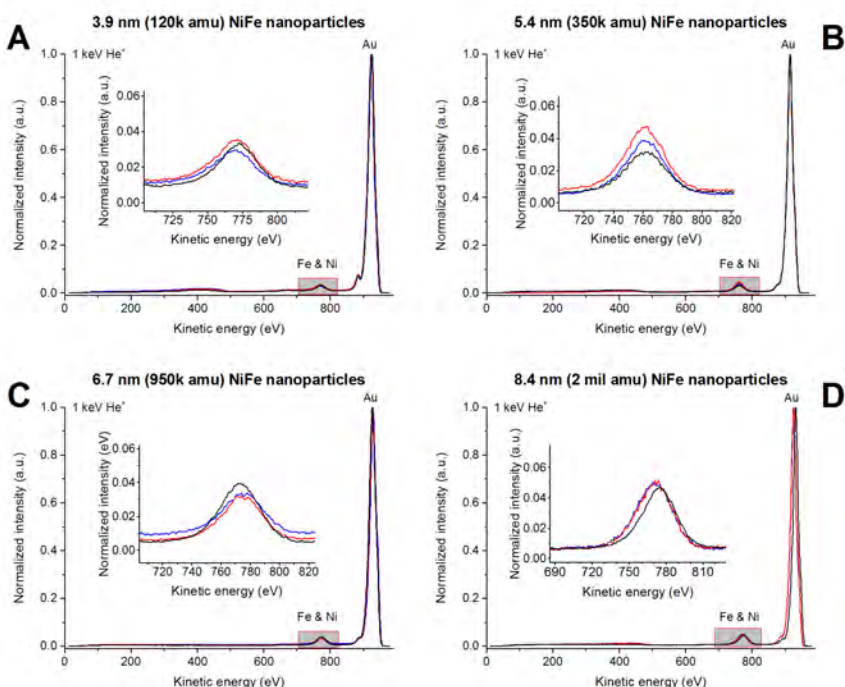


Figure 4.4: Reproducibility of NiFe nanoparticle depositions on pcAu stubs shown by ISS spectra taken without exposing the samples to atmosphere. For each size the 3 samples which were included in the activity data are shown. A: 3.9 nm (120k amu), B: 5.4 nm (350k amu), C: 6.7 nm (950k amu) and D: 8.4 nm (2 mil amu).

4.4.3 Comparison between the particles after deposition and after activity test

Experiments indicated that sputtering of the pcAu stubs makes the blank substrates more active in the OER. Therefore, significant effort was made to keep the ion dose during the ISS measurements low and the same in case of all the samples, including the blank substrates used to determine the background for the activity measurements. For each sample the same sputtering parameters (emission current, He gas pressure, raster size) and data acquisition parameters (start and finish energy, dwell time, energy step size and number of cycles) - thus total sputtering time - were used and relatively fast scans of the energy range were made. To check the cleanliness of the samples and to make sure that the broad Au peak in the ISS spectra does not cover any contaminants,

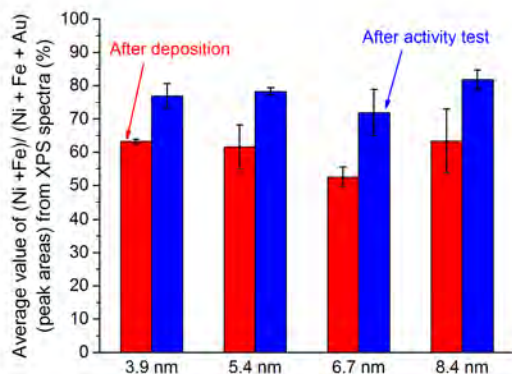


Figure 4.5: Reproducibility of NiFe nanoparticle depositions on pcAu stubs shown by the peak areas in the XPS spectra. The columns show the Ni + Fe peak areas divided by the peak areas of all the metal on the surface after deposition and after activity testing. The data are averaged over the 3 samples included in the activity data for each size. Error bars were calculated as the standard deviation of the data.

XPS spectra were recorded of all the samples after deposition and after activity testing too. Apart from the survey spectra, detailed spectra of the Ni 2p_{3/2}, Fe 2p_{3/2}, O 1s, C 1s and Au 4f region were recorded. All spectra were shifted to attain a binding energy of 84 eV for the Au 4f_{7/2} peak and the signals were normalized with the area of the Au 4f doublet. Sputtering during ISS reduces the oxidized NiFe particles (Appendix A), therefore all XPS spectra shown after activity testing were recorded before the corresponding ISS measurements. We chose to record only the 3/2 part of the Ni 2p and Fe 2p doublets. The reason for this was to attain better signal to noise ratio for the low signal from the nanoparticles, especially in case of the Fe peaks. As shown in [101] by Biesinger and co-workers this creates some uncertainties in the quantification of the XPS spectra, because the background fitting is less accurate. However, as all the spectra were treated the same way the values before and after activity testing should be comparable to each other, even if the absolute values might be a slightly inaccurate.

4.4.3.1 ISS spectra and XPS survey spectra after deposition and after activity testing

Figure 4.6 shows the ISS spectra recorded after deposition and after activity testing on a sample having 5.4 nm (350k amu) NiFe particles. The intensities were normalized

with the Au peak intensity. As it can be seen, even though the sample was thoroughly rinsed with water, the ISS detects a large amount of K from the electrolyte. The K is covering the surface, so the absolute value of the Au peak is significantly lower than in case of the spectrum recorded after deposition (indicated by the signal to noise ratio). Nevertheless, Ni and Fe can still be detected on the surface.

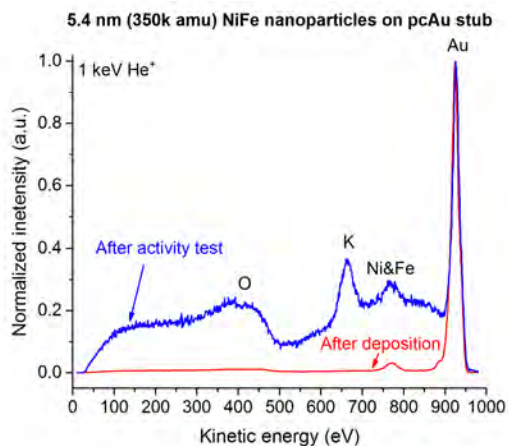


Figure 4.6: ISS spectra of 5.4 nm (350k amu) NiFe nanoparticles on pcAu after deposition and after OER activity testing (same sample as in Figure 4.7). After thoroughly rinsing the sample with mili-Q water there is still a significant amount of K from the electrolyte detected on the surface. Intensities normalized with the Au peak intensity.

Figure 4.7 shows XPS survey spectra of the same sample after deposition without breaking the vacuum and after activity test and transfer between the setups under atmospheric conditions. Both after deposition and after activity testing there is a small amount of C contaminant. This is most probably due to exposure to air during sample transfer and can be found on almost every sample investigated in XPS after loading them into a vacuum chamber. In the spectrum recorded after activity testing, there is a significantly larger O peak compared to the spectrum measured after deposition. This is because of the formation of oxidized Ni and Fe species (see in Section 4.4.3.3) and most probably also C-O or O-H bonds. The amount of K ($RSF_K = 4.04$) detected with XPS seems lower compared to the ISS spectra (Figure 4.6), showing the different information depth of the two methods.

4.4.3.2 Fe content of the particles

In order to quantify the Fe content of the nanoparticles, Shirley backgrounds were fitted to the Ni $2p_{3/2}$ and Fe $2p_{3/2}$ peaks and the area of the peaks was determined.

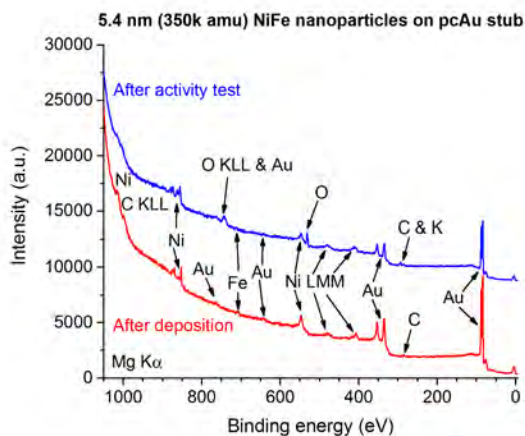


Figure 4.7: XPS survey spectra of 5.4 nm (350k amu) NiFe nanoparticles on pcAu after deposition and after OER activity testing (same sample as in Figure 4.6). The sample was thoroughly rinsed with mili-Q water before loading it into the UHV chamber. Intensities were offset for better visibility.

The start and end points of the fitted backgrounds in case of both peaks are summarized in Table 4.1. The Fe content of the particles in at% was calculated according to (4.1) where A_{Ni} and A_{Fe} are the areas of the Ni $2p_{3/2}$ and Fe $2p_{3/2}$ XPS peaks after background subtraction and RSF_{Ni} and RSF_{Fe} are the relative sensitivity factors of the Ni $2p_{3/2}$ and Fe $2p_{3/2}$ XPS peaks, respectively (see Section 2.1.1.1).

$$\frac{\frac{A_{Fe}}{RSF_{Fe}}}{\frac{A_{Ni}}{RSF_{Ni}} + \frac{A_{Fe}}{RSF_{Fe}}} \times 100 \quad (4.1)$$

	After deposition (binding energy, eV)	After activity test (binding energy, eV)
Ni $2p_{3/2}$	863.5 → 849	868.5 → 849
Fe $2p_{3/2}$	715 → 703.5	719 → 707

Table 4.1: Summary of the start and endpoints of the Shirley backgrounds fitted to the Ni $2p_{3/2}$ and Fe $2p_{3/2}$ XPS peaks recorded of the NiFe nanoparticles on pcAu stubs .

Figure 4.8 shows the calculated Fe contents of the NiFe nanoparticles having different sizes after deposition and after activity testing (averaged over the 3 samples

included the activity data for each size). Even though the nanoparticles were deposited using targets with the same composition, particles with different sizes have different Fe contents. However, after activity testing the Fe content of the particles are similar regardless of their size. This means that the activity results for the different sizes can be readily compared. It also shows that either a segregation process during atmospheric exposure while transferring the samples or leeching out of the Fe content in the electrolyte is changing the Fe content of the particles as detected with XPS.

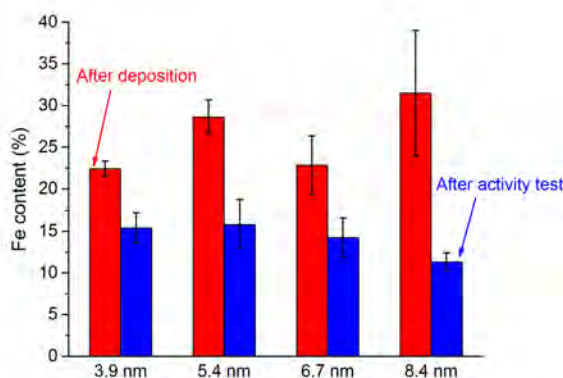


Figure 4.8: Average Fe content of the NiFe nanoparticles having different sizes as determined by XPS. Values shown for each size are the average of the Fe contents determined for the three different samples included in the activity data. Errorbars are the standard deviations of the data.

4.4.3.3 Binding state of Ni and Fe

Example detailed XPS spectra of the Ni $2p_{3/2}$ and Fe $2p_{3/2}$ regions for each nanoparticle size are shown in Figure 4.9 and Figure 4.10. The structure of the 2p peaks of first row transition metal elements tend to be complex due to asymmetries, shake-up and plasmon loss features and small binding energy differences between the different compounds [102]. Nevertheless, in case of both Ni and Fe studies in detail exist about the nature of the 2p peaks [101–105]. Unfortunately neither the limitation of our equipment (e.g. non-monochromatized X-ray source) nor the low signals from the small amount of nanoparticles on the surface (we used 50 eV pass energy to increase the signal) permits such detailed analysis of the Fe peaks recorded. Nevertheless, based on the studies mentioned before binding state information for Ni can be gained

from our recorded spectra and the oxidation number of Fe on the surface can be determined.

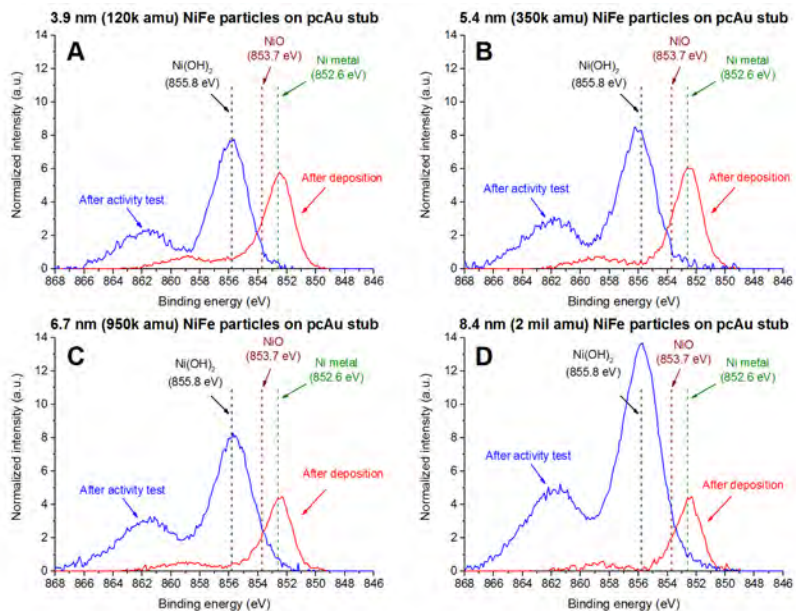


Figure 4.9: Example XPS detailed spectra of the Ni 2p_{3/2} region after deposition and after OER activity testing in case of all 4 sizes of NiFe nanoparticles. Intensities normalized with Au 4f area. A: 3.9 nm (120k amu), B: 5.4 nm (350k amu), C: 6.7 nm (950k amu) and D: 8.4 nm (2mil amu).

After deposition both Ni and Fe are in a metallic (0 oxidation number) state. This is due to the oxygen free environment in the vacuum chamber. However, after activity testing the binding states change. Ni is present on the surface as Ni(OH)₂ (Ni²⁺). In case of Fe the low signal, broad peak and close lying binding energies do not permit to distinguish the binding state between FeOOH and Fe₂O₃. The binding state is either one of these or a mixture of the two but regardless of the actual compound, Fe is present as Fe³⁺ on the surface. Furthermore, no metallic component of Ni or Fe can be detected after activity testing regardless of the nanoparticle size. The information depth of XPS at the corresponding electron kinetic energies is around 1 nm (Figure 2.2). This means that most of the material in the nanoparticles is probed with XPS, especially in case of the smaller nanoparticles. The oxidation numbers for Ni and Fe determined from the XPS spectra are identical to the ones determined by in-situ XAS for Ni and Fe below the on-set potential of OER earlier by Friebel and co-workers [94]. In order to further characterize the binding state of Ni and Fe and to investigate the effect of OER conditions a sample having 6.7 nm (950k amu)

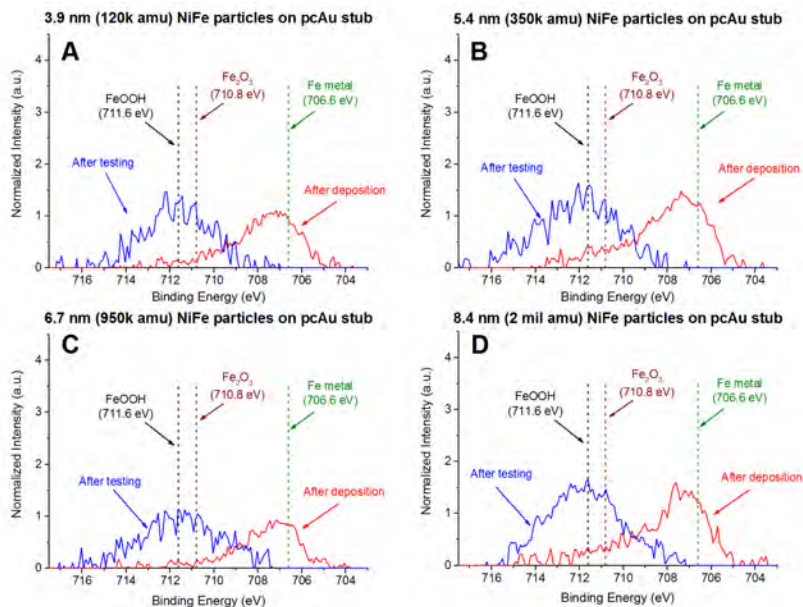


Figure 4.10: Example XPS detailed spectra of the Fe $2p_{3/2}$ region after deposition and after OER activity testing in case of all 4 sizes of NiFe nanoparticles. Intensities normalized with Au 4f area. A: 3.9 nm (120k amu), B: 5.4 nm (350k amu), C: 6.7 nm (950k amu) and D: 8.4 nm (2mil amu).

particles was exposed to air for 14h and another sample with the same nanoparticle size was stored in 1 M KOH for 2.5 h at open circuit potential (OCV). A timespan of 2.5 h was chosen as it is approx. the same time as the measurement of the activity takes. Figure 4.11 shows the detailed spectra recorded of the Ni $2p_{3/2}$ and Fe $2p_{3/2}$ regions for these samples, along with the corresponding spectra of a sample having nanoparticles of the same size and which went through activity testing.

In case of the sample exposed to air for 14 h a significant portion of metallic Ni and Fe can be detected (Figure 4.11/C & D). This behaviour was reported earlier for Ni(001) [106]. Under atmospheric conditions Ni forms a thin oxide layer and afterwards an $\text{Ni}(\text{OH})_2$ layer starts to slowly grow inwards. The fact that no metallic component can be seen in the sample exposed to OER conditions (Figure 4.11/A & B) and there is a significant metallic component in case of the sample exposed to air confirms that the electrolyte interacts with the bulk of the particle under OER conditions, at least to the same extent as the information depth of XPS. On the other hand, unfortunately this measurement does not provide any evidence whether the bulk of the particle is active in the process or whether there is a metallic core after exposing the particles to OER conditions. It is interesting that the particles get

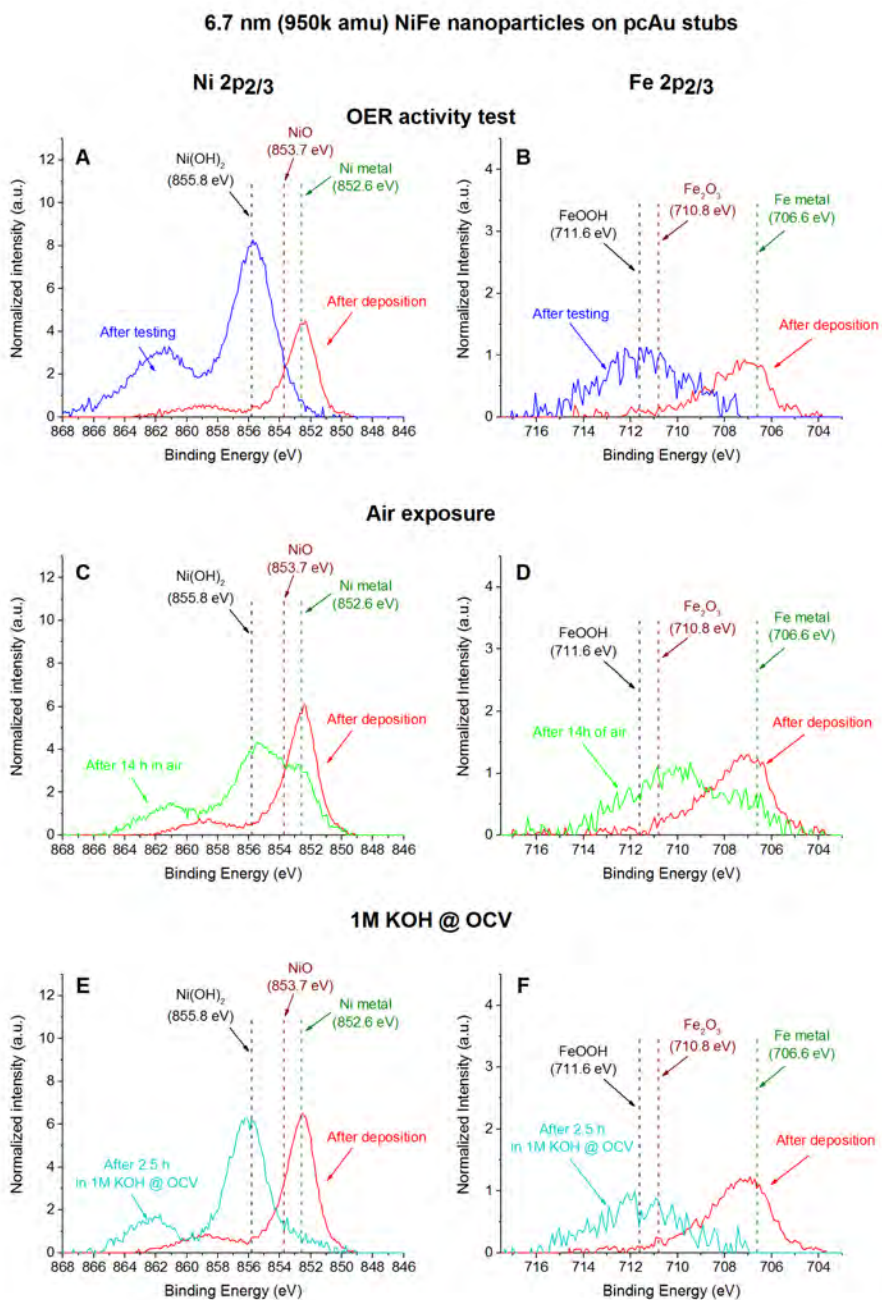


Figure 4.11: Comparison of the Ni 2p_{3/2} (A & C & E) and Fe 2p_{3/2} (B & D & F) XPS detailed spectra of 6.7 nm (950k amu) NiFe nanoparticles after activity testing (A & B), after 14 h of air exposure (C & D) and after 2.5 h in 1 M KOH at OCV (E & F). For each test a different sample was used. Intensities normalized with Au 4f area.

oxidized at least as deep as the information depth of the XPS (approx. 1 nm), even when they are exposed to the electrolyte at OCV (Figure 4.11/E & F).

4.5 Electrochemical measurements

4.5.1 Cyclic voltammetry measurements

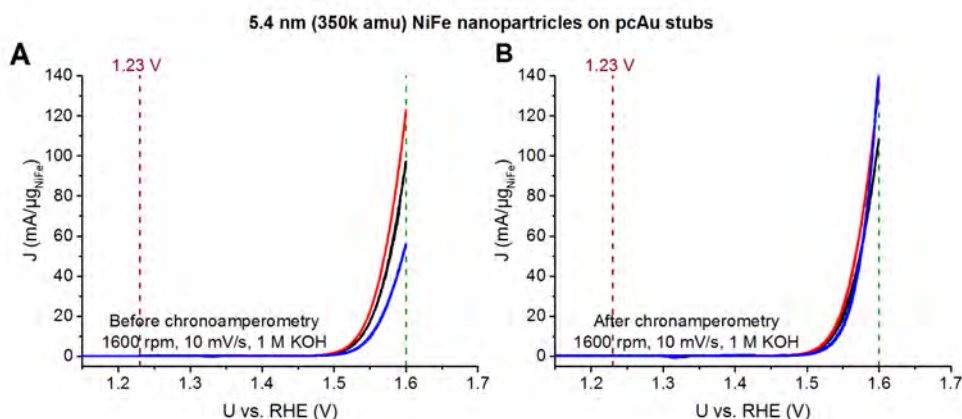


Figure 4.12: Cyclic voltammetry (CV) measurements of three samples with 5.4 nm (350k amu) NiFe nanoparticles before (A) and after (B) 2 h chronoamperometry at 1.6 V vs. RHE. The different colours depict different samples. 1.23 V vs. RHE is the equilibrium potential. Figure courtesy of Claudie Roy.

Figure 4.12 shows cyclic voltammetry measurements between 0.9 V and 1.6 V vs. RHE recorded before (Figure 4.12/A) and after (Figure 4.12/B) 2 h chronoamperometry at 1.6 V vs. RHE. The different colours in Figure 4.12 depict the three different samples having 5.4 nm (350k amu) NiFe nanoparticles included in the activity data. As a result of the 2 h chronoamperometry the activity and reproducibility of the samples increase. This might be the result of Fe leeching out of the particles, and a dynamic equilibrium establishing between the Fe content of the nanoparticles and the electrolyte (Section 4.4.3.2).

4.5.2 Activity vs. the nanoparticle size

We chose turnover frequency (TOF) as the unit for reporting our activities to be able to compare our results to the literature and to be able to investigate different

assumptions on the active sites. We calculated two different TOFs with different assumptions: TOF_{\min} is calculated using the assumption that all deposited metal atoms are active. The number of Ni and Fe atoms can be straightforwardly calculated from the composition, number of deposited particles (from the deposition current) and the mass of the deposited particles. TOF_{\max} is calculated with the assumption, that only the surface metal atoms of the particles are active. The number of these atoms can be calculated knowing the number of deposited particles (from the deposition current), the diameter of the particles (from Section 4.4.1) and the surface structure of NiFe mixed catalysts under OER conditions. The latter was determined and reported by Friebel and co-workers earlier [94]. Nevertheless, the size dependence of these values in theory should provide information about the active sites: if all the bulk Ni and Fe atoms are active, TOF_{\min} should be constant regardless of the size assuming no transport restrictions of reactants or products. In case only the surface metal atoms are active, TOF_{\max} should be constant regardless of particle size, again assuming no transport limitations. Figure 4.13 shows the TOFs calculated for the different NiFe nanoparticle sizes at 300 mV overpotential.

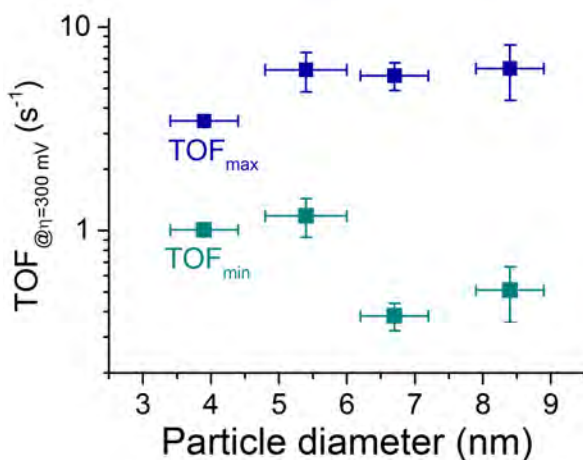


Figure 4.13: Calculated TOFs of the different NiFe nanoparticle sizes at 300 mV overpotential. If all metal atoms would be active for OER, TOF_{\min} would be constant assuming no mass transport limitations. In case only the surface metal atoms are active, one would expect TOF_{\max} to be constant regardless of the nanoparticle size again assuming no mass transport limitations. Figure courtesy of Claudie Roy.

Regardless of the assumption on the active sites, the particles having a diameter of 5.4 nm are the most active (Figure 4.13). It is quite obvious that neither TOF_{\min} nor TOF_{\max} is constant as a function of particle size. This could indicate that neither of our assumptions are true. On the other hand, except for the smallest size (3.9 nm),

the TOF_{max} values are all between 5.76 to 6.26 s^{-1} which is very close to being constant. The fact that the 3.9 nm nanoparticle size does not fit this trend can be caused by for example the increasing number of undercoordinated sites on the small particle. The increasing number of undercoordinated sites might invalidate our assumption of a spherical particle or the assumption of the surface structure determined by Friebel and co-workers on thin films [94]. It can also be an effect of the particles getting closer, which proved to decrease the activity (Section 4.5.4). Monte Carlo simulation showed that the average particle-particle distance is monotonously decreasing with the particle size, if the projected surface area coverage is kept constant. However, we do not observe a monotonously decreasing trend in our data. The behaviour of the TOF_{min} values is also interesting. One could imagine a situation where in case of small particles the entire particles get oxidized and the entire bulk is active for OER. As the size increases a metallic core appears, which contains metal atoms which are not active. This could explain the step in the TOF_{min} values between 5.4 nm and 6.7 nm particle sizes. Unfortunately none of the experiments showed so far can determine which explanation is true. However, identical location HRTEM imaging before and after oxidizing the particles in 1 M KOH is planned in the near future to further investigate the structure of the particles and gain insight into their oxidation properties.

Taking the most active size (5.4 nm), the TOFs calculated for our particles can be compared to some of the more detailed studies in the literature, where TOFs are reported or can be determined. Figure 4.14 shows the TOF of non-noble metal alkaline OER catalysts at 300 mV overpotential. Our catalyst is one of the most active on a TOF basis.

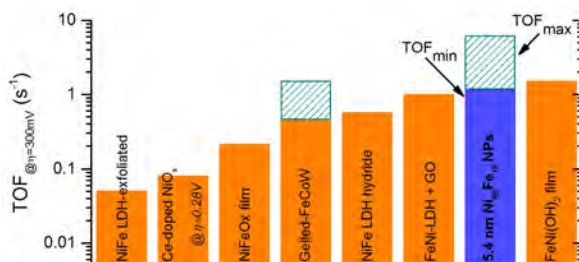


Figure 4.14: TOF of the 5.4 nm NiFe particles compared to values found in the literature at 300 mV overpotential. NiFe LDH-exfoliated from [107], Ce-doped NiO_x from [108], NiFeO_x film from [95], Gelled-FeCoW from [109], NiFe LDH hydride from [110], FeNi-LDH + GO from [111] and FeNi(OH)₂ film from [93]. Figure courtesy of Claudie Roy.

4.5.3 Stability of the nanoparticles under OER conditions

The stability of the particles was investigated by long term chronoamperometry measurements at 1.6 V vs. RHE using pcAu foils as substrates. The 85% iR corrected data recorded during one of these measurements can be seen in Figure 4.15, normalized with the total deposited mass of the particles. The total NiFe loading of the sample was around 100 ng and in a chronoamperometric measurement all changes in the activity should be exponential in the measured current. We have stopped the measurement after 1000(!) h. The performance of our sample seems to be stable during this time frame with small changes in activity and spikes, which are most probably results of external effects (e.g. people working in the laboratory).

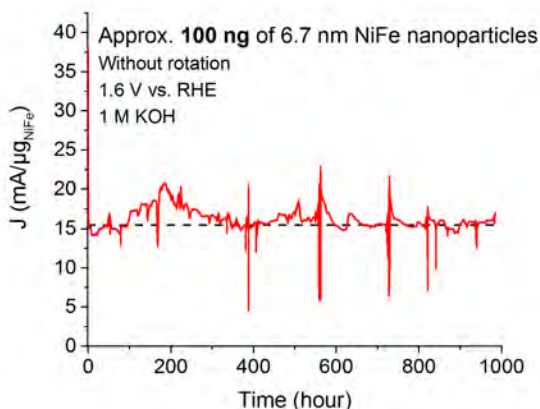


Figure 4.15: Long term chronoamperometric measurement of a sample with 6.7 nm NiFe nanoparticles at 1.6 V vs. RHE in 1 M KOH. Figure courtesy of Claudie Roy.

4.5.4 Effect of the particle proximity on the OER activity

In order to investigate the effect of particle proximity on the activity, I deposited samples having 6.7 nm (950k amu) NiFe particles with a loading of 12.5%, 10% and 5% projected surface area coverage on top of the samples with 15% coverage we already tested. In order to determine the average nearest neighbour distance (NND) between the centre points of the particles as a function of the loading I investigated TEM grids with the different nanoparticle loadings. Furthermore, one sample of each loading was imaged with SEM after electrochemical testing. I have also created a Monte Carlo simulation assuming completely random particle positions to simulate the NND as a function of loading. Because the investigation of the activity was based

on the assumption of the particles landing independently of each other and creating a random pattern, I analysed the randomness of the particle positions by calculating the corresponding average radial distribution functions (RDFs) from the microscopy images with a self written script. More details of RDFs, the script and its validation can be found in Appendix E.

4.5.4.1 NNDs and RDFs of the different nanoparticle loadings

I have deposited lacey C covered Cu TEM grids having 5%, 10%, 12.5% and 15% projected surface coverage under similar conditions as the actual samples. The grids were placed behind the mask the same position as the samples were to create grids where the conditions (e.g. electrical field or geometry) are the same as during the deposition of the samples. Figure 4.16 shows representative bright field TEM images for each of the loadings investigated.

For each loading one out of the 3 pcAu stubs tested for OER was imaged with SEM after activity testing. Figure 4.17 shows example images of the 4 different loadings of NiFe particles on pcAu stubs. The SEM imaging was done in order to check the actual samples going through electrochemical measurements and to explore the effect of surface roughness on the position of the particles.

Based on the TEM images the particles have a tendency to form chains and pairs (especially prevalent in Figure 4.16/A), which might be a result of the ferromagnetic nature of NiFe. The darker patches around the particles in the SEM images could indicate that the particles are following the surface morphology (mostly visible in Figure 4.17/B). In both cases the randomness of the particle positions might be influenced by these. In order to characterize the randomness of the particle positions, RDFs were calculated based on the TEM and SEM images of each loading by the method and self written script discussed in Appendix E. I also calculated the average NNDs based on the position of the particles. The data presented is based on at least 500 particles in case of each loading.

Figure 4.17 shows the calculated RDFs of the different loadings based on the TEM and the SEM images. In case of the TEM images taken of grids having 5% and 15% loading there is a short range order indicated by a peak in the RDFs. This is most probably the effect of chains or pairs forming and it is a lot less prevalent in case of the samples having 12.5% or 10% loadings. This might be because of a difference between the grids or the particles. If it is so, no physical evidence is pointing towards the nature of this difference. There is no long range (>10 nm) order on the surface of any of the samples. In case of the RDFs determined based on the SEM images, the particle positions seem completely random. The lack of the peak indicating chain formation is most probably due to the low resolution of the images. In the SEM images used it is very difficult to separate two nanoparticles with a diameter of around 7 nm if they land close to each other. Our samples were immersed in KOH before SEM imaging (for activity testing) making contamination a problem and imaging difficult.

Figure 4.19 shows the NNDs determined by Monte Carlo simulation and by investigating the TEM and SEM images. The errorbars correspond to 5px error in

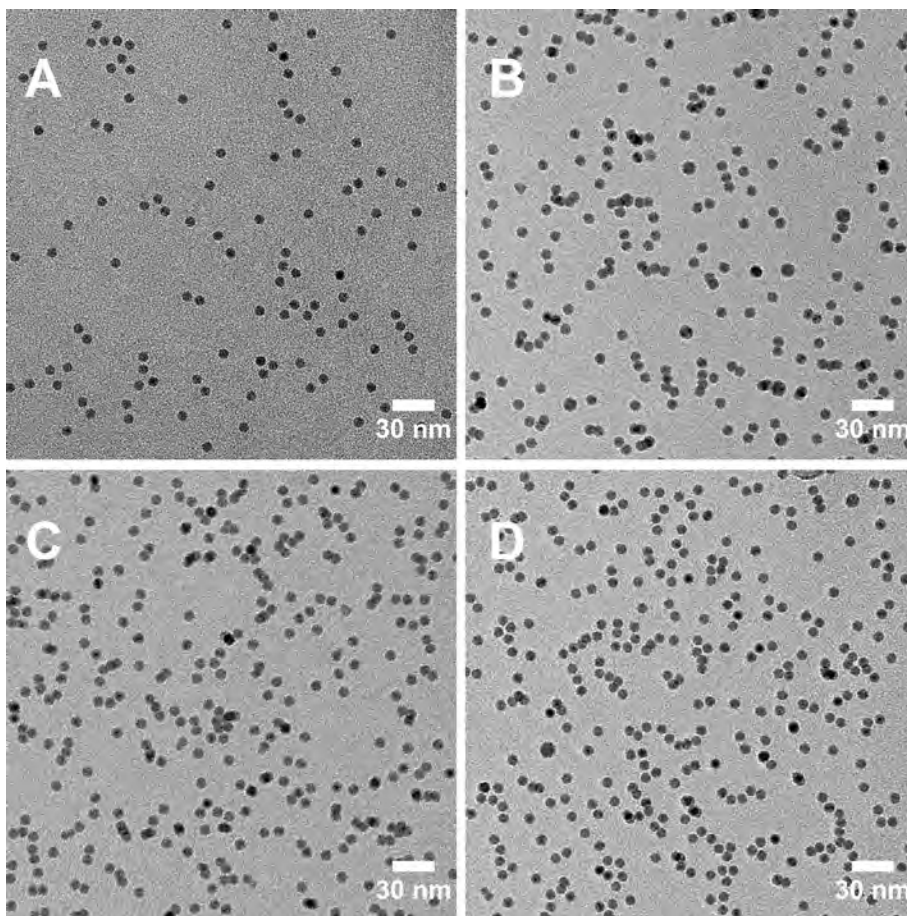


Figure 4.16: Bright field TEM images of lacey C covered Cu TEM grids having different loadings of 6.7 nm (950k amu) NiFe nanoparticles. A: 5%, B: 10%, C: 12.5% and D: 15% projected surface area coverage.

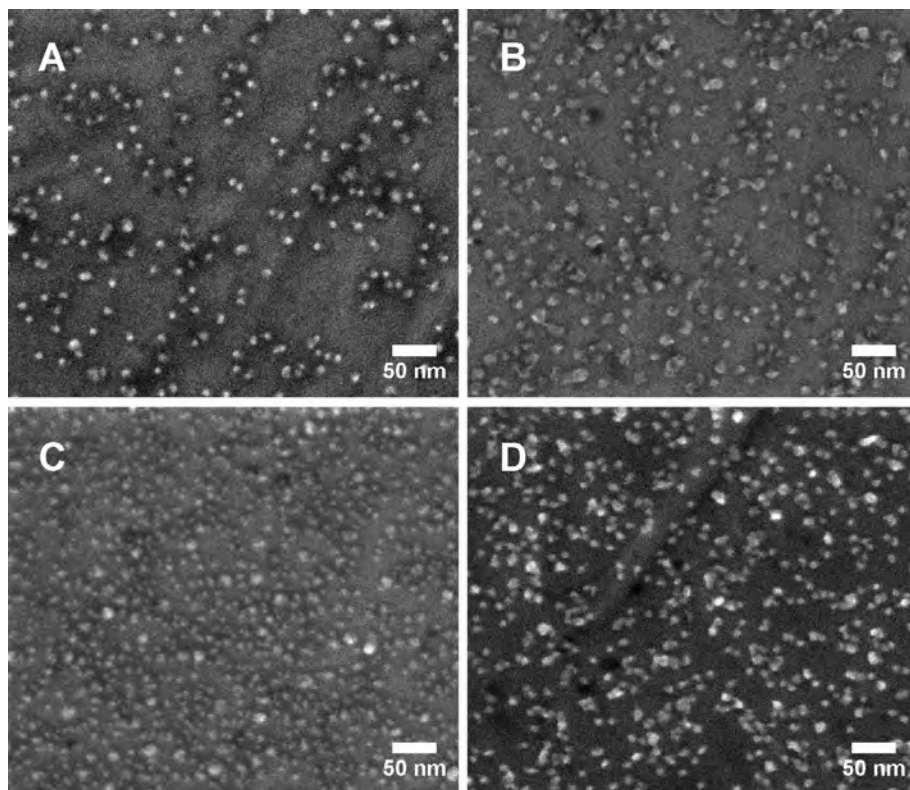


Figure 4.17: SEM images of pcAu stubs having different coverages of 6.7 nm (950k amu) NiFe nanoparticles. A: 5%, B: 10%, C: 12.5% and D: 15% projected surface area coverage.

the distances. The NNDs determined from the TEM images are following the Monte Carlo simulated line reasonably well. However, the NNDs determined from the SEM images are overestimating the distances determined from the TEM images and the simulated values. The reason for this is most probably the relatively low resolution of the SEM images and the difficulty of separating closely landed particles from each others. This is why at 5% loading (lowest number of overlapping particles) the 3 values agree relatively well and as the loading (and the number of closely landed or overlapping particles) increases the NNDs determined from the SEM images deviate from the other data. In Figure 4.19 there is an extra data point corresponding to a TEM grid with 2.5% projected surface area loading. I made this grid to have an extra point at low loadings to compare with the Monte Carlo simulation. This loading was not investigated for OER and there were no SEM images taken. Another interesting feature of this investigation is that the NND determined for the 12.5% loading

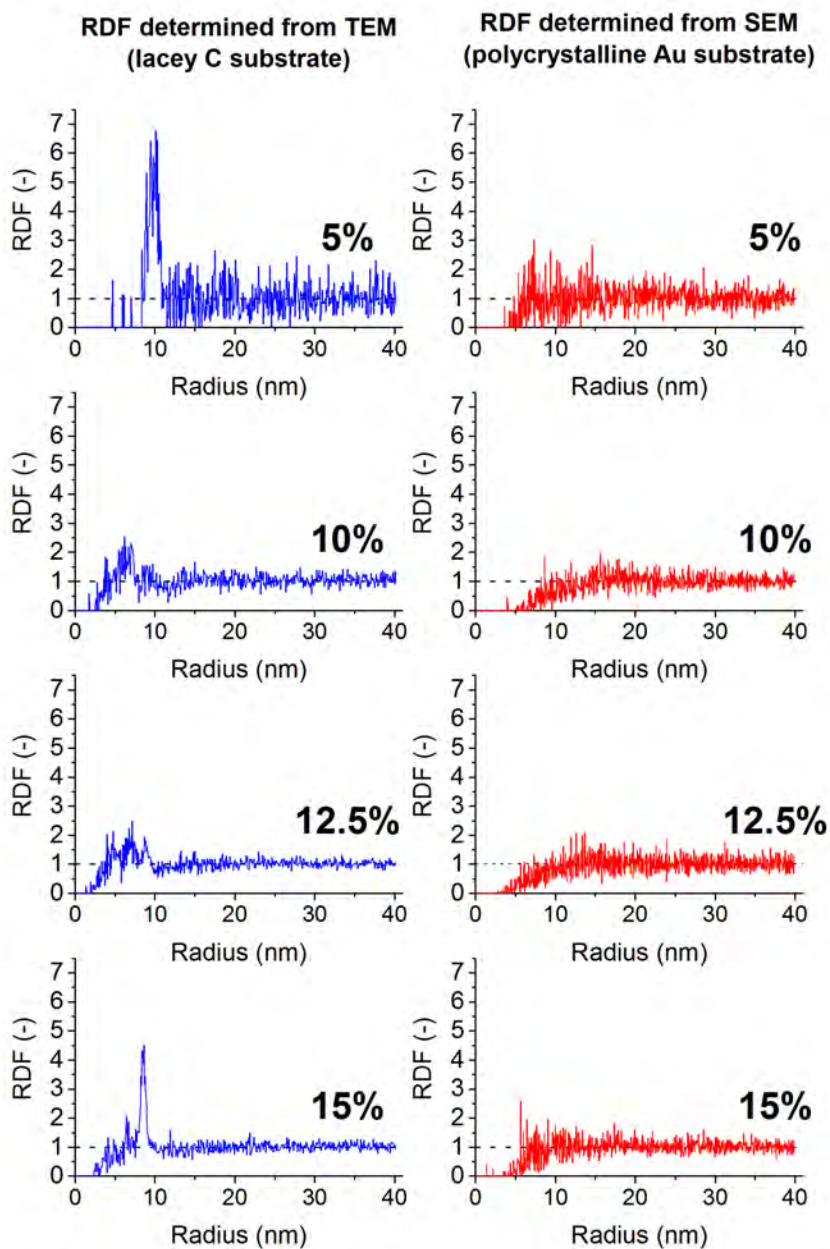


Figure 4.18: Calculated RDFs based on TEM and SEM images taken of samples with different loadings of 6.7 nm (950k amu) NiFe particles.

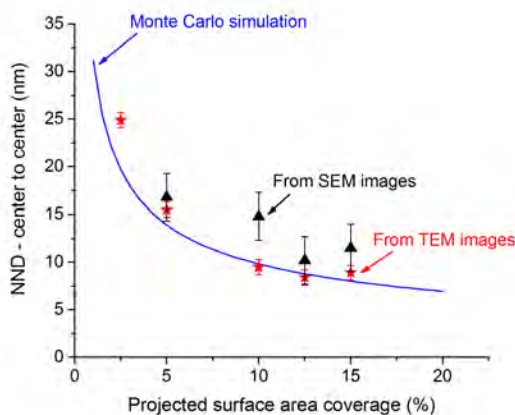


Figure 4.19: Average NND of 6.7 nm (950k amu) NiFe nanoparticles as a function of loading as determined from the analysis of multiple TEM and SEM images and by Monte Carlo simulation. A TEM grid was made with 2.5% loading to give an extra data point to compare the Monte Carlo simulation to. Error bars correspond to an error of 5 px in the microscopy images.

is smaller than determined for the 15% loading. This is most probably because of the inaccuracies the loadings or the inhomogeneity of our depositions. This is also underlined by the fact that the average number of particles on the TEM images made of the grid with 12.5% loading is higher than the average number of particles on the images recorded of the grids with 15% loading (Appendix B). For the following I will use the average distances determined from the TEM images.

4.5.4.2 Effect of the NND of the nanoparticles on the OER activity

Figure 4.20 shows the mass activity of 6.7 nm (950k amu) NiFe particles as a function of the average NND at two different overpotentials. There is a prevalent effect: as the particles are getting closer (in average), their activity is decreasing. The first idea which could explain this behaviour is mass transport limitation. As the particles are getting closer, faster and faster mass transport in the electrolyte is required to fully utilize their activity. Unfortunately, so far we do not have experimental evidence to elucidate whether this is what is happening or a different effect. There is a small issues with presenting our data like this. As Figure 4.18 shows, the placement of the particles are neither perfectly random, nor a 2D lattice, therefore using the average NND to present the data is not entirely correct. We are planning to model the activity of our electrodes by taking into account the actual distribution of the

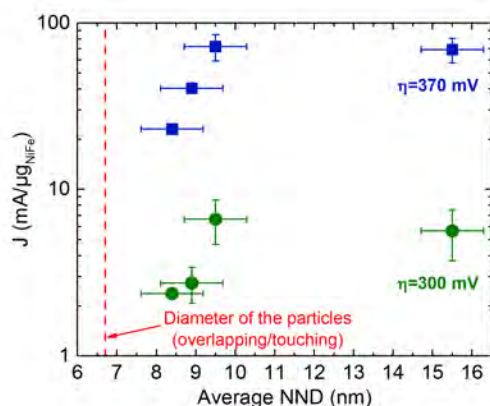


Figure 4.20: Mass activity of 6.7 nm (950k amu) NiFe nanoparticles as a function of the average NND at 300 mV and at 370 mV overpotential. The particles are getting less active as the average distance between them decreases. Please note, that the x-axis depicts the center-to-center distance of the particles, thus two particles touching would be at 6.7 nm on this axis. Errorbars in the distance correspond to an error of 5 px on the TEM images.

particle positions determined from the microscopy images in the near future.

As Figure 4.14 shows, making the size dependence study (Section 4.5.2) with a lower projected surface area loading would have increased the measured TOF of the particles. On the other hand, the increase is not an order of magnitude, thus the comparison to TOF values from literature (Figure 4.14) would not change significantly.

4.6 Summary

During this study we managed to investigate the effect of particle size and particle-particle proximity on the OER activity of NiFe mass-selected nanoparticles. The Fe content of the nanoparticles as a result of electrochemical testing got close to the same value, thus the results for the different sizes were readily comparable. As it turned out, the Fe concentration we measured with XPS after EC measurement (approx. 15%) is very close to the ideal value reported in the literature [93, 94].

At the time of writing this (March, 2017) we are planing identical location HRTEM imaging of the particles before and after oxidizing them in 1 M KOH (Elisabetta Fiordaliso, DTU CEN). We already have glancing angle XRD data measured on NiFe particles before and after oxidizing them in 1 M KOH awaiting data treatment. We are

also planning some other experiments to further elucidate the way NiFe nanoparticles behave under OER conditions. There are also simulations planned to investigate the effect of the particle-particle distances further, while taking into account the actual distribution of the particle positions determined from the microscopy images. Nevertheless, the results contained in this chapter are already being written up into a paper draft and I hope to achieve a publishable version with all the data in the near future.

4.6.1 Note on TiO₂ protected Si photoabsorbers with nanoparticulate catalyst as photoanodes for water-splitting

One question arises: why were the NiFe particles not tested as photocatalysts on the TiO₂ protected Si photoabsorber to make a similar study as with the Pt particles in Chapter 3? Sadly, the TiO₂ protected Si photoabsorber approach is not working in case of photoanodes with nanoparticulate catalysts. The reason for this is a pinch-off effect, which creates unfavourable band bending at the TiO₂-electrolyte interface making the conduction of electrons from the catalyst to the conduction band of TiO₂ difficult. This issue is not the case with thin film catalysts. In that case, the electrolyte is not in contact with the TiO₂ layer. On the other hand, thin film catalyst significantly decrease the efficiency of the photoabsorber with their reflectivity. Detailed investigation of the band structure and the effect of catalysts in different forms (nanoparticles, μm scale islands, thin film) on the behaviour of TiO₂ protected doped Si photoabsorbers can be found in [112].

CHAPTER 5

Investigation of gas phase heterogeneous catalytic reactions in μ -reactors using mass-selected nanoparticles

During my three years in the laboratory at DTU I have participated in multiple projects concerning heterogeneous catalytic reactions for which we used the μ -reactor platform developed in our laboratory earlier and outlined in Section 2.2. I would like to describe two of these projects, in which I had a major role. During the projects we discovered practical issues with the μ -reactors (temperature measurement and control and our depositions), which are also shown in this chapter (Section 5.3).

During these projects Jakob Nordheim Riedel played an important role, he handled the activity measurements and I was mainly responsible for the production and physical characterization of the samples. As a result of this, figures containing activity measurement data of the NiFe bimetallic nanoparticles are reproduced from his thesis which he handed in at DTU in 2016 and some of the characterization results made by me were already included in his thesis as well [113]. Elisabetta Fiordaliso (DTU CEN) helped us with identical location SEM measurements. In case of the AuTi bimetallic nanoparticles, we collaborated with the Nanoscale Physics Research Laboratory (NPRL) at the School of Physics and Astronomy of the University of Birmingham (UoB) and the Department of Material Science at the University of Milano-Bicocca

(UNIMIB) as part of the CATSENSE ITN. We produced the samples together with Yubiao Niu (NPRL) during my external stays at NPRL. Yubiao conducted the STEM investigations at NPRL and visited DTU as his external stay where we made the XPS, ISS and activity measurements together with the help of Jakob Riedel. Philomena Schlexer (UNIMIB) made DFT calculations supporting the experimental results. I would also like to mention Niels Dyreborg Nielsen (DTU SurfCat) who had worked as part of a special project under my supervision and whose main task was to investigate the reproducibility of the μ -reactors. He had a major role in discovering the issues discussed in Section 5.3.

SEM images taken during the projects can have different contrasts depending on the amount of contaminants on the surface of the samples. The contaminants are mainly carbonaceous material cracked to the surface by the electron beam. In order to make features visible in printing I used gamma correction on the images to make the contrast and brightness higher where it was necessary.

Note: I am presenting all the data as we gathered them at the time of the measurements, unaware of the problems with temperature measurement and reproducibility discovered later, in order to convey the story of these investigations. I will underline which results are compromised along the way.

5.1 AuTi bimetallic mass-selected nanoparticles for CO oxidation

Au is one of the most famous materials, when one would like to illustrate size-effects in catalysis and the importance of nanoparticulate material research in scope of catalysis. Macroscopic Au is considered the most stable and chemically inert metal ("The noblest of all metals") [114]. It is quite interesting that even though Au is extremely inert and does not adsorb molecules or atoms at a gas-metal or liquid-metal interface, it readily forms alloys and intermetallic compounds with other metals [114]. Even though the inertness of macroscopic Au, there is a report already from 1906 stating that a hot Au mesh can facilitate the combination of O_2 and H_2 [115] which refers to even earlier works from 1823 (written in French). There is also a report already from 1925 that Au is capable of catalysing the oxidation of CO to CO_2 [116]. Nevertheless, as Au is fairly expensive and the reported reaction rates were lower compared to other metals, Au was not considered as a catalyst up until the groundbreaking work of Haruta and co-workers [117]. They found that metal oxide supported Au nanoparticles are capable of effectively catalysing the oxidation of CO even at $-70^\circ C$. After this result was published, there was a huge uprising of studies on nanoparticulate Au catalysts and numerous articles were published on the matter. An exhaustive review of the properties of Au and catalysis on Au was written by Bond and co-workers in 1999 [118]. Au seems to be able to catalyse a multitude of reactions, but here I

will concentrate on CO oxidation, because it is one of the simplest reaction gold can catalyse and CO is a frequently used probing molecule of surface science.

In their study Hvolbæk and co-workers compiled the experimental results of the CO oxidation activity of Au nanoparticles on different supports as a function of the particle size [119]. They collected the experimental results of numerous groups and studies into a figure illustrating how Au in the nanometer size regime becomes active for the CO oxidation reaction (Figure 5.1). The main conclusion is that Au particles are only active below about 5 nm diameter and they are getting more active as the size decreases. This effect is more pronounced than the dependence of the activity on the support material. Several explanation were proposed for the source of the activity of Au nanoparticles and its support dependence [119], among others charge transfer to and from the support, support induced strain or oxygen spill-over to and from the support. As the μ -reactors are made of Si, they present a SiO_2 support and based on Figure 5.1 this means, that Au particles should not be very active for CO oxidation regardless of their size.

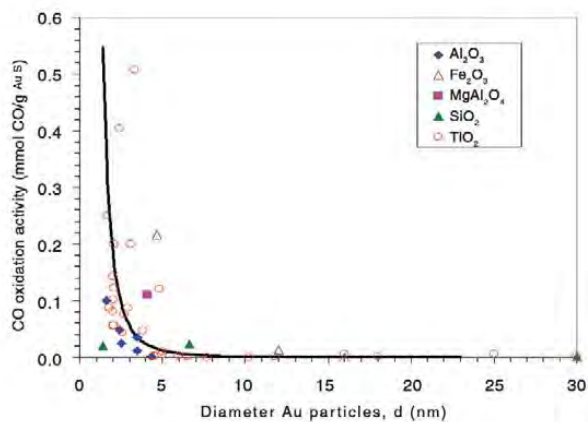


Figure 5.1: CO oxidation activity of Au nanoparticles on different substrates as a function of their size. Adapted from [119–121].

An issue hindering the use of Au particles is their rapid sintering. It has been shown that Au atoms are mobile and can migrate to form 3D islands on a TiO_2 surface even at 150–160 K [122, 123]. Based on the work of Yang and co-workers [124], on TiO_2 Au clusters sinter by Ostwald ripening between 300 K and 410 K and the sintering is accelerated by a mixture of CO and O_2 present. There are fewer studies on the behaviour of Au on SiO_2 , most probably because of the lack of catalytic activity. Nevertheless, Au growth on thin SiO_2 was studied earlier and it was found, that Au clusters preferentially occupy different defects on surface of SiO_2 [125]. An interesting study by Wallace and co-workers reports that the addition of TiO_x on a SiO_2 surface stabilizes Au clusters and dramatically decreases the sintering rate of

them [126].

In summary, if we could find a way to stabilize small Au species on a surface and provide them with the required metal-support interaction (regardless of the actual mechanism), we might be able to create a highly active CO oxidation catalyst and open-up the possibility to Au catalysis. A possibility to achieve this is to deposit AuTi bimetallic nanoparticles into μ -reactors. Ti will most likely segregate to the surface of the particles under CO oxidation conditions and hopefully it will phase separate and form TiO_x islands anchoring the Au nanoparticles to the SiO_2 surface. Or we might end up with small Au species on a TiO_x island on a SiO_2 support.

5.1.1 Deposition of mass-selected AuTi bimetallic nanoparticles

Mass-selected nanoparticles were deposited at the UoB using a similar nanoparticle source to the one described in Section 2.1.2. The differences between the two sources are the base pressure (the one at UoB has a base pressure of around 10^{-8} mbar), slightly different magnetron head design and the fact that positively charged particles were used for the depositions. Au_{2057} and 400k amu AuTi nanoparticles were deposited sputtering an Au or a 50 at% Au / 50 at% Ti target (both are from PI-KEM Ltd., 99.99%). The 400k amu mass was chosen as it is similar to the mass of Au_{2057} (approx. 405k amu). The particles were landed using a kinetic energy of approx. 0.5 eV/atom (1000 V on the substrate).

Both μ -reactors (Section 2.2) and Cu TEM grids with suspended SiO_x layers (EMS, USA) were deposited under the same conditions. Before deposition the μ -reactors were sputtered by an Ar^+ beam from the nanoparticle source, with a beam current of approx. 1 nA for 500 s (1000 eV Ar^+) in order to clean the surface and create defects to act as anchor points for the particles. With AuTi particles both sputtered and unsputtered TEM grids were made and with Au particles only unsputtered ones. As the beam of nanoparticles at UoB is smaller than the 4 mm (TEM grids) or the 10 mm (μ -reactors) aperture used for the deposition, the substrates were physically rastered (moved) during deposition to produce a homogeneous distribution of particles. The loadings of the μ -reactors were kept at 10% projected surface area coverage (Appendix B). The deposited TEM grids were investigated at UoB with an aberration corrected JEOL 2100F transmission electron microscope operated in HAADF-STEM mode at 200 kV electron energy. The μ -reactors were transported back to DTU and most of them were characterized with XPS, ISS and SEM, cold bonded, tested in the μ -reactor setup, opened and characterized again. As the experiments progressed, in case of some of the reactors one or two steps were skipped in the process.

5.1.2 STEM investigation of the deposited nanoparticles

As the STEM investigation was not performed by me and it will be a significant part of the PhD thesis of Yubiao Niu (UoB), only a brief report is given here to show how the particles looked like. Figure 5.2 shows representative HAADF-STEM images of

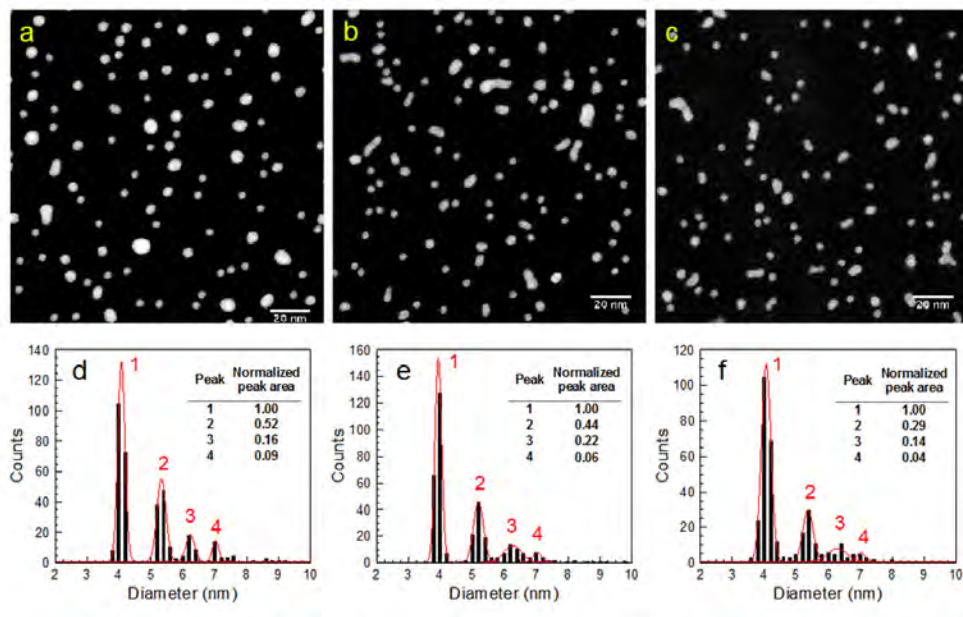


Figure 5.2: Representative HAADF-STEM images of Au₂₀₅₇ (unspun TEM grid) and 400k amu AuTi (without and with Ar⁺ sputtering of the TEM grid) nanoparticles on SiO_x along with their size distributions. a&d: Au₂₀₅₇ particles (unspun grid); b&e: 400k amu AuTi particles (unspun grid) and c&f: 400k amu AuTi particles deposited on an Ar⁺ sputtered grid. Figure courtesy of Yubiao Niu (UoB, NPRL).

the different samples along with their size-distributions. During the depositions care was taken to avoid double mass-double charge particles (Appendix B). As expected from the high mobility and weak bonding of Au atoms / particles, the Au particles sinter strongly and form bigger agglomerates. In case of the AuTi particles the effect is less pronounced, especially in case of the TEM grid which was Ar⁺ sputtered before deposition. The differences between the sputtered and unspun substrates could be the topic of a complete new study along with the characterization of the induced defects, which we have not pursued.

Investigating the sintering of the Au and AuTi nanoparticles on unspun SiO_x TEM grids under electron irradiation (Figure 5.3) shows that alloying with Ti slows down the sintering process significantly. If the AuTi particles are further apart and no "bridge" can be formed by mobile atoms, they will not coalesce (Figure 5.4). This reduced sintering effect is also supported by DFT calculations on small Au and AuTi clusters on silica surfaces made by Philomena Schlexer (UNIMIB).

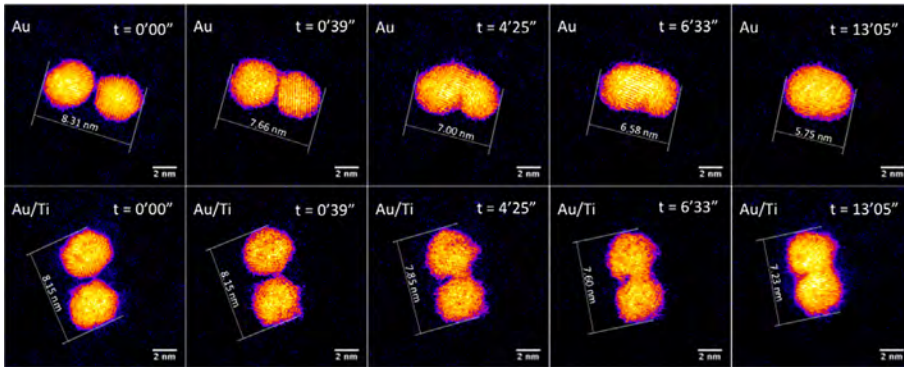


Figure 5.3: Sequential HAADF-STEM images of Au and AuTi dimers sintering under electron irradiation on unspun SiO_x . Notice the "bridge" between the AuTi nanoparticles. Figure courtesy of Yubiao Niu (UoB, NPRL).

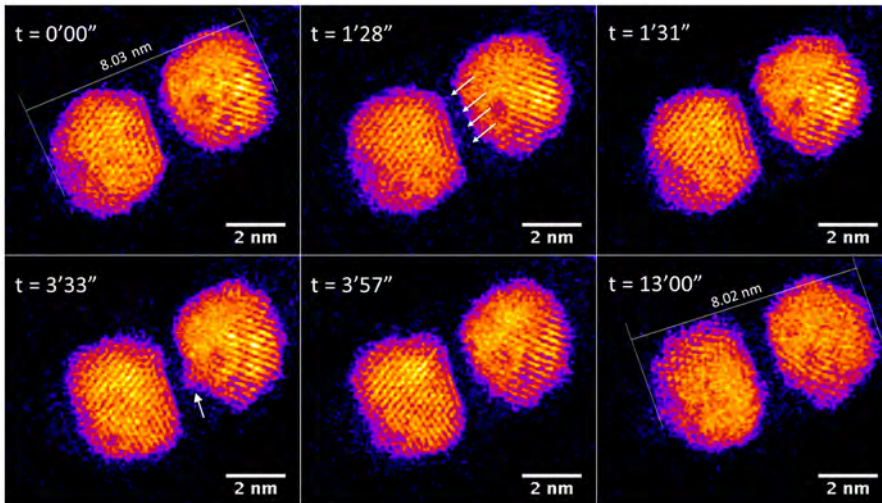


Figure 5.4: Sequential HAADF-STEM images of AuTi dimers further apart under electron irradiation on unspun SiO_x . Notice the lack of "bridge" between the particles as they are too far apart for the atoms to form one. Figure courtesy of Yubiao Niu (UoB, NPRL).

5.1.3 Investigation of the activity of the samples in μ -reactors and their characterization with XPS, SEM and ISS

All the μ -reactors used to investigate the activity of the particles were sputtered before deposition using the Ar^+ beam from the nanoparticle source as described earlier. In order to try and limit the contamination of the reactor chambers during transport to DTU, pyrex lids were placed on them right after taking them out of the deposition chamber at UoB and they were wrapped in aluminium foil so the lids would stay in place. Even though they were not bonded, it can be assumed that the lid is closing the reactor chamber relatively tight, at least it is completely shielding it from dust or mechanical effects (scraping off the particles for example). As the following section will show, the first reactor with AuTi particles we tested showed a CO oxidation activity which we could not reproduce even though we tried with numerous samples. As a result we decided to make a sintering study. This also ended with inconclusive results with the μ -reactors, but it taught us how to handle the μ -reactors, especially how to open them safely and gave best practices which are described in the PhD thesis of Jakob Riedel [113] (and in Section 2.2) and which have already been used in other projects. At the time we did not understand why the experiments are not working out with the relatively straightforward sintering study and why our results were completely inconclusive. A possible explanation will be given in Section 5.3 as we discovered problems with the temperature measurement and control of the μ -reactors.

5.1.3.1 Activity measurements using the μ -reactors

After their arrival to DTU, the μ -reactors were characterized with XPS, ISS and SEM, they were cold bonded (Section 2.2.2) and mounted in the μ -reactor setup [113]. This process was maintained, except for the activity test of the first AuTi reactor as we wanted to see in advance whether it shows any activity or not, so we recorded no XPS or ISS spectrum before testing it. The initial tests were run with temperature ramps between room temperature and 100°C under a gas mixture of $\text{O}_2:\text{CO}=4:1$ with a total pressure of 1 bar. In order to follow the activity of the samples the CO_2 ($m/z=44$) signal was recorded with the QMS. The figures contained in this section show this signal with a background subtracted. The background subtraction was necessary, as the flow of O_2 creates CO_2 in the QMS itself on the heated filament used for the ionization of the gases. Therefore the background subtracted contained a constant part (the background of CO_2 in the mass filter) and a part which is proportional to the O_2 signal. The proportionality factor was determined at room temperature using the QMS signals after the gas flows stabilized, before the first heating ramp was started.

The only reactor showing activity was the very first one installed to the μ -reactor setup with 400k amu AuTi particles, where we did not have SEM images, XPS or ISS spectrum before activity testing. It showed initial activity and deactivation with the temperature ramps (Figure 5.5). During the course of the following almost a year, none of the approx. 25 μ -reactors tested showed any activity. Figure 5.6/A shows an

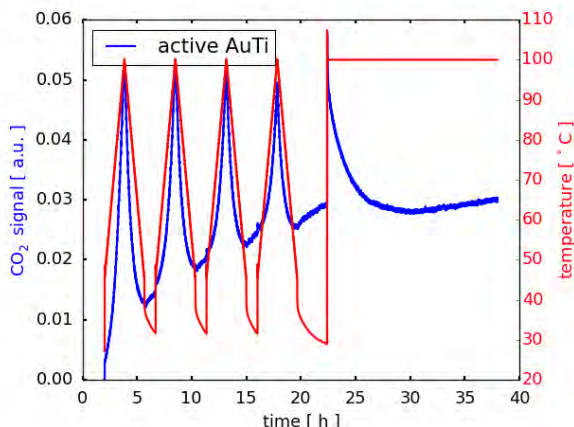


Figure 5.5: The very first μ -reactor tested with 400k amu AuTi nanoparticles showing CO oxidation activity and deactivation below 100°C (1 bar, $O_2:CO=4:1$). A background was subtracted from the CO_2 (44 amu) signal, consisting of a constant and a part proportional to the O_2 signal. Figure courtesy of Jakob Riedel.

example for a μ -reactor with Au_{2057} particles showing no activity as expected from SiO_2 supported Au particles. We tried running experiments at higher temperature (150°C) with μ -reactors containing 400k amu AuTi particles without any success (an example is shown in Figure 5.6/B) and also empty reactors to try and find the source of the initial activity (Figure 5.6/C). A few of the tested empty reactors produced some CO_2 signal at 150°C which was also not reproducible and might have been dependent on the Si wafer the particular reactor has been made of. And these signals were a lot lower, than the signal from the first reactor (Figure 5.5).

5.1.3.2 SEM characterization of the μ -reactors before and after activity testing

As the aim of the project was to prove that we can stabilize small Au species on the surface of the μ -reactors while having catalytic activity, most of the μ -reactors were imaged by SEM before and after testing. Our plan was to make SEM images and show the difference between the sintering of the particles. As the project proceeded and more and more odd results were collected, in case of some of the μ -reactors we did not acquire (identical location) SEM images. Here I would like to show some of our results to convey the puzzlement we felt during the project.

We started out by running temperature ramps during testing as depicted in Figures 5.5 and 5.6. Based on SEM images the Au_{2057} particles seem to sinter already at room temperature without heating, which gets worse with the temperature ramps to 100 °C (Figure 5.7). Figure 5.8 shows SEM images of μ -reactors with 400k amu AuTi

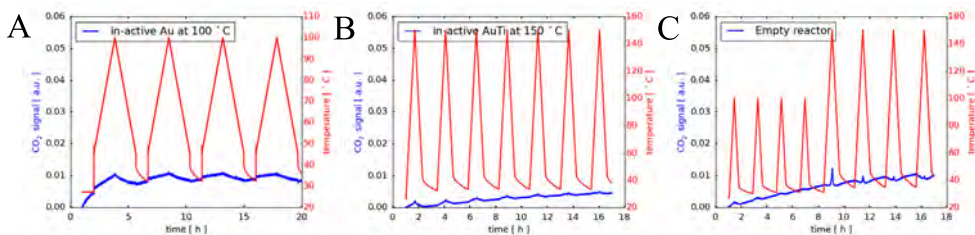


Figure 5.6: Examples of CO oxidation activity measurements with μ -reactors containing Au₂₀₅₇ and 400k amu AuTi nanoparticles as well as the result of running the same test with an empty μ -reactor. A: μ -reactor containing Au₂₀₅₇ particles; B: μ -reactor containing 400k amu AuTi particles and C: empty μ -reactor running a similar flow and temperature program. A background was subtracted from the CO₂ (44 amu) signal, consisting of a constant and a part proportional to the O₂ signal. Figure courtesy of Jakob Riedel.

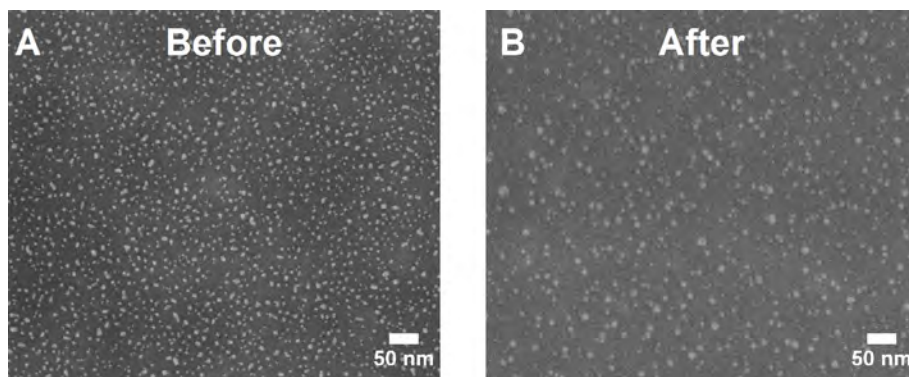


Figure 5.7: SEM images of Au₂₀₅₇ particles in a μ -reactor before testing (A) and after testing (B) with temperature ramps to 100°C. Note that the images are not from the same reactor. Images courtesy of Elisabetta Fiordaliso (DTU CEN).

particles which have undergone testing with temperature ramps to 100°C (Figure 5.8 A&B) and to 150°C (Figure 5.8 C&D). The particles heated to 150°C sinter strongly, while the particles tested at 100°C remain relatively stable as also shown by the size distributions determined from the SEM images (Figure 5.9) by similar methods as described in Appendix D.

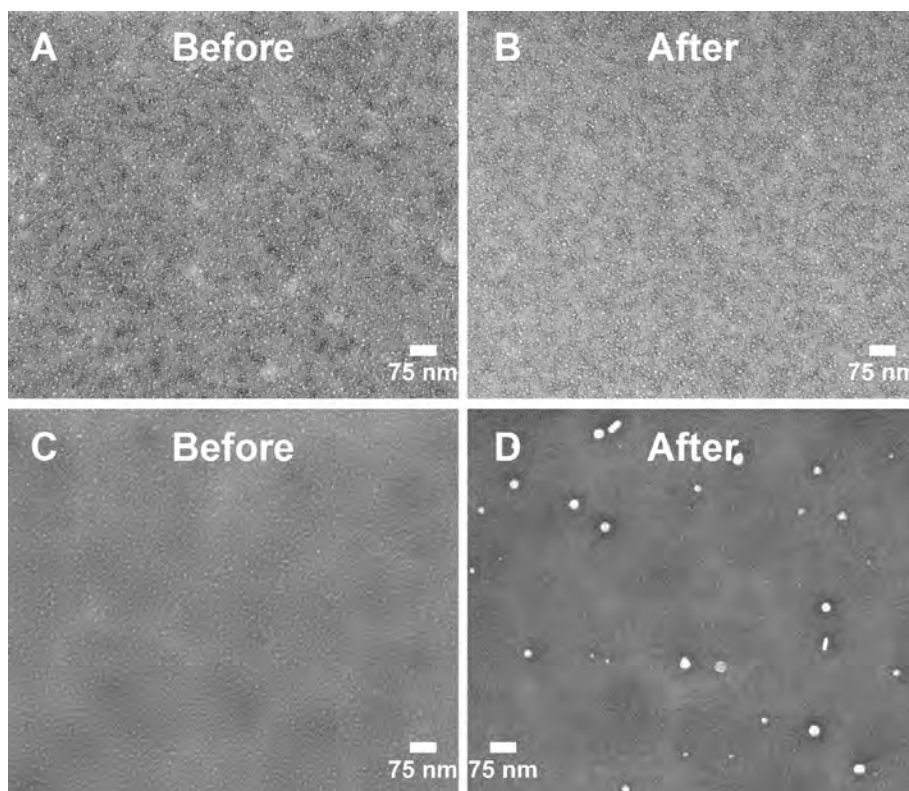


Figure 5.8: Representative SEM images of 400k amu AuTi nanoparticles in μ -reactors before testing and after testing with temperature ramps to 100°C and 150°C. A&B: Before and after 100°C ramps and C&D: Before and after 150°C ramps. Images courtesy of Elisabetta Fiordaliso (DTU CEN).

The particles behaved as we expected regarding their sintering, but we could not find any activity even though there was clearly Au on the surface of the reactors even after testing (see in Section 5.1.3.3). Therefore, we decided to make a sintering study under CO oxidation conditions (1 bar, $O_2:CO=4:1$) and changed the temperature profile to a constant 100°C for 1 h instead of the temperature ramps. We hoped to see the Au particles sintering as seen before under milder conditions (Figure 5.7) and

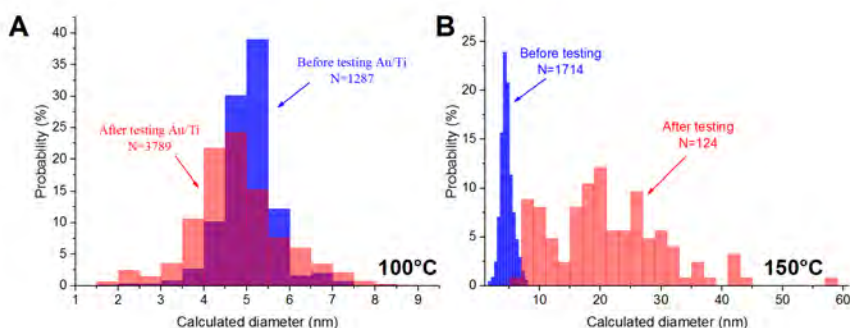


Figure 5.9: Size-distributions of 400k amu AuTi particles deposited on μ -reactors before and after CO oxidation activity testing with temperature ramps to 100°C (A) and 150°C (B).

the AuTi particles staying stable. Instead what happened is exactly the opposite (Figure 5.10). The Au particles seemed to have stayed stable (Figure 5.10 A&B) and the AuTi particles developed odd, relatively big features (Figure 5.10 C&D). At the time we were completely puzzled by the results. However, in hindsight some of the later revelations made this behaviour understandable, as the temperature measurement and control turned out to be unreliable (Section 5.3). We also found different odd features with SEM which seemed contaminants we did not come across later during the project with the NiFe nanoparticles. I can only ascribe them to different contaminants, because at the UoB we were not able to clean the reactors as thoroughly as at DTU and they were not bonded immediately after taking them out of the vacuum chamber.

5.1.3.3 XPS and ISS characterization of the Au and AuTi nanoparticles in the μ -reactors before and after CO oxidation activity test

In order to investigate the composition of the particles and to check for contaminants in the μ -reactors, XPS spectra were recorded of the μ -reactors with Au₂₀₅₇ and 400k amu AuTi particles before and after 1 h at 100°C (examples are shown in Figure 5.11). The XPS spectra show significant C 1s peaks, which are most probably due to exposure to air. No other contaminants could be detected. Based on the XPS spectra, the Au:Ti ratio of the 400k amu AuTi particles after receiving them was approx. 60:40, which changed to approx. 40:60 after heating. This could be an indication of a segregation process. However, because the sintering behaviour proved inconsistent, we did not make any further investigation of this process.

Example ISS spectra recorded in case of the same μ -reactors are shown in Figure 5.12. In order to investigate the immediate surface of the samples, the first

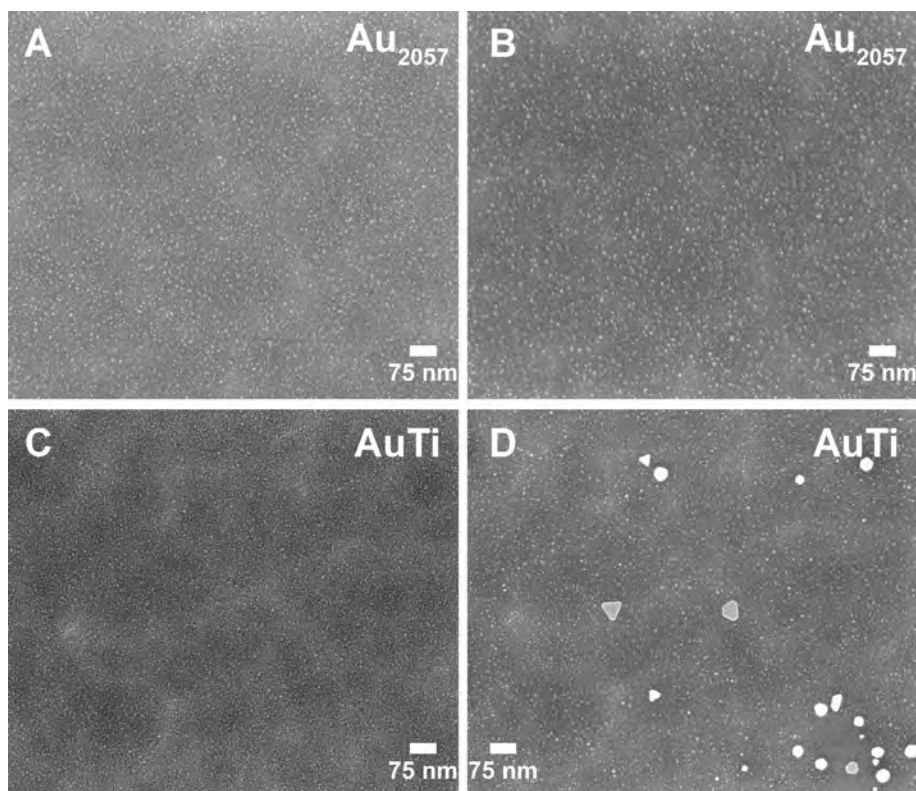


Figure 5.10: Identical location SEM images of Au and AuTi nanoparticles in μ -reactors after heating them to 100°C for 1 h under CO oxidation conditions (1 bar, O₂:CO=4:1). A&B: Au₂₀₅₇ particles before (A) and after (B) heating; C&D: 400k amu AuTi particles before (C) and after (D) heating. Images courtesy of Elisabetta Fiordaliso (DTU CEN).

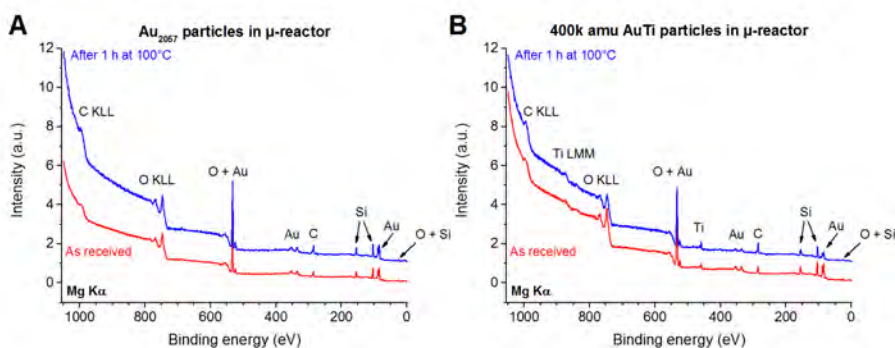


Figure 5.11: XPS spectra of μ -reactors with Au_{2057} and 400k amu AuTi nanoparticles before and after 1 h at 100°C under CO oxidation conditions (1 bar, $\text{O}_2:\text{CO}=4:1$). Spectra were shifted to give an Au $4f_{7/2}$ binding energy of 84 eV and were normalized with the area of the Si 2s peak. The plots were offset in y direction for better visibility. Same μ -reactors whose ISS spectra are depicted in Figure 5.12. A: Au_{2057} and B: 400k amu AuTi particles in μ -reactors.

spectra recorded (minimum sputtering time) are shown. In case of the μ -reactor with Au_{2057} nanoparticles deposited, the relative amount of carbonaceous contaminants (shoulder below the O peak) increase after testing, thus covering some of the Si and Au (Figure 5.12/A). The spectrum of AuTi particles after testing (Figure 5.12/B) shows relatively high amount of carbonaceous contaminants, but a small Au peak is still visible, indicating that there are Au atoms on the immediate surface. Carbon contamination is also diminishing the Si and Ti signals almost entirely. With increasing sputtering time, as the carbon contaminants are sputtered away, both the Si, Ti and Au signals were found to be increasing.

Figure 5.13 shows the ISS spectrum recorded in case of the μ -reactor with 400k amu AuTi nanoparticles which showed CO oxidation activity below 100°C (Figure 5.5). The spectrum depicts the first ISS scan taken and it was recorded after testing. Based on Figure 5.13 there are Au atoms on the surface after testing, thus Ti is not forming a complete TiO_x shell around an Au core. Together with the STEM results this indicates that by alloying Au with some metal forming an anchor, it might be possible to create active and stable Au catalysts.

The contaminations found on the surface with ISS might have been there initially or might have gotten to the surface while opening the reactor. This was one of the first reactors we opened after testing and we were still learning how to do it properly (Section 2.2.2). The Ba contamination (confirmed by XPS multiple occasions in

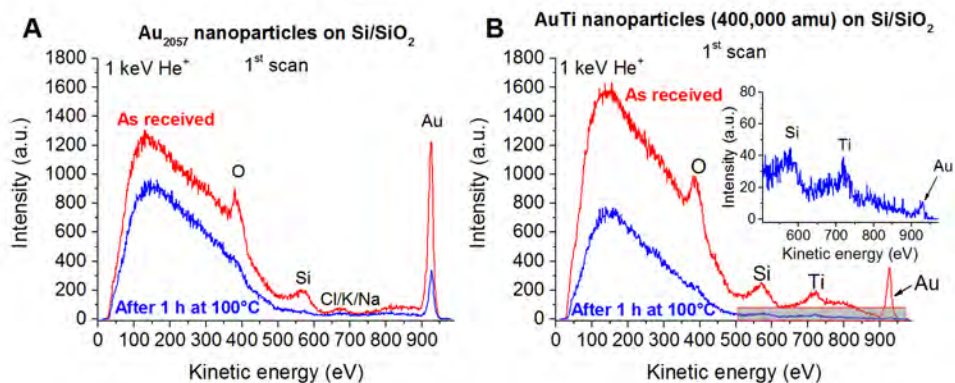


Figure 5.12: ISS spectra of μ -reactors with Au₂₀₅₇ and 400k amu AuTi nanoparticles before and after 1 h at 100°C under CO oxidation conditions (1 bar, O₂:CO=4:1). Same μ -reactors whose XPS spectra are depicted in Figure 5.11. A: Au₂₀₅₇ and B: 400k amu AuTi particles in μ -reactors.

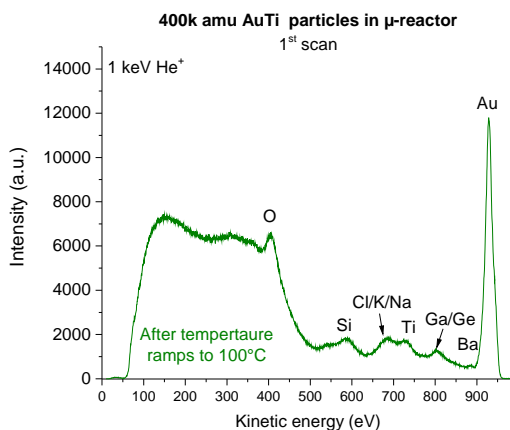


Figure 5.13: ISS spectrum recorded after activity test with temperature ramps to 100°C in case of the only μ -reactor with 400k amu AuTi nanoparticles which showed CO oxidation activity. It shows Au and Ti atoms on the surface along with different contaminants. Based on the spectrum Ti does not form a complete TiO_x shell around an Au core.

different μ -reactors, see details in Appendix F) present is a problem, which has been seen before in case of certain μ -reactors and was traced back to the clean room. Unfortunately, the role of Ba (or other contaminants) in the initial activity we have seen (Figure 5.5) cannot be ruled out.

5.1.4 Summary of the investigation of AuTi nanoparticles in μ -reactors

Even though the activity measurements during this project were not successful, the project gave us valuable information about the μ -reactors. Looking at the results it was clear, that we had to establish a way to clean the μ -reactors properly before depositions. This issue is explored in Appendix F. We also managed to come up with a clean, reproducible and safe way to open up the anodically bonded μ -reactors (Section 2.2.2). We also proved, that the idea of anchoring Au particles by an alloyed element to create more stable Au catalysts might work. This is underlined by the fact that there were Au atoms on the surface of the samples with AuTi nanoparticle-seven after activity testing based on the ISS spectra and the STEM results showed slower sintering. A manuscript is in preparation about the sintering investigation of the Au₂₀₅₇ and AuTi particles with STEM (Yubiao Niu, UoB), supported by DFT simulations of small Au and AuTi clusters on silica surfaces (Philomena Schlexer, UNIMIB) along with XPS and ISS characterization.

5.2 NiFe bimetallic mass-selected nanoparticles for the methanation reaction

This project was running parallel with the investigation of the oxygen evolution reaction on NiFe particles (Chapter 4). The particles for methanation were deposited onto μ -reactors from the same targets under the same conditions as the particles we used to investigate OER. We were planning to make both a gas phase heterogeneous model study of methanation and a study of OER with the same nanoparticles at the same time.

5.2.1 Introduction - methanation reaction in the gas phase on Ni and Ni alloy catalysts

The production of CH₄ from a mixture of CO and H₂ could be a viable option for turning renewable resources into a high energy density energy carrier, which has an established infrastructure and technology [127]. CO could be produced from biomass [128, 129] and H₂ could be produced by (photo)electrocatalytic water-splitting where the energy required comes from renewable sources [20, 71, 81].

5.2.1.1 Activity of transition metals as methanation reaction catalysts

The catalysts used for methanation in the industry is most often comprised of Ni based particles dispersed on an oxide support [127, 130]. Ni is a primary product of its ore and it is relatively cheap and abundant [64]. It has been investigated and optimised as a catalyst for over a 100 years [131]. The activity of Ni and other transition metals along with the kinetics of methanation were systematically investigated in the '70s [132–137]. These contain dedicated studies of the kinetics of methanation over Ni [136] and methanation activity of metals supported by silica [137]. Vannice in the '70s found a linear relationship between the methanation activity of metals and the heat of adsorption of CO on their surface, with the methanation activity being higher when the heat of adsorption is lower [134]. He also found in a later study that at conditions relevant for the μ -reactors (1 bar of pressure, temperatures below 300°C) and at a reactant ratio of $\text{H}_2:\text{CO}=3$ all of the investigated transition metals produced mainly methane [137]. In this study with updated heats of CO adsorption values he found a volcano shaped curve for the activity of the different metals. On silica support he published the following order for the activity of metals based on their turnover frequency (TOF): Co (most active), Ru, Fe, Ni and the order of the other metals inconsistent, depending on the method of determining the TOF [137]. A more recent DFT study showed that the activity descriptor is not the adsorption energy of molecular CO, but the dissociative adsorption energy of CO molecules on the surface [138]. The volcano curve attained is depicted in Figure 5.14 showing Ru and Co as the most active metals, followed by Ni and Fe. Based on Figure 5.14, alloys or intermetallic compounds of Ni and Fe have a possibility for a high methanation activity.

The formation of a highly active methanation catalyst by alloying Ni and Fe has been shown earlier both by DFT calculations [139] and experimentally [140]. These reports investigated the ideal composition of a bimetallic Fe-Ni methanation catalyst and it was found that both under industrial conditions below 300°C and under conditions relevant for the μ -reactors the ideal composition is FeNi_3 . All the Ni-Fe catalysts investigated in these studies show high activity and high selectivity towards methane.

During methanation the Boudard (or CO disproportionation) reaction (5.1) deposits carbon on the surface of the catalyst, effectively blocking it (coking). The kinetics of this process in the mixture of CO and H_2 has been extensively investigated in case of silica supported Ni particles [141, 142] and different Ni surfaces [11, 143]. The carbon formed by this process on the surface can be reacted off by heating the catalyst in O_2 or H_2 , also opening a way to characterize it based on the temperature required for its removal and determine its quantity [144].



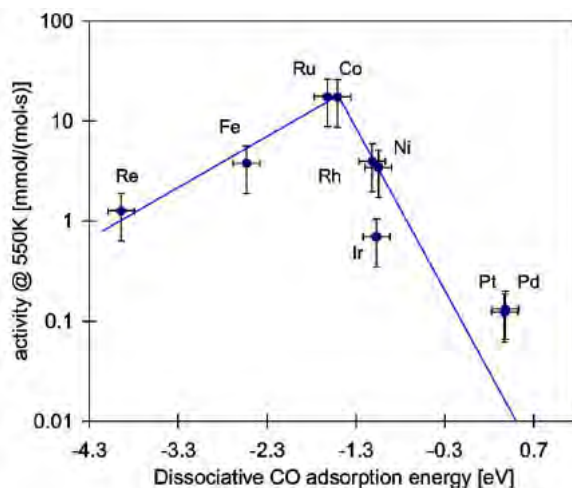


Figure 5.14: Volcano curve depicting the methanation activity of selected metals at 550 K in a flow reactor with 1% CO in H₂ as a function of the dissociative adsorption energy of CO calculated by DFT. Reprinted from [138].

5.2.2 Deposition of the particles

The NiFe particles were deposited in a similar way as described in Chapter 4. We deposited four different sizes of particles: 120k amu, 350k amu, 950k amu and 2 mil amu corresponding to 3.5 nm, 5 nm, 7 nm and 9 nm diameters assuming bulk density and spherical shape using the same 75 at% Ni and 25 at% Fe sputter targets (Kurt J. Lesker, 99.95%). The only differences between the depositions compared to the ones described in Chapter 4 were the aperture used (9 mm diameter instead of 4.5 mm) and the substrate (μ -reactors instead of Au stubs). Each μ -reactor deposited was thoroughly checked and cleaned according to the the following procedure (for further details see Appendix F). First the μ -reactors were sonicated in ethanol and thoroughly rinsed with mili-Q water (18.2M Ω cm resistivity). Both heater elements and the RTD were checked with a multimeter for breaks in the Pt layers. The etching of the channels were inspected by eye, to ensure that they are not blocked. After loading the reactor in the vacuum chamber, each one was sputtered for 40 min with 1 keV Ar⁺ to remove all carbonaceous contaminants and to create defects for anchoring the nanoparticles. The nanoparticles were deposited after these treatments through an aperture with a diameter of 9 mm to cover most of the reactor chamber. The loading of the reactors was 10% projected surface area coverage.

As the conditions of the depositions were the same as in case of the NiFe particles for OER, the size distribution of the particles is the same as shown in in Chapter 4 (Figure 4.3), determined from lacey carbon covered Cu TEM grids with bright field

TEM imaging.

5.2.3 Activity as a function of particle size

The cleaned, deposited and characterized (XPS, ISS) reactors were cold bonded (Section 2.2.2) immediately after they have been taken out of the vacuum chamber to minimize exposure to air and the chance of any contamination. The only exceptions were μ -reactors imaged with SEM before bonding. After bonding, the reactors were mounted for activity testing. First after the reactor was mounted and pumped down to vacuum, 1 bar of H_2 was let in the reactor and it was heated to 225°C . This was done to remove as much of the carbonaceous contaminants from the surface as possible according to the reaction: $C + H_2 \rightarrow CH_4$. After 10 min under H_2 at 225°C , the reactor was pumped down (still at 225°C) and flushed with 1 bar of Ar twice to remove all H_2 of the system. After the second Ar flush the reactor was pumped down and cooled down under vacuum. The practice of pumping H_2 out while the reactor is hot and flushing it with Ar twice helped to avoid H_2 remaining absorbed in the particles or rubber O-rings or adsorbed to the walls of the chamber. We used H_2 to clean the surface of the catalyst instead of O_2 , to avoid segregation of Fe to the surface of the catalyst and the formation of an FeO_x shell.

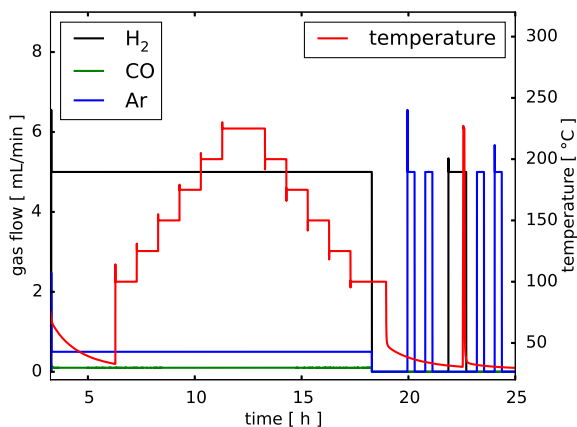


Figure 5.15: Gas flow and temperature profile used for testing the activity of NiFe mass-selected nanoparticles as model catalyst for the methanation reaction in μ -reactors. The total pressure in the μ -reactor during the gas-flows was 1 bar. This measurement block was repeated twice in order to test the stability of the catalyst. Figure courtesy of Jakob Riedel and it was reprinted from [113].

After the initial cleaning process, we ran two consecutive "methanation blocks"

depicted in Figure 5.15. After the μ -reactor had cooled down from the previous step (either the initial cleaning or the previous "methanation block"), H_2 , CO and Ar flows were started with a ratio of $\text{H}_2:\text{CO}:\text{Ar}=100:2:10$. A surplus of H_2 was added to decrease the coking of the catalyst. After the flows and the set pressure of 1 bar have stabilized a step-wise heating was initiated. The temperature was increased in the following steps lasting 1 h each: 100°C , 125°C , 150°C , 175°C , 200°C and 225°C . The last step at 225°C was held for 2 h to investigate the stability of the catalyst and the temperature steps were repeated cooling down the reactor. After the last step to 100°C , the reactor was pumped down to vacuum before cooling it down and it was flushed with Ar twice. After flushing with Ar, H_2 was reintroduced and the temperature was raised to 225°C with a ramp of $2^\circ\text{C}/\text{s}$ to conduct a H_2 temperature programmed reduction (H_2 -TPR) experiment. This was done in order to try and quantify the amount of carbon on the surface while at the same time removing it and reactivating the catalyst. It has to be stated here that we tried with multiple μ -reactors to conduct CO temperature programmed desorption (CO-TPD) and H_2 -TPR experiments without success. We were not able to produce reproducible and meaningful results with these techniques using the μ -reactors. Which in hindsight, knowing the issues with the RTDs we have discovered later (Section 5.3), is hardly surprising.

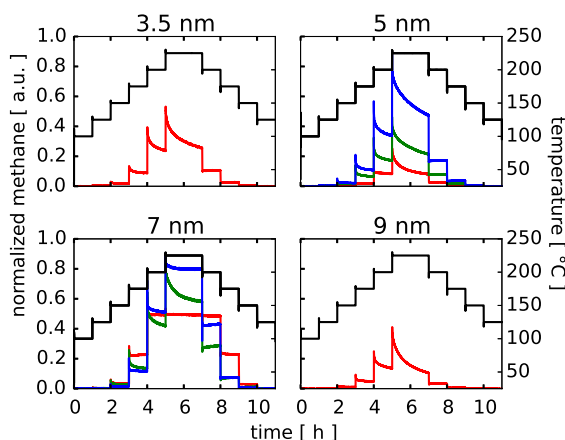


Figure 5.16: Methanation activity of NiFe mass-selected nanoparticles as measured with μ -reactors. The methane signals ($m/z=15$) were normalized with the H_2 ($m/z=2$) signals. The results are from the first methanation runs. The figure shows the sizes as calculated assuming spherical shape and bulk density. The different colours in each plot depict different μ -reactors deposited under identical conditions. The black curves indicate the temperature (shown on the right axis). Figure courtesy of Jakob Riedel and it was reprinted from [113].

Figure 5.16 shows the activity of the NiFe mass-selected nanoparticles as a function of size in the methanation reaction. The methane signals were normalized with the corresponding H_2 ($m/z=2$) signals to account for the temperature dependent flow through the capillary to the QMS (Section 2.2.1). The H_2 signal was used, as even though it is a reactant, the amount of H_2 converted was very low compared to the total amount H_2 (the reaction was run in surplus of H_2). As we tested multiple μ -reactors with 5.4 nm (350k amu) and 6.7 nm (950k amu) particles deposited using the same conditions, the figure also shows the poor reproducibility of our measurements. All the deposited μ -reactors had the same projected surface area coverage regardless of particle size. Therefore, the number of metal surface atoms in each reactor should have been approx. the same (assuming spherical particle shape) as described in Appendix B, making them directly comparable. Unfortunately, the Fe content of the particles is changing with the size as described in Section 4.4.3.2, therefore the possible effects are not just from the size or the structure, but most probably the changing Fe content too. Nevertheless, it seems that the most active size is approx. 7 nm (6.7 nm), but the reproducibility of the data is poor. The figure also shows that the particles are deactivating, indicated by the decreasing signal at constant temperature and the difference between the signals during ramping up and during ramping down the temperature. Comparing the methane signals from the first and second methanation block (Figure 5.17), it seems that some of the activity can be regained by reducing the catalyst in H_2 at 225°C between the methanation runs. Further details along with Arrhenius plots and apparent activation energies can be found in [113], but in light of later discoveries (Section 5.3) should be treated cautiously.

5.2.4 Physical characterization of the particles in the μ -reactors

The size-distribution of the particles and their Fe content determined from XPS (approx. 22-25 at% depending on the size) is assumed to be the same as discussed before in Section 4.4.3.2 (the Fe content was checked in case of multiple μ -reactors). As a consequence, I concentrate on the data unique to the μ -reactors and some of which led to a detailed investigation of the reproducibility of our μ -reactors described in Section 5.3.

5.2.4.1 Identical location SEM imaging before and after methanation activity tests

In order to check whether the particles are sintering or not, some of the μ -reactors were imaged with SEM before bonding and after testing and opening them. The smallest (120k amu, 3.9 nm) particles were not possible to image with SEM, thus we do not have images of a μ -reactor containing them. Figure 5.18 shows example identical location SEM images before and after testing in case of μ -reactors with 5.4 nm (350k amu), 6.7 nm (950k amu) and 8.4 nm (2 mil amu) NiFe particles deposited.

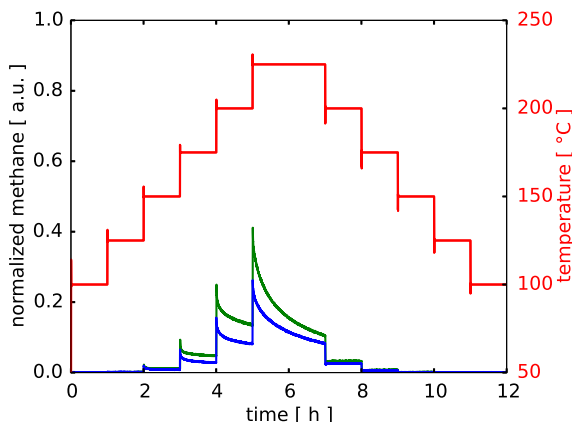


Figure 5.17: Effect of the reduction (1 bar H_2 , 225°C) between methanation runs on the activity of the NiFe mass-selected nanoparticles. Signals from the same μ -reactor containing 8.4 nm (2 mil amu) NiFe nanoparticles recorded in the first (green) and second (blue) methanation run. The methane signal ($m/z=15$) was normalized with the H_2 ($m/z=2$) signal. The red curve depicts the temperature shown on the right axis. Figure courtesy of Jakob Riedel and it was reprinted from [113].

Based on the images, the particles seem relatively stable on the surface under the methanation conditions.

5.2.4.2 ISS and XPS characterization of the deposited particles

Figure 5.19 shows XPS survey spectra and detailed spectra of the Ni $2p_{3/2}$ region of the same μ -reactor after deposition of 6.7 nm (950k amu) NiFe nanoparticles (without breaking the vacuum) and after activity testing and opening the μ -reactor. As expected, the amount of carbonaceous contaminants increased significantly as a result of exposure to air and catalytic testing. After deposition the Ni was in a metallic binding state, which changed to a mixture of $\text{Ni}(\text{OH})_2$ and Ni/NiO. This is in agreement with the oxidation behaviour of Ni described in Section 4.4.3.3. The slight difference between binding energy for metallic Ni from the literature and the measured peak energy might be a result of using the relatively broad Si 2p peak to compensate for charging in the spectra.

After plotting the ISS spectra recorded after deposition in case of μ -reactors containing different sizes of NiFe nanoparticles (Figure 5.20) an interesting phenomenon can be discovered. Samples which are supposed to be identical can have significantly different ISS signals (and also activity as shown in Figure 5.16). As ISS is almost exclusively sensitive to the surface, a signal which is proportional to the number of

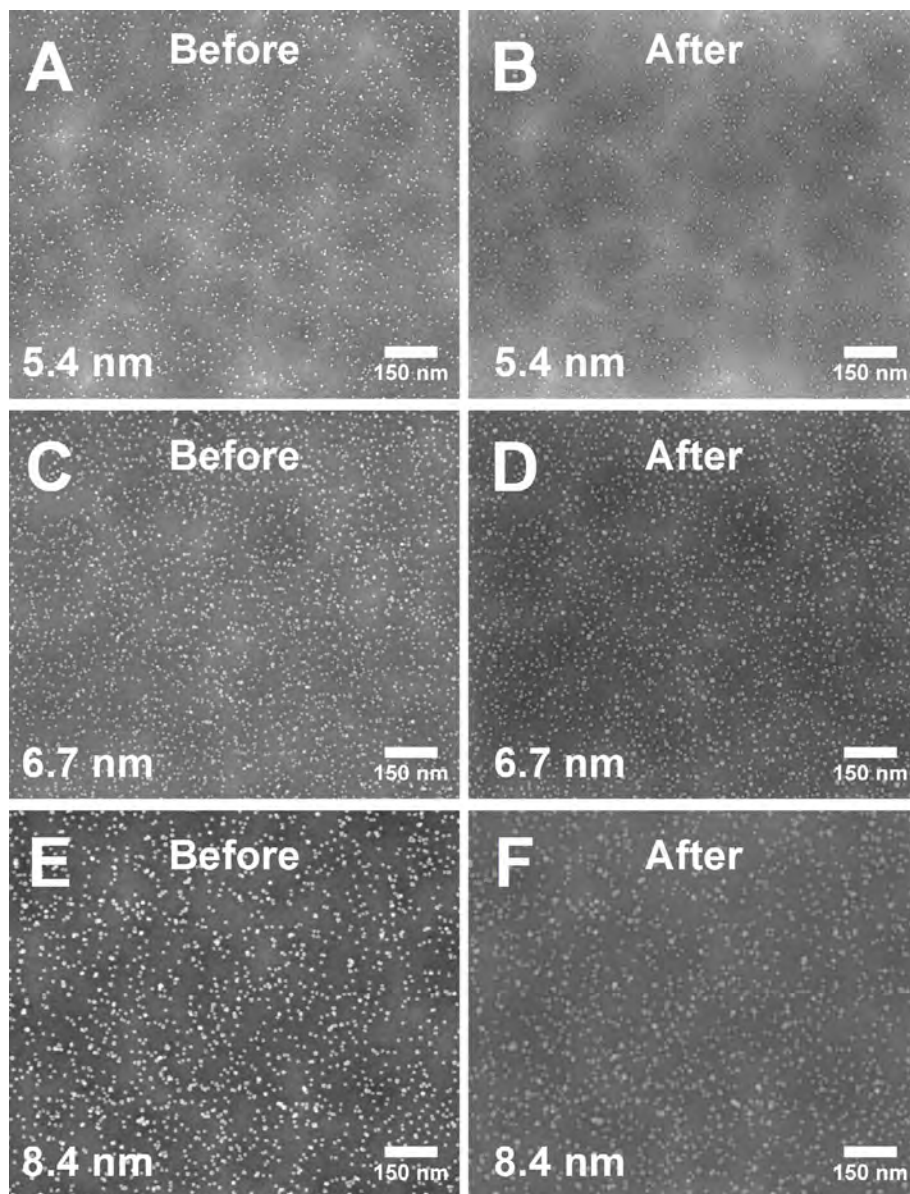


Figure 5.18: Identical location SEM images of NiFe mass-selected nanoparticles having different mass deposited into μ -reactors before (A&C&E) and after (B&D&F) methanation activity testing. A&B: 5.4 nm (350k amu); C&D: 6.7 nm (950k amu) and E&F: 8.4 nm (2mil amu). Images courtesy of Elisabetta Fiordaliso.

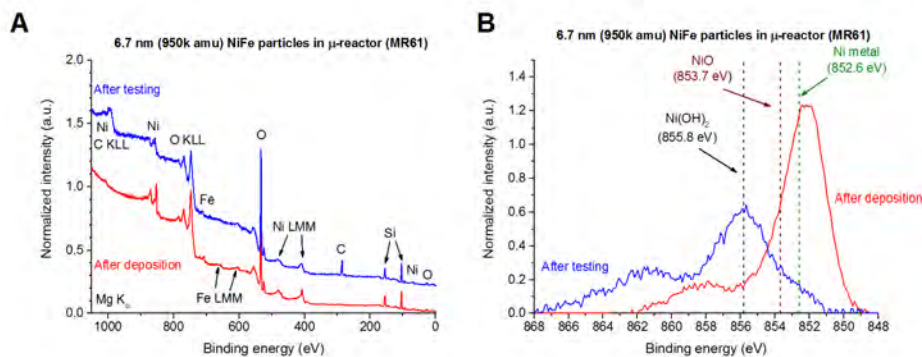


Figure 5.19: XPS survey and Ni 2p_{3/2} detailed spectra of the same μ -reactor containing 6.7 nm (950k amu) NiFe mass-selected nanoparticles after deposition and after methanation activity testing. The spectra were shifted to give a Si 2p binding energy of 103.4 eV [23] and normalized with the area of the Si 2p peak. A: Survey spectra (the spectrum after testing was offset in y direction for ease of viewing); B: Detailed spectra of the Ni 2p_{3/2} region after the subtractions of Shirley-backgrounds.

surface Ni&Fe atoms was expected. That would mean that regardless of the particle size or sample, the Ni&Fe peak should be around the same compared to the Si peak as the projected surface area coverage of the samples was the same. This is the case with the samples deposited under identical conditions for the OER study, where the Ni&Fe peaks in the ISS spectra are roughly the same in case of the different sizes and samples (Figure 4.4). In order to investigate this further, in Figure 5.21 I have plotted the detailed Ni 2p_{3/2} XPS spectra, normalized with the corresponding Si 2p peak areas, recorded after deposition of the samples, whose activity is shown in Figure 5.16. The XPS signals do not correlate with the ISS signals, there are differences between the relative peak areas measured. For example MR60 and MR65 have the smallest XPS peaks for Ni, but with ISS MR65 has a relatively high signal while MR60 has a low signal. This could be caused by for example different Fe contents, aiming differently with the XPS and ISS in the chamber or different deposited metal loadings. A systematic investigation of this effect is shown in Section 5.3.1.

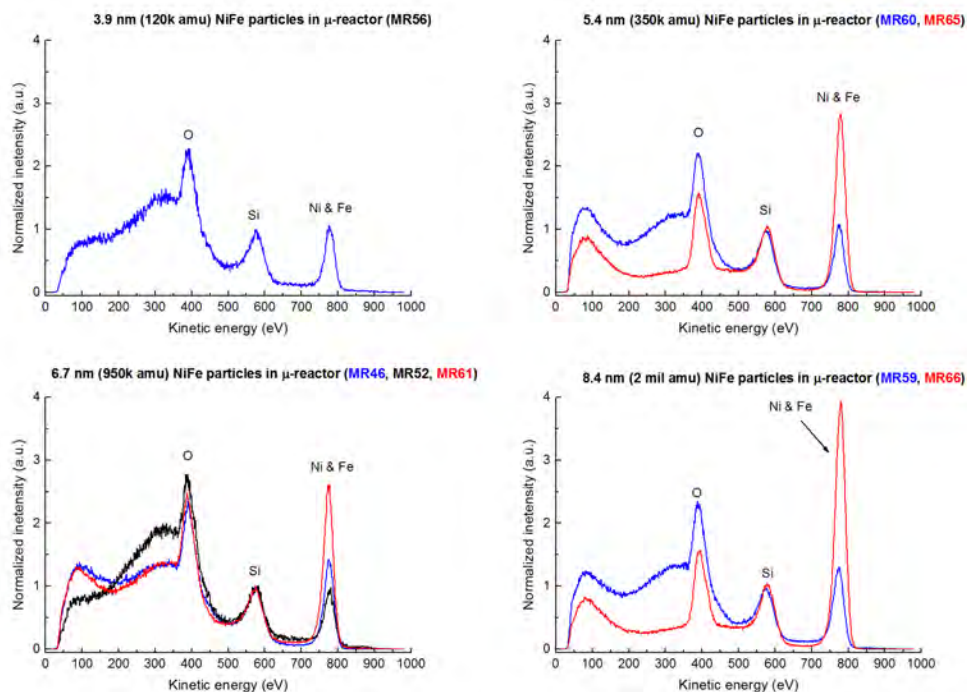


Figure 5.20: ISS spectra recorded after deposition in case of μ -reactors with NiFe mass-selected nanoparticles having different mass. The different colours in each figure depict different samples with theoretically the same particle mass and deposited loading. Intensities were normalized to the Si peak height and the figure shows the second scans taken. Figure adapted from [113].

5.2.5 Summary of the methanation activity tests with NiFe bimetallic nanoparticles

The deposited NiFe mass-selected nanoparticles are proved to be active for the methanation reaction and fairly resistant against sintering. There is a trend visible in their activity as a function of size (Figure 5.16) and it seems that either 5.4 or the 6.7 nm particles are the most active. However, the reproducibility of the data is poor. In hindsight this was caused by two problems: we had issues with temperature measurement and control and issues with the deposition of particles. The latter seemingly only effected the μ -reactors and not the samples for electrochemical measurements which were deposited during the same timeframe from the same target(s), by the

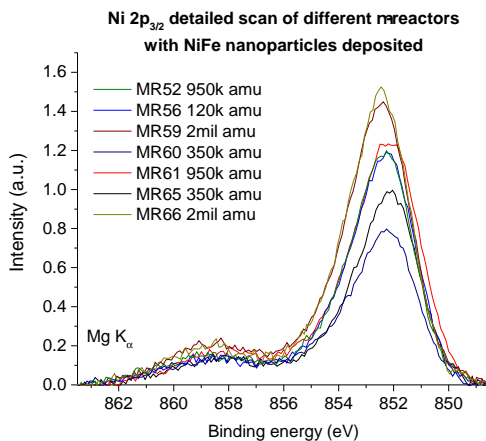


Figure 5.21: XPS detailed spectra of the Ni 2p_{3/2} region recorded in case of as deposited μ -reactors with NiFe mass-selected nanoparticles having different mass. The different colours mean different samples. The spectra were shifted to give a Si 2p binding energy of 103.4 eV (SiO₂ from [23]), Shirley-background subtracted and normalized with the area of the Si 2p peak.

same person. Nevertheless, the experiments showed in this section gave incentive for a more detailed study on the reproducibility of the μ -reactors shown in the following.

5.3 Problems with the μ -reactors and the depositions discovered

In order to try and understand our odd experiences with the μ -reactors, we decided to make a systematic study on the reproducibility of the μ -reactor measurements and our particle depositions. We chose to deposit pure Ni mass-selected nanoparticles (99.99% Ni target, Kurt J. Lesker) in order to simplify the investigated system. This project was part of the special course of Niels Dyreborg Nielsen (DTU SurfCat), who participated in the deposition and characterization of the μ -reactors and conducted measurements with the μ -reactor setup.

5.3.1 Problems with the reproducibility of particle depositions

We deposited nine μ -reactors with 980k amu Ni particles (approx. 7 nm diameter assuming spherical shape and bulk density), having 10% projected surface area coverage

during the course of three days. Physically the same target was used with exactly the same conditions (sputtering power, pressure in the aggregation zone etc.) in each case. Furthermore, all of the deposited μ -reactors went through exactly the same cleaning process (described in Appendix F). We used physically the same three sample holders each day and positioned them at exactly the same position behind the mask with the micrometers on the manipulator. Even though Niels participated in the depositions during one of the days, the nanoparticle source was operated mainly by the same person (me). As much care as possible was taken to aim at the same place on the μ -reactors every time with XPS and ISS. Our plan was to run the same gas-flow and temperature profile we used for the NiFe particles (described in Section 5.2.3) in the μ -reactor setup to measure the activity of the samples, but unfortunately we discovered problems even before making any activity measurements.

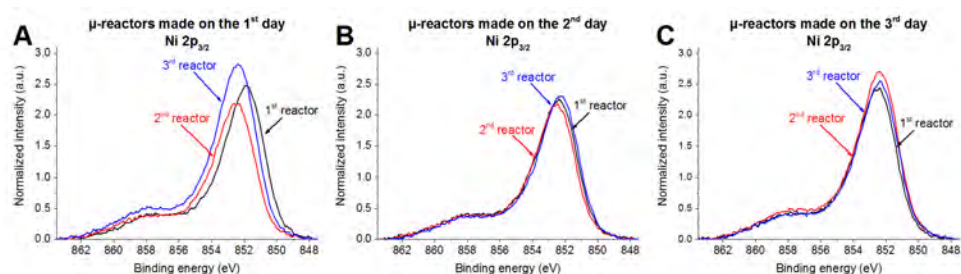


Figure 5.22: XPS detailed spectra of the Ni $2p_{3/2}$ region recorded in case of nine μ -reactors after deposition of 980k amu (approx. 7 nm) mass-selected Ni nanoparticles. The different colours depict different samples. The spectra were shifted to give a Si 2p binding energy of 103.4 eV corresponding to SiO_2 [23], Shirley-backgrounds were subtracted and the intensities were normalized with the Si 2p peak area. A: μ -reactors deposited the first day; B: μ -reactors deposited the second day and C: μ -reactors deposited the third day of the reproducibility study.

Figure 5.22 shows the detailed XPS spectra of the Ni $2p_{3/2}$ region recorded in case of the μ -reactors made on the three different days. The intensities were normalized with the Si 2p peak area, but the raw data shows a similar reproducibility as the Si 2p peak area was changing by less than 5% between the nine μ -reactors. The Ni $2p_{3/2}$ peak areas seem reproducible and consistent, especially for the second and third day. The binding energy recorded in case of the first μ -reactor of the first day is shifted slightly. The reason for this is most probably that the reactor was not attached to the sample holder properly, charged up during XPS and the spectra had to be shifted by approx. 6 eV compared to the shifts of the other reactors which were below 1 eV. As Si 2p is not a sharp peak, this could have caused some misalignment of the spectrum.

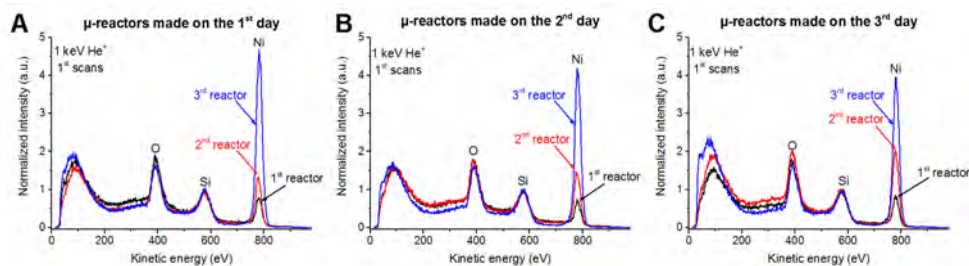


Figure 5.23: ISS spectra recorded in case of the nine μ -reactors after deposition of 980k amu (approx. 7 nm) Ni mass-selected nanoparticles. The intensities were normalized with the Si peak height. A: μ -reactors deposited the first day; B: μ -reactors deposited the second day and C: μ -reactors deposited the third day of the reproducibility study.

Similarly, the ISS spectra of the samples made on each day can be plotted (Figure 5.23). An odd trend can be discovered. Depending on the time during the day of when the deposition was made (or maybe how many samples were made before the given sample that day) the ISS signals in case of the μ -reactors are significantly different. The ISS signals are consistently higher in case of reactors made later during the days. There is no clear connection between the XPS and ISS signals. There were a few ideas which came up when we were trying to explain this behaviour: (1) aiming with the ISS and/or XPS or with the depositions, (2) something is covering the surface or (3) something is changing in the nanoparticle source. Naturally there could be differences between the aiming, but I have made everything possible to avoid it. Also if this would be a random process of aiming differently, the results and trends would not be reproducible throughout three days. There could be something covering the surface of the Ni nanoparticles or the SiO_2 substrate. If this is the case, we have some information about it as neither the ISS spectra nor the XPS survey spectra show any contaminants. Knowing the sensitivity of these methods H_2 is the only possibility, even though we do not know where would it come from apart from ideas like the Ti sublimation pump in the chamber, which seems highly unlikely. And finally changes in the nanoparticle source. During the nights the nanoparticle source is not baked, the liquid nitrogen cooled aggregation zone warms up gradually to room temperature. During the day when it is cooled down it acts as a cryopump, therefore the differences could come from the declining efficiency of the trapping of some contaminant in the gas feeds and causing some changes in the aggregation zone. If this is the case, the only contaminant which would be possible is again H_2 , as anything else would be picked up by either XPS or ISS. It is also worth noting that this problem did not show up with the NiFe particles made for the OER project, even though the similarity of depositions, the only differences being the substrates, sample holders and the

aperture size in the mask.

5.3.2 Problems with temperature measurement and control

After we have deposited the μ -reactors for testing the reproducibility of our methods and practices another problem was found with the μ -reactors by Ann-Louise Christoffersen (DTU SurfCat). She had problems with inconsistent temperature readings from the RTDs on the backside of the μ -reactors and a thermocouple placed on top of the reactor. She created a holder to test the RTD temperature readings with three thermocouples attached at different points of a mounted reactor. With her repeated experiments instability and inconsistency was found among the RTDs. This instability is illustrated in Figure 5.24. A μ -reactor was heated according to the temperature profile described in Section 5.2.3 and the figure shows the voltage on one of the heater elements (the other one behaves similarly) and the measured RTD temperature at a temperature step from what was supposed to be 200°C to 225°C. At a constant temperature abrupt changes in the heater voltage can be seen while the RTD temperature is staying stable (Figure 5.24). This indicates that the Pt RTD is changing during measurements as the heater is compensating its changing resistance. Furthermore, the changes of the heater voltage are not negligible compared to the change at the actual temperature step.

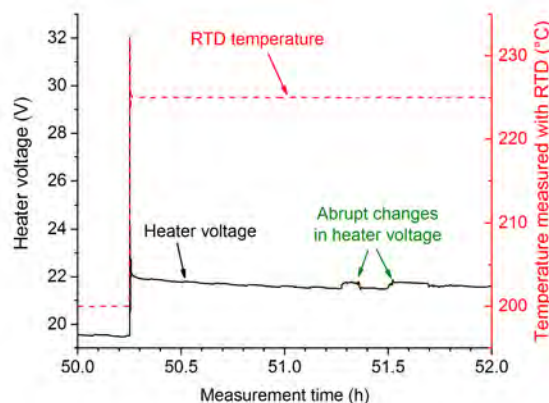


Figure 5.24: Illustration of the instability of the Pt RTDs on the backside of the μ -reactors. During constant temperature operation abrupt changes in the heater voltage can be seen. This is most probably due to changes in the Pt RTD and shows its instability.

In order to investigate this problem further, Thomas Pedersen (DTU Danchip) made an SEM investigation on the shadowmasks used for the deposition of the Pt

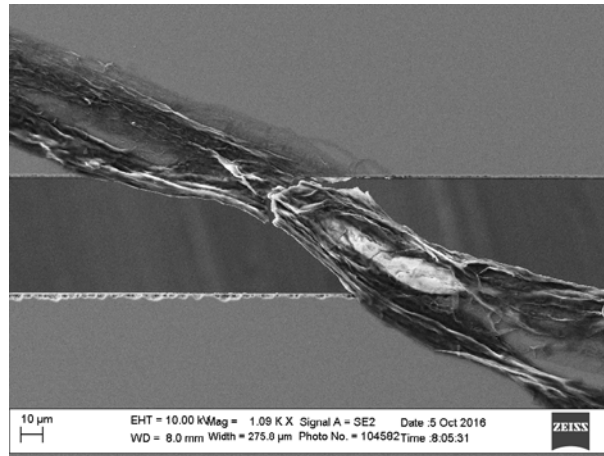


Figure 5.25: SEM image of a filament blocking the shadowmask used for the deposition of the Pt RTDs on the backside of the μ -reactors taken from the shadow side of the shadowmask. Image courtesy of Thomas Pedersen (DTU Danchip).

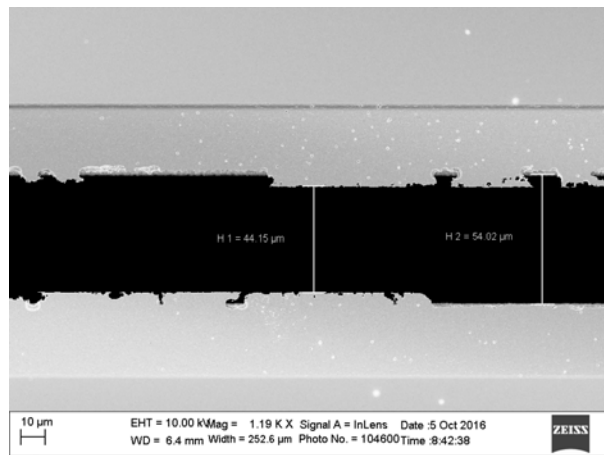


Figure 5.26: SEM image of a constriction in the shadowmask used for the deposition of the Pt RTDs on the backside of the μ -reactors taken from the deposition side of the shadowmask. Image courtesy of Thomas Pedersen (DTU Danchip).

RTDs and heater elements on the backside of the μ -reactors. He used SEM to meticulously check the shadowmasks used and found sections, where the openings for the RTD (and also the heater elements) were constricted and filaments of most probably Pt were blocking the shadowmasks (Figures 5.25 and 5.26). These findings might explain the broken RTDs sometimes encountered and could be the cause of the problems with the unreliable temperature readouts and inconsistencies. The thickness of the RTD/heater elements is 100 nm, therefore having constriction might increase the current density to values where electromigration becomes a problem.

In order to solve the problems discovered, new shadowmasks were made and from now on they will be thoroughly cleaned after every deposition in order to remove any residual Pt on them and to avoid the constriction of the evaporated conductors. The thorough testing of the μ -reactors with the new RTDs and heaters in terms of reproducibility and accuracy is an ongoing process.

5.3.3 Summary of the issues with the μ -reactors discovered

During the course of the last nine months we discovered two serious issues with the μ -reactor setup and the way we deposit μ -reactors in the Omicron vacuum system. One of this issues is a problem which was hopefully fixed after an investigation (RTD problems). The other issue with the odd ISS signals remains unexplained and something which has to be investigated further. I hope that by including these issues here, they will remain in the minds of my colleagues and will be at some point resolved. Our problems with the RTDs might very well explain the inconclusive results with the sintering and activity of the AuTi particles. The issue with the depositions of the μ -reactors together with the uncertain temperature readings and control can also explain the unreproducible results in case of the activity of NiFe particles in the methanation reaction.

CHAPTER 6

Conclusion and outlook

The projects reported in this thesis all revolve around producing, characterizing and testing the catalytic activity of mass-selected nanoparticles. Not everything reported can or will be published, but I hope that even those sections will be useful for new people working in the laboratory. I also hope that by including most of this information, some of the mistakes will be avoided in the future. As the final chapter of my thesis, I would like to give a short and subjective summary of the projects and their possible future perspectives as I see them.

Pt as a TW scale HER (photo)electrocatalyst Pt is by far the best HER catalyst, but its price and scarcity makes its use seemingly impractical for large scale hydrogen production. However, in a PEC device current is limited by sunlight and our results show that in case an overpotential comparable to non-noble HER catalysts is accepted, ultra low loadings of Pt can be used. Based on our measurements and simulations the amount of Pt required for TW scale solar HER is actually low enough to make Pt a feasible alternative. This study has broad implications. It sets a standard to compare new, non-noble HER catalyst for solar water splitting to. Furthermore, it shows the importance of analytical techniques: even Pt loadings which cannot be detected by XPS can have significant catalytic activity, which has implications for non-noble HER catalyst research. As our experiments showed, ultra low loadings of Pt nanoparticles are fairly unstable due to contaminations, thus their industrial use might be limited. However, there is a possibility that these issues can be solved and solar watersplitting can be used to produce H_2 with Pt as a catalyst on the TW scale.

NiFe mass-selected nanoparticles as active and stable OER catalyst We investigated the particle size effect and the effect of particle proximity on the activity of NiFe nanoparticles for OER in alkaline media. Furthermore, we assessed the stability of the particles and investigated the binding states of Ni and Fe with XPS. Some additional experiments and data treatment are still missing, but I am convinced that in the near future we will complete this study. We are planning identical location HRTEM imaging of particles to investigate

their structure and the effect of OER conditions on them. We are also planning experiments with isotopically labelled electrolyte, to further elucidate the mechanism of OER on the particles. I believe that we will be able to provide valuable information about the workings of OER on NiFe nanoparticles. This might prove useful, as the mixture of Ni and Fe is active, cheap, abundant and already used in the industry as a catalyst, therefore all additional information about how these material work is directly applicable.

AuTi bimetallic nanoparticles for CO oxidation Our results show that by alloying Au particles with Ti, it might be possible to create an active Au based CO oxidation catalyst which is resistant against sintering. Apart from ISS, computational studies on small AuTi species also indicate that a TiO_x anchor forms towards the SiO_2 substrate, while Au atoms should still be present on the surface of the particles. Based on STEM imaging, alloying seems to increase the stability of the particles on the surface. A paper is in preparation combining the STEM imaging, computational details and physical characterization (XPS and ISS) of the particles. I believe that after getting rid of the practical issues with the μ -reactors, investigating AuTi bimetallic nanoparticles could provide interesting activity data as well.

NiFe bimetallic nanoparticles for methanation We investigated mass-selected NiFe nanoparticles in the methanation reaction and even though the activity data is inconclusive, there is a trend in activity with the size in the investigated size range (3.9 nm - 8.4 nm). It seems that 6.7 nm particles are the most active. Experiments also showed that the particles are deactivating, most probably due to carbon deposition on the surface, and they can be reactivated by reducing them in H_2 . However, apart from these results even more valuable were the best practices and methods we had to come up with during the project and the problems with the μ -reactors discovered. I hope that by including this information here, future operators of the Omicron and the μ -reactor setups can take advantage of our work.

I think that the projects with Pt as a solar HER catalyst and the NiFe bimetallic nanoparticles as OER catalyst will have an influence in the future. In case of the projects with the μ -reactors, they will most likely be more valuable for the laboratory, as practical issues were discovered and best practices established.

On a personal note I would like to add that I had a great time in the three years and gained a lot of new connections, knowledge and experience. And finally, I would like to conclude this thesis by thanking you for reading it!

APPENDIX **A**

Reduction of oxidized NiFe nanoparticles by sputtering with He^+ (ISS)

I have found an interesting consequence of ISS measurements during the experiments reported in Chapter 4. The NiFe nanoparticles oxidized during electrochemical measurements are readily reduced by ion sputtering during ISS measurement (1 keV, He^2). This is illustrated in Figure A.1 with the Ni $2p_{3/2}$ XPS spectra recorded after OER activity testing on two different samples with 6.7 nm (950k amu) NiFe nanoparticles. In one case the XPS spectrum was recorded before ISS measurement and in the other case it was recorded after ISS measurement. Bombarding the sample with ions clearly reduces Ni. This effect has been reported earlier for both Ni and Fe [145]. This also shows that ISS is indeed a destructive method capable of changing the surface of the samples. All XPS spectra shown for oxidized Ni and Fe in the thesis were recorded before ISS measurements, except in Figure A.1.

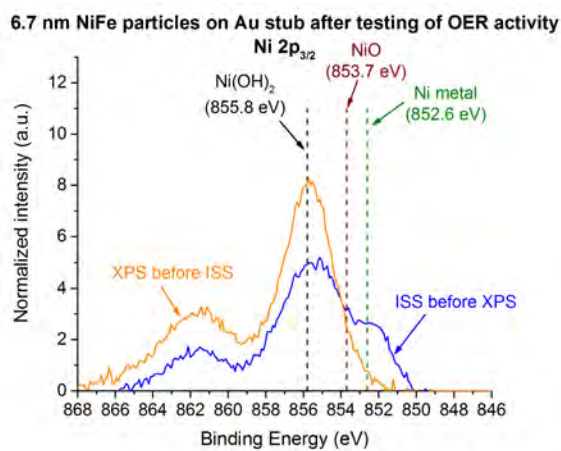


Figure A.1: Reduction of Ni by bombardment with He⁺ ions as shown by the detailed XPS spectra of the Ni $2p_{3/2}$ region. The two XPS spectra were taken of identical samples (6.7 nm NiFe particles) going through OER activity measurements. The only difference is whether the XPS spectrum was taken before recording an ISS spectrum or after.

APPENDIX B

Additional details of the depositions

Problems caused by particles having double and half mass

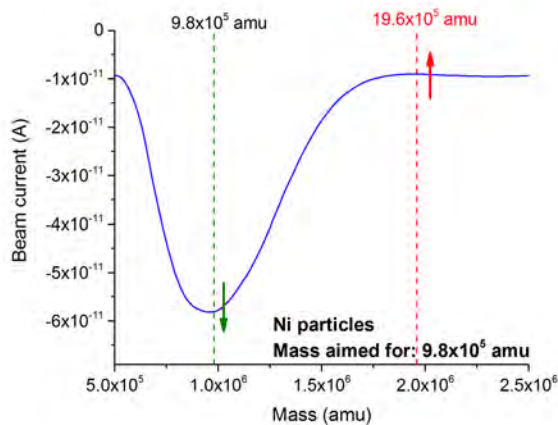


Figure B.1: Mass spectrum of particles leaving the aggregation zone. The single and double mass signals are shown by dashed lines. Deposition using these conditions would result in particles with a poor size distribution.

As described in Section 2.1.2, the mass filter is filtering on the basis of m/z . Vast majority of the charged nanoparticles leaving the aggregation zone of the nanoparticle source are carrying a single charge (either an excess or a missing e^-), but there are nanoparticles carrying double charge as well. This also means that there is a chance of forming nanoparticles having double the mass and double the charge ($2m/2z$) and they will pass the mass filter exactly as a single mass nanoparticle having a

single charge would. These particles show up in the TEM images as particles having $\sqrt[3]{2}$ times bigger diameter than the ones with mass m . This phenomenon and its implications for catalytic model systems have been explored in [146]. In general we can assume that the amount of nanoparticles carrying double charge is proportional to the amount of the nanoparticles having the same mass with single charge. Therefore, a simple way to avoid double mass - double charge particles getting through the mass filter is to minimize the amount of double mass - single charge particles leaving the aggregation zone. In practice this means that while tuning the conditions of the nanoparticle source, it is not only the current at the desired mass which has to be maximized, but at the same time the current at the double mass has to be minimized as well (see in Figure B.1). Experience shows that a ratio of 10 or higher between the beam current at the mass we want to deposit and the beam current at the double mass hinders the deposition of significant amounts of double mass particles. During deposition the conditions in the nanoparticle source can drift slightly. This can shift the mass-distribution of the particles produced towards higher masses, meaning higher current at double mass. Because of this after every deposition the mass-distribution is checked again and if significant amount of beam current at double mass is found the sample is discarded. The prevalence of particles having double mass in the size distribution is most obvious in case of heavy particles (Figure 4.3). There are two reasons for this: on one hand the difference between the diameters of the single and double mass particles are bigger, thus they are more separated from each other in the size-distribution. On the other hand, experience shows that it is more difficult to find conditions with low double mass signals for heavier nanoparticles. Figure B.2 shows an example TEM image with double mass particles clearly visible among the deposited particles.

A similar issue was recently discovered with particles half the mass of the ones aimed for. Particles cannot have half e^- charge, but there is a chance of a neutral and a charged particle colliding and sticking together without forming a round particle (Figure B.2). This means that also the current of the particles at half the desired mass has to be minimised in the mass spectrum before deposition.

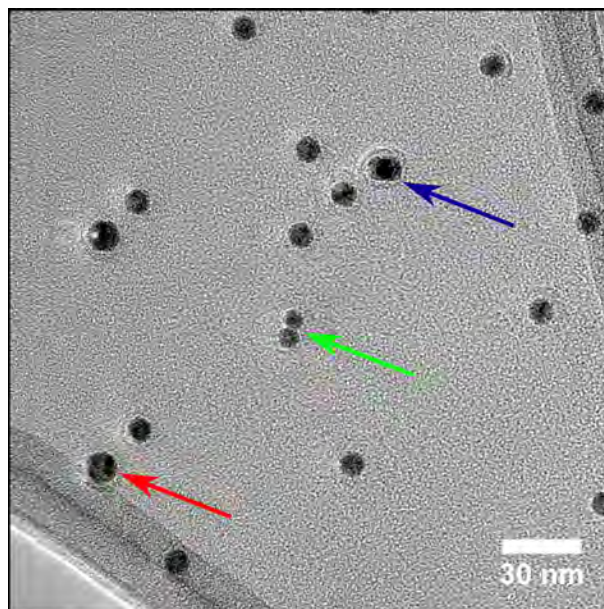


Figure B.2: TEM image showing overlapping NiFe nanoparticles (blue arrow), particles having double mass (e.g. red arrow) and doublet of half mass particles (green arrow) too. The particles were supposed to be 8.4 nm (2 mil amu) NiFe nanoparticles.

Determination of the deposited loadings and their accuracy

We are controlling the mass of the produced particles, thus when we want to deposit a certain size we have to calculate the corresponding mass. Or the other way around: we would like to approximate the deposited catalyst surface area for particles having a given mass. For this a simple way to convert particle mass to diameter and diameter to particle mass is needed. This is of course done by determining the size-distribution of the deposited particles (Appendix D), but that is a relatively slow process and cannot be done on the go while depositing samples or planning experiments. Therefore, for all of our size and loading calculations we assume perfectly spherical particles having bulk density (ρ_{bulk}). This is the simplest assumption and provides an easy way to calculate the mass of a single particle (m_p) with a given diameter (d_p) according to (B.1) or the diameter of a particle with a given mass according to (B.2). This seems like an overly simplified assumption, but it gives a good approximation of the sizes (e.g. Sections 3.2.1 and 4.4.1) and provides an easy way to calculate certain parameters (e.g. total surface area of the particles) which can be later refined by the

size-distributions derived from TEM images.

$$m_p = \frac{1}{6} d_p^3 \pi \rho_{bulk} \quad (\text{B.1})$$

$$d_p = \sqrt[3]{\frac{6m_p}{\pi \rho_{bulk}}} \quad (\text{B.2})$$

Determination of the deposited loading

If we assume that all particles carry a single charge and the desired mass, the deposited mass (m_{depo}) can be easily calculated from the electrical current of the beam reaching the sample (deposition current, I_{depo}), the time of deposition (t_{depo}) and the mass of a single particle (m_p):

$$m_{depo} = I_{depo} \times t_{depo} \times 6.242 \times 10^{18} \times m_p \quad (\text{B.3})$$

$$m_{depo}[\text{ng}] = I_{depo}[\text{pA}] \times t_{depo}[\text{min}] \times m_p[\text{amu}] \times 6.22 \times 10^{-9} \quad (\text{B.4})$$

Here 6.242×10^{18} is the number of nanoparticles in 1 C of charge if we assume particles carrying single charge. It is usually easier to think and talk about the mass of the particles in amu, the current in pA, the deposited mass in ng and the deposition times in minutes as these are the orders of magnitudes of the usual values. If we use these units a simple expression can be derived for the deposited mass (B.4). This means that determining the mass loading is fairly straightforward. For some practical reasons however, we regularly use projected surface area loadings where we calculate the ratio of the area on the surface of the substrate which the particles cover assuming perfectly spherical particles and divide it by the entire area of the deposition (diameter of the hole in the mask, see Figure 2.9). This can be visualized as the fraction of the surface covered by the nanoparticles in an SEM image. This notation is useful because if the projected surface area coverage is kept constant over different samples with particles having different diameters the total surface area of the deposited particles (thus the number of surface atoms) will be the same. The mass loading will change, the number of deposited particles will change, but the total surface area of the particles remains the same, thus samples will be straightforward to compare in activity measurements.

(B.3) and (B.4) depend on the determination of the deposition current. Theoretically this current is simple to measure, since there is no current on the sample when it is not hit by the beam and there is the beam current when the beam is hitting the sample surface. However, the current is on the order of pA, which require sensitive equipment. Furthermore, the sample is biased to +45 V during deposition and the manipulator used for deposition is not ideal. It has multiple heating facilities built in with different electrical contacts and thermocouples attached. Also the ceramics used as insulators are slowly getting dirty from all the depositions and introduce a leak

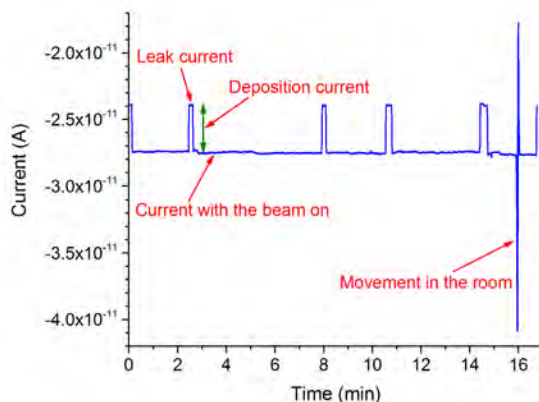


Figure B.3: Illustration for the determination of the deposition current (I_{depo}). The beam is regularly diverted away from the sample and put back again. The current without the beam (approx. 24 pA) is the leak current. When the beam is back on, a current of approx. 27.5 pA is measured, thus the deposition current is around 3.5 pA. The spike at around 16 min is caused by someone walking by the setup in the laboratory.

current, which is on the order of 20-40 pA. Even worse, this leak current can change slightly on the timescale of the depositions. It is difficult to get rid of the leak current completely, as the resistance towards ground is on the order of T Ω , thus nothing is "broken" in the manipulator. However, as described in Section 2.1.2, the beam of nanoparticles can be diverted away from the mass filter and back again practically instantaneously by means of ionoptical lenses. So the usual way of determining the deposition current is regularly diverting the nanoparticle beam away from the sample, determining the leak current and letting the beam hit the sample again. This process can be seen multiple times during the deposition depicted in Figure B.3. The difference between the current with the beam on and the beam diverted is the deposition current (I_{depo}). Figure B.3 shows another issue with measuring the small current of the nanoparticle beam. If people are moving in the room (e.g. someone is working on the other setup situated in the same room), spikes appear in the current vs. time graphs. No evidence was found that these spikes would influence a deposition, they are most probably the result of slight movement in the cabling due to the movement of air.

Investigating the accuracy and reproducibility of the loadings determined from the deposition current is not a straightforward task due to the small amount of material deposited. However, we have some indirect evidence. The similar measured activity of the samples deposited for the OER study with a given NiFe nanoparticle size

(Section 4.2) shows that the loadings are at least reproducible. The different ICP-MS measurements confirming that our Pt loadings are at least on the same order of magnitude as they should be (Chapter 3) also roughly indicate the accuracy of our loadings. A direct observation of the loadings can be made by using the TEM images of different loadings of 6.7 nm (950k amu) NiFe nanoparticles recorded for the determination of nearest neighbour distances and the radial distribution functions (Section 4.5.4 and Appendix E). I have deposited TEM grids with particles having the same size and determined the positions of these particles on the grids. For each loading and grid I took multiple images with the same magnification and the average number of particles on a single image can easily be calculated from the available data. The expected number of nanoparticles/image can be calculated assuming a homogeneous deposition, knowing the total area of deposition ($1.6 \times 10^7 \mu\text{m}^2$), the number of particles deposited (calculated from the deposition current) and the area depicted in a single TEM image ($9.91 \times 10^{-2} \mu\text{m}^2$). Even though I investigated multiple images (approx. 20) for each loading, the total area depicted by these images is negligible compared to the total area of the deposition. This means if the deposition is not perfectly homogeneous the numbers can be misleading. Still, this method provides an interesting and direct way of comparing the loadings calculated from the deposition current to the loading found on the samples (Table B.1). Based on the data in Table B.1, it seems that our loadings are within 15% to the expected values. The only exception is the lowest loading (2.5% projected surface area loading), where the loading determined based on the TEM images is significantly lower than expected. This is also shown in the average NND determined for this loading, which is significantly higher than expected (Figure 4.19). The reason for this might be the short deposition time or a human error. Nevertheless, based on the TEM images I expect that our actual loadings in general are within $\pm 15\text{-}20\%$ to the ones determined from the deposition current.

Projected surface area loading (from I_{depo} , %)	Number of particles on an image calculated from I_{depo}	Average number of particles on an image determined from TEM
2.5 %	64.9	42.2 ± 11.4
5 %	129.8	103.6 ± 10.7
10 %	259.9	280.7 ± 32.3
12.5%	321.7	351.4 ± 40.9
15 %	386.8	344.1 ± 47.4

Table B.1: Comparison between the number of 6.7 nm (950k amu) NiFe nanoparticles in a given area (TEM image) calculated based on the deposition current and determined based on TEM images. Knowing the area of the deposition and the area depicted on 1 TEM image the expected number of particles/image can be calculated based on the total number of deposited particles as determined from I_{depo} . The average number of particles/image was calculated using multiple (approx. 20) TEM images in case of each loading. Uncertainties given for the averages calculated from the TEM images are 2σ of the data.

APPENDIX C

New sample holder designs

During the 3 years in the laboratory I have designed new modular sample holders for our Omicron system using SolidWorks. They were built in the workshop at DTU Physics by Dan Shacham and Peder Heise. The original Omicron sample holders were designed for flat and thin samples maximum approx. 13x13 mm in size. Our substrates are often significantly larger, e.g. the μ -reactors are 16x27 mm. Furthermore, we did not have sample holders for TEM grids, which could be placed as close to the mask as the actual sample. This made statistical analysis of the particle positions and distances with TEM imaging unreliable, because of the extra distance the particles had to travel after the hole in the mask (Figure 2.9). We were also limited by the number of sample holders: there was only 1 holder for μ -reactors, 1 for TEM grids and 3 for stubs for electrochemical measurements. Our loadlock is able to accommodate 3 samples at the same time, therefore having 5 or 6 sample holders of each type can speed up sample handling significantly. Furthermore, the original μ -reactor sample holder did not fit into the stage in the analytical chamber, meaning that we could not use the analytical capabilities of the Omicron chamber with μ -reactors. We were also lacking reproducibility for sample placement, especially in case of the μ -reactors: the placement of the μ -reactors on the old sample holder was not constrained. This meant that the position of the μ -reactor on the sample holder changed from sample to sample, making "aiming" with the depositions very difficult.

Taking all of the above into consideration, the following were needed: new sample holders for different use (stubs, TEM grids, general use, μ -reactors) which can fit into all the positions in the Omicron chamber and provide a constrained substrate placement to make aiming easier. Three types of sample holders were made: holders for μ -reactors (and big samples), for stubs and for general use (and TEM grids). I would like to show these sample holders, as I think they made our life easier and I am hoping they will do so for others in the future too. All three of the different kinds of sample holders follow a general design: a top plate to help with substrate placement, a middle block made of stainless steel for assembly and fixing the samples (in case of stubs) and a baseplate made of 1 mm stainless steel having the same dimensions as the original Omicron sample plates (approx. 20x19 mm). The baseplate has a handle

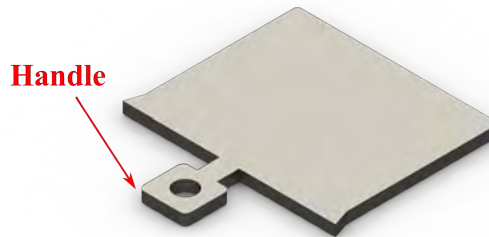


Figure C.1: Rendered image of the original Omicron sample plate used to transfer samples in the chamber and on which all the sample holder designs are based (dimensions of the plate are approx. 20x19 mm).

(Figure C.1), which serves as the point where the manipulators in the chamber grab the sample holders and makes it possible to securely move samples inside the chamber. The entire area of the sample holders cannot be used, as in the chamber they slide into sockets with molybdenum springs which keep them in place. This means that the samples cannot extend all the way to the edges of the sample holders, otherwise the springs would brake them or force them to come off. Also the thickness and width of both the top and the bottom plates are set by these slots and springs.

General use sample holder

The first sample holder I have designed was originally to mount thin glassy carbon windows clamped by stainless steel masks. The sample holder design evolved from there. The holders have a flat top plate made of stainless steel, with 6 M1.2 threaded holes to attach samples with M1.2 screws. They also have small indentations for TEM grids (3.1 mm in diameter and approx. 0.05 mm deep). The TEM grids are kept in place by a 0.1 mm stainless steel mask (Figure C.2) fastened to the holder by M1.2 screws. This way, the TEM grids can be placed at exactly the same position behind the mask in the deposition chamber as the samples. This sample holder proved useful for flat, moderately sized samples and when screws were required.



Figure C.2: Rendered image of the general use sample holder with the mask for TEM grids. The sample holder is made of stainless steel and has 6 vented threaded holes to attach samples or other extensions with M1.2 screws. The small indents (3.1 mm in diameter and 0.05 mm deep) for TEM grids and the thin stainless steel plate to keep the grids in place are also depicted in the image. The sample holder is kept together with M1.6 screws with sunk heads in vented holes.

Sample holder for μ -reactors

This sample holder was the most difficult to design, because the μ -reactors are by far the largest substrate we use (17x21 mm) and they are much larger than what the Omicron system was designed for. Nevertheless, the design (Figure C.3) can accommodate the μ -reactors while fitting to all the sample positions in the chamber. The sides of the top plate (made out of molybdenum) rise above the plane of the fitted μ -reactor, keeping the molybdenum springs away from the surface of the Si chip. The μ -reactors can only be attached in a single way, the sides of the top plate and the pyrex spacer on the μ -reactors setting their place on the sample holder (Figure C.4). This means that the attached μ -reactors are always at the same position in the chamber compared to the manipulators. When attached, the μ -reactor is kept in place with conductive double sided adhesive carbon tape (SPI).



Figure C.3: Rendered image of the μ -reactor sample holder used for μ -reactors and other large, flat and thin substrates. The top plate (made out of molybdenum) has sides above its plane. This is to prevent the molybdenum springs scraping and breaking the μ -reactor, when the sample holder is in its place in the chamber. This sample holder can fit into the analytical stage in the chamber and allows surface analytical investigation of the μ -reactors after deposition without breaking the vacuum.

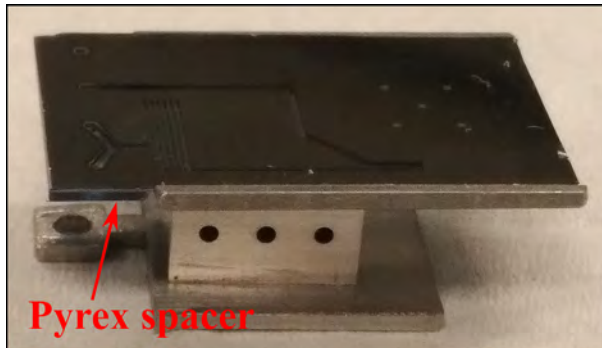


Figure C.4: Image of the μ -reactor sample holder with a μ -reactor attached. The μ -reactor is kept in place with conductive double sided adhesive carbon tape (SPI). The position of the μ -reactor compared to the sample holder is set by the sides of the top plate and the pyrex spacer bonded to the μ -reactor.

Sample holder for RDE stubs

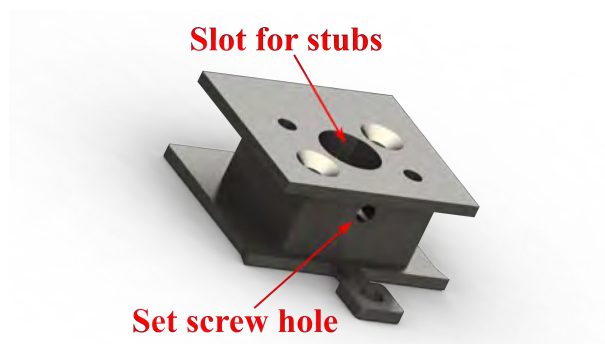


Figure C.5: Rendered image of the sample holder for RDE stubs. The stubs having 5 mm diameter slide into the slot and they are fixed with an M1.6 set screw from the side. The sample holder is held together with two M1.6 screws with sunk heads from both the front and back sides.

These sample holders are designed to hold cylinders 5 mm in diameter and approx. 4 mm height (RDE stubs). The stubs slide into the slot, which has a diameter slightly above 5 mm and they are held in place by an M1.6 set screw from the side. A small hole from the bottom side provides a way to easily remove an attached stub after deposition without contaminating the surface by pushing a small Allen key through the hole and lifting the stub out of the slot.

APPENDIX D

Determination of the size-distribution of nanoparticles with bright field TEM imaging

In order to determine the size-distribution of nanoparticles, multiple bright field TEM images were taken and analyzed with ImageJ [147] as explained here and as shown in Figure D.1. First each image (Figure D.1/A) was processed with an FFT bandpass filter to get rid of the noise from the background (Figure D.1/B). Afterwards, the images were thresholded by the method developed by Otsu [148] (Figure D.1/C). Finally, the area of the particles were measured by ImageJ Analyze particles... function. Figure D.1/D shows the outlines of the nanoparticles found by ImageJ overlaid on the original image.

In order to get rid of particles which has landed on top of each other, a strict limit to the circularity ($4\pi \times \frac{[\text{Area}]}{[\text{Perimeter}]^2}$) of automatically detected nanoparticles was introduced. Only nanoparticles with a circularity between 0.8 and 1 were taken into account. Nevertheless, some particles which have landed on top of each other still get into the analysis and these were removed by hand. Figure D.2 shows an image of NiFe particles (2 mil amu, 8.4 nm), where the deposition parameters did not stay stable and a strong double mass feature developed during the deposition. As this image shows, distinguishing between double mass particles - which are taken into account for the size-distribution and an example is marked by a blue arrow - and single mass particles landing on top of each other (marked by red arrow) is usually simple by eye.

After determining the projected area of the particles a diameter can be calculated

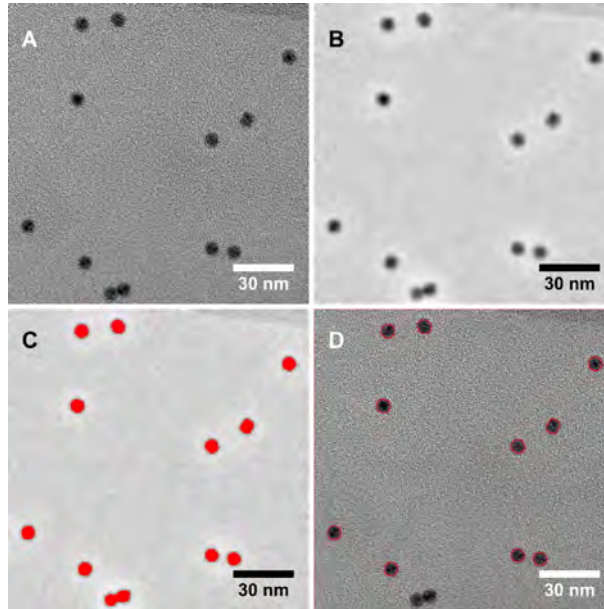


Figure D.1: Steps of determining the size-distribution of nanoparticles from bright field TEM images. A: original image; B: after FFT band-pass filtering; C: after thresholding; D: Original image with the outlines of the nanoparticles found by ImageJ.

by assuming a perfectly spherical shape using $d_{calc} = \sqrt{\frac{4A_{NP}^{TEM}}{\pi}}$, where d_{calc} is the calculated diameter of the nanoparticle and A_{NP}^{TEM} is the area of the projection of the nanoparticle determined from the TEM image. Having a constraint on the circularity during analysing the images ensures that assuming a spherical shape is a suitable assumption, at least for the projection visible in the TEM image. Having a sufficiently large number of particles a histogram can be made and a normal distribution can be fitted to it. This distribution gives the average size and an indication of the size variations. These variations can arise from the fact that the mass-resolution of the mass-filter is not infinite (Section 2.1.2) or because different projections show up of the particles in the TEM images. Another factor limiting the accuracy of the determination of the size is the resolution of the TEM and especially in case of the small particles the lack of contrast. Even the choice of thresholding algorithm influences the size determined. Considering these factors, the sizes determined must be taken carefully. Nevertheless, they can be used to compare samples to each other.

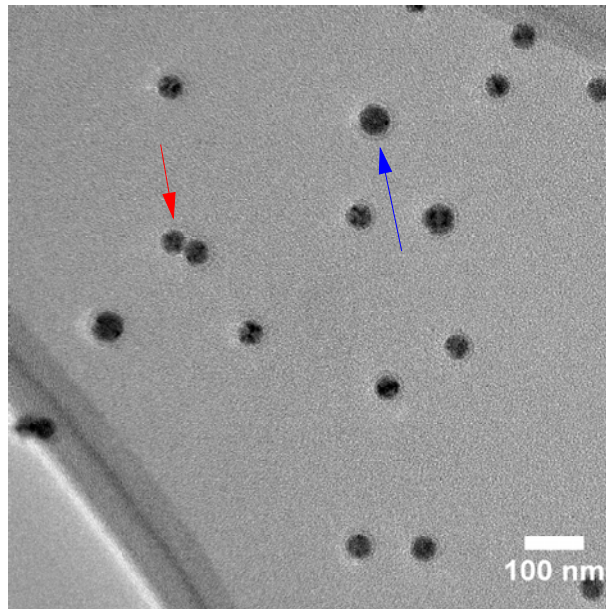


Figure D.2: Bright field TEM image of NiFe particles (intended mass 2 mil amu, 8.4 nm), where double mass nanoparticles (blue arrows) and nanoparticles landed on top of each other (red arrow) can be seen along with the single mass nanoparticles.

APPENDIX E

Calculation of the radial distribution function and the centre to centre nearest neighbour distance: method and validation

Radial distribution function in 2D and its calculation

Radial distribution functions (RDFs) play important role in different scattering techniques and can provide information about a number of material properties i.e crystal or domain structure, diffusion coefficients or melting properties. They are a vital part of understanding amorphous materials (for example liquids [149], polymers [150] or relaxation in amorphous materials [151]). The theory, usage and possibilities of RDF analysis is a very wide and complex field, so here I will only show the part which is relevant to this thesis: the detection of structure in 2D.

Simply put the RDF ($g(r)$) gives the average particle number density at a distance of r normalized to the number density in an ideal gas (random placement in 2D). Therefore, the average number density of particles $\rho_{ND}(r)$ at a distance of r is given by (E.1) where $\rho_{ND}^{rand}(r)$ is the average number density of randomly distributed particles.

In case of a randomly distributed ensemble of particles $g(r) \equiv 1$.

$$\rho_{ND}(r) = g(r)\rho_{ND}^{rand} \quad (\text{E.1})$$

Calculation of the RDF in 2D

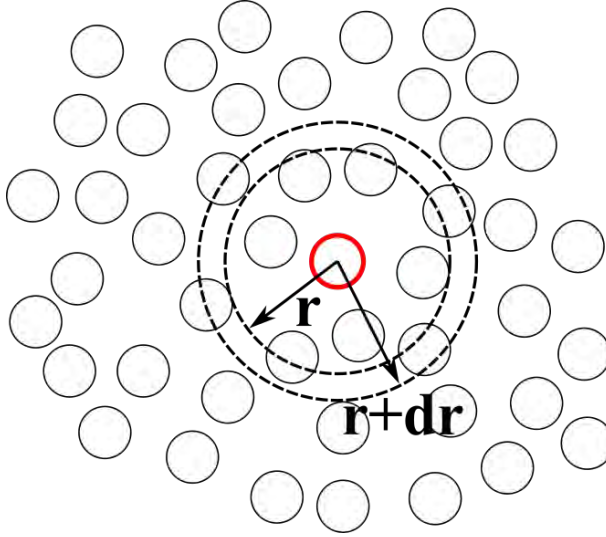


Figure E.1: Illustration for the calculation of the RDF in 2D.

In order to calculate the RDF, the coordinates of the centre points of the particles are needed. The average RDF of a 2D ensemble can be calculated by the following method: first a particle is chosen and the distance of all other particles are calculated measured from this particle. These distances are than binned into a histogram, where each bin represents the number of particles which are between r and $r + dr$ distance away from the particle initially chosen (Figure E.1). The bins are divided by the area of the annulus formed between the circles having a radius of r and $r + dr$ to provide the number density histogram of the particles as function of r . Finally the bins of the histogram are normalized by the average number density of the particles. This process is repeated for each particles and the RDFs of the particles are averaged in order to get the average RDF of the ensemble. Because the coordinates were determined based on TEM and SEM images (Section 4.5.4) in my case, the edges of the images can influence the results. In order to avoid this, only the RDF of particles at least $1.2 \times R_{max}$ distance from the edges were calculated and taken into account, where R_{max} is the maximum of the radius investigated in the calculation of the RDF. On the other hand, to calculate these RDFs the positions of all the particles in the image were considered. The NNDs were determined by a simple search algorithm to find

the closest lying neighbour based on the centre point coordinates. The average NND was also calculated with a similar approach to the edges in order to avoid particles at the edges influencing the results.

Validation of the script for the calculation of RDF and NND

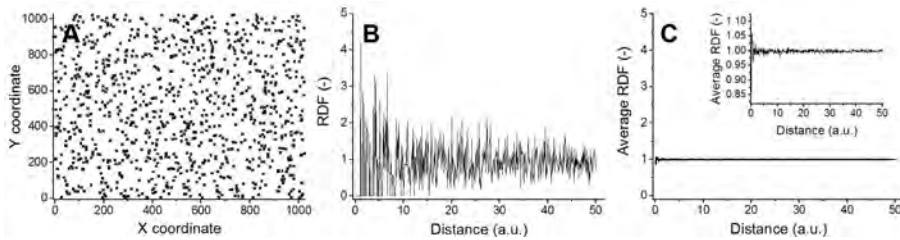


Figure E.2: Validation of the self-written script calculating RDFs in 2D: RDF of random ensembles. A and B: an example of random points and the corresponding RDF; C: RDF after averaging over 10000 randomly generated ensembles.

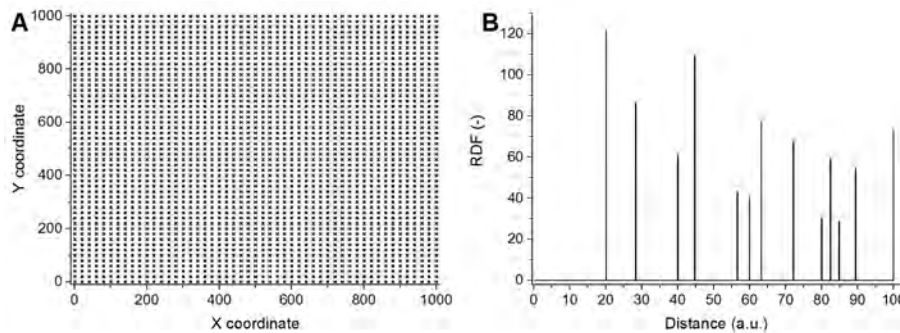


Figure E.3: Validation of the self-written script calculating RDFs in 2D: 2D square lattice. A: 2D square lattice and B: the corresponding RDF. Lattice constant (distance between points in x and y direction) is 20 units.

The self-written script can be validated by ensembles of coordinates with known RDFs. The simplest of these are random placement (Figure E.2) and a 2D square lattice (Figure E.3). Creating an ensemble of random coordinates (Figure E.2/A) and then calculating the average RDF with the MATLAB script results in a noisy signal which seems to be centred around 1 (Figure E.2/B). If this process is repeated 10000 times and the calculated RDFs are averaged, the result is a smoother signal (Figure E.2/C) which is clearly centred around 1 as expected in case of randomly dis-

tributed ensembles. The calculated RDF in case of a 2D square lattice contains only the distances expected with the known lattice constant of 20 units (Figure E.3/A): 20, 28.28 ($20 \times \sqrt{2}$), 40 and so on (Figure E.3/B). Based on these examples, the script seems to work as expected and provides correct results.

Determination of the centre point coordinates of the particles

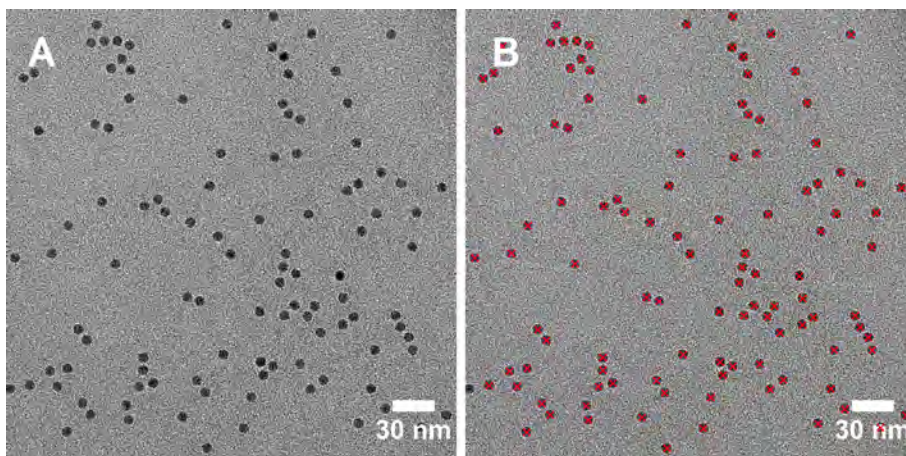


Figure E.4: Determination of the particle positions from TEM images. Lacey C covered Cu TEM grid with 5% projected surface area coverage of 6.7 nm (950k amu) NiFe nanoparticles. A: Original image; B: particle centre points overlaid.

In order to determine the particle positions, the Analyze particles... function of ImageJ was used [147]. I treated the images similarly than in case of determining the size distributions, meaning an FFT bandpass filter first, then thresholding the images and measuring particles with a circularity of at least 0.8 (Appendix D). The particles touching the edges of the images were excluded from the automatic particle detection. Even with constraining the circularity to 0.8 or higher some particles landing close to each other are detected as single particles. On the other hand, most of the particles overlapping are not automatically chosen, even though their coordinates should also be recorded. Thus, after automatic particle detection I inspected each image and added the coordinates of the overlapping particles by deleting the automatically determined coordinates (if applicable) and estimating the centre points by eye, placing markers and determining the positions of these markers with ImageJ. Examples of 5% loading of 6.7 nm (950k amu) NiFe nanoparticles on a TEM grid imaged with TEM and the same loading on a pcAu stub imaged with SEM are shown in Figure E.4 and Figure E.5 with the determined centre points overlaid.

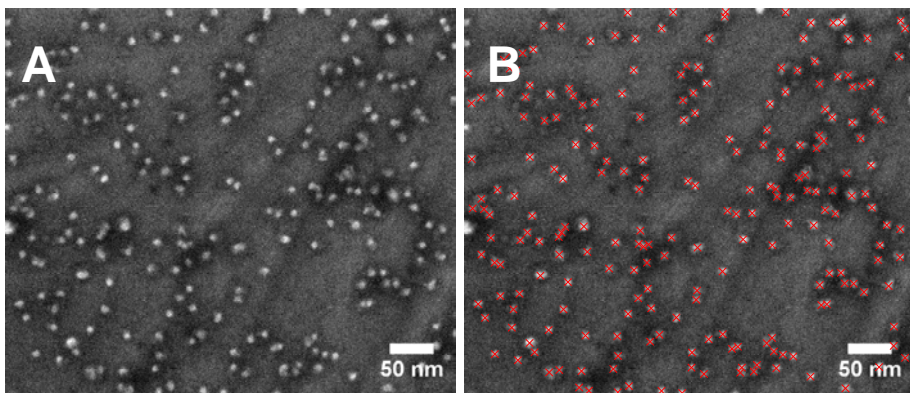


Figure E.5: Determination of the particle positions from SEM images. Image taken of a pcAu stub after activity testing with 5% projected surface area coverage of 6.7 nm (950k amu) NiFe nanoparticles. A: Original image; B: particle centre points overlaid.

APPENDIX F

Cleaning of the μ -reactors

In order to create reproducible and reliable results with the μ -reactors, I wanted to establish a method to eliminate all contaminations from their surface before deposition. These contaminants included Ba, which was traced back to the cleanroom and the production of μ -reactors years earlier and it sometimes appeared and disappeared over the years. In this appendix I would like to present the cleaning protocol I came up with and show that it is effective and reproducible.

Odd contamination: Ba

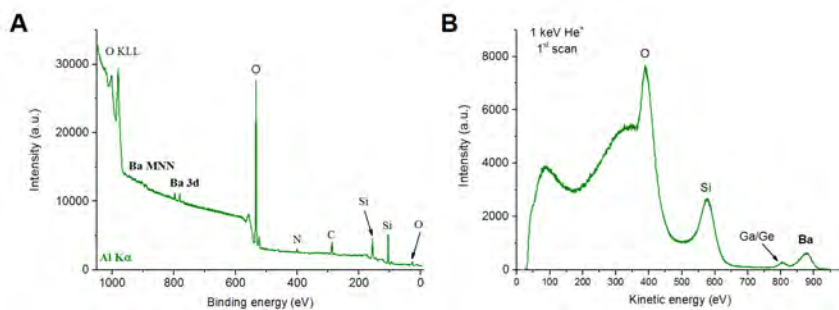


Figure F.1: XPS and ISS spectra of an uncleaned, undeposited μ -reactor showing signs of Ba and Ga/Ge contamination. A: XPS survey spectrum taken using the Al $K\alpha$ line; B: ISS spectrum, 1st scan.

The first signs of Ba contamination were detected with ISS in case of the μ -reactors deposited at UoB. With ISS it was difficult to elucidate which element is the one around 130 amu on the surface, thus we made a more detailed search. After recording XPS and ISS spectra of an uncleaned and undeposited μ -reactor, we were

able to determine that the μ -reactor has an odd Ba contamination (Figure F.1). The XPS spectrum also shows a relatively high amount of C (RSF_{C 1s}=1) contamination on the surface of the μ -reactor (Figure F.1/A). Fortunately the Ba contamination was proven to be easy to get rid off. Sonicating the μ -reactors in ethanol and then rinsing them thoroughly with mili-Q water removes it from the surface completely.

Removing the adventitious carbon

In order to get rid of the adventitious carbon contamination on the surface, the μ -reactors were sputter cleaned before deposition with 1 keV Ar⁺ ions. To determine the sputtering time needed, I conducted a test where I sputtered a μ -reactor and recorded XPS spectra at different sputtering times. As Figure F.2 shows around 30 minutes of Ar⁺ sputtering (with a sample current of around 500 pA) was needed to get rid of the adventitious carbon contamination. Based on this measurement, each μ -reactor was sputtered for 40 min before deposition to make sure all the carbon contamination is removed from the surface. This not only cleans the surface, but also creates defects which can act as anchor points for the particles and help to prevent sintering. Another effect of the sputtering is the emergence of an Ar peak in the spectra which is most probably due to implanted Ar.

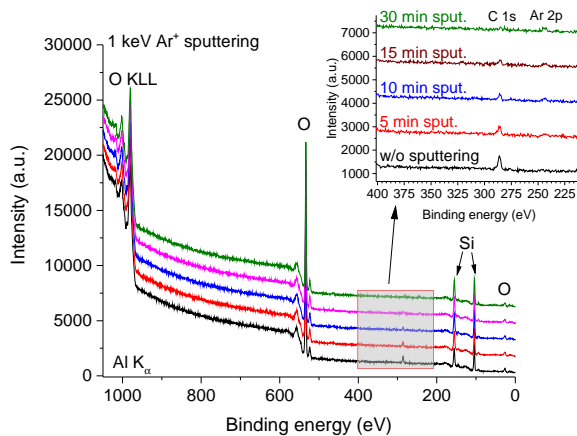


Figure F.2: Determination of the sputter time needed to remove the adventitious carbon contamination from the surface of the μ -reactors by ion sputtering (1 keV Ar⁺) based on XPS spectra. The spectra were offset in y direction for ease of view.

Cleaning of the μ -reactors

Finally, in order to show that the cleaning method is reproducible and it is working with the μ -reactors from different wafers too I would like to show XPS and ISS spectra recorded in case of 3 μ -reactors cleaned and checked the following way: First the correct etching of the gas channels is checked by eye and in general the μ -reactor is inspected for cracks and faults. Then both heater elements and the RTD is tested with a multimeter to ensure they are not broken. Afterwards, the μ -reactor is sonicated in ethanol for 2 minutes and then rinsed thoroughly with mili-Q water. After sonication both the heater elements and the RTD is retested. If they are still intact, the reactor is mounted on a sample holder and loaded into the vacuum chamber. And Finally the reactor is sputtered for 40 min with 1 keV Ar^+ ions with a sample current of around 300-500 pA before deposition. Figure F.3 shows XPS and ISS spectra of 3 reactors which have undergone this treatment. No adventitious carbon or any other contaminant is apparent from the XPS spectra and no elements are detected except O and Si with ISS. All the deposited μ -reactors which were cleaned this way proved to be free of Ba and adventitious carbon after deposition, regardless of which wafer they came from.

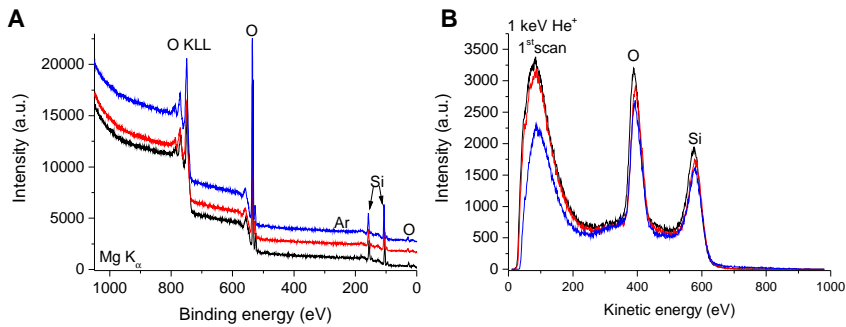


Figure F.3: XPS and ISS spectra recorded of 3 undeposited but previously cleaned μ -reactors. No contamination can be detected in the spectra. A: XPS spectra, which are offset in y direction for ease of view; B: ISS spectra

Bibliography

1. Chorkendorff, I. & Niemantsverdriet, J. W. *Concepts of Modern Catalysis and Kinetics, 2nd edition* ISBN: 9783527316724 (Wiley-VCH Verlag GmbH & Co. KGaA, Weinheim, FRG, 10/2007).
2. Smil, V. Nitrogen cycle and world food production. *World Agric.* **2**, 9–13 (2011).
3. Frydendal, R. *Improving performance of catalysts for water electrolysis: The MnOx case* PhD thesis (2015).
4. Sabatier, P. Hydrogénations et déshydrogénations par catalyse. *Berichte der Dtsch. Chem. Gesellschaft* **44**, 1984–2001. ISSN: 03659496 (07/1911).
5. Nørskov, J. K., Bligaard, T., Rossmeisl, J. & Christensen, C. H. Towards the computational design of solid catalysts. *Nat. Chem.* **1**, 37–46. ISSN: 1755-4330 (04/2009).
6. *Statistical Review of World Energy 2016, BP* <http://www.bp.com/en/global/corporate/energy-economics/statistical-review-of-world-energy.html>. (2017).
7. Pedersen, A. *Elucidating oxygen electrocatalysis with synchrotron X-rays: PEM fuel cells and electrolyzers: An experimental study* PhD thesis (2016).
8. *US National Oceanic & Atmospheric Administration, Earth System Research Laboratory, Global Monitoring Division* <https://www.esrl.noaa.gov/gmd/ccgg/trends/full.html>. (2017).
9. *Global Climate Change, Vital Signs of the Planet, NASA* <https://climate.nasa.gov/vital-signs/carbon-dioxide/>. (2017).
10. *Market data of the Danish energy and gas network, Energinet* <http://energinet.dk/DA/El/Engrosmarked/Udtraek-af-markedsdata/Sider/default.aspx>. (2017).
11. Andersson, M. *et al.* Structure sensitivity of the methanation reaction: H₂-induced CO dissociation on nickel surfaces. *J. Catal.* **255**, 6–19. ISSN: 00219517 (04/2008).
12. Hernandez-Fernandez, P. *et al.* Mass-selected nanoparticles of Pt_xY as model catalysts for oxygen electroreduction. *Nat. Chem.* **6**, 732. ISSN: 1755-4330 (2014).

13. Mai, H. H. *et al.* Nonlinear Optical Properties of Ag Nanoclusters and Nanoparticles Dispersed in a Glass Host. *J. Phys. Chem. C* **118**, 15995–16002. ISSN: 1932-7447 (07/2014).
14. Fenwick, O. *et al.* Tuning the energetics and tailoring the optical properties of silver clusters confined in zeolites. *Nat. Mater.* **15**, 1017–1022. ISSN: 1476-1122 (06/2016).
15. Brok, E. *et al.* Magnetic properties of ultra-small goethite nanoparticles. *J. Phys. D. Appl. Phys.* **47**, 365003. ISSN: 0022-3727 (09/2014).
16. Wulff, G. XXV. Zur Frage der Geschwindigkeit des Wachstums und der Auflösung der Krystallflächen. *Zeitschrift für Krist. - Cryst. Mater.* **34**. ISSN: 2196-7105. doi:10.1524/zkri.1901.34.1.449. <http://www.degruyter.com/view/j/zkri.1901.34.issue-1-6/zkri.1901.34.1.449/zkri.1901.34.1.449.xml> (01/1901).
17. Brodersen, S. H., Grønbjerg, U., Hvolbæk, B. & Schiøtz, J. Understanding the catalytic activity of gold nanoparticles through multi-scale simulations. *J. Catal.* **284**, 34–41. ISSN: 00219517 (11/2011).
18. Tyo, E. C. & Vajda, S. Catalysis by clusters with precise numbers of atoms. *Nat. Nanotechnol.* **10**, 577–588. ISSN: 1748-3387 (07/2015).
19. Vajda, S. & White, M. G. Catalysis Applications of Size-Selected Cluster Deposition. *ACS Catal.* **5**, 7152–7176. ISSN: 2155-5435 (12/2015).
20. Kemppainen, E. *et al.* Scalability and feasibility of photoelectrochemical H₂ evolution: the ultimate limit of Pt nanoparticle as an HER catalyst. *Energy Environ. Sci.* **8**, 2991–2999. ISSN: 1754-5692 (2015).
21. Niemantsverdriet, J. W. *Spectroscopy in Catalysis* ISBN: 9783527611348. doi:10.1002/9783527611348. <http://doi.wiley.com/10.1002/9783527611348> (Wiley-VCH Verlag GmbH & Co. KGaA, Weinheim, Germany, 06/2007).
22. Einstein, A. Über einen die Erzeugung und Verwandlung des Lichtes betreffenden heuristischen Gesichtspunkt. *Ann. Phys.* **322**, 132–148. ISSN: 00033804 (1905).
23. Wagner, C., Riggs, W., Davis, L., Moulder, J. & Mullenberg, G. *Handbook of X-ray Photoelectron Spectroscopy* (Perkin-Elmer Corporation, Eden Prairie, Minnesota, 1979).
24. Krause, M. O. & Ferreira, J. G. K X-ray emission spectra of Mg and Al. *J. Phys. B At. Mol. Phys.* **8**, 2007–2014. ISSN: 0022-3700 (08/1975).
25. Somorjai, G. A. *Chemistry in two dimensions : surfaces* ISBN: 0801411793 (Cornell University Press, Ithaca, 1981).
26. Seah, M. P. & Dench, W. A. Quantitative electron spectroscopy of surfaces: A standard data base for electron inelastic mean free paths in solids. *Surf. Interface Anal.* **1**, 2–11. ISSN: 0142-2421 (02/1979).

27. *NIST X-ray Photoelectron Spectroscopy Database Version 4.1* <http://srdata.nist.gov/xps>. (2012).
28. Shirley, D. A. High-Resolution X-Ray Photoemission Spectrum of the Valence Bands of Gold. *Phys. Rev. B* **5**, 4709–4714. ISSN: 0556-2805 (06/1972).
29. *CasaXPS - Processing Software for XPS, AES, SIMS and More* <http://www.casaxps.com/>. (2017).
30. Smith, D. P. Scattering of Low-Energy Noble Gas Ions from Metal Surfaces. *J. Appl. Phys.* **38**, 340–347. ISSN: 0021-8979 (01/1967).
31. Brongersmal, H. & Mu, P. Analysis of the outermost atomic layer of a surface by low-energy ion scattering. *Surf. Sci.* **35**, 393–412. ISSN: 00396028 (03/1973).
32. Brongersma, H. H., Draxler, M., de Ridder, M. & Bauer, P. Surface composition analysis by low-energy ion scattering. *Surf. Sci. Rep.* **62**, 63–109. ISSN: 01675729 (2007).
33. Cushman, C. V. *et al.* Low Energy Ion Scattering (LEIS). A Practical Introduction to its Theory, Instrumentation, and Applications. *Anal. Methods*, 3419–3439. ISSN: 1759-9660 (2016).
34. Mikhailov, S. N. *et al.* Quantification in low-energy ion scattering: elemental sensitivity factors and charge exchange processes. *Nucl. Inst. Methods Phys. Res. B* **93**, 149–155. ISSN: 0168583X (1994).
35. Niehus, H. & Spitzl, R. Ion-solid interaction at low energies: Principles and application of quantitative ISS. *Surf. Interface Anal.* **17**, 287–307. ISSN: 0142-2421 (06/1991).
36. Niehus, H., Heiland, W. & Taglauer, E. Low-energy ion scattering at surfaces. *Surf. Sci. Rep.* **17**, 213–303. ISSN: 01675729 (05/1993).
37. Strebel, C. *Structure and reactivity of nanoparticles: CO dissociation on Ruthenium, CO induced surface reconstruction of Platinum, Platinum and Platinum-Yttrium alloys for electrochemical Oxygen Reduction Reaction* PhD thesis (2012).
38. Pratontep, S., Carroll, S. J., Xirouchaki, C., Streun, M. & Palmer, R. E. Size-selected cluster beam source based on radio frequency magnetron plasma sputtering and gas condensation. *Rev. Sci. Instrum.* **76**, 045103. ISSN: 00346748 (2005).
39. West, J. B., Bradford, R. S., Eversole, J. D. & Jones, C. R. Flow system for the production of diatomic metal oxides and halides. *Rev. Sci. Instrum.* **46**, 164–168. ISSN: 0034-6748 (02/1975).
40. Granqvist, C. G. & Buhrman, R. A. Ultrafine metal particles. *J. Appl. Phys.* **47**, 2200–2219. ISSN: 0021-8979 (05/1976).
41. Mühlbach, J., Recknagel, E. & Sattler, K. Inert gas condensation of Sb, Bi and Pb clusters. *Surf. Sci.* **106**, 188–194. ISSN: 00396028 (05/1981).

42. Riley, S. J., Parks, E. K., Mao, C. R., Pobo, L. G. & Wexler, S. Generation of continuous beams of refractory metal clusters. *J. Phys. Chem.* **86**, 3911–3913. ISSN: 0022-3654 (09/1982).
43. Sattler, K., Mühlbach, J. & Recknagel, E. Generation of Metal Clusters Containing from 2 to 500 Atoms. *Phys. Rev. Lett.* **45**, 821–824. ISSN: 0031-9007 (09/1980).
44. Frank, F., Schulze, W., Tesche, B., Urban, J. & Winter, B. Formation of metal clusters and molecules by means of the gas aggregation technique and characterisation of size distribution. *Surf. Sci.* **156**, 90–99. ISSN: 00396028 (06/1985).
45. Yatsuya, S., Kamakura, T., Yamauchi, K. & Mihama, K. A New Technique for the Formation of Ultrafine Particles by Sputtering. *Jpn. J. Appl. Phys.* **25**, L42–L44. ISSN: 0021-4922 (01/1986).
46. Penfold, A. S. & Thornton, J. A. *Electrode type glow discharge apparatus* 1975.
47. Thornton, J. A. Magnetron sputtering: basic physics and application to cylindrical magnetrons. *J. Vac. Sci. Technol.* **15**, 171–177. ISSN: 0022-5355 (03/1978).
48. Thornton, J. A. High rate sputtering techniques. *Thin Solid Films* **80**, 1–11. ISSN: 00406090 (06/1981).
49. Hahn, H. & Averback, R. S. The production of nanocrystalline powders by magnetron sputtering. *J. Appl. Phys.* **67**, 1113–1115. ISSN: 0021-8979 (01/1990).
50. Haberland, H. & Karrais, M. Thin films from energetic cluster impact: A feasibility study. *J. Vac. Sci. Technol. A Vacuum, Surfaces, Film.* **10**, 3266–3271. ISSN: 07342101 (1992).
51. Hihara, T. & Sumiyama, K. Formation and size control of a Ni cluster by plasma gas condensation. *J. Appl. Phys.* **84**, 5270–5276. ISSN: 0021-8979 (11/1998).
52. Window, B. & Sharples, F. Magnetron sputtering sources for ferromagnetic material. *J. Vac. Sci. Technol. A Vacuum, Surfaces, Film.* **3**, 10–13. ISSN: 0734-2101 (01/1985).
53. Milchev, A. & Malinowski, J. Phase formation — Stability and nucleation kinetics of small clusters. *Surf. Sci.* **156**, 36–43. ISSN: 00396028 (06/1985).
54. Paoli, E. A. *et al.* Oxygen evolution on well-characterized mass-selected Ru and RuO₂ nanoparticles. *Chem. Sci.* **6**, 190–196. ISSN: 2041-6520 (2015).
55. Wucher, a. & Wahl, M. The formation of clusters during ion induced sputtering of metals. *Nucl. Instruments Methods Phys. Res. Sect. B Beam Interact. with Mater. Atoms* **115**, 581–589. ISSN: 0168583X (07/1996).
56. Plant, S. R., Cao, L. & Palmer, R. E. Atomic Structure Control of Size-Selected Gold Nanoclusters during Formation. *J. Am. Chem. Soc.* **136**, 7559–7562. ISSN: 0002-7863 (05/2014).
57. Von Issendorff, B. & Palmer, R. E. A new high transmission infinite range mass selector for cluster and nanoparticle beams. *Rev. Sci. Instrum.* **70**, 4497. ISSN: 00346748 (1999).

58. Popok, V. N., Barke, I., Campbell, E. E. & Meiwes-Broer, K.-H. Cluster–surface interaction: From soft landing to implantation. *Surf. Sci. Rep.* **66**, 347–377. ISSN: 01675729 (10/2011).
59. Henriksen, T. R., Olsen, J. L., Vesborg, P., Chorkendorff, I. & Hansen, O. Highly sensitive silicon microreactor for catalyst testing. *Rev. Sci. Instrum.* **80**, 124101. ISSN: 1089-7623 (12/2009).
60. Quaade, U. J., Jensen, S. & Hansen, O. Fabrication and modeling of narrow capillaries for vacuum system gas inlets. *J. Appl. Phys.* **97**, 044906. ISSN: 0021-8979 (02/2005).
61. Roth, A. *Vacuum technology* 554. ISBN: 9780444880109 (North-Holland, 1990).
62. O’Hanlon, J. F. *A User’s Guide to Vacuum Technology* ISBN: 9780471467168. doi:10.1002/0471467162. <http://doi.wiley.com/10.1002/0471467162> (John Wiley & Sons, Inc., Hoboken, NJ, USA, 06/2003).
63. Wallis, G. & Pomerantz, D. I. Field Assisted Glass-Metal Sealing. *J. Appl. Phys.* **40**, 3946–3949. ISSN: 0021-8979 (09/1969).
64. Vesborg, P. C. K., Olsen, J. L., Henriksen, T. R., Chorkendorff, I. & Hansen, O. Note: Anodic bonding with cooling of heat-sensitive areas. *Rev. Sci. Instrum.* **81**, 016111. ISSN: 1089-7623 (01/2010).
65. Jensen, R. *μ -reactors for Heterogeneous Catalysis* PhD thesis (2012).
66. Ursua, A., Gandia, L. M. & Sanchis, P. Hydrogen Production From Water Electrolysis: Current Status and Future Trends. *Proc. IEEE* **100**, 410–426. ISSN: 0018-9219 (02/2012).
67. Neyerlin, K. C., Gu, W., Jorne, J. & Gasteiger, H. A. Study of the Exchange Current Density for the Hydrogen Oxidation and Evolution Reactions. *J. Electrochem. Soc.* **154**, B631. ISSN: 00134651 (2007).
68. Sheng, W., Gasteiger, H. A. & Shao-Horn, Y. Hydrogen Oxidation and Evolution Reaction Kinetics on Platinum: Acid vs Alkaline Electrolytes. *J. Electrochem. Soc.* **157**, B1529. ISSN: 00134651 (2010).
69. *NREL Reference Solar Spectral Irradiance: Air Mass 1.5* <http://rredc.nrel.gov/solar/spectra/am1.5/>. (2017).
70. Seger, B., Hansen, O. & Vesborg, P. C. K. A Flexible Web-Based Approach to Modeling Tandem Photocatalytic Devices. *Sol. RRL* **1**, e201600013. ISSN: 2367198X (01/2017).
71. Montoya, J. H. *et al.* Materials for solar fuels and chemicals. *Nat. Mater.* **16**, 70–81. ISSN: 1476-1122 (12/2016).
72. Pourbaix, M. *Atlas of Electrochemical Equilibria in Aqueous Solutions* ISBN: 978-0915567980 (Pergamon Press Ltd., 1966).
73. McCrory, C. C. L., Jung, S., Peters, J. C. & Jaramillo, T. F. Benchmarking Heterogeneous Electrocatalysts for the Oxygen Evolution Reaction. *J. Am. Chem. Soc.* **135**, 16977–16987. ISSN: 0002-7863 (11/2013).

74. Williams, D. B. & Carter, C. B. *Transmission Electron Microscopy* ISBN: 978-0-387-76500-6. doi:10.1007/978-0-387-76501-3. <http://link.springer.com/10.1007/978-0-387-76501-3> (Springer US, Boston, MA, 2009).
75. Goldstein, J. I. *et al.* *Scanning Electron Microscopy and X-ray Microanalysis* ISBN: 978-1-4613-4969-3. doi:10.1007/978-1-4615-0215-9. <http://link.springer.com/10.1007/978-1-4615-0215-9> (Springer US, Boston, MA, 2003).
76. Paul, W. & Steinwedel, H. Notizen: Ein neues Massenspektrometer ohne Magnetfeld. *Zeitschrift für Naturforsch. A* **8**. ISSN: 1865-7109. doi:10.1515/zna-1953-0710. <http://www.degruyter.com/view/j/zna.1953.8.issue-7/zna-1953-0710/zna-1953-0710.xml> (01/1953).
77. Paul, W., Reinhard, H. P. & von Zahn, U. Das elektrische Massenfilter als Massenspektrometer und Isotopentrenner. *Zeitschrift für Phys.* **152**, 143–182. ISSN: 0044-3328 (04/1958).
78. *The 30-minute guide to ICP-MS, Technical note* https://www.perkinelmer.com/CMSResources/Images/44-74849tch_icpmsthirtyminuteguide.pdf. (2017).
79. Dasgupta, N. P., Liu, C., Andrews, S., Prinz, F. B. & Yang, P. Atomic Layer Deposition of Platinum Catalysts on Nanowire Surfaces for Photoelectrochemical Water Reduction. *J. Am. Chem. Soc.* **135**, 12932–12935. ISSN: 0002-7863 (09/2013).
80. Vesborg, P. C. K. & Jaramillo, T. F. Addressing the terawatt challenge: scalability in the supply of chemical elements for renewable energy. *RSC Adv.* **2**, 7933. ISSN: 2046-2069 (2012).
81. Vesborg, P. C. K., Seger, B. & Chorkendorff, I. Recent Development in Hydrogen Evolution Reaction Catalysts and Their Practical Implementation. *J. Phys. Chem. Lett.* **6**, 951–957. ISSN: 1948-7185 (03/2015).
82. Roske, C. W. *et al.* Comparison of the Performance of CoP-Coated and Pt-Coated Radial Junction n + p-Silicon Microwire-Array Photocathodes for the Sunlight-Driven Reduction of Water to H₂ (g). *J. Phys. Chem. Lett.* **6**, 1679–1683. ISSN: 1948-7185 (05/2015).
83. Seger, B. *et al.* Using TiO₂ as a Conductive Protective Layer for Photocathodic H₂ Evolution. *J. Am. Chem. Soc.* **135**, 1057–1064. ISSN: 0002-7863 (01/2013).
84. Bae, D. *et al.* Back-illuminated Si photocathode: a combined experimental and theoretical study for photocatalytic hydrogen evolution. *Energy Environ. Sci.* **8**, 650–660. ISSN: 1754-5692 (2015).
85. Cuevas, A. The Recombination Parameter J₀. *Energy Procedia* **55**, 53–62. ISSN: 18766102 (2014).
86. Seger, B. *et al.* Silicon protected with atomic layer deposited TiO₂: durability studies of photocathodic H₂ evolution. *RSC Adv.* **3**, 25902. ISSN: 2046-2069 (2013).

87. NREL Utility-Scale Energy Technology Capacity Factors http://www.nrel.gov/analysis/tech_cap_factor.html. (2017).
88. Meier, J. C. *et al.* Stability investigations of electrocatalysts on the nanoscale. *Energy Environ. Sci.* **5**, 9319. ISSN: 1754-5692 (2012).
89. LEROY, R. Industrial water electrolysis: Present and future. *Int. J. Hydrogen Energy* **8**, 401–417. ISSN: 03603199 (1983).
90. Dionigi, F. & Strasser, P. NiFe-Based (Oxy)hydroxide Catalysts for Oxygen Evolution Reaction in Non-Acidic Electrolytes. *Adv. Energy Mater.* 1600621. ISSN: 16146832 (07/2016).
91. Dionigi, F. & Strasser, P. NiFe-Based (Oxy)hydroxide Catalysts for Oxygen Evolution Reaction in Non-Acidic Electrolytes. *Adv. Energy Mater.* **6**, 1600621. ISSN: 16146832 (12/2016).
92. Trotochaud, L., Young, S. L., Ranney, J. K. & Boettcher, S. W. Nickel-Iron oxyhydroxide oxygen-evolution electrocatalysts: The role of intentional and incidental iron incorporation. *J. Am. Chem. Soc.* **136**, 6744–6753. ISSN: 15205126 (2014).
93. Klaus, S., Cai, Y., Louie, M. W., Trotochaud, L. & Bell, A. T. Effects of Fe Electrolyte Impurities on Ni(OH)₂/NiOOH Structure and Oxygen Evolution Activity. *J. Phys. Chem. C* **119**, 7243–7254. ISSN: 1932-7447 (04/2015).
94. Friebel, D. *et al.* Identification of Highly Active Fe Sites in (Ni,Fe)OOH for Electrocatalytic Water Splitting. *J. Am. Chem. Soc.* **137**, 1305–1313. ISSN: 0002-7863 (2015).
95. Trotochaud, L., Ranney, J. K., Williams, K. N. & Boettcher, S. W. Solution-cast metal oxide thin film electrocatalysts for oxygen evolution. *J. Am. Chem. Soc.* **134**, 17253–17261. ISSN: 00027863 (2012).
96. Diaz-Morales, O., Ferrus-Suspedra, D. & Koper, M. T. M. The importance of nickel oxyhydroxide deprotonation on its activity towards electrochemical water oxidation. *Chem. Sci.* **7**, 2639–2645. ISSN: 2041-6520 (2016).
97. Nesselberger, M. *et al.* The effect of particle proximity on the oxygen reduction rate of size-selected platinum clusters. *Nat. Mater.* **12**, 919–924. ISSN: 1476-1122 (2013).
98. Mistry, H. *et al.* Tuning Catalytic Selectivity at the Mesoscale via Interparticle Interactions. *ACS Catal.* **6**, 1075–1080. ISSN: 2155-5435 (02/2016).
99. Batchellor, A. S. & Boettcher, S. W. Pulse-Electrodeposited Ni–Fe (Oxy)hydroxide Oxygen Evolution Electrocatalysts with High Geometric and Intrinsic Activities at Large Mass Loadings. *ACS Catal.* **5**, 6680–6689. ISSN: 2155-5435 (11/2015).
100. Görlin, M. *et al.* Tracking Catalyst Redox States and Reaction Dynamics in Ni–Fe Oxyhydroxide Oxygen Evolution Reaction Electrocatalysts: The Role of Catalyst Support and Electrolyte pH. *J. Am. Chem. Soc.* **139**, 2070–2082. ISSN: 0002-7863 (02/2017).

101. Biesinger, M. C., Payne, B. P., Lau, L. W. M., Gerson, A. & Smart, R. S. C. X-ray photoelectron spectroscopic chemical state quantification of mixed nickel metal, oxide and hydroxide systems. *Surf. Interface Anal.* **41**, 324–332. ISSN: 01422421 (04/2009).
102. Biesinger, M. C. *et al.* Resolving surface chemical states in XPS analysis of first row transition metals, oxides and hydroxides: Cr, Mn, Fe, Co and Ni. *Appl. Surf. Sci.* **257**, 2717–2730. ISSN: 01694332 (2011).
103. Grosvenor, A. P., Kobe, B. A., Biesinger, M. C. & McIntyre, N. S. Investigation of multiplet splitting of Fe 2p XPS spectra and bonding in iron compounds. *Surf. Interface Anal.* **36**, 1564–1574. ISSN: 01422421 (2004).
104. Grosvenor, A. P., Biesinger, M. C., Smart, R. S. C. & McIntyre, N. S. New interpretations of XPS spectra of nickel metal and oxides. *Surf. Sci.* **600**, 1771–1779. ISSN: 00396028 (2006).
105. Payne, B. P., Biesinger, M. C. & McIntyre, N. S. Use of oxygen/nickel ratios in the XPS characterisation of oxide phases on nickel metal and nickel alloy surfaces. *J. Electron Spectros. Relat. Phenomena* **185**, 159–166. ISSN: 03682048 (2012).
106. Lambers, E. S., Dykstal, C. N., Seo, J. M., Rowe, J. E. & Holloway, P. H. Room-temperature oxidation of Ni(110) at low and atmospheric oxygen pressures. *Oxid. Met.* **45**, 301–321. ISSN: 0030-770X (1996).
107. Song, F. & Hu, X. Exfoliation of layered double hydroxides for enhanced oxygen evolution catalysis. *Nat. Commun.* **5**, 1–9. ISSN: 2041-1723 (2014).
108. Ng, J. W. D. *et al.* Gold-supported cerium-doped NiOx catalysts for water oxidation. *Nat. Energy* **1**, 16053. ISSN: 2058-7546 (04/2016).
109. Zhang, B. *et al.* Homogeneously dispersed multimetal oxygen-evolving catalysts. *Science (80-.)*. **352**, 333–337. ISSN: 0036-8075 (04/2016).
110. Gong, M. *et al.* An Advanced Ni–Fe Layered Double Hydroxide Electrocatalyst for Water Oxidation. *J. Am. Chem. Soc.* **135**, 8452–8455. ISSN: 0002-7863 (06/2013).
111. Long, X. *et al.* A Strongly Coupled Graphene and FeNi Double Hydroxide Hybrid as an Excellent Electrocatalyst for the Oxygen Evolution Reaction. *Angew. Chemie Int. Ed.* **53**, 7584–7588. ISSN: 14337851 (07/2014).
112. Mei, B. *et al.* Crystalline TiO₂: A Generic and Effective Electron-Conducting Protection Layer for Photoanodes and -cathodes. *J. Phys. Chem. C* **119**, 15019–15027. ISSN: 1932-7447 (07/2015).
113. Riedel, J. *μ-reactor measurements of catalytic activity of mass selected nanoparticles* PhD thesis (2016).
114. Hammer, B. & Norskov, J. K. Why gold is the noblest of all the metals. *Nature* **376**, 238–240. ISSN: 0028-0836 (07/1995).

115. Bone, W. A. & Wheeler, R. V. The Combination of Hydrogen and Oxygen in Contact with Hot Surfaces. *Philos. Trans. R. Soc. A Math. Phys. Eng. Sci.* **206**, 1–67. ISSN: 1364-503X (01/1906).
116. Bone, W. A. & Andrew, G. W. Studies upon Catalytic Combustion. Part I. The Union of Carbon Monoxide and Oxygen in Contact with a Gold Surface. *Proc. R. Soc. A Math. Phys. Eng. Sci.* **109**, 459–476. ISSN: 1364-5021 (11/1925).
117. Haruta, M., Kobayashi, T., Sano, H. & Yamada, N. Novel Gold Catalysts for the Oxidation of Carbon Monoxide at a Temperature far Below 0 °C. *Chem. Lett.* **16**, 405–408. ISSN: 0366-7022 (02/1987).
118. BOND, G. C. & THOMPSON, D. T. Catalysis by Gold. *Catal. Rev.* **41**, 319–388. ISSN: 0161-4940 (01/1999).
119. Hvolbæk, B. *et al.* Catalytic activity of Au nanoparticles. *Nano Today* **2**, 14–18. ISSN: 17480132 (08/2007).
120. Lopez, N. *et al.* On the origin of the catalytic activity of gold nanoparticles for low-temperature CO oxidation. *J. Catal.* **223**, 232–235. ISSN: 00219517 (04/2004).
121. Janssens, T. V. W. *et al.* Insights into the reactivity of supported Au nanoparticles: combining theory and experiments. *Top. Catal.* **44**, 15–26. ISSN: 1022-5528 (06/2007).
122. Zhang, L., Persaud, R. & Madey, T. E. Ultrathin metal films on a metal oxide surface: Growth of Au on TiO₂ (110). *Phys. Rev. B* **56**, 10549–10557. ISSN: 0163-1829 (10/1997).
123. Parker, S., Grant, A., Bondzie, V. & Campbell, C. Island growth kinetics during the vapor deposition of gold onto TiO₂(110). *Surf. Sci.* **441**, 10–20. ISSN: 00396028 (10/1999).
124. Yang, F., Chen, M. S. & Goodman, D. W. Sintering of Au Particles Supported on TiO₂ (110) during CO Oxidation. *J. Phys. Chem. C* **113**, 254–260. ISSN: 1932-7447 (01/2009).
125. Min, B. K., Wallace, W. T., Santra, A. K. & Goodman, D. W. Role of Defects in the Nucleation and Growth of Au Nanoclusters on SiO₂ Thin Films. *J. Phys. Chem. B* **108**, 16339–16343. ISSN: 1520-6106 (10/2004).
126. Wallace, W., Min, B. & Goodman, D. The stabilization of supported gold clusters by surface defects. *J. Mol. Catal. A Chem.* **228**, 3–10. ISSN: 13811169 (03/2005).
127. Gao, J. *et al.* Recent advances in methanation catalysts for the production of synthetic natural gas. *RSC Adv.* **5**, 22759–22776. ISSN: 2046-2069 (2015).
128. Kiendl, I., Klemm, M., Clemens, A. & Herrman, A. Dilute gas methanation of synthesis gas from biomass gasification. *Fuel* **123**, 211–217. ISSN: 00162361 (05/2014).

129. Kopyscinski, J., Seemann, M., Moergeli, R., Biollaz, S. & Schildhauer, T. Synthetic natural gas from wood: Reactions of ethylene in fluidised bed methanation. *Appl. Catal. A Gen.* **462-463**, 150–156. ISSN: 0926860X (07/2013).
130. *Haldor Tops e SNG methanation catalysts* <http://www.topsoe.com/processes/sng>. (2017).
131. Sabatier, M. P. & Senderens, J.-B. Nouvelles sunthèses du méthane. *C. R. Hebd. Seances Acad. Sci.* **134**, 514–516 (1902).
132. Mills, G. A. & Steffgen, F. W. Catalytic Methanation. *Catal. Rev.* **8**, 159–210. ISSN: 0161-4940 (01/1974).
133. VANNICE, M. The catalytic synthesis of hydrocarbons from H₂/CO mixtures over the group VIII metals I. The specific activities and product distributions of supported metals. *J. Catal.* **37**, 449–461. ISSN: 00219517 (06/1975).
134. VANNICE, M. The catalytic synthesis of hydrocarbons from H₂/CO mixtures over the group VIII metals II. The kinetics of the methanation reaction over supported metals. *J. Catal.* **37**, 462–473. ISSN: 00219517 (06/1975).
135. VANNICE, M. The catalytic synthesis of hydrocarbons from H₂/CO mixtures over the group VIII metals III. Metal-support effects with Pt and Pd catalysts. *J. Catal.* **40**, 129–134. ISSN: 00219517 (10/1975).
136. VANNICE, M. The catalytic synthesis of hydrocarbons from H₂/CO mixtures over the group VIII metals IV. The kinetic behavior of CO hydrogenation over Ni catalysts. *J. Catal.* **44**, 152–162. ISSN: 00219517 (07/1976).
137. VANNICE, M. The catalytic synthesis of hydrocarbons from H₂/CO mixtures over the Group VIII metals V. The catalytic behavior of silica-supported metals. *J. Catal.* **50**, 228–236. ISSN: 00219517 (11/1977).
138. Bligaard, T. *et al.* The Brønsted–Evans–Polanyi relation and the volcano curve in heterogeneous catalysis. *J. Catal.* **224**, 206–217. ISSN: 00219517 (05/2004).
139. ANDERSSON, M. *et al.* Toward computational screening in heterogeneous catalysis: Pareto-optimal methanation catalysts. *J. Catal.* **239**, 501–506. ISSN: 00219517 (04/2006).
140. Tian, D. *et al.* Bimetallic Ni–Fe total-methanation catalyst for the production of substitute natural gas under high pressure. *Fuel* **104**, 224–229. ISSN: 00162361 (02/2013).
141. Tavares, M. CO Disproportionation on Silica-Supported Nickel and Nickel-Copper Catalysts. *J. Catal.* **147**, 525–534. ISSN: 00219517 (06/1994).
142. Tavares, M., Alstrup, I., Bernardo, C. & Rostrup-Nielsen, J. Carbon Formation and CO Methanation on Silica-Supported Nickel and Nickel–Copper Catalysts in CO + H₂Mixtures. *J. Catal.* **158**, 402–410. ISSN: 00219517 (02/1996).
143. Engbæk, J., Lytken, O., Nielsen, J. H. & Chorkendorff, I. CO dissociation on Ni: The effect of steps and of nickel carbonyl. *Surf. Sci.* **602**, 733–743. ISSN: 00396028 (02/2008).

144. Liu, C.-j., Ye, J., Jiang, J. & Pan, Y. Progresses in the Preparation of Coke Resistant Ni-based Catalyst for Steam and CO₂ Reforming of Methane. *Chem-CatChem* **3**, 529–541. ISSN: 18673880 (03/2011).
145. Kim, K. & Winograd, N. X-ray photoelectron spectroscopic studies of nickel-oxygen surfaces using oxygen and argon ion-bombardment. *Surf. Sci.* **43**, 625–643. ISSN: 00396028 (06/1974).
146. Masini, F. *et al.* Exploring the phase space of time of flight mass selected Pt x Y nanoparticles. *Phys. Chem. Chem. Phys.* **16**, 26506–26513. ISSN: 1463-9076 (2014).
147. *ImageJ - Image Processing and Analysis in Java (National Institutes of Health, USA)* <https://imagej.nih.gov/ij/>. (2017).
148. Otsu, N. A Threshold Selection Method from Gray-Level Histograms. *IEEE Trans. Syst. Man. Cybern.* **9**, 62–66. ISSN: 0018-9472 (01/1979).
149. Barker, J. A. & Henderson, D. What is "liquid"? Understanding the states of matter. *Rev. Mod. Phys.* **48**, 587–671. ISSN: 0034-6861 (10/1976).
150. Wilhelm, J. & Frey, E. Radial Distribution Function of Semiflexible Polymers. *Phys. Rev. Lett.* **77**, 2581–2584. ISSN: 0031-9007 (09/1996).
151. Srolovitz, D., Egami, T. & Vitek, V. Radial distribution function and structural relaxation in amorphous solids. *Phys. Rev. B* **24**, 6936–6944. ISSN: 0163-1829 (12/1981).



Cite this: *Energy Environ. Sci.*, 2015, 8, 2991

Scalability and feasibility of photoelectrochemical H₂ evolution: the ultimate limit of Pt nanoparticle as an HER catalyst†

E. Kemppainen,^a A. Bodin,^b B. Sebok,^b T. Pedersen,^c B. Seger,^b B. Mei,^b D. Bae,^b P. C. K. Vesborg,^b J. Halme,^a O. Hansen,^c P. D. Lund^a and I. Chorkendorff^{*b}

The recent surge in investigating electrocatalysts for the H₂ evolution reaction is based on finding a cheap alternative to Pt. However platinum's excellent catalytic activity means very little catalyst needs to be used. The present study combines model experiments with numerical modeling to determine exactly how little catalyst is needed. Specifically we investigate ultra-low Pt loadings for use in photoelectrochemical H₂ evolution using TiO₂-Ti-pn⁺Si photocathodes. At a current density of 10 mA cm⁻², we photocathodically evolve H₂ at +465, +450, +350 and +270 mV vs., RHE at Pt loadings of 1000, 200, 50, and 10 ng cm⁻² corresponding to HER overpotentials of $\eta_{1000\text{ng}} = 32$ mV, $\eta_{200\text{ng}} = 46$ mV, $\eta_{50\text{ng}} = 142$ mV, and $\eta_{10\text{ng}} = 231$ mV. To put this in perspective, if 30% of the world's current annual Pt production was used for H₂ evolution catalysis, using a loading of 100 ng cm⁻² and a current of 10 mA cm⁻² would produce 1 TW_{average} of H₂. The photoelectrochemical data matched the modeling calculations implying that we were near the fundamental maximum in performance for our system. Furthermore modeling indicated that the overpotentials were dominated by mass transfer effects, rather than catalysis unless catalyst loadings were less than 1000 ng cm⁻².

Received 15th July 2015,
Accepted 25th August 2015

DOI: 10.1039/c5ee02188j

www.rsc.org/ees

Broader context

In the last decade there has been an enormous push to find a cheaper, more earth-abundant catalyst than Pt for the hydrogen evolution reaction. This push is based on the theory that Pt is un-scalable if society would completely convert to a H₂ based society. Interestingly, there have been relatively few works actually investigating if and how un-scalable using platinum as a H₂ evolution catalyst actually is. In this manuscript we take the specific case of using a photoelectrochemical water splitting device, and determine how little Pt is needed (and thus the scalability) to effectively evolve H₂ from both an experimental and a theoretical modeling standpoint. Our experimental results allow us to come very close to achieving our limit imposed by our modeling, but not surpass it. We feel this verifies the validity of our model, and thus the fundamental limits of Pt for H₂ evolution in our system. From these results we find that the Pt consumed/terawatt would be on the order of 10% of the annual worldwide Pt production (depending upon photocurrent and overpotential). Thus this work should help to quantitatively put into perspective the scalability of Pt for photoelectrochemical water splitting.

Introduction

Currently the primary energy source for electricity and transportation is from fossil fuels, and the replacement of these fuels by hydrogen is one of the ways to continue to fulfil society's energy demand, while simultaneously reducing greenhouse gas emissions.^{1,2}

While we have ways to convert between hydrogen and electricity (*via* fuel cells and (photo)electrolysers), there are still several challenges that need to be addressed.²⁻⁵

Renewable hydrogen can be produced using different approaches, *i.e.* electrolysis powered by a renewable source of energy, like wind energy or sunlight. Additionally, an integrated photoelectrocatalytic (PEC) approach, where solar energy is directly converted into hydrogen is also a possibility.²⁻⁵ Nevertheless, industrial scalability of both technologies requires reduction of capital costs to obtain hydrogen prices on a \$ per J level compatible to those of today's fossil fuel prices. It is widely considered that capital costs of either electrolysers or PEC devices can be reduced by utilizing cheap and abundantly available materials to drive the hydrogen evolution reaction (HER) or the oxygen

^a Department of Applied Physics, New Energy Technologies Group, Aalto University, P.O. Box 14100, FI-00076 AALTO, Finland

^b Department of Physics, CINP, Technical University of Denmark, DK-2800, Kgs. Lyngby, Denmark. E-mail: ibchork@fysik.dtu.dk

^c Department of Micro- and Nanotechnology, Technical University of Denmark, DK-2800, Kgs. Lyngby, Denmark

† Electronic supplementary information (ESI) available: Simulation details. See DOI: 10.1039/c5ee02188j



evolution reaction (OER) to replace platinum group metals, which are relatively scarce and expensive.⁶ In particular in the last 5–10 years fast progress has been made in the development of nonprecious metal HER catalysts to be implemented into these clean-energy technologies.^{2,7–14} Nevertheless, to date platinum is still the most widely used HER catalyst due to its world-record exchange current density and low Tafel slope. Additionally, Pt is known to be highly durable in the acidic environments used in electrolyzers or PEC devices.¹⁵

While a low Tafel slope is certainly an important requirement for HER catalysts used in electrolyzers, typically operated at high current densities ($\sim \text{A cm}^{-2}$), in photoelectrocatalytic devices high Pt exchange current density appears to be a more important criterion when chosen the HER catalyst.² This is due to the lower current densities of 5–20 mA cm^{-2} , which PEC devices will operate at due to solar flux limitations. Furthermore, it is often neglected in the development of efficient PEC devices that catalysts (HER or OER) will absorb light reducing the light limited current density provided by the photon absorber. Consequently, the catalysts amount used to drive HER or OER in such a device is a critical issue and significant light absorption by the catalyst material must be reduced.¹⁶

The best nonprecious metal HER catalysts reported so far can be separated into different classes of materials such as sulphides and phosphides, which usually contain transition metal cations of Mo, Co, Fe, or Ni.^{2,10–14} With an overpotential of 50 mV to produce current densities of 10 mA cm^{-2} in acidic electrolytes, FeP nanoparticles are the state-of-the-art nonprecious HER catalysts.¹⁷ Nevertheless exchange current densities are still an order of magnitude lower than that of conventional Pt HER catalysts. In general, high loadings are required for these non-noble HER catalysts to obtain low overpotentials. Hence, cost savings are lower than would be expected and the high-catalyst loading required might prevent the use in PEC devices. Indeed it was recently shown for CoP-modified Si photocathodes that significantly higher mass loadings (10 times) are required to achieve fill factors similar to those of Pt-modified electrodes, which is in agreement with the lower HER activity of CoP.¹⁸ These high loadings of CoP drastically reduced the photocurrent density due to parasitic light absorption decreasing the overall efficiency of the Si-based photocathode.¹⁸ While this might not be an issue for small band gap photocathodes on the backside of a monolithic device, the efficiency will be limited in a design with a large band gap photocathode and Pt appears to be still the optimal choice for HER catalysts in these PEC devices.^{16,19} Additionally the stability of these non-precious metal catalysts have yet to be proven. The state-of-the-art FeP dissolves rather fast¹⁷ and the reported data on Ni₂P and CoP also suggest that these materials are far from being stable making it a challenge to utilize them with low coverage.^{11,12} It should also be mentioned that although there is no particular reason to believe Pt should not be stable under the conditions described here, there could also be long term issues that have not been realized yet.²⁰ Thus even though these new classes of recently discovered HER materials are promising alternatives to the conventional Pt-group metals, a material matching the performance of Pt has not yet been

reported. Taking this into account Pt appears to be still the optimal choice for HER catalysts in PEC devices and the question arises if Pt HER catalysts might be feasible on a TW level in a PEC device?

With an annual Pt production of 180 ton per year⁶ the Pt loading necessary to operate a photocathode at moderate current densities (on the order of 10 mA cm^{-2}),^{2,21} and low overpotentials (<50 mV) determines the potential for Pt to be used in a PEC device. Only recently have researchers started to probe the idea that ultra-low Pt loadings for the HER could make this catalyst scalable even on the TW level. Dasgupta *et al.*²² used atomic layer deposition (ALD) to produce Pt nanoparticles on the surface of TiO₂-coated Si microwire arrays. However, due to the procedure and the substrate used, defining an exact limit for the required Pt loading appears to be difficult. Thus, the Pt nanoparticle loadings that were studied ranged from $\sim 280 \text{ ng cm}^{-2}$ (per geometrical electrode area) to several micrograms per cm^2 , and the Pt nanoparticle size-distribution was loading dependent. Another approach is to nanostructure or pattern the HER catalyst.^{23,24} Chen *et al.*²⁴ investigated patterned Pt structures with different electrode filling fractions to reduce the parasitic light absorption effect of HER catalysts.²⁴ While the authors obtained quite impressive results from these films, the exact loading was difficult to determine due to surface roughness of the films.

In this work we investigate ultra-low loadings of Pt nanoparticles for scalable photocathodic H₂ evolution. This approach differs from the film based approach and allows us a uniform dispersion of platinum across our electrode. While we use a cluster-source sputtering approach to optimize the conditions, there are many methods to produce nanoparticles cheaper *via* solution based methods.

In this work we use well defined, size-selected Pt nanoparticles (diameter of 5 nm). The photoelectrocatalytic performance of planar TiO₂-protected n⁺p-Si photocathodes in acidic solutions was investigated experimentally. Furthermore, a model combining the effects of mass transport, equilibrium hydrogen coverage and HER kinetics was used to describe the current-overpotential characteristics of these planar Si-photoelectrodes partially covered with Pt HER nanoparticles. The effect of mass transport and HER kinetics on the catalytic properties of individual Pt particles and the photoelectrode assemblies were assessed by this model and a good agreement between the experimental and theoretical data was obtained. Thus, using a combined experimental and theoretical approach the Pt HER catalyst amount needed for TW scale-up was assessed. The data provided here shows the dependence of Pt nanoparticle loading on overpotential for hydrogen evolution. For an acceptable HER overpotential of 50 mV, 54 tons of Pt metal, corresponding to a coverage of 100 ng cm^{-2} Pt ($d = 5 \text{ nm}$) on a planar electrode, is required to achieve a TW scale-up with a PEC device operated at 10 mA cm^{-2} (12% solar-to-hydrogen efficiency). If larger overpotentials for HER are feasible, even lower Pt utilization is possible. This work shows that the use of Pt nanoparticles HER catalyst may potentially be a viable option for terawatt scale PEC applications.

It should be noted that for any PEC device, there needs to be a corresponding anodic reaction. While understanding these



anodic reactions (such as O₂ evolution) is important, this work only focuses on photocathodic H₂ evolution and its corresponding overpotential and does not analyse anodic reactions or their corresponding overpotentials. For readers interested in how overpotentials at both electrodes effect photocatalytic efficiency we refer to the excellent review by Walter *et al.*²⁵ and more recent works by Hu *et al.*²⁶ and Seitz *et al.*²⁷

Experimental

Preparation of TiO₂-protected Si-based photocathodes

TiO₂ protected silicon photocathodes with n⁺p junctions were produced as in our previous work.^{19,28}

Preparation of Pt nanoparticle and electrochemical characterization

Mass-selected Pt nanoparticles were produced in a five-step process by (1) sputtering a Pt target with Ar⁺-ions in a magnetron sputter head, (2) allowing the sputtered Pt to condense into nanoparticles in a LN₂-cooled “aggregation zone”, where both He and Ar was present to facilitate faster aggregation,²⁹ (3) super-sonic expanding the nanoparticles from the aggregation zone into UHV through an aperture and into an electronic lens system, which focuses the negatively charged particles into a narrow beam, (4) mass-selecting the nanoparticles in a lateral time-of-flight mass-selector,³⁰ and (5) landing the particles on the substrate.

The particle production was conducted in a Nano-Beam 2011 nanoparticle source (Birmingham Instruments Inc.) with a base pressure in the low 10⁻¹⁰ mbar range, which is connected to another UHV system (Omicron NanoTechnology), wherein the nanoparticles are deposited. This latter chamber is equipped with characterization techniques such as XPS (SPECS XR 50 X-ray gun coupled to Omicron NanoSAM 7 channel energy analyser), ISS (Omicron ISE100 ion gun) and SEM (ZEISS UHV-Gemini Supra), and has a base pressure in the low 10⁻¹¹ mbar range. For further details about the preparation of mass selected nanoparticles see Hernandez-Fernandez *et al.*³¹

Platinum particles having a mass of 850 000 amu were deposited on the planar TiO₂-protected Si photocathodes with calculated loadings of 10, 50, 200 and 1000 ng cm⁻², respectively. The deposited photocathodes were characterized in UHV with XPS using Mg K α radiation. Furthermore, one additional sample for each loading was made, for investigation with SEM. The 10 ng cm⁻² sample was also investigated with ISS, in order to verify that Pt was on the surface.

The mass of 850 000 amu was chosen for the time-of-flight mass-selector because it corresponds to a particle diameter of 5 nm. The size distribution of the deposited nanoparticles was determined with *ex situ* TEM imaging (Tecnai T20 G2) with samples prepared on TEM grids under the same deposition conditions as the photocathodes. (Higher resolution TEM images can be found in the ESI†.) The size of the nanoparticles on the pictures was examined using the software ImageJ. Only particles with circularity between 0.8–1 were analysed in order to avoid taking into account particles that were landed on top of

each other. SEM images were taken of one sample of each loading. The images were obtained with an acceleration voltage of 7 kV, and a beam current of 400 pA with an in-lens detector, which detects almost exclusively secondary electrons in order to visualize the topography of the surface.

All Pt wires were cleaned immediately before use in photoelectrochemical testing. Cleaning consisted first of a 15 second rinse in fresh aqua regia, then thorough washing in millipore water. Finally the electrodes were flame annealed.

For the photoelectrochemical measurements, a Bio-Logic VSP potentiostat along with EC Lab software was used. The photoelectrochemical H₂ evolution experiments were performed in a three-electrode cell with an H-cell design and a glass frit between the working and counter electrode compartments to prevent any crossover. The experiments were carried out in an aqueous 1 M HClO₄ (Aldrich 99.99%) solution. The electrolyte was cleaned overnight using a chronoamperometric measurement with two Pt mesh electrodes used as working and counter electrodes. For PEC measurements a Pt mesh counter electrode and saturated Hg/HgSO₄ reference electrode (VWR International) were used. The solution was saturated with hydrogen gas 30 minutes before the start of any experiment, and for the entire duration of the experiment.

A 1000 W xenon lamp (Oriel) was used with a 635 nm cut-off filter and an AM1.5 filter to simulate the red part of the solar spectrum. The light intensity reaching the sample was calibrated to match that of the total light intensity of the red part of the solar spectrum ($\lambda > 635$ nm, 38.6 mW cm⁻²). For all cyclic voltammograms (CV's) the electrodes were scanned at a sweep rate of 50 mV s⁻¹. The 3rd anodic sweep is shown in all graphs. The actual loading of Pt nanoparticles was verified using Inductively Coupled Plasma Mass Spectrometry (ICP-MS, iCAP-QC ICP-MS, Thermo Fisher Scientific) after dissolving the size-selected Pt nanoparticles in aqua regia solution. For all samples, the ICP-MS results closely matched that determined from the cluster source deposition.

Simulation details

All calculations were done for a model system where spherical Pt nanoparticles of 5 nm diameter were simulated. It was assumed that each Pt nanoparticle was embedded 0.25 nm into a 100 nm thick TiO₂ substrate (Fig. 1). This means that 95% of its (free sphere-) surface area was exposed to electrolyte. The conductivity of the TiO₂ substrate was assumed to be 1 S m⁻¹,³² corresponding to slightly reduced TiO₂ but it could be much lower without affecting the modelling results (Table 1). The electrode was assumed to be an array of identical unit cells, so to simplify calculations it was simulated as a single Pt particle in a 2D cylindrical unit cell, corresponding to a diffusional domain approximation with uniform particle spacing.^{33,34} Periodic boundary conditions were replaced by zero-flux boundary conditions at the outer edge of the cell, whose area (*i.e.* radius, R_{cell}) corresponds to the average Pt loading (L_{Pt}) over the electrode area.

$$R_{\text{cell}} = \frac{d_{\text{c-c}}}{2} = \sqrt{\frac{4r_{\text{Pt}}^3 \rho_{\text{Pt}}}{3L_{\text{Pt}}}} \quad (1)$$



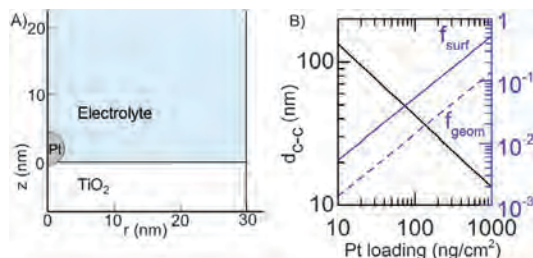


Fig. 1 (A) Detail of the model geometry near the Pt particle. Symmetry axis is at $r = 0$ and the vertical line at $r \approx 30$ nm is the outer wall of the simulation cell (Pt loading is 50 ng cm^{-2}). The TiO_2 substrate continues to $z = -100$ nm and electrolyte to $z = 100 \mu\text{m}$. (B) The properties of the simulated unit cell. The black line shows the average center-to-center distance of the platinum nanoparticles as a function of the loading. The solid blue line shows the ratio of Pt surface area to the geometrical electrode area (f_{surf}) and the dashed blue line the fraction of the electrode area covered with Pt (f_{geom}).

where $d_{\text{c-c}}$ is the average center-to-center distance between nearest neighbor nanoparticles, r_{Pt} the radius of the nanoparticles (2.5 nm), ρ_{Pt} the density of Pt (21.45 g cm^{-3}) and L_{Pt} the amount of Pt per electrode area ($10\text{--}1000 \text{ ng cm}^{-2}$). As shown in Fig. 1 a Pt loading of 10 ng cm^{-2} corresponds to an average center-to-center $d_{\text{c-c}}$ of 134 nm , while a Pt loading of 1000 ng cm^{-2} corresponds to about a 13.4 nm distance. For comparison, simulations were performed for a TiO_2 film covered with a 2.5 nm thick uniform Pt film, later referred to as “flat Pt”. The radius of the simulation cell was set to 50 nm in that case.

The current density $i_{\text{Pt/geom}}$ was calculated by integrating the local current density at the Pt surface over the exposed surface area and dividing it by either the exposed Pt area (A_{Pt}) or the area of the unit cell (A_{geom}).

The steady state was calculated with a transient simulation starting from equilibrium conditions at 0 V vs. RHE . The concentration profiles took at most about 10 seconds simulation

time to converge to steady state, and all simulations were run for 20 s simulation time to ensure steady state. IV -curves were calculated using the state at the last calculated time point.

To facilitate comparisons between simulated overpotential and measured IV -curves of the whole devices, the effect of the silicon PV cell was simulated with the IV -curve of an ideal PV cell

$$i = i_{\text{ph}} + i_{\text{rec}} \left(e^{\frac{q_c V}{n k_B T}} - 1 \right) \quad (2)$$

where i_{ph} is the photocurrent density (and in this model also the short circuit current density), i_{rec} corresponds to recombination rates in the device, V is the photovoltage, and n is the ideality factor. With PV cells made of silicon diffusion current ($n = 1$) dominates the IV curve near the open circuit voltage, so $n = 1$ was used to simulate the losses in the PV device.³⁹ Under the chosen illumination ($\lambda > 635 \text{ nm}$, 38.6 mW cm^{-2}) the maximum photocurrents of the measured Si-based photocathodes were determined to be between -22 and -22.4 mA cm^{-2} and the average open circuit voltage was 0.495 V vs. RHE in agreement with previous reports on similar Si-based photocathodes.²⁸ Therefore, i_{ph} and $V = V_{\text{OC}}$ were chosen to be -22.0 mA cm^{-2} and 0.495 V vs. RHE ($i_{\text{rec}} = 9.8196 \times 10^{-8} \text{ mA cm}^{-2}$), respectively. The material properties and simulation parameters used in this work are summarized in Table 1 (for further information about the simulations, e.g. the hydrogen evolution kinetics see ESI†).

Results and discussion

Characterization of size-selected Pt nanoparticles

TEM images of the Pt nanoparticles were taken from different areas of the Cu TEM grids they were deposited on, and the resulting size distribution along with a close-up picture of typical particles (Fig. 2A) is shown in Fig. 2. According to the determined size-distribution, the average particle size is $5.0 \pm 0.3 \text{ nm}$.

Table 1 Material properties and simulation parameters

Symbol	Explanation	Value
T	Temperature	298.15 K
h_{el}	Electrolyte diffusion layer thickness	$5 \mu\text{m}$
h_{TiO_2}	TiO_2 layer thickness	100 nm
σ_{TiO_2}	Conductivity of TiO_2	$1 \text{ S m}^{-1.32}$
d_{Pt}	Pt particle diameter	5 nm
ρ_{Pt}	Pt density	$21450 \text{ kg m}^{-3.35}$
σ_{Pt}	Pt conductivity	$9.43 \times 10^6 \text{ S m}^{-1.35}$
$i_{0,V}$	Volmer reaction exchange current density	$100 \text{ mA cm}^{-2.36}$
Γ_{H}	Ratio of Heyrovsky and Volmer rates	0.36
Γ_{T}	Ratio of Tafel and Volmer rates	9.5
Θ^0	Equilibrium H-coverage	0.67^{37}
$c_{\text{H}^+,0}$	Bulk proton concentration	1.0 M
$c_{\text{H}_2,0}$	Bulk H_2 concentration	0.7698 mM^{38}
D_{H^+}	Proton diffusion coefficient	$9.3110 \times 10^{-5} \text{ cm}^2 \text{ s}^{-1.35}$
$D_{\text{ClO}_4^-}$	Perchlorate ion diffusion coefficient	$1.7908 \times 10^{-5} \text{ cm}^2 \text{ s}^{-1.35}$
D_{H_2}	H_2 diffusion coefficient	$5.1100 \times 10^{-5} \text{ cm}^2 \text{ s}^{-1.35}$
μ_{H^+}	Proton mobility	$3.624 \times 10^{-3} \text{ cm}^2 (\text{V s})^{-1.35}$
$\mu_{\text{ClO}_4^-}$	Perchlorate ion mobility	$6.970 \times 10^{-4} \text{ cm}^2 (\text{V s})^{-1.35}$
i_{ph}	Si PV-cell photocurrent density	-22.0 mA cm^{-2}
V_{oc}	Si PV-cell open circuit voltage	0.495 V vs. RHE
i_{rec}	Recombination current density	$9.8196 \times 10^{-8} \text{ mA cm}^{-2}$



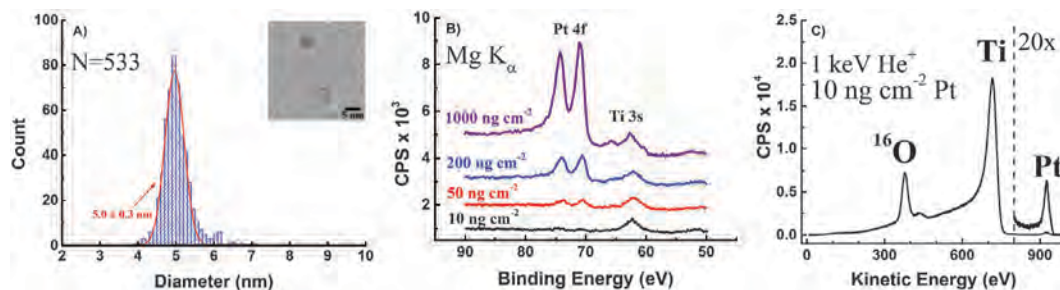


Fig. 2 Characterization of size-selected Pt nanoparticles: (A) size-distribution of the deposited Pt nanoparticles determined by bright-field TEM imaging and Gaussian distribution fitted to the data (red curve). The inset shows a close-up of typical particles. (B) XPS spectra of Pt 4f peaks for different particle loadings. (C) ISS spectra of a sample with 10 ng cm^{-2} Pt loading confirming the successful deposition of Pt particles.

Furthermore, Pt nanoparticles deposited on TiO_2 -protected Si photocathodes were investigated by XPS. Wide range survey spectra only showed O, Ti, C and Pt on the surface of the samples confirming that the Si surface was fully covered by a TiO_2 film (Fig. S2 in ESI†).

Detailed spectra of the region around the Pt 4f peaks taken in case of each loading are shown in Fig. 2B.

The Pt 4f peak is decreasing with each loading and finally disappears in case of the 10 ng cm^{-2} Pt loading due to the low loading, which is below the detection limit of XPS. However, significant catalytic activity and reasonably low overpotentials were determined for the sample with 10 ng cm^{-2} Pt loading, meaning that Pt contaminations (e.g. during catalyst preparation or from the electrolyte) below the detection limit of XPS could significantly contribute to the activity of presumably Pt-free materials. Thus, XPS analysis is certainly not a reliable way to prove the absence of Pt in non-noble metal catalyst used in ORR or HER reaction and surface spectroscopic methods with much higher sensitivity are required to unambiguously show the absence of trace amounts of noble metals like Pt. Here, in order to have spectroscopic evidence for the successful deposition of 10 ng cm^{-2} Pt on TiO_2 -protected Si photocathodes, the sample was further investigated using ISS. The peak at approx. 927 eV can clearly be assigned to Pt (Fig. 2C). The intensity of the signal suggests that even lower Pt loadings can be easily identified using ISS which makes ISS more suitable for detecting trace amounts of Pt in non-noble metal catalysts.

Finally, each of the 4 different loading Pt samples were investigated with SEM. Pt particles can be seen as bright dots on the rough TiO_2 substrate, and the differences in coverage's are clearly distinguishable (Fig. 3).

Photoelectrochemical hydrogen evolution with size-selected Pt nanoparticles on $\text{TiO}_2/\text{np}^+\text{-Si}$ photocathodes

The mass-selected Pt nanoparticle ($d = 5 \text{ nm}$) modified TiO_2 -protected Si photocathodes with Pt mass loadings of 10, 50, 200 and 1000 ng cm^{-2} (confirmed by ICP-MS) were tested in photoelectrochemical hydrogen evolution in acidic electrolyte. The respective *IV*-curves of the four different samples are shown in Fig. 4. For all samples an open-circuit photovoltage (V_{oc}) of $495 \pm 4 \text{ mV}$ and a light-limited photocurrent of $\sim 22 \text{ mA cm}^{-2}$

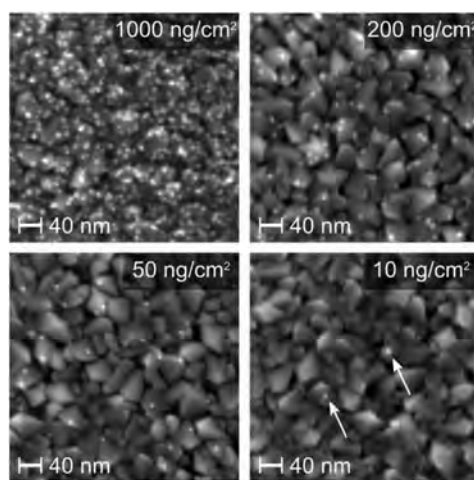


Fig. 3 SEM micrographs of four samples of different Pt nanoparticle loading. The particles in the lowest-loading image are marked by arrows.

was obtained. These values are in good agreement with our previously reported TiO_2 -protected Si photocathodes modified with Pt nanoparticles using a conventional drop casting procedure of a Pt-salt solution.^{20,28} Furthermore, the results indicate that light blocking due to the HER catalyst is completely circumvented in these experiments.¹⁹

For comparison of the different Pt mass-loadings the overpotential η (defined as $V_{\text{oc}} - V_{10 \text{ mA cm}^{-2}}$) necessary to drive a current density of 10 mA cm^{-2} will be used as a figure of merit. The overpotentials required to achieve 10 mA cm^{-2} are highly dependent on the Pt nanoparticle loading. With the highest Pt loading (1000 ng cm^{-2}) $\eta_{1000 \text{ ng}} = 32 \text{ mV}$ was obtained, which is also in good agreement with similar previously reported Si-based photocathodes modified by drop casted Pt nanoparticles or compact Pt films.^{20,28} With lower loadings the required overpotential increases and overpotential of $\eta_{200 \text{ ng}} = 46 \text{ mV}$, $\eta_{50 \text{ ng}} = 142 \text{ mV}$, and $\eta_{10 \text{ ng}} = 231 \text{ mV}$ were measured, respectively.

One issue we did find with the ultra-low loading Pt samples was that even after extensive cleaning, there were still issues



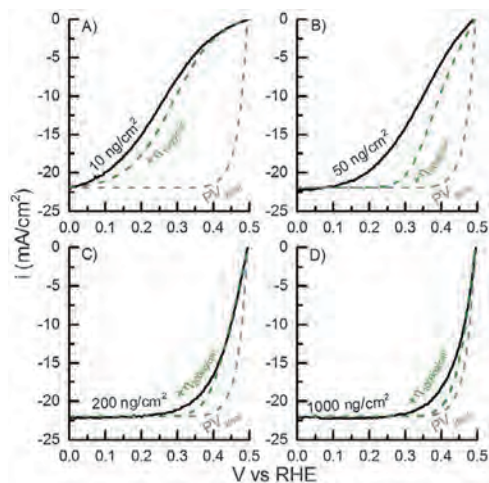


Fig. 4 Measured IV -curves of 10, 50, 200 and 1000 ng cm^{-2} Pt loadings on TiO_2 -covered $p^+|p|n^+$ -Si PV cell (black lines) and the simulated IV -curves for the same loadings including the calculated HER overpotentials (η) (green dashed lines). The IV -curve for an ideal PV cell with $n = 1$ (grey dashed line, eqn (2)) is shown for comparison.

with contamination during photoelectrochemical testing. This was attributed to the epoxy resin encasing the photoelectrode. As expected, the issues due to contamination worsened with decreasing loading. Nevertheless for all of the samples shown in this work, at least 5 stable scans were completed before any noticeable drops in performance were measured. However, due to these contamination issues, we could not accurately do long term testing such as chronoamperometry measurements.

Simulations

Effects of Pt loading on HER overpotential. To fully describe the experimental behaviour observed the IV -curves for the different Pt nanoparticle loadings were simulated using a ratio of Tafel and Volmer rates (r_T) of 9.5 and a diffusion layer thickness of $5 \mu\text{m}$ (for further explanation see text in ESI† and Fig. S4 and S7). The comparison between the simulated IV -curves revealed that the simulation describes the trend for the different Pt nanoparticle loadings quite well (Fig. 4, green). For the lowest Pt nanoparticle loading (10 ng cm^{-2} , Fig. 4A) the measured IV -curve is described accurately at low overpotentials and low current densities. Hence, the exchange current density assumed in the simulations is close to the real exchange rate, which is supported by simulations for different exchange current densities (Fig. S7, ESI†). In case of highest Pt nanoparticle loadings (200 ng cm^{-2} and 1000 ng cm^{-2} , Fig. 4C and D) the calculations, however, slightly overestimated the HER overpotential initially at low current densities, which was most likely due to differences between true and simulated mass transport conditions (see next section and Fig. S5, ESI†). For the two low Pt nanoparticle loadings (10 ng cm^{-2} and 50 ng cm^{-2} , Fig. 4A and B), HER reaction kinetics is a major part of the total overpotential. Therefore, the effects of reaction kinetics and mass transport were thoroughly analyzed.

Independent of the Pt nanoparticle loading, the deviation of the calculated overpotential and the experimental data increases with higher current densities and the simulation clearly underestimates the experimental HER overpotential. The difference between calculated and measured IV -curve at current densities higher than 15 mA cm^{-2} may be related to ideal PV cell characteristics overestimating the fill factor compared to the real silicon PV device used in the experiment.

HER mass transport losses. To elaborate on the differences between measured and calculated IV -curves, the effect of mass transport phenomena on the simulated IV -curves (dashed green curves in Fig. 4) for the different Pt nanoparticle loadings was further explored. To analyze the effects due to mass transport losses we can write the overpotential as followed:

$$\eta_{\text{total}} = \eta_{\text{kinetic}} + \eta_{\text{MT}} \quad (3)$$

where η_{total} is the total overpotential and η_{kinetic} and η_{MT} are the losses due to kinetic and mass transfer, respectively. While losses due to mass transfer are not typically thought of as overpotentials, denoting it this way allows us to directly compare the kinetic and mass transfer losses. Although this direct summation of the two components appears convenient, it is accurate only with small current densities, because eqn (3) is an approximation based on the Taylor expansion of Butler-Volmer equation.⁴⁰ However, both total and mass transport overpotential could be determined accurately (eqn (S5b) and (S11b)) and the relative significance of mass transfer and reaction kinetics could be distinguished.

Fig. 5A shows the average current density, normalized by the geometric electrode area i_{geom} as a function of total overpotential (solid lines), and pure mass transfer overpotential for the different Pt nanoparticle loadings used in Fig. 4. The mass transport overpotential was determined almost completely by H_2 concentration, because the changes in the surface concentrations of protons and H_2 were similar (both due to HER and mass transport), but the equilibrium concentration of H_2 was small compared to the proton concentration, and therefore it dominated the Nernst potential.

The dashed lines in Fig. 5A overlap, which illustrates that mass transport losses are almost independent of Pt loading. The losses increase slightly when loading is decreased, but in all cases they correspond to approximately the same H_2 transport rate. The fact that mass transfer losses are basically independent of Pt loadings can be rationalized by realizing that the H_2 molecules have to travel a much longer distance in the axial direction (about $5 \mu\text{m}$, see Fig. S5, ESI†) than the distance between two neighboring Pt particles (134 nm for 10 ng cm^{-2}).

Although the H_2 transport rate in simulations for Fig. 4 and 5 was unusually high, it explains the total overpotential with 1000 ng cm^{-2} better than our initial estimate that was based on typical literature values (Fig. S5, ESI†).^{41,42} The cause of high mass transport rate may be associated to the potential sweep rate used in the photoelectrochemical hydrogen evolution experiments, which was partly necessitated by contamination and performance drop with low loadings (for further details see ESI†).

Fig. 5B illustrates what fraction of the total overpotential is due to mass transfer, and it is evident that with 1000 ng cm^{-2} , even with the high mass transport rate, mass transport losses



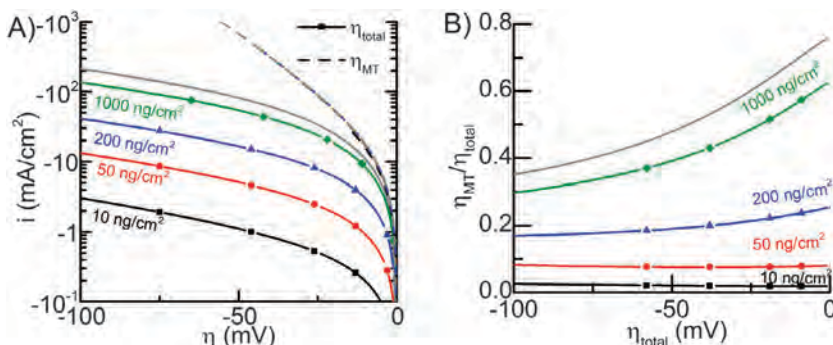


Fig. 5 (A) The simulated HER overpotentials for various loadings. Dotted lines indicate i - V curves assuming only mass transfer losses with no kinetic losses (i.e. perfect catalysis). Solid lines indicate i - V curves of total overpotential (i.e. mass transfer losses plus kinetic losses). (B) The fraction of mass transport overpotential of the total overpotential. The grey lines in both (A) and (B) correspond to a flat Pt surface.

correspond to more than half of the total overpotential up to about 20 mA cm^{-2} current density (25 mV total overpotential).

Considerations of Pt consumption for efficient PEC hydrogen evolution devices

Using the experimental and theoretical results obtained for the well-defined, mass-selected Pt nanoparticle modified photocathodes investigated in this study, the Pt consumption depending on an affordable overpotential for hydrogen evolution can be defined based on the calculated iV -curves. The amount of H_2 needed to be produced if society switches to a completely sustainable future is unknown, but it will most likely be in the terawatt range. The average PEC power density is calculated using:

$$P_{\text{avg}} = 0.15 \times i \times 1.23 \text{ V} = 0.1854 \text{ V} \times i \quad (4)$$

where 0.15 is the capacity factor of sunlight and i current density. A capacity factor of 0.15 is a conservative estimate and usually a capacity factor of 20% is suggested by NREL.⁴³ For 10 mA cm^{-2} this yields an average power (H_2 generation rate) of 18.54 W m^{-2} , or 1.854 mW cm^{-2} . The required area per TW is given by:

$$A_{\text{TW}} = 1 \frac{\text{TW}}{P_{\text{avg}}} = \frac{542000 \text{ km}^2}{i [\text{mA cm}^{-2}]} \quad (5)$$

The required area can be calculated to be 54200 km^2 and 27100 km^2 for 10 mA cm^{-2} and 20 mA cm^{-2} , respectively. Finally, Pt consumption is calculated by multiplying the area per TW by the Pt loading.

Depending on the acceptable overpotential the total Pt consumption can finally be calculated (Fig. 6). While the exact numbers for irradiation, capacity factor, and efficiency can be debated, the current numbers allow an order of magnitude determination of the feasibility of using Pt in photoelectrochemical devices and although some simulation parameters might not correspond to the actual reaction kinetics, they provide a reasonably good fit to experimental results for current densities up to 20 mA cm^{-2} .

For a photocathode covered with a compact Pt film the overpotential to achieve a current density of 10 mA cm^{-2} in the

simulated conditions is 9 mV, while for high Pt nanoparticle loadings of 1000 ng cm^{-2} , 12 mV overpotential is required. The portion of mass transport losses is about 6.5 mV, so higher Pt loadings will not significantly improve the photoelectrode performance (Fig. 5) and a Pt loading of 1000 ng cm^{-2} can be considered as a compact Pt film electrode with negligible kinetic losses. Therefore, in a photoelectrochemical device with minimal overpotential losses, Pt nanoparticle loadings of 1000 ng cm^{-2} are sufficient for standard illumination conditions (AM1.5) and the total Pt consumption would be 542.4 tons per TW. On the other hand, if an increase in overpotential to 50 mV, which is well within the range of a good non-noble metal HER catalyst,^{10–13,17} is acceptable due to a sufficient photovoltage, the Pt consumption drops by an order of magnitude to about 100 ng cm^{-2} , corresponding to 54 tons per TW_{avg} (for Pt nanoparticles with $d = 5 \text{ nm}$).

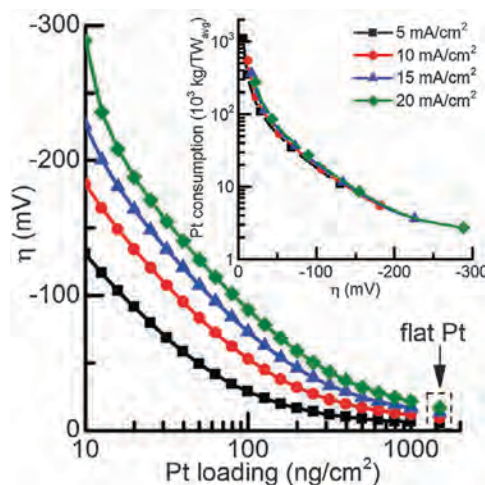


Fig. 6 Overpotential as a function of Pt loading for current densities in the range from 5–20 mA cm^{-2} . The inset the total Pt consumption to reach $1 \text{ TW}_{\text{avg}}$ of water splitting as a function of overpotential using a capacity factor of 15%.



For comparison, the total global mining production of Pt is around 180 tons per year and the annual net consumption for jewelry and automotive catalytic converters are ~ 70 ton and ~ 65 ton respectively. In this light, the use of Pt in an efficient PEC system might be feasible even on a TW scale.^{6,44,45} The total energy demand could realistically be an order of magnitude larger (10 TW) but the investment will also be distributed over many years and furthermore Pt can be recovered.

When platinum is compared to the scalability of other well-known non-noble metal HER catalysts (Table 2), such as MoS₂,⁴⁶ CoP,¹² Ni₂P,¹¹ and FeP¹⁷ it appears to be one of the most scalable. In Table 2 we assumed a photoelectrolysis capacity factor of 15% for all materials and used 2010 materials production data.⁶ In most cases the metal would be the limiting factor in production, however for FeP it would be the phosphorous. An overpotential of 75 mV was used because all of the optimal catalysts have data at this point. Choosing a lower overpotential would increase the amount of catalyst needed per TW for all of the materials, but it would have the least effect on Pt since it has the lowest Tafel slope. For our Pt data we used the modelled value at 50 ng cm⁻² because at that loading we can reach the order of magnitude of current (~ 10 mA cm⁻²) that will be needed in a photoelectrolysis device. It should be noted that if we used our experimental values at 50 ng cm⁻² in Table 2, the amount needed would be slightly higher, but would still be relatively low in comparison to MoS₂, CoP, and Ni₂P.

An important thing to consider when reviewing Table 2 is to realize that the value for Pt is extremely optimized whereas materials such as MoS₂ and phosphides still have a much larger potential to be optimized by nanoscaling and better dispersion. While FeP appears very promising from Table 1, it has severe durability issues (doubling of overpotential within ~ 16 hours) thus limiting its current applicability. Since FeP has only recently been discovered, it is unknown whether these durability issues are fundamental or are simply a technical barrier that can be overcome.

In the present model, Pt nanoparticles with a diameter of 5 nm are assumed. It should be noted that the particle size also affects the overpotential for a given Pt loading: for larger particles less surface area per mass unit is available, so local current densities are higher and higher kinetic overpotentials are expected for the same mass loading. Correspondingly, the overpotential will decrease as the Pt nanoparticle diameter decreases and less Pt is needed to match a given overpotential for any current density. This effect is highlighted in Fig. S7 (ESI[†]) for Pt nanoparticles with different diameters ($d = 2, 5,$

and 10 nm). However, this will come with a cost of stability as the surface energy will go up with decreasing diameter and the particles will be more prone to sintering and corrosion.⁴⁷ Durability is an issue that we have not analyzed with respect to platinum's practical feasibility. Whether the Pt consumption/terawatt for a PEC water splitting device will be stable/durable for 1 month, 1 year or 10 years would obviously be of critical importance.

Interestingly, this approach of reducing the catalyst loading having well-dispersed nanoparticles may not work for a photoanode. In case of photoanode protection with TiO₂ thin films we have recently shown that band bending in TiO₂ protection layers should be avoided and a pinch-off effect will occur when using nanoparticulate OER catalysts.⁴⁸ Thus, even if another less scarce OER catalyst than IrO₂ applicable for water oxidation in acidic environment will be found, the well-dispersed nanoparticle approach would not work using TiO₂ protection layers. Unfortunately, except for compact IrO₂ thin films, TiO₂ protection layers, currently are the only known protection layers suitable in these conditions.^{20,28,48–50} On the other hand photoanode protection might be easier in alkaline electrolyte and NiO thin films might be most promising.⁵¹

Conclusions

In this work an experimental and theoretical approach was used to address the scalability of a photoelectrochemical device to the TW level using a TiO₂-Ti-pn⁺Si photocathode as stable photon absorber and Pt as hydrogen evolution catalyst. The experimentally determined dependence of the HER overpotential with Pt nanoparticle loading was reproduced in the modelling approach. Thus, effects of mass-transport and hydrogen evolution kinetics could be investigated and the modelling results could be utilized to connect the Pt loadings and overpotentials required for hydrogen evolution. The presented data clearly shows that for an acceptable overpotential of 50 mV, which is the current state-of-the-art overpotential for non-noble metal HER catalysts (FeP: 1 mg cm⁻²), only 100 ng cm⁻² of Pt or 54 tons per TW_{avg} are needed to scale-up a PEC device to the TW scale. Thus, this work demonstrated that 30% of the world's current annual Pt production could be utilized to achieve a 1 TW_{avg} worth of H₂ generation (assuming current densities of 10 mA cm⁻² and a capacity factor of 15%) at overpotentials of 50 mV (Pt nanoparticles $d = 5$ nm).

Acknowledgements

For funding we gratefully acknowledge the Danish National Research Foundation's Center for Individual Nanoparticle Functionality (DNRF54) and Nordic Energy Research for Nordic Initiative for Solar Fuel Development (N-I-S-F-D).

Notes and references

- 1 N. S. Lewis and D. G. Nocera, *Proc. Natl. Acad. Sci. U. S. A.*, 2006, **103**, 15729–15735.

Table 2 Current state-of-the-art H₂ evolution catalysts and what percent of the global production (2010 values) would be needed to produce 1 TW worth of H₂ at an overpotential of 75 mV and 15% capacity

Catalyst	Ref.	$i@75$ mV η (mA mg ⁻¹)	% of Annual production/TW
MoS ₂	46	0.6	2200 (of Mo)
CoP	12	6.5	670 (of Co)
Ni ₂ P	11	1.5	220 (of Ni)
FeP	17	48	0.13 (of P)
Pt	This work	171 600	16



- 2 P. C. K. Vesborg, B. Seger and I. Chorkendorff, *J. Phys. Chem. Lett.*, 2015, 951–957.
- 3 H. B. Gray, *Nat. Chem.*, 2009, 1, 112.
- 4 S. Dahl and I. Chorkendorff, *Nat. Mater.*, 2012, 11, 100–101.
- 5 N. S. Lewis, *Science*, 2007, 315, 798–801.
- 6 P. C. K. Vesborg and T. F. Jaramillo, *RSC Adv.*, 2012, 2, 7933.
- 7 J. K. Nørskov, T. Bligaard, A. Logadottir, J. R. Kitchin, J. G. Chen, S. Pandalov and U. Stimming, *J. Electrochem. Soc.*, 2005, 152, J23.
- 8 B. Hinnemann, P. G. Moses, C. J. Bonde, K. P. Jørgensen, J. H. Nielsen, S. Hørch, I. Chorkendorff and J. K. Nørskov, *J. Am. Chem. Soc.*, 2005, 127, 5308–5309.
- 9 T. F. Jaramillo, K. P. Jørgensen, J. Bonde, J. H. Nielsen, S. Hørch and I. Chorkendorff, *Science*, 2007, 317, 100–102.
- 10 J. R. McKone, B. F. Sadtler, C. A. Werlang, N. S. Lewis and H. B. Gray, *ACS Catal.*, 2013, 3, 166–169.
- 11 E. J. Popczun, J. R. McKone, C. G. Read, A. J. Biazchi, A. M. Wiltrout, N. S. Lewis and R. E. Schaak, *J. Am. Chem. Soc.*, 2013, 135, 9267–9270.
- 12 E. J. Popczun, C. G. Read, C. W. Roske, N. S. Lewis and R. E. Schaak, *Angew. Chem., Int. Ed.*, 2014, 53, 5427–5430.
- 13 J. Kibsgaard and T. F. Jaramillo, *Angew. Chem., Int. Ed.*, 2014, 53, 14433–14437.
- 14 Y. Hou, B. L. Abrams, P. C. K. Vesborg, M. E. Björketun, K. Herbst, L. Bech, A. M. Setti, C. D. Damsgaard, T. Pedersen, O. Hansen, J. Rossmeisl, S. Dahl, J. K. Nørskov and I. Chorkendorff, *Nat. Mater.*, 2011, 10, 434–438.
- 15 S. Trasatti, *Electrochim. Acta*, 2000, 45, 2377–2385.
- 16 B. Seger, I. E. Castellì, P. C. K. Vesborg, K. W. Jacobsen, O. Hansen and I. Chorkendorff, *Energy Environ. Sci.*, 2014, 7, 2397–2413.
- 17 J. F. Callejas, J. M. McEnaney, C. G. Read, J. C. Crompton, A. J. Biazchi, E. J. Popczun, T. R. Gordon, N. S. Lewis and R. E. Schaak, *ACS Nano*, 2014, 8, 11101–11107.
- 18 C. W. Roske, E. J. Popczun, B. Seger, C. G. Read, T. Pedersen, O. Hansen, P. C. K. Vesborg, B. S. Brunenschwig, R. E. Schaak, I. Chorkendorff, H. B. Gray and N. S. Lewis, *J. Phys. Chem. Lett.*, 2015, 2, 1679–1683.
- 19 D. Bae, T. Pedersen, B. J. Seger, M. Malizia, A. Kuznetsov, O. Hansen, I. Chorkendorff and P. C. K. Vesborg, *Energy Environ. Sci.*, 2015, 8, 650–660.
- 20 B. Seger, D. S. Tilley, T. Pedersen, P. C. K. Vesborg, O. Hansen, M. Grätzel and I. Chorkendorff, *RSC Adv.*, 2013, 3, 25902–25907.
- 21 J. R. McKone, N. S. Lewis and H. B. Gray, *Chem. Mater.*, 2014, 26, 407–414.
- 22 N. P. Dasgupta, C. Liu, S. Andrews, F. B. Prinz and P. Yang, *J. Am. Chem. Soc.*, 2013, 135, 12932–12935.
- 23 L. Ji, M. D. McDaniel, S. Wang, A. B. Posadas, X. Li, H. Huang, J. C. Lee, A. a. Demkov, A. J. Bard, J. G. Ekerdt and E. T. Yu, *Nat. Nanotechnol.*, 2014, 10, 84–90.
- 24 Y. Chen, K. Sun, H. Audesirk, C. Xiang and N. Lewis, *Energy Environ. Sci.*, 2015, 8, 1736–1747, DOI: 10.1039/C5EE00311C.
- 25 M. Walter, E. L. Warren, J. R. McKone, S. W. Boettcher, Q. Mi, E. A. Santori and N. S. Lewis, *Chem. Rev.*, 2010, 110, 6446–6473.
- 26 S. Hu, C. Xiang, S. Haussener, A. D. Berger and N. S. Lewis, *Energy Environ. Sci.*, 2013, 6, 2984–2993.
- 27 L. C. Seitz, Z. Chen, A. J. Forman, B. a. Pinaud, J. D. Benck and T. F. Jaramillo, *ChemSusChem*, 2014, 7, 1372–1385.
- 28 B. Seger, T. Pedersen, A. B. Laursen, P. C. K. Vesborg, O. Hansen and I. Chorkendorff, *J. Am. Chem. Soc.*, 2013, 135, 1057–1064.
- 29 H. Haberland, *J. Vac. Sci. Technol., A*, 1992, 10, 3266.
- 30 B. von Issendorff and R. E. Palmer, *Rev. Sci. Instrum.*, 1999, 70, 4497–4501.
- 31 P. Hernandez-Fernandez, F. Masini, D. N. McCarthy, C. E. Strebler, D. Friebel, D. Deiana, P. Malacrida, A. Nierhoff, A. Bodin, A. M. Wise, J. H. Nielsen, T. W. Hansen, A. Nilsson, I. E. L. Stephens and I. Chorkendorff, *Nat. Chem.*, 2014, 6, 732–738.
- 32 U. Diebold, *Surf. Sci. Rep.*, 2003, 48, 53–229.
- 33 H. Reller, E. Kirowa-Eisner and E. Gileadi, *J. Electroanal. Chem. Interfacial Electrochem.*, 1982, 138, 65–77.
- 34 R. G. Compton, G. G. Wildgoose, N. V. Rees, I. Streeter and R. Baron, *Chem. Phys. Lett.*, 2008, 459, 1–17.
- 35 *CRC Handbook of Chemistry and Physics*, ed. D. R. Lide, CRC Press, 95th edn, 2014.
- 36 J. Durst, C. Simon and H. A. Gasteiger, *J. Electrochem. Soc.*, 2015, 162, F190–F203.
- 37 N. M. Markovic and P. N. J. Ross, *Surf. Sci. Rep.*, 2002, 45, 117–229.
- 38 K. Aoki, H. Toda, J. Yamamoto, J. Chen and T. Nishiumi, *J. Electroanal. Chem.*, 2012, 668, 83–89.
- 39 U. Stutenbaumer and B. Mesfin, *Renewable Energy*, 1999, 18, 501–512.
- 40 A. J. Bard and L. R. Faulkner, *Electrochemical Methods: Fundamentals and Applications*, WILEY-VCH Verlag, 2001.
- 41 K. Stephan and H. Vogt, *Electrochim. Acta*, 1979, 24, 11–18.
- 42 C. A. C. Sequeira, D. M. F. Santos, B. Šljukić and L. Amaral, *Braz. J. Phys.*, 2013, 43, 199–208.
- 43 http://www.nrel.gov/analysis/tech_cap_factor.html.
- 44 P. J. Loferski, *2012 Minerals Yearbook*, Platinum-group metals, 2013.
- 45 World Platinum Investment Council, *Platinum Quarterly Q1 2015*, 2015.
- 46 H. Wang, Z. Lu, D. Kong, J. Sun, T. M. Hymel and Y. Cui, *ACS Nano*, 2014, 8, 4940–4947.
- 47 J. C. Meier, I. Katsounaros, C. Galeano, H. J. Bongard, A. A. Topalov, A. Kostka, A. Karschin, F. Schüth and K. J. J. Mayrhofer, *Energy Environ. Sci.*, 2012, 5, 9319.
- 48 B. Mei, T. Pedersen, P. Malacrida, D. Bae, R. Frydendal, O. Hansen, P. C. K. Vesborg, B. Seger and I. Chorkendorff, *J. Phys. Chem. C*, 2015, 119, 15019–15027.
- 49 S. Hu, M. R. Shaner, J. A. Beardslee, M. Lichterman, B. S. Brunenschwig and N. S. Lewis, *Science*, 2014, 344, 1005–1009.
- 50 B. Mei, B. Seger, T. Pedersen, M. Malizia, O. Hansen, I. Chorkendorff and P. C. K. Vesborg, *J. Phys. Chem. Lett.*, 2014, 5, 1948–1952.
- 51 B. Mei, A. A. Permyakova, R. Frydendal, D. Bae, T. Pedersen, P. Malacrida, O. Hansen, I. E. L. Stephens, P. C. K. Vesborg, B. Seger and I. Chorkendorff, *J. Phys. Chem. Lett.*, 2014, 5, 3456–3461.



Oxygen evolution on well characterized mass-selected NiFe nanoparticles: mechanism and size-effect

Claudie Roy^{1*}, Bela Sebok^{1*}, Elisabetta M. Fiordaliso², Anders Bodin¹, Søren B Scott¹, Daniel B Trimarco¹, Christian D. Damsgaard^{1,2}, Jakob Kibsgaard¹, Ifan E L Stephens¹, Ib Chorkendorff¹

¹: Department of Physics, SurfCat, Technical University of Denmark, DK-2800, Kgs. Lyngby, Denmark

²: Center for electron nanoscopy, Technical University of Denmark, DK-2800 Kgs. Lyngby, Denmark

Abstract In our current study, we investigated well-characterized model systems of mass-selected NiFe nanoparticles for the oxygen evolution reaction in alkaline media. We tested the catalysts electrochemically in 1 M KOH and our results show that the particles have one of the highest turnover frequency in alkaline media among the non-noble oxygen evolution catalysts reported. During a 1000 h chronoamperometric measurement at 1.6 V vs RHE the particles showed no degradation of performance. We also investigated the effect of particle proximity on the activity and found that the particles are less active the closer they are to each other. Furthermore, we explored the changes induced by reaction conditions in the crystal structure of the particles with XRD and HRTEM and the changes in the binding state of Ni and Fe with XPS.

*: These authors contributed equally to the manuscript

Sintering of mass-selected Au and AuTi clusters on SiO₂: A STEM and computational study

Yubiao Niu¹, Philomena Schlexer², Bela Sebok³, Ib Chorkendorff³, Gianfranco Pacchioni², Richard E Palmer¹

¹: Nanoscale Physics Research Laboratory, School of Physics and Astronomy, University of Birmingham, B15 2TT, Birmingham, United Kingdom

²: Dipartimento di Scienza dei Materiali, Università di Milano-Bicocca, 20125 Milano, Italy

³: Department of Physics, SurfCat, Technical University of Denmark, DK-2800, Kgs. Lyngby, Denmark

Abstract In our current study we explore the potential of stabilizing nanometer sized Au particles on SiO₂ by alloying them with Ti. The sintering of mass-selected Au and AuTi nanoparticles is investigated with atomic resolution aberration corrected HAADF STEM imaging and computational modelling, showing increased resistance against sintering in case of the particles alloyed with Ti. We also show with ISS that after heating in an oxidative environment there are still gold atoms on the surface of the alloyed particles.